Mechanism and Prediction of Mild Steel Corrosion in Aqueous Solutions Containing

Carboxylic Acids, Carbon Dioxide, and Hydrogen Sulfide

A dissertation presented to

the faculty of

the Russ College of Engineering and Technology of Ohio University

In partial fulfillment

of the requirements for the degree

Doctor of Philosophy

Aria Kahyarian

December 2018

This dissertation titled

Mechanism and Prediction of Mild Steel Corrosion in Aqueous Solutions Containing

Carboxylic Acids, Carbon Dioxide, and Hydrogen Sulfide

by

ARIA KAHYARIAN

has been approved for the Department of Chemical and Biomolecular Engineering and

the Russ College of Engineering and Technology by

Srdjan Nesic

Professor of Chemical and Bimolecular Engineering

Dennis Irwin

Dean, Russ College of Engineering and Technology

ABSTRACT

KAHYARIAN, ARIA, Ph.D., December 2018, Chemical Engineering

Mechanism and Prediction of Mild Steel Corrosion in Aqueous Solutions Containing

Carboxylic Acids, Carbon Dioxide, and Hydrogen Sulfide

Director of Dissertation: Srdjan Nesic

Pipeline corrosion in upstream oil and gas production and transmission facilities is a major design and maintenance concern. Corrosion in such environments is, to the most part, the results of the presence of an aqueous phase containing weak acids such as carboxylic acids, carbonic acid, and hydrogen sulfide. The proper understanding of encountered corrosion processes and reliable predicted corrosion rates are essential for major design decisions relating to material selection, pipe wall thickness allowance and adoption of appropriate maintenance procedures, such as use of corrosion inhibitors and frequency of in-line inspections. The health, safety, and environmental impact of possible failures and the significant economic burden of maintenance has been the driving force for the better understanding of corrosion mechanisms and more accurate and reliable corrosion rate predictions.

The present study is focused on improving the mechanistic understanding of the corrosion process in such environments and further use of the developed knowledge to improve the prediction of corrosion rate. In this regard, the fundamental mechanisms of corrosion in the presence of all the major corrosive species, specifically, carboxylic acids, carbonic acid, and hydrogen sulfide, are discussed. In contrast to the commonly accepted corrosion mechanisms involving these species, the findings in the present study suggest

that they are not directly reduced during the corrosion process. The high corrosivity of such environments was therefore determined to be the result of their chemical dissociation at the vicinity of the metal surface that acts as an additional source for hydrogen ions. The findings of the present study showed that corrosion of mild steel in such environments is in fact a much simpler process than it was believed previously, and in electrochemical sense it is no differenet from steel corrosion in acidic solutions. That is of great significance, both in terms of the general understanding of the corrosion process and also in terms of developing mechanistic corrosion rate predictive models. These models commonly use experimental data obtained in laboratory settings for calibration and are expected to reasonably predict the behavior of such systems in much harsher and more complex conditions encountered in industrial environments. Since extrapolation is an inherent part of such calculations, these models are only as reliable as the accuracy of their mechanistic foundations. Ultimately, the mechansitic findings of this study were used to propose a unified perspective into corrosion in the presence of weak acids to sevrve as a framework for other similar corrosion scenarios with any weak acid that might be present in the solution.

DEDICATION

To my Parrents, Effat and Reza, for all their support and

sacrifice throught my life long journey.

ACKNOWLEDGEMENTS

It has been a great privilege to have Prof. Srdjan Nesic as my mentor and academic advisor. Without his guidance and critical inputs this study would not be concluded. I am forever grateful for his support and advice in both my academic and personal life.

I would like to also acknowledge the faculty and staff at the Institute for Corrosion and Multiphase Flow Technology, whom without their commitment and effort the experimental work in this study would not be possible.

I would like to extend my appreciation to my dissertation committee members, Dr. Marc Singer, Dr. John Staser, Dr. Howard Dewald, and Dr. Dina Lopez, for generous dedication of their precious time and expertise to this study.

TABLE OF CONTENTS

Page

LIST OF TABLES

LIST OF FIGURES

PREFACE

On March 2, 2006, in Prudhoe Bay, Alaska, an estimated 5,000 barrel oil spill was detected [1]. The incident ultimately brought production in one of the largest US oil fields to a halt for necessary maintenance, depriving the country of about 8% of its total crude oil production at the time. The economic impact reverberated in Alaska and in the east coast states as their local refineries and petrochemical industries relied on the supply of Alaskan crude oil. Beyond that, global crude oil prices rose and US and European stock prices dropped in the response to the shutdown [2]. The cause of the spillage was determined to be corrosion inside transmission pipelines. The incident cost the company more than $270 million in penalties and civil suits, the shutdown resulted in an estimated loss or deferment in production of more than 30 million barrels of oil [3,4].

In November 2013, a leakage in an underground gas pipeline in Qingdao in eastern China led to an explosion. The cause of the leakage was determined to be the corrosion inside the pipeline. The incident left 62 fatalities and 136 injured. In addition, the material cost of the incident was estimated to be $124.9 million [5].

In August 2000, the leakage and explosion of a gas pipeline as a results of pipe wall thinning by internal corrosion in New Mexico left behind 12 fatalities and $16.5 million in property loss and civil penalties [6].

Perhaps it is the possibility of such tragic accidents that signifies the importance of understanding, detection and mitigation of corrosion. Corrosion is known to be the cause of most pipeline failures in the Gulf of Mexico [7], and it has been responsible for several of the largest incidents in oil and gas refineries [8]. In fact, corrosion is the

continuously occurring deterioration of existing multibillion-dollars facilities and infrastructural networks. In a study by the US Federal Highway Administration, the direct cost of corrosion in the US in 1998 was estimated to be $276 billion, equivalent to 3.1% of the nation's gross domestic production (GDP) [9]. The same study reports a $5.1 billion direct cost of corrosion in both the oil and gas exploration/production and petroleum refining sectors. The global cost of corrosion in 2013 was estimated by NACE[1] to be a staggering $2.5 trillion [10], more than the GDP of Switzerland, Netherland, and Saudi Arabia, combined. The same study suggests that adoption of good practices in corrosion detection and prevention can reduce this cost by 15% to 35%.

The literature on the significance of pipeline corrosion in the oil and gas industry can be traced back to 1940s. However, the subject area was not developed into a scientific matter until 1970s. There have been tremendous developments in the understanding of the corrosion of mild steel on many fronts ever since. In the particular case of the oil and gas industry, despite the high corrosivity of the environment, due to the economical and availability issues mild steel remains the first choice of material for large facilities such as pipelines. The use of mild steel, with its low resistance to corrosion, makes the understanding, prediction, detection, and mitigation of corrosion an essential for this industry.

The corrosion in the oil and gas production and transmission facilities is usually caused by the presence of the co-produced aqueous phase, acid gases, and dissolved acidic compounds. The three major compounds causing the high corrosivity in such

---

[1] National Association of Corrosion Engineers.

environments are carboxylic acids, carbon dioxide (CO_2), and hydrogen sulfide (H_2S). The presence of these species in the aqueous phase makes an acidic, highly corrosive solution. The present study is an effort to further elucidate *how mild steel corrosion occurs*, and *how it can be quantified*. As it becomes apparent in the following chapters, the gradual improvements in understanding of the corrosion process, the development of better experimental practices, and the easier access to comprehensive mathematical simulations, have set the stage for an in depth investigation of the underlying fundamental mechanistic aspects of this process.

The scopes of this dissertation were expanded multiple times over the course of the study, as the new findings paved the way for more in-depth investigations. In an attempt to reflect this gradually improved understanding, this document is presented as a series of self-contained articles. These chapters are aimed to determine the role of the following species: carboxylic acids, carbon dioxide, and hydrogen sulfide, in corrosion of mild steel, some of which have already been published as papers in peer reviewed journals. The chapters, the analysis, and discussions are structured in three main parts associated with each species.

In *Part A*, the role of carboxylic acids is initially discussed based on a series of targeted experimental measurments. The discussion is then further expanded in order to verify mechanistic observations in a wider range of environmental conditions, and allow for development of a detailed mechanistic model for prediction of corrosion rates in such environments.

In *Part B*, the mechanism of mild steel corrosion in the presence of carbon dioxide, the most common type of corrosion in the oil and gas industry, is discussed. This section starts with a detailed review of the existing literature, as far as it concerns the basic mechanisms and mathematical modeling of this system. Later on, the knowledge gap is identified, the scope of the study is defined, a hypothesis is developed, and the necessary environmental conditions for its verification are discussed. The experimentation and theoretical analyses in the present study were done in two parts. The first part covers the moderate carbon dioxide partial pressures and the corresponding mathematical model was developed under an ideal solution assumption. The second part expands the scope of the study both experimentally and computationally. In that part, the partial pressure of carbon dioxide was increased to higher levels and the mathematical model was expanded to include non-ideal solution properties. The results of the second part confirmed the initial mechanistic findings, while the extended range of the environmental conditions reveals additional valuable mechanistic information.

In *Part C*, the mechanism of mild steel corrosion in the presence of hydrogen sulfide is discussed. This subject has recently been investigated systematically. Nevertheless, considering the findings of the first two parts of the present study, it appeared that the previous interpretation of the experimental results involving hydrogen sulfide corrosion might have been inadequate. In this part, the mechanism of corrosion in the presence of hydrogen sulfide was theoretically investigated, based on the mechanistic findings of the corrosion by carboxylic acids and carbon dioxide. The existing experimental data were reinterpreted using comprehensive mechanistic mathematical

simulations. Contrary to previous arguments, the results in this part showed that the corrosion mechanism in the presence of hydrogen sulfide is similar to that of carboxylic acid and carbon dioxide.

The findings of the three individual cases above led to a more generic realization that is further elaborated in the generalization and conclusion section as the final discussion in the present document. This chapter puts all these individual cases under one umbrella, that is the "corrosion of mild steel in presence of weak acids", as one unified and generic corrosion scenario.

The micro-kinetics of the hydrogen evolution reaction from the hydrogen ion and possibly weak acids in aqueous acidic solutions were also investigated. However, since the discussions in these studies deviate from the main subject of this dissertation, the results are included as appendices to the main document for interested readers.

PART A: THE CASE OF CARBOXYLIC ACIDS

- Chapter A.1: An experimental investigation on the role of acetic acid in corrosion of mild steel

- Chapter A.2: Acidic corrosion of mild steel in the presence of acetic acid: mechanism and prediction

Chapter A.1: An experimental investigation on the role of acetic acid in corrosion of mild steel[2]

A.1.1: Introduction

Due to its prevalence, acetic acid is considered as representative of all carboxylic acids in corrosion studies as they relate to the oil and gas industry. In this chapter, the mechanism of the cathodic reactions in acetic acid containing solutions was experimentally investigated. In the conventional view, acetic acid is believed to be directly reduced at the surface, hence, increasing the rate of corrosion by increasing the cathodic current. Recently, it was suggested that acetic acid is not significantly electro-active, and its sole role in the corrosion process is through its ability to buffer the hydrogen ion concentration at the metal surface. Based on these two possible mechanisms, a hypothesis was developed here and experimentally examined in terms of its implication for observed cathodic polarization curves. At the same time, the effect of alloying elements was investigated by comparing the polarization behavior obtained on a pure iron surface with that for a mild steel surface.

A.1.2: Background

The mechanisms of cathodic reactions in aqueous corroding systems in the presence of weak acids have been the subject of numerous studies [11–18]. Carbonic acid, hydrogen sulfide, and carboxylic acids are the most common weak acids found in oil and

---

[2] A version of this chapter is published as: "Mechanism of Cathodic Reactions in Acetic Acid Corrosion of Iron and Mild Steel", Aria Kahyarian, Bruce Brown, Srdjan Nesic in Corrosion 2016 (72), p. 1539-1546. (Reference number [62])

gas production, transmission and processing infrastructure. It is well known that corrosion rates in the presence of these weak acids are significantly higher when compared to strong acids at the same pH [19,20]. Therefore, a mechanistic understanding of the role of these weak acids in increasing the corrosion rate is crucial for accurate corrosion rate estimation and, thus, for effective corrosion mitigation strategies.

Reports on the significance of carboxylic acids in corrosion of pipeline steel can be found as early as the 1940s [21]. It was suggested that small concentrations of carboxylic acids (300 ppm_m) can cause severe corrosion of pipeline steel [21]. At the same time, studies on the formation water composition found in oil and gas wells reported carboxylic acid concentrations in the range of several hundred milligrams per liter [22–24]. Due to its prevalence [25], the effect of acetic acid (HAc) on mild steel corrosion has frequently been studied as the representative carboxylic acid [25–30].

The partial dissociation of weak acids has generally been considered the main factor responsible for the increased corrosion rates. Unlike strong acids, weak acids only partially dissociate in an aqueous solution. Hence, the dissolved weak acid is present in both its dissociated and undissociated forms. This chemical equilibrium for acetic acid is shown by Reaction:
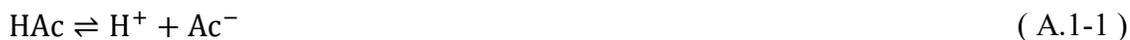
$$HAc \rightleftharpoons H^+ + Ac^- \qquad\qquad (A.1\text{-}1)$$

The equilibrium Reaction (A.1-1) is mathematically described by Equation (A.1-2), where K_{HAc} is the corresponding equilibrium constant, i.e., 1.75×10^{-5} (M) at 25 °C [15].

$$K_{HAc} = \frac{[\text{H}^+][\text{Ac}^-]}{[\text{HAc}]}$$

(A.1-2)

The effect of acetic acid on the corrosion of mild steel has been extensively studied [12,25–27,31–36]. Based on an analogy with other weak acids, such as carbonic acid and hydrogen sulfide, the increased corrosion rates in the presence of acetic acid were conventionally associated with the electroactivity of the undissociated acetic acid [32,35,37–41]. Garsany et al. [31] studied the reduction reactions of sodium chloride solutions containing acetic acid and carbon dioxide on platinum and X65 mild steel electrodes. The reported limiting currents were found to correspond with the mass transfer of acetic acid. However, the authors suggest that the underlying charge transfer process cannot be distinguished from that of hydrogen ion reduction at such conditions, due to the fast kinetics of acetic acid dissociation. The authors also reported a double wave in their voltammograms obtained on X65 mild steel in acetic acid containing solutions. It was suggested that both waves are resulting from the reduction of acetic acid while the rate limiting process is different. That is, the first wave was caused by charge transfer limitation, probably due to a change in the reaction mechanism, and the second wave is the mass transfer limitation of the electroactive species [31]. In 2007, George and Nesic [32] studied the effect of acetic acid on the carbon dioxide corrosion of mild steel using a series of potentiodynamic sweeps and corrosion rate data. It was reported that the observed corrosion rates significantly increased in the presence of acetic acid, which was found to be more pronounced at higher temperatures (60 ˚C). Therefore, the authors concluded that the undissociated acetic acid was directly reduced at the metal surface [32]. Using a similar approach, Okafor et al. [38] studied the effect of acetic acid on carbon

dioxide corrosion in extended temperature (up to 80 ˚C) and acetic acid concentration (5000 ppm$_m$) ranges. The authors concluded that the undissociated acetic acid was directly reduced, and further proposed a reaction mechanism that included a surface dissociation of adsorbed acetic acid followed by an electron transfer reaction [38]. A generally similar line of argument and experimental approach, leading to the same conclusion (direct acetic acid reduction), is frequently found in the literature [25,27,35,40,42]. This corrosion mechanism presumes two parallel cathodic reactions, namely, hydrogen ion reduction (Reaction (A.1-3)) and acetic acid direct reduction (Reaction (A.1-4)). This reaction pathway is referred to as the "direct reduction" mechanism [12,43].

$$2H^+ + 2e^- \rightleftharpoons H_2 \qquad\qquad\qquad\qquad (A.1\text{-}3)$$

$$2HAc + 2e^- \rightleftharpoons H_2 + 2Ac^- \qquad\qquad\qquad (A.1\text{-}4)$$
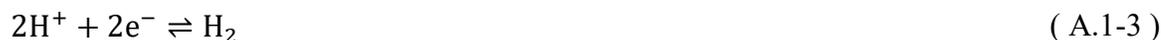
The development of comprehensive mathematical models in the early 2000s provided the opportunity for detailed quantitative analysis of the water chemistry inside the diffusion layer [15,44–46]. This included the ability to account for the effect of homogeneous reactions related to the presence of weak acids on the chemistry of the solution adjacent to the metal surface. These studies showed that the undissociated weak acid not only buffers the *bulk* solution, but can also act as a reservoir of hydrogen ions at the *metal surface* as they are consumed during the corrosion process [15,43,45,47].

In mildly acidic environments, the decay of the surface hydrogen ion concentration due to its consumption by the corrosion process plays a significant role in limiting the corrosion rate [48,49]. In strong acid solutions, mass transfer from the bulk is the only means of supplying the hydrogen ions to the surface. However, the presence of

undissociated weak acids provides an additional source of hydrogen ions through the dissociation reaction. That is due to the shift in the equilibrium by the decreased hydrogen ion concentration (Reaction (A.1-1)). Therefore, the hydrogen ion concentration at the metal surface is buffered, which in turn results in increased corrosion rates under such conditions.

Over the last decade, the ability of weak acids (such as acetic acid and carbonic acid) to buffer the surface pH was emphasized to the extent that suggests the direct reduction of the undissociated acid does not have a significant role in the increased corrosion rates. In 2011, Amri et al. studied the effect of acetic acid on the top of the line corrosion of mild steel [36]. The authors reported that at conditions where the corrosion current was under charge transfer control, the presence of acetic acid had no significant influence on the corrosion rate, concluding that the undissociated acetic acid was not electrochemically active [36]. In 2013, Tran et al. [12] investigated the mechanism of steel corrosion in the presence of acetic acid in more detail. The authors suggested using stainless steel as a more noble electrode material in order to minimize interference by the iron dissolution reaction. This resulted in voltammograms with charge transfer cathodic currents over a wider potential range. The reported results in that study indicated a clear Tafel behavior of the cathodic currents, as the signature of pure charge transfer control. Furthermore, the charge transfer controlled currents showed no significant response to increasing concentrations of acetic acid up to 1000 ppm$_m$. Therefore, it was concluded that direct reduction of acetic acid was insignificant. The reasoning behind this argument is discussed below in more detail. These recent studies suggest that the only cathodic

reaction involved in the corrosion process is hydrogen ion reduction, while the role of acetic acid is buffering the hydrogen ion concentration through the dissociation reaction [11,12,50]. This reaction mechanism is referred to as the "buffering effect" mechanism [11,12,43,50].

In the discussion above, the buffering effect and direct reduction are not two mutually exclusive mechanisms; rather they can be seen as two possible pathways for the hydrogen evolution reaction. Note that the direct reduction mechanism is related to the electroactivity of the undissociated weak acid, while the buffering effect mechanism is related to the dissociation of the weak acid inside the diffusion layer. Nevertheless, as discussed in this short review, the relative significance of these two reaction pathways for acetic acid has been disputed [11,12,36,50].

These two mechanisms (direct reduction and buffering effect) are compared in Figure A.1-1, where their corresponding hypothetical polarization curves are illustrated for two extreme cases. The first case (Figure A.1-1.A) shows the condition where the weak acid is electrochemically active and is directly reduced, while it has no buffering ability. The second case is where the weak acid is not electroactive and the only cathodic reaction is the hydrogen ion reduction, while the weak acid can readily dissociate to buffer the surface pH (Figure A.1-1.B). The governing mechanism of the cathodic reaction in the presence of a weak acid can be differentiated by the behavior of the cathodic voltammograms at various undissociated weak acid concentrations and at a constant pH, as shown in Figure A.1-1. Depending on the chemical and electrochemical

properties of a weak acid, a different characteristic polarization behavior is expected; both in the mass transfer controlled and charge transfer controlled currents.

For the first case (Figure A.1-1.A), the weak acid reduction and hydrogen ion reduction are two independent electrochemical reactions. Therefore, a "double wave" in the mass transfer controlled currents of the polarization curves can be observed in a certain concentration range of the weak acid. This behavior stems from two distinct limiting currents, one for hydrogen ion reduction and the other for weak acid direct reduction. For example, aqueous hydrogen sulfide is believed to be one such weak acid where a double wave similar to what is schematically shown in Figure A.1-1.A was observed [13,16,17,51]. This double wave was shown to be associated with the mass transfer limiting currents of hydrogen ion reduction and hydrogen sulfide direct reduction [13].

A)

B)
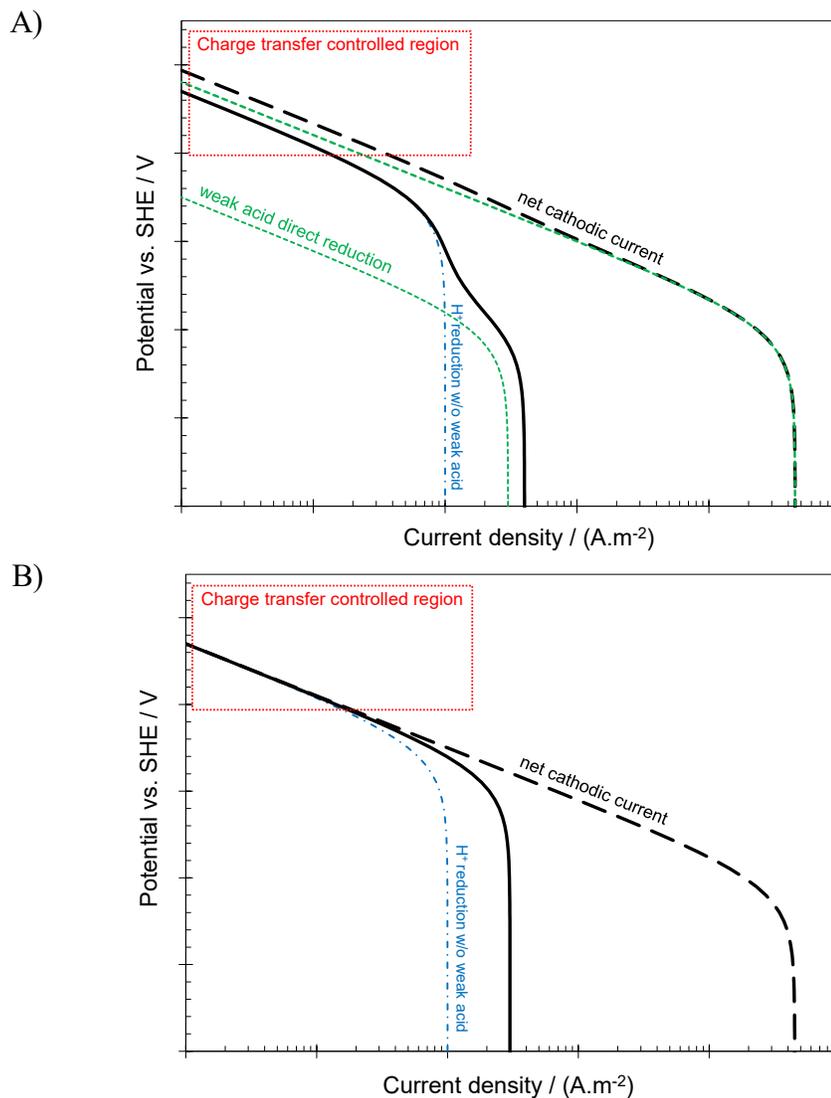
Figure A.1-1. Illustration of the hypothetical cathodic polarization curves at a constant pH and two different concentrations of a weak acid (solid black line < dashed black line). Black lines: net current, dotted-dashed blue lines: H^+ reduction without weak acid present, dashed green lines: weak acid direct reduction. A) Direct reduction mechanism. B) Buffering effect mechanism.

While the presence of the double wave may indicate weak acid direct reduction, its absence is not conclusive evidence for dismissing this reaction. The latter can be the case where the weak acid is also a strong buffer, i.e., it can readily dissociate. In such conditions, regardless of the electroactivity of the weak acid, the limiting current behavior is similar to that of the second case as shown in Figure A.1-1.B.

Here, the electrochemical activity of a weak acid can be investigated based on the characteristic behavior of the charge transfer controlled currents for the two cases discussed above. This concept is also illustrated in Figure A.1-1 by showing the distinct behavior of the charge transfer currents at different weak acid concentrations. In the case where the direct reduction of the weak acid is significant, the charge transfer controlled cathodic current (in the area denoted by the box in Figure A.1-1) should increase at higher weak acid concentrations as depicted in Figure A.1-1.A. On the other hand, when the weak acid is not electrochemically active, and hydrogen ions are the only reducible species, the charge transfer controlled current should remain unaffected by the change in weak acid concentration, as shown in Figure A.1-1.B.

The main obstacle in verification of these two hypothetical behaviors is related to the difficulty in observing the pure charge transfer controlled cathodic currents in typical corrosion experiments [26,32,35,38]. This is due to the interference of the iron dissolution reaction which obscures the cathodic currents in the potential range where they are under charge transfer control. As mentioned above, this issue has been addressed in the studies of Tran et al. [12,50] by using stainless steel electrodes. However, considering the effect of the alloying compounds (~ 20 wt. % Cr, and 10 wt. % Ni [12]) and the passive layer on the electroactivity of the metal surface, possibly changing the mechanism of the cathodic reactions, the experimental findings on stainless steel should not be considered valid for mild steel without further verification.

Using an improved experimental apparatus, the present research investigated this hypotheses using pure iron and X65 steel electrodes, in order to directly verify the

mechanism proposed by Tran et al. [12] without the complicating effect introduced by using a stainless steel electrode.

A.1.3: Material and methods

All experiments were conducted using a conventional 2 L, three electrode glass cell. A saturated Ag/AgCl reference electrode was connected to the cell through a Luggin capillary. The counter electrode was a platinum wire with significantly higher surface area than the working electrode. The working electrodes were made from 99.99% pure iron or API 5L X65 mild steel (see Table A.1-1 for the chemical composition). These electrodes were 5 mm in diameter, press fit into PTFE rotating disk electrode (RDE) holders. Each electrode was initially abraded using 1000 grit silicon carbide paper and then mirror polished using successively finer diamond suspensions down to 0.25 μm. Electrodes were then rinsed and sonicated in isopropanol and further electrochemically cleaned prior to each test with a series of decreasing magnitude galvanic steps ($\pm$ 5 A.m^{-2}, ±2 A.m^{-2}, and ±1 A.m^{-2}) in the study solution. Each step was 60 seconds long followed by 120 seconds rest at zero current. Finally, the electrode was left at open circuit potential (OCP) for 20 minutes before potential sweep measurements were taken.

Table A.1-1. Chemical composition of the X65 mild steel in wt.%.

S	P	V	C	Cr	Mo	Si	Ni	Mn	Fe
0.009	0.009	0.047	0.13	0.14	0.16	0.26	0.36	1.16	Balance

This electrochemical cleaning procedure was devised based on the thermodynamic stability of the iron oxide layer [52], and implemented in order to enhance

the removal of any iron oxide layer that may have formed during electrode preparation. Considering the reported iron/iron oxide Pourbaix diagrams in aqueous environments [52], iron (III) oxide is thermodynamically unstable in the pH and the potential range of the present study. Therefore, the oxide layer is spontaneously reduced to ferrous ions, which can be further kinetically enhanced by polarizing the electrode cathodically. On the other hand, the anodic polarizations were considered to minimize the adsorption/absorption of the hydrogen atoms that are produced during the cathodic polarization, knowing that the formation of any solid products during this step is thermodynamically infeasible at the conditions of the present study. Figure A.1-2 demonstrates the polarization behavior of an iron electrode during this cleaning process.
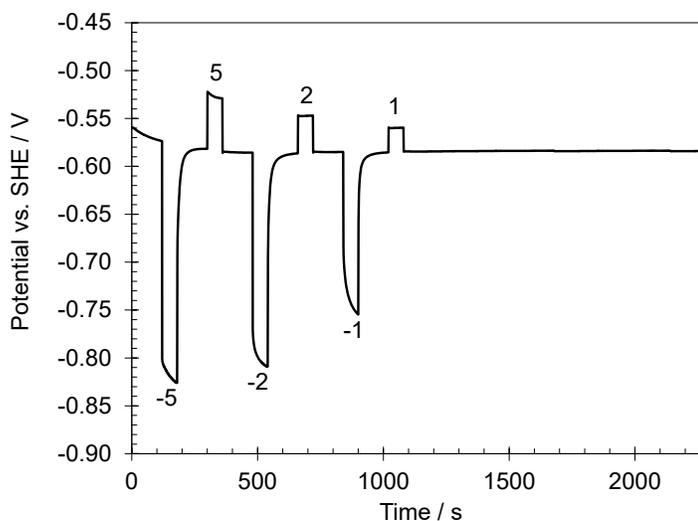
Figure A.1-2. Electrode potential during the electrochemical cleaning procedure on an iron electrode at pH 5, 25 °C, 2000 rpm RDE, 1 wt.% NaCl. Labels are the applied current densities in $A.m^{-2}$.

The potential sweep measurements were conducted at a 1 $mV.s^{-1}$ scan rate. The voltammograms reported in the present study were corrected for Ohmic drop using the

solution resistance obtained at high frequency range by electrochemical impedance measurements obtained after each potential sweep measurement.

As noted, the acetic acid concentration reported in the present study is the sum of its dissociated and undissociated forms, or in other words, the total concentration of acetate species (C_t). The concentration of undissociated acid at a known pH can be calculated based on Equation (A.1-2) and by mass conservation, as follows:

$$[\text{HAc}] = \frac{C_t \, [\text{H}^+]}{K_{HAc} + [\text{H}^+]}$$

(A.1-5)

Equation (A.1-5) suggests that at pH 4, 85% of the total acetic acid in the solution is in undissociated form, while at pH 5 this value decreased to 36%. A summary of the experimental conditions can be found in Table A.1-2.

Table A.1-2. Summary of the experimental conditions.

Experimental conditions	
Test apparatus	Rotating disk electrode Three electrode glass cell
Temperature	25 ˚C
Rotation rate	2000 RPM
Electrode material	Pure iron, X65 mild steel
Supporting electrolyte	1 wt.% NaCl
pH	4.0, 5.0
Total acetate concentration	0 ppm$_m$ 100 ppm$_m$ (1.66 mM) 500 ppm$_m$ (8.30 mM) 1000 ppm$_m$ (16.60 mM)

A.1.4: Results and discussion

The voltammograms reported in Figure A.1-3 and Figure A.1-5 show that employing RDE working electrodes with high rotation speed enabled observation of Tafel behavior for the cathodic reaction by increasing the mass transfer limiting current. The steady state voltammograms obtained at pH 4 and pH 5 on iron electrodes are shown in Figure A.1-3. The charge transfer controlled cathodic currents observed in Figure A.1-3 show no significant variation at different acetic acid concentrations. This behavior was in accordance with the buffering effect mechanism as shown in Figure A.1-1.B, which is a similar behavior to that reported by Tran et al. on stainless steel electrodes [12]. The only apparent discrepancy between the hypothesized and observed behavior was seen at pH 5 in the absence of acetic acid, where significantly lower cathodic currents were observed. This was due to mass transfer controlled current over the entire cathodic range of potentials in this particular condition. On the other hand, the anodic branches of the voltammograms shown in Figure A.1-3 were shifted toward lower current densities as the concentration of acetic acid was increased. This same behavior has been reported in the literature suggesting that acetic acid slightly retards the iron dissolution reaction [25,35,36].

The open circuited potentials reported in Figure A.1-3 were also slightly shifted toward more positive potentials with increasing acetic acid concentrations. This was found to be in accordance with the above discussion, where the charge transfer controlled cathodic currents in the vicinity of the OCP were not affected by increased acetic acid concentrations, while, the anodic currents were slightly inhibited at higher acetic acid

concentrations. Therefore, their intersect (OCP) was expected to slightly shift toward more positive potentials with increased acetic acid concentrations, a similar behavior as observed in Figure A.1-3.
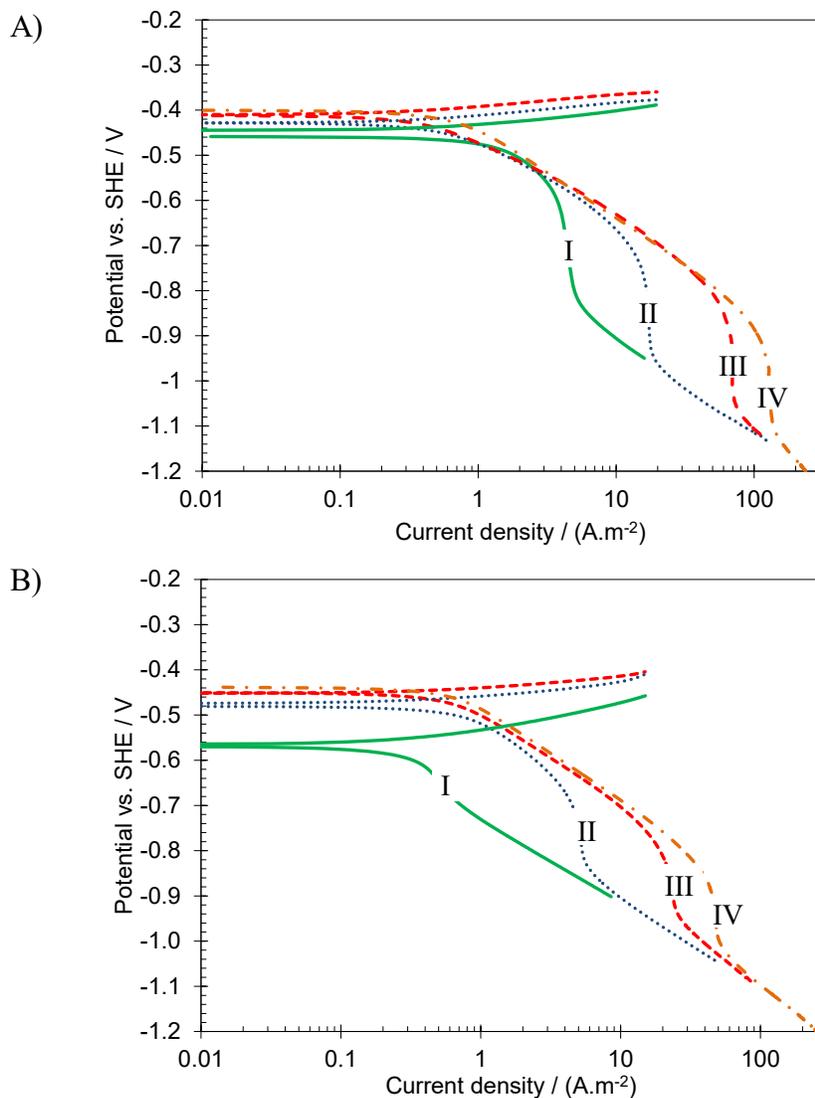
Figure A.1-3. Polarization curves obtained on iron at 25° C, 2000 rpm RDE, 1wt.% NaCl and various total acetate concentrations. I: 0 mM, II: 1.66 mM, III: 8.30 mM, IV: 16.60 mM. A) pH 4, B) pH 5.

The comparison of limiting currents in Figure A.1-3.A and Figure A.1-3.B, where no acetic acid was present, showed an order of magnitude increase with decreasing pH

from 5 to 4. That was the behavior expected from the Levich equation describing the mass transfer limiting current density (i_{lim} A.m^{-2}) for a RDE [53] with conversion to SI units:

$$i_{lim} = 0.62 \times 10^3 \, nFD^{2/3}\omega^{1/2}v^{-1/6}C_b \qquad\qquad (\text{A.1-6})$$

where C_b (M) is the bulk concentration of the reactant and D (m^2.s^{-1}) is its diffusion coefficient, v (m^2.s^{-1}) is the kinematic viscosity of the solution, ω (rad.s^{-1}) is angular velocity, F (C.mol^{-1}) is Faraday's constant and n is the number of electrons transferred.
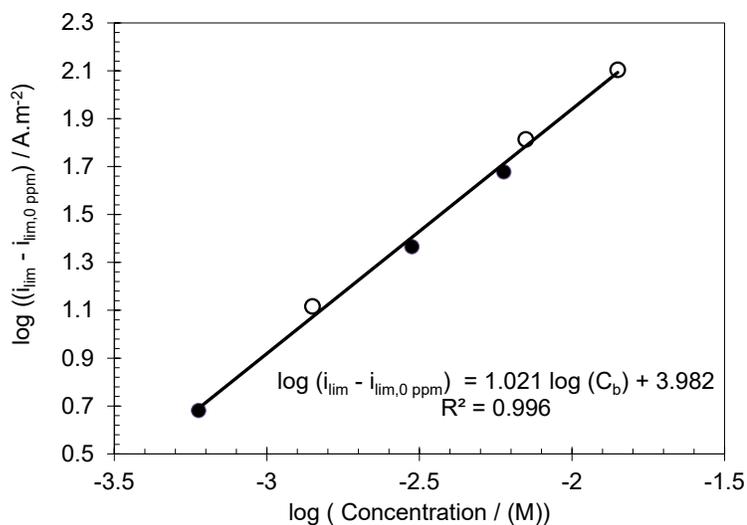
Figure A.1-4. The increase in the limiting current density at various concentrations of undissociated acetic acid reported in Figure A.1-3, obtained on iron at 25° C, 2000 rpm RDE, and 1wt.% NaCl. Open circles: pH 4, closed circles: pH 5. The trend-line is shown as the solid line with the equation at the bottom.

Figure A.1-4 shows the increase of the limiting current in the presence of acetic acid versus the concentration of the undissociated acetic acid in a log-log plot. Considering that the slope of the trend-line in this graph is nearly unity (1.02), the increase of the limiting current due to the presence of acetic acid is linearly correlated

with the concentration of undissociated acetic acid (R^2=0.996), regardless of the bulk pH. Furthermore, the intercept of the trend-line (3.98) was found to agree well with the theoretically obtained value of 4.01 from the Levich equation (Equation (A.1-6)) (diffusion coefficients and water kinematic viscosity from Nordsveen et al. [15]). This agreement indicated that the measured limiting currents are under pure mass transfer control, thus, the surface concentration of undissociated acetic acid was negligibly small. The latter further suggests that the kinetics of the proceeding acetic acid dissociation reaction (Reaction (A.1-1)) is not rate determining.

Figure A.1-5 shows the voltammograms obtained on an API 5L X65 mild steel electrode. A similar behavior of the limiting current with respect to both pH and undissociated weak acid concentration was observed on the mild steel surface as that of iron. The pure charge transfer controlled currents for the cathodic reactions on X65 steel were also not significantly affected by acetic acid concentration, in accordance with the buffering effect mechanism. The slightly retarded anodic currents and the behavior of the OCP with increasing concentrations of acetic acid on mild steel were also similar to that seen on iron electrodes.
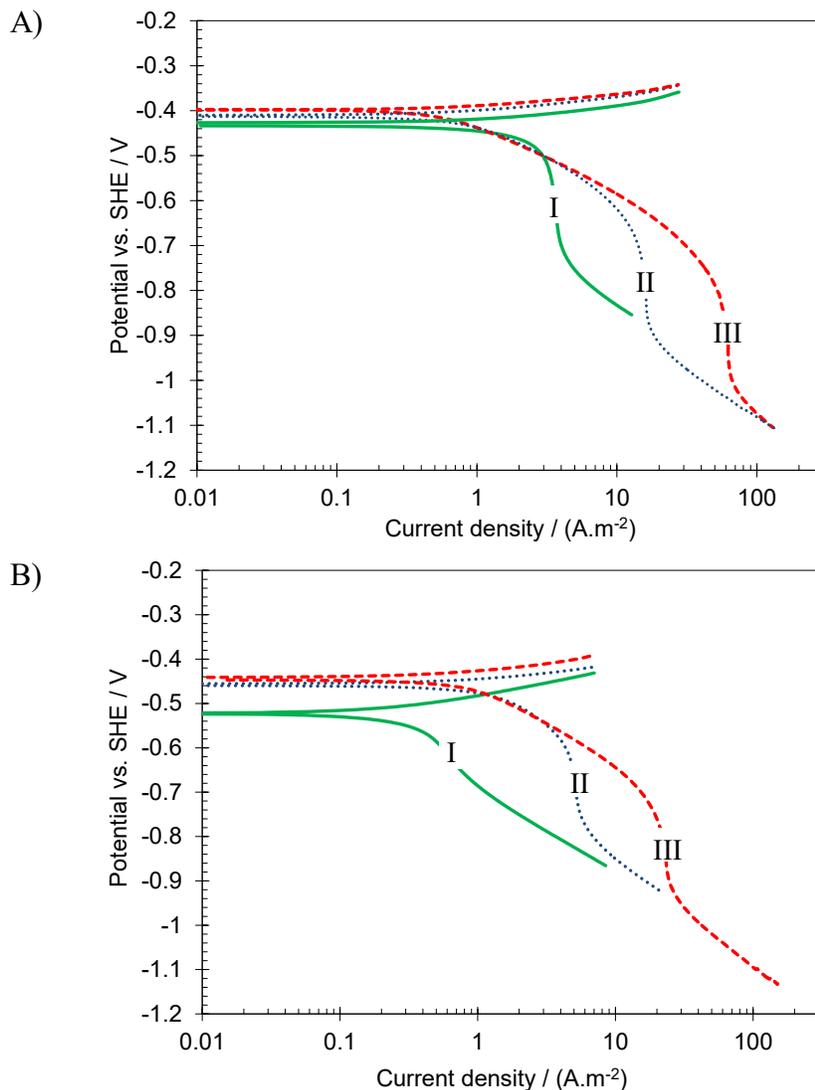
Figure A.1-5. Polarization curves obtained on X65 mild steel at 25° C, 2000 rpm RDE, 1wt.% NaCl and various total acetate concentrations. I: 0 mM, II: 1.66 mM, III: 8.30 mM. A) pH 4, B) pH 5.

The cathodic currents observed on pure iron and mild steel in acid solution and the presence of acetic acid are directly compared in Figure A.1-6. A similar limiting current was observed on both mild steel and pure iron, as expected. Additionally, the charge transfer controlled currents show similar behavior for both metals, suggesting that the mechanism of the hydrogen evolution reaction from hydrogen ions and water was the same on pure iron and API 5L X65 mild steel. However, the cathodic currents of the

hydrogen ion reduction as well as water reduction on mild steel are higher than that observed on iron. That suggests mild mild steel is a more active catalyst for these reactions, which is in accordance with the behavior previously reported on the iron electrodes containing alloying impurities by Bockris and Drazic [54].
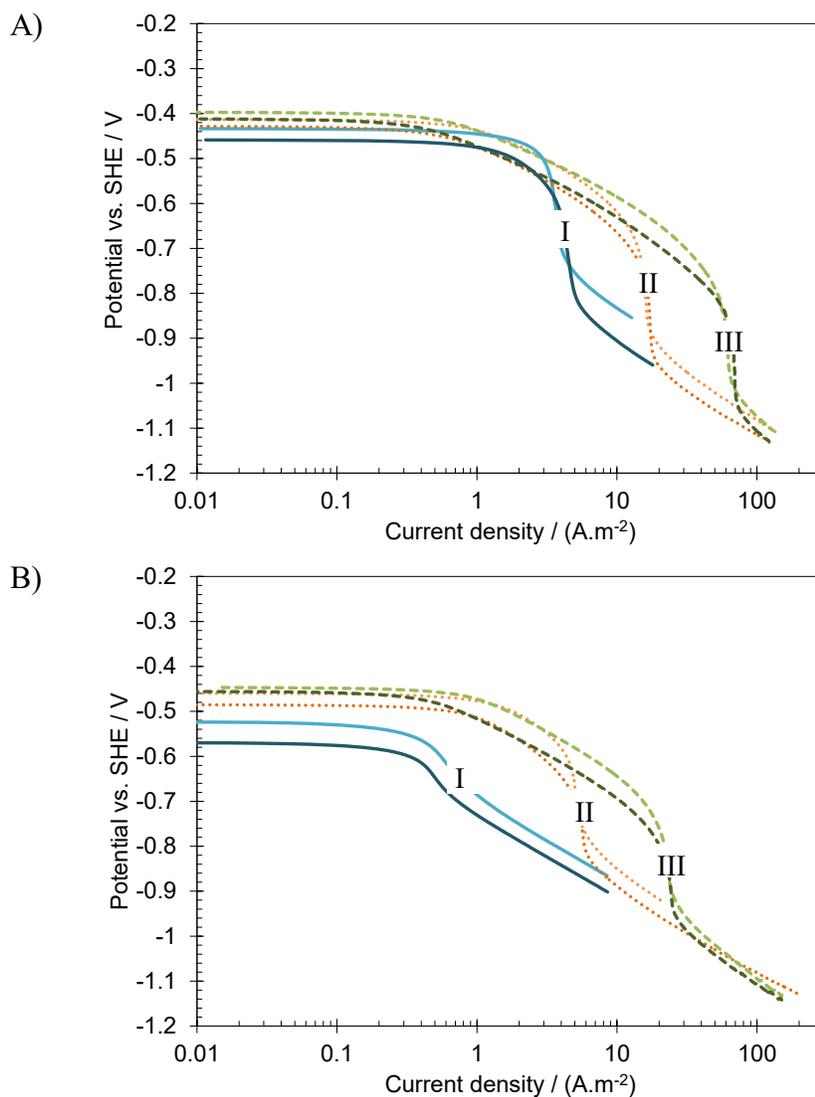
Figure A.1-6. Comparison of the polarization curves obtained on iron (dark shades) and X65 steel (light shades) at 25° C, 2000 rpm RDE, 1wt.% NaCl and various total acetate concentrations. I: 0 mM, II: 1.66 mM, III: 8.30 mM. A) pH 4, B) pH 5.

An example of the repeatability of the cathodic polarization measurements is shown in Figure A.1-7 for both pure iron and mild steel electrodes at pH 5 in the presence of acetic acid. The error bars represent the standard deviation of the current density at selected potentials for at least three measurements. Generally, a similar variation range was observed throughout the measurements while the reproducibility was slightly decreased at higher pH values and higher acetic acid concentrations.
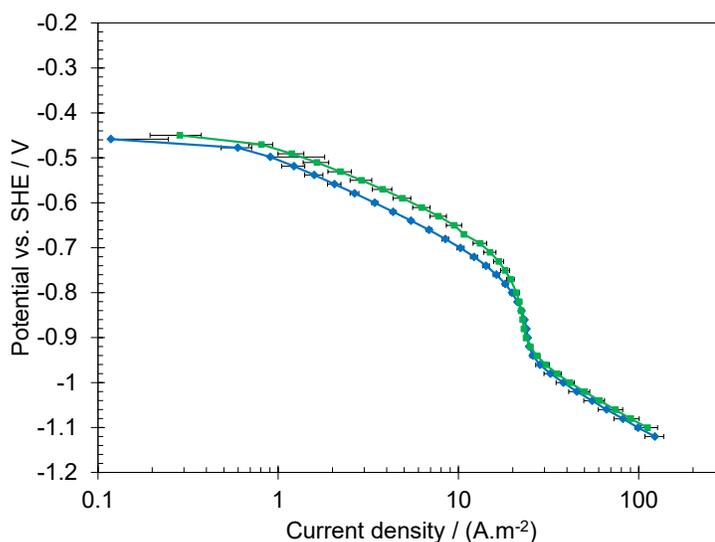
Figure A.1-7. Repeatability of the Polarization curves at pH 5, 8.30 mM total acetate concentration, 25˚ C, 2000 rpm RDE and 1wt.% NaCl on pure iron (blue diamonds) and X65 mild steel (green squares), at selected potentials. Error bars represent the standard deviation of at least three measurements.

A.1.5: Summary

The behavior of cathodic currents on pure iron and API 5L X65 mild steel in mildly acidic sodium chloride solutions containing acetic acid was investigated. The pure charge transfer controlled cathodic currents observed in the experimental data showed no significant response to increasing acetic acid concentration, indicating that direct acetic acid reduction was insignificant at the conditions covered in this study. The increase in

the limiting current density in the presence of acetic acid was in linear correlation with undissociated acetic acid concentration as expected from the Levich equation, suggesting that the surface concentration of this species is negligible at limiting currents. The similar cathodic behavior observed on pure iron and mild steel suggests that the mechanism of the hydrogen evolution reactions was the same on both surfaces.

Chapter A.2: Corrosion of mild steel induced by acetic acid: mechanism and prediction[3]

A.2.1: Introduction

Considering the findings reported in the previous chapter, the scope in this part of the study was extended in order to solidify the experimental mechanistic observations, and ultimately develop a comprehensive mechanistic model to estimate the corrosion rate of mild steel in acetic acid containing aqueous solutions. That included a more inclusive literature review, collection of experimental data in an extended range of conditions, and a detailed quantification of the observed effects associated with the presence of acetic acid. The model developed based on the presented mechanistic arguments was found to be able to reasonably predict both the polarization behavior of this system and the corrosion rates. In light of such detailed calculations, the apparent inconsistencies reported in the previous literature on the effect of acetic acid on the observed corrosion rates are resolved.

A.2.2: Background

Besides carbon dioxide (CO_2) and hydrogen sulfide (H_2S), short (alkyl) tail carboxylic acids such as formic acid (FA), acetic acid (HAc), and propionic acid (PPA) are amongst the common corrosive species encountered in the oil and gas industry [20,28,47,55,56]. Carboxylic acids are commonly reported to be present in the co-produced aqueous phase with concentrations up to several hundred milligrams per liter [22,57–59].

---

[3] A version of this chapter is published as: "Acidic Corrosion of Mild Steel in the Presence of Acetic Acid: mechanism and prediction", Aria Kahyarian, Alex Schumaker, Bruce Brown, Srdjan Nesic, Electrochimica Acta, 258 (2017), 639-652. (Reference number [201])

Amongst the carboxylic acids, acetic acid is the most abundant species [22,25,57,58], which has been commonly used to represent the effect of all carboxylic acids in corrosion studies, at least as far as it concerns the oil and gas industry.

Reports on the significance of carboxylic acids in corrosion of pipeline steel can be found as early as the 1940s [21], however, the subject gained little attention until the 1980s. To date, there seems to be a consensus on the significance of acetic acid in corrosion of mild steel, however, the reported effect of acetic acid on the observed corrosion rates in the literature appears inconsistent or even contradictory in some cases.

Numerous research studies have focused on elucidating the corrosion mechanisms related to the presence of acetic acid in oil and gas transmission pipelines. Gulbrandsen and Bilkova [35] studied the effect of acetic acid on CO_2 corrosion of X65 mild steel. The authors reported mixed behavior of corrosion rates at low and high temperatures as the concentration of acetic acid was increased. Based on their observations at 25˚C, corrosion rates decreased with increasing acetic acid concentrations, whereas the opposite behavior was reported at 80˚C. This was justified based on observation of an inhibitive effect of acetic acid on the anodic reaction. The authors argued that the combination of anodic reaction retardation and increase in cathodic reaction rate, as a result of direct acetic acid reduction, leads to this mixed behavior. In 2007, George and Nesic [32] investigated the effect of acetic acid on aqueous X65 mild steel corrosion under CO_2 and N_2 atmospheres in controlled pH experiments. The reported corrosion rates at pH 4, with or without CO_2 present, showed a significant increase with addition of a 100 ppm (1.66 mM) acetic acid, whereas a further increase of acetic acid concentration to 1000 ppm (16.6 mM) did not

result in significantly higher corrosion rates. The authors also reported that as temperature was increased to 40°C and 60°C, the addition of 100 ppm acetic acid had a more pronounced effect on increasing the corrosion rates. The increased corrosion rates in the presence of acetic acid was associated with direct acetic acid reduction during the corrosion process. The authors also confirmed the previous reports of a slight inhibitive effect of acetic acid on the iron dissolution reaction. Using a similar approach to George and Nesic [32], Okafor et al. [38] studied the effect of acetic acid at temperatures up to 80°C and acetic acid concentrations up to 5000 ppm. It was reported that increasing the acetic acid concentration resulted in higher corrosion rates at all the studied conditions. The increased corrosion rates were justified by the direct reduction of acetic acid, its occurrence was claimed to be supported by a higher activation energy obtained for cathodic reactions when acetic acid was present. However, the reported cathodic polarization curves in that study appear to be significantly influenced by the limiting current in almost all conditions, hence, the electrochemical activation energies could not be obtained with reasonable confidence. In 2012, Jia et al. studied the effect of acetic acid in CO_2 corrosion of 3Cr low-alloy steel [42], reporting a significant increase of corrosion rates by increasing the total acetic acid concentration from 0 to 2000 ppm. The author associated the higher corrosion rates with the direct reduction of acetic acid as well as its effect on degrading the protective corrosion product layer. Nevertheless, the arguments used to justify the observed behavior could be questioned when considering the lack of proper solution speciation control in their experiments. One should consider that increasing the acetic acid concentration from 0 to 2000 ppm could decrease the solution

pH dramatically; a key factor when discussing the corrosion behavior which was not included in analysis of data in that study [42]. Zhu et al. [30] also studied the CO_2 corrosion of N80 carbon steel in acetic acid containing solutions with emphasis on elevated temperatures and CO_2 partial pressures. A significant increase of corrosion rates with increasing acetic acid concentrations at 90°C was reported, which were justified by similar arguments used by Jia et al. [42].

Considering the brief review above, the increased corrosion rates in the presence of acetic acid were commonly justified by presuming that acetic acid is directly reduced at the metal surface. According to this mechanistic view, as a weak acid, acetic acid is only partially dissociated in the aqueous phase (Reaction (A.2-1)). Hence, both acetate ions (Ac⁻) and undissociated acetic acid (molecular HAc) are present in an aqueous solution, while their relative concentrations are defined by the solution pH (Figure A.2-1).

$$HAc_{(aq)} \rightleftharpoons H^+_{(aq)} + Ac^-_{(aq)} \qquad\qquad (A.2\text{-}1)$$

In this corrosion mechanism, the anodic iron dissolution (Reaction (A.2-2)) is accompanied by two parallel cathodic reactions, namely, hydrogen ion reduction (Reaction (A.2-3)) and the direct reduction of the undissociated acetic acid (Reaction (A.2-4)).

$$Fe^{2+}_{(aq)} + 2e^- \rightleftharpoons Fe_{(s)} \qquad\qquad (A.2\text{-}2)$$

$$2H^+_{(aq)} + 2e^- \rightleftharpoons H_{2\,(g)} \qquad\qquad (A.2\text{-}3)$$

$$2HAc_{(aq)} + 2e^- \rightleftharpoons H_{2(g)} + 2Ac^-_{(aq)} \qquad\qquad (A.2\text{-}4)$$

However, in more recent years, evidence has been mounting that suggests acetic acid is not a significant electroactive species and its sole contribution to the cathodic currents is through the homogeneous Reaction (A.2-1). In this mechanistic view, acetic acid merely acts as a hydrogen ion carrier in the solution and its presence would only increase the mass transfer limit of the cathodic currents. This mechanism points to the fact that at mass transfer limiting current, where the surface pH is increased, the chemical equilibrium of acetic acid (Reaction (A.2-1)) shifts towards acetic acid dissociation, therefore, acetic acid acts as an additional source of hydrogen ions at the metal surface. In 2011, Amri et al. [36] studied the effect of acetic acid in CO_2 corrosion in the context of top of the line corrosion of X65 mild steel. The authors reported that when the corrosion current was controlled by the electrochemical reaction rates at lower pH values (as opposed to mass transfer limited), increasing the acetic acid concentration did not significantly affect the observed corrosion rates or the corrosion mechanism. It was reported that the effect of acetic acid was mainly related to increasing the limiting current and that the direct reduction of acetic acid was insignificant. It was also suggested that acetic acid inhibits the anodic reaction and therefore local changes in its surface concentration could trigger localized attack. In another, more systematic, study, Tran et al.[12] investigated the behavior of the cathodic polarization curves in mildly acidic environments, with acetic acid being the only weak acid present in solution. The polarization curves were obtained on 304 stainless steel in order to eliminate the interference of anodic reactions on the observed cathodic current. It was explicitly shown that the concentration of acetic acid did not affect the charge transfer controlled portion

of the cathodic sweeps. Therefore, the authors concluded that acetic acid is not involved in a charge transfer processes on a stainless steel surface, and its main contribution was buffering the surface hydrogen ion concentration, thereby increasing the limiting currents. However, considering the possible influence of the alloying elements of 304 stainless steel (~ 20 wt. % Cr, and 10 wt. % Ni) and the passive layer on the electro-activity of the metal surface, the experimental findings of Tran et al.[12] on stainless steel may not be considered valid for mild steel, without further verification.

In Chapter A.1: , the mechanism of the cathodic reactions in acetic acid containing solutions was experimentally investigated directly on pure iron and X65 mild steel surfaces. Based on the experimental data obtained using rotating disk electrodes and potentiodynamic measurements, it was shown that acetic acid did not significantly contribute to the charge transfer controlled currents for concentrations up to 1000 ppm. Hence, the mechanism proposed by Tran et al. [12] was also proven to be valid for iron and mild steel surfaces.

The present part of the study expands on the experimental conditions covered previously in Chapter A.1: , in order to further elucidate the underlying mechanisms of the aqueous mild steel corrosion in the presence of acidic acid. A quantitative analysis of the results, using comprehensive mathematical calculations, is included in the present discussion, to provide a detailed description of the mechanistic observations. Ultimately, these mathematical relationships can be incorporated into mechanistic corrosion rate predictive models [43,60] for application in more complicated corrosion scenarios.

A.2.3: Materials and methods

A.2.3.1: Experimental procedure

The experiments were carried out in a 1 L glass cell with a conventional three electrode arrangement and a silver/silver chloride reference electrode, similar to that described in an earlier study [61]. The supporting electrolyte was a 0.1 M solution of sodium chloride in deionized water in all of the reported experiments. The targeted solution composition was achieved by addition of the desired amount of glacial acetic acid followed by adjustment of the solution pH using small amounts of dilute HCl or NaOH solutions. All the chemicals used in the present study were analytical grade. The solution was then purged using nitrogen gas for a minimum of 90 minutes while the oxygen content of the outlet gas was monitored (using a Orbisphere 410). The maximum allowed dissolved oxygen content before introducing the working electrode into the solution was 1 ppb.

The working rotating disc electrode (RDE) was made of an API 5L X65 mild steel disc (composition given in Table A.2-1) with 5 mm diameter, press-fitted into a Teflon™ electrode holder (Pine instruments). The electrode was abraded with 1000 grit silicon carbide paper and further mirror polished using successively finer diamond suspensions, down to 0.25 μm, prior to each test. The electrode was then rinsed and sonicated in isopropanol for 5 minutes and dried with nitrogen gas. The working electrode was inserted into the glass cell while the nitrogen gas flow was temporarily increased and further electrochemically treated as described in detail elsewhere [62]. As the last step, the open circuit potential (OCP) was monitored for 10 minutes prior to

electrochemical measurements in order to assure a steady OCP reading (maximum

allowed drift of ±2 mV over 5 min).

Table A.2-1. Chemical Composition of the X65 Mild Steel in wt%.

S	P	V	C	Cr	Mo	Si	Ni	Mn	Fe
0.009	0.009	0.047	0.13	0.14	0.16	0.26	0.36	1.16	Balance

The polarization curves were obtained using staircase voltammetry with the scan

rate of 0.5 mV.s^{-1} and a sampling period of 2 s^{-1}. The anodic and cathodic polarization

curves were obtained in separate experiments, by sweeping the potentials from OCP

towards more positive and more negative potentials, respectively. The reported results

were corrected for Ohmic drop using the solution resistance obtained from

electrochemical impedance spectroscopy (EIS) measurements, performed after

polarization measurements. The EIS measurements were conducted at OCP in the

frequency range of 0.2 Hz to 5 kHz with an AC perturbation potential of ±5 mV.

The reported corrosion rates were obtained from linear polarization resistance

(LPR) measurements, conducted in separate experiments, following the abovementioned

preparation procedure. For LPR measurements, the potential range of ±5mV vs. OCP and

scan rate of 0.125 mV.s^{-1} was used. The experimental conditions are summarized in Table

A.2-2.

Table A.2-2. Summary of the Experimental Conditions.

Test apparatus	Rotating disk electrode Three-electrode glass cell
Temperature	30°C unless stated otherwise
Rotation rate	2,000 rpm
Electrode material	API 5L X65 mild steel
Supporting electrolyte	0.1 M NaCl
pH	3.0, 4.0, 5.0
Total acetate concentration	0 mM 1.66 mM (100 ppm$_m$) 8.30 mM (500 ppm$_m$) 16.60 mM (1,000 ppm$_m$) 41.50 mM (2,500 ppm$_m$)

A.2.3.2: Numerical methods and mathematical modeling

A.2.3.2.1: Water chemistry calculation

The solution speciation was obtained considering the chemical equilibria of the involved homogeneous reactions. In an aqueous solution containing acetic acid, the two homogeneous reactions are the acetic acid dissociation shown *via* Reaction (A.2-5) and water dissociation shown *via* Reaction (A.2-6).
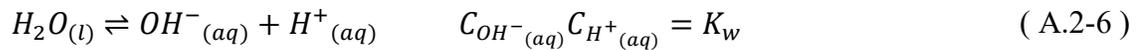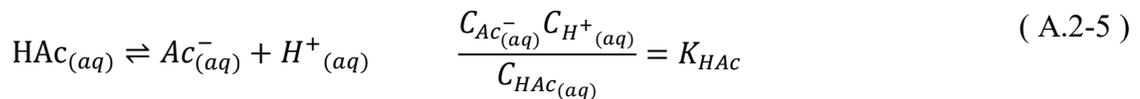
$$HAc_{(aq)} \rightleftharpoons Ac^-_{(aq)} + H^+_{(aq)} \qquad \frac{C_{Ac^-_{(aq)}} C_{H^+_{(aq)}}}{C_{HAc_{(aq)}}} = K_{HAc} \qquad (A.2\text{-}5)$$

$$H_2O_{(l)} \rightleftharpoons OH^-_{(aq)} + H^+_{(aq)} \qquad C_{OH^-_{(aq)}} C_{H^+_{(aq)}} = K_w \qquad (A.2\text{-}6)$$

The chemical equilibria corresponding to acetic acid and water dissociation can be mathematically expressed as Equation (A.2-5) and Equation (A.2-6), respectively, using the equilibrium constants listed in Table A.2-3.

Table A.2-3. Equilibrium and reaction rate constants where K=k_f/k_b.

Reaction rate constant	Reference
$K_{HAc} = 10^{\left(-\frac{1500.65}{T} - 6.50923 \times log(T) - 0.0076792 \times T + 18.67257\right)}$ (M)	63
$K_w = (10^{-3}\rho_w)^2\, 10^{-\left(a1 + \frac{a2}{T} + \frac{a3}{T^2} + \frac{a4}{T^3} + \left(a5 + \frac{a6}{T} + \frac{a7}{T^2}\right) log(10^{-3}\rho_w)\right)}$ (M ^{2}) a_1= -4.098, a_2= -3245.2, a_3= 2.2362, a_4= -3984E7, a_5= 13.957, a_6= -1262.3, a_7= 8.5641E5	64
$k_{f,HAc} = 8.7 \times 10^5$ (1/s)	65
$k_{b,w} = 1.4 \times 10^{11}$ (1/M.s)	66,67

Assuming that acetic acid concentration in the gas phase was negligible, the total acetate concentration ($C_{t,HAc}$) may be related to undissociated acetic acid concentration (C_{HAc}) through a mass balance relationship described as Equation (A.2-7).

$$C_{t,HAc} = C_{HAc} + C_{Ac^-} \qquad\qquad\text{(A.2-7)}$$

In a solution without an externally induced electric field, the concentration of ions must also satisfy the electroneutrality constraint as shown by Equation (A.2-8).

$$\sum_i z_i C_i = 0 \qquad\qquad\text{(A.2-8)}$$
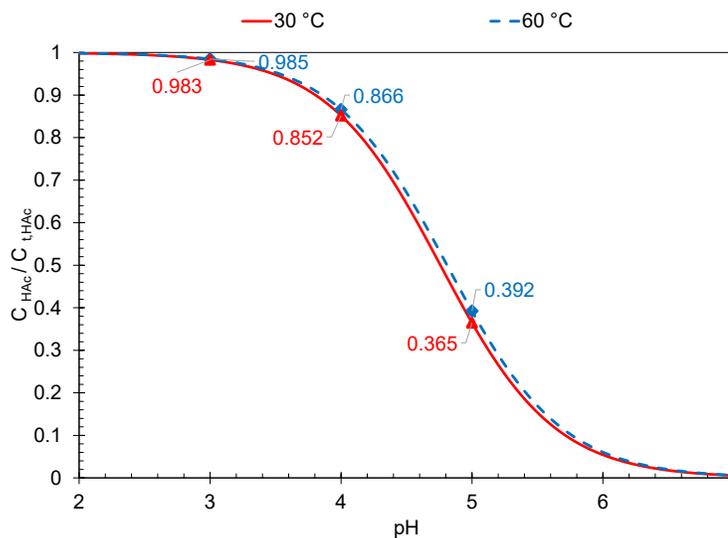
Figure A.2-1. The ratio of undissociated acetic acid concentration to total acetate species concentration in 0.1M NaCl solution for various pH values at 30°C and 60°C.

In addition to the four equations discussed above (Equations (A.2-5) to (A.2-8)), the known solution pH and NaCl concentration can be used to fully resolve the system of equations in order to obtain the concentration of six chemical species ($H^+_{(aq)}$, $HAc_{(aq)}$, $Ac^-_{(aq)}$, $OH^-_{(aq)}$, $Na^+_{(aq)}$, $Cl^-_{(aq)}$). Considering that there are no ferrous ions present in the solution initially, the concentration of this species in the bulk solution was arbitrarily taken to be 10^{-6} M. The results obtained from the water chemistry calculation are shown in Figure A.2-1, where the ratio of undissociated acetic acid to the total acetic acid concentration is demonstrated for various pH values at 30°C and 60°C. At low pH values, the high concentration of hydrogen ion shifts the acetic acid dissociation equilibrium towards the left-hand side, so that most of the acetate species are in the form of undissociated acetic acid. On the other hand, the dissociation equilibrium dictates that the majority of acetate species is in acetate ion form at near neutral pH values. Figure A.2-1

also shows that a moderate change in temperature does not profoundly alter the solution speciation.

A.2.3.2.2: Electrochemical model

In order to quantify the polarization behavior of the studied systems, and also to ultimately estimate the corrosion rates, a comprehensive mathematical model of electrochemical/mass transfer behavior was developed similar to that discussed in detail elsewhere [43,60]. While the electrochemical reactions at the metal surface define the observed current/potential response of the system, the rate of these reactions themselves are dictated by the surface concentration of the involved electroactive species; which are determined by the mass transfer towards/away from the electrode surface. The mass transfer for a RDE consists of three parallel processes: *convective flow* of the bulk fluid leading to a flux of the chemical species; *molecular diffusion* as a result of the concentration gradient of the chemical species; and *electromigration* of the ionic species arising from the presence of an induced or spontaneous electric field. The flux of any given species *i* can be described through Equation (A.2-9) [68].

$$N_i = -z_i u_i F C_i \nabla \phi - D_i \nabla C_i + v C_i \qquad (A.2\text{-}9)$$

The concentration distribution of each chemical species may be calculated using the species conservation law, which can be mathematically expressed *via* Equation (A.2-10), also known as the Nernst-Planck equation.

$$\frac{\partial C_i}{\partial t} = -\nabla . N_i + R_i \qquad (A.2\text{-}10)$$

Considering the symmetrical geometry of the RDE, the tangential and radial species flux components of Equation (A.2-9) and Equation (A.2-10) can be neglected.

Furthermore, the mobility of ions can be estimated using the Nernst-Einstein relationship ($u_i = D_i/RT$), with diffusion coefficients listed in Table A.2-4. Therefore, for a one-dimensional semi-infinite geometry in the direction x normal to the metal surface, Equation (A.2-9) and Equation (A.2-10) can be simplified to Equation (A.2-11) and Equation (A.2-12) , respectively.

$$N_i = -D_i \frac{\partial C_i}{\partial x} - \frac{z_i D_i F C_i}{RT} \frac{\partial \phi}{\partial x} + v_x C_i \tag{A.2-11}$$

$$\frac{\partial C_i}{\partial t} = D_i \frac{\partial}{\partial x} \frac{\partial C_i}{\partial x} + \frac{\partial}{\partial x}\left(\frac{z_i D_i F C_i}{RT} \frac{\partial \phi}{\partial x}\right) - v_x \frac{\partial C_i}{\partial x} + R_i \tag{A.2-12}$$

The average bulk movement of the fluid in the direction normal to the surface is accounted for by the convective flow term $v_x C$, where v_x describes the velocity profile inside the diffusion layer. For a laminar flow regime of a RDE, the analytical solutions for the velocity profile (v_x) and the diffusion layer thickness (δ) are shown as Equation (A.2-13), where $a = 0.510$, and Equation (A.2-14), respectively [69].

$$v_x = -a\omega \left(\frac{\omega}{\upsilon}\right)^{1/2} x^2 \tag{A.2-13}$$

$$\delta = \left(\frac{3D_{lim}}{a\upsilon}\right)^{1/3} \left(\frac{\omega}{\upsilon}\right)^{-1/2} \tag{A.2-14}$$

Furthermore, the effect of homogeneous chemical reactions, acetic acid and water dissociation are reflected by the R_i term in Equation (A.2-12). In a generic form, the rate of chemical reaction j (Reaction (A.2-15)) can be calculated as shown in Equation (A.2-16).

$$\sum_{r=1}^{n_r} C_r \rightleftharpoons \sum_{p=1}^{n_p} C_p \tag{A.2-15}$$

$$R_j = k_{f,j} \prod_{r=1}^{n_r} C_r - k_{b,j} \prod_{p=1}^{n_p} C_p \tag{A.2-16}$$

The rate of production (or consumption) of a species i (R_i in Equation (A.2-12)) can be expressed in a matrix format as Equation (A.2-17). The kinetic rate constants of the chemical reactions can be found in Table A.2-3.

$$\begin{bmatrix} R_{H^+_{(aq)}} \\ R_{HAc_{(aq)}} \\ R_{Ac^-_{(aq)}} \\ R_{OH^-_{aq}} \end{bmatrix} = \begin{bmatrix} 1 & 1 \\ -1 & 0 \\ 1 & 0 \\ 0 & 1 \end{bmatrix} \times \begin{bmatrix} R_{HAc} \\ R_w \end{bmatrix} \tag{A.2-17}$$

Considering the discussion so far in this section, Equation (A.2-12) is applicable for each chemical species present in the system (H^+, HAc, Ac^-, OH^-, Fe^{2+}, Na^+, Cl^-) in order to determine their concentration distribution inside the diffusion layer. However, for this set of equations to be complete, the electric potential appearing in the electromigration term also needs to be specified. This parameter can be characterized through an additional relationship known as the "electroneutrality" constraint as described by Equation (A.2-8).

Table A.2-4. Reference diffusion coefficients at 25 °C.

Species	Diffusion coefficient $\times 10^9$ (m²/s)	Reference
HAc	1.29	70
Ac^-	1.089	70
H^+	9.312	68
OH^-	5.273	70
Na^+	1.334	68
Cl^-	2.032	68,70
Fe^{2+}	0.72	68

Initial and boundary conditions

At the initial time ($t = 0$), it can be assumed that a well-mixed solution comes into contact with the metal surface. Hence, the concentrations of the chemical species throughout the diffusion layer are constant known values, defined by the chemical equilibria of the solution, as discussed in Section A.2.3.2.1: .

At the bulk solution boundary, where $x = \delta$, the concentration of chemical species remains unchanged at all times ($t \geq 0$). Therefore, a Dirichlet type boundary condition can be defined there based on the known concentration of species, identical to those of the initial conditions.

The boundary condition at the metal/solution interface is based on the electrochemical reaction rate calculations. For an electroactive chemical species, the flux at the metal/solution boundary is equal to the rate of the corresponding electrochemical reaction. Therefore, for species i involved in electrochemical reaction j, the flux at the metal surface can be described through Equation (A.2-18).

$$N_i|_{x=0} = -\frac{s_{ij}i_j}{n_j F} \qquad \text{(A.2-18)}$$

Based on the analysis of the experimental results (Section A.2.4.1:), acetic acid was not considered to be involved in the electrochemical reaction. Also, considering that the water reduction reaction is insignificant at the corrosion potential, it was not included in the model. Hence, the electrochemical reactions considered in the model consisted only of one cathodic reaction, hydrogen ion reduction (Reaction (A.2-3)), and one anodic reaction, iron oxidation (Reaction (A.2-2)). Due to the negligible concentration of H_2 in the solution (which is stripped out by the nitrogen bubbling through the

solution), no significant contribution by the hydrogen oxidation reaction over the potential range of interest is expected. Hence, the current density resulting from hydrogen ion reduction was calculated in the form shown in Table A.2-6, which considers the cathodic half reaction only. The related kinetic parameters, including the transfer coefficient α, the reaction rate constant k_o, and the reaction order m_{H^+}, were obtained based on the experimental data as discussed in the following.

The anodic current density resulting from iron dissolution (Reaction (A.2-2)) can be calculated by considering the anodic half reaction only, since the ferrous ion reduction may also be assumed negligible, because of its low concentration and the potential range of interest. The rate of the iron oxidation reaction, at the active dissolution range observed in lower pH values (e.g. below 5), is known to have a first order pH dependence [71,72]. It is also known that the mechanism of the iron oxidation reaction in the vicinity of the corrosion potential changes at near neutral pH values [15,71,72]. Therefore, two different reaction rate relationships were considered, one for lower and the other for higher pH values, as shown in Table A.2-6. These relationships are based on previously reported behavior, with a strong pH dependence in more acidic solutions and no dependence at higher pH values [15,71]. The change of mechanism is also reported to coincide with a change of apparent Tafel slope. The kinetic parameters reported in Table A.2-6 were obtained based on the experimental results of the present study.

The current/potential relationships used to calculate the rate of electrochemical reactions are listed in Table A.2-6. The negative sign in Equation (A.2-18) is due to a sign convention where cathodic currents are taken as negative while anodic currents are

positive. Furthermore, all the reactions are written in "cathodic" form (e.g. Reactions (

A.2-2) and (A.2-3)), so the reactants on the left hand side are represented with a

negative stoichiometric coefficient (s_{ij}) and the products on the right hand side are

represented as positive values.

Equation (A.2-18) can be expanded using a matrix notation in order to include

all the electro-active species:

$$
\begin{bmatrix} N_{Fe_{(aq)}^{2+}}|_{x=0} \\ N_{H_{(aq)}^{+}}|_{x=0} \end{bmatrix} = \begin{bmatrix} 1 & 0 \\ 0 & -1 \end{bmatrix} \times \begin{bmatrix} i_{Fe}/2F \\ i_{H^{+}}/F \end{bmatrix}
\tag{A.2-19}
$$

For non-electroactive species, the flux at the metal surface is zero, as it is a non-

porous non-reactive barrier:

$$
N_i|_{x=0} = 0
\tag{A.2-20}
$$

The flux Equations (A.2-19) and (A.2-20) can be used to describe the boundary

conditions for all chemical species at the metal surface.

In order to calculate the cathodic and anodic current in Equations (A.2-19), the

potential at the metal surface (E_{app}) needs to be known. That is true for the case where

electrode potential is the controlled parameter (such as in potentiodynamic

measurements). However, when the calculations are done to obtain the corrosion rates,

the potential at the metal surface is not explicitly known. In that case, an additional

relationship is required to relate the potential at the metal surface to other known

parameters. This can be achieved by introducing the charge conservation at the electrode

surface based on the mixed potential theory: the net current resulting from all j

electrochemical reactions is equal to zero, mathematically expressed as Equation (A.2-21).

$$\sum_j i_j = 0 \qquad\qquad (\text{A.2-21})$$

Numerical Solution

Table A.2-5 summarizes all the relevant mathematical equations required to develop a comprehensive mathematical model as discussed above. These equations form a set of non-linear, coupled, partial differential equations to be solved numerically. Considering a simple one-dimensional computational space, the finite difference method can be used to solve the equations.

Table A.2-5. Summary of equations used in the mathematical model.

Electrode surface boundary	
$N_i\|_{x=0} = -\dfrac{s_{ij}i_j}{n_jF}$	For electroactive species
$N_i\|_{x=0} = 0$	For non-active species
$\displaystyle\sum_i z_iC_i = 0$	
$\displaystyle\sum_j i_j = 0$	For unknown electrode potential

Diffusion boundary layer	
$\dfrac{\partial C_i}{\partial t} = D_i\dfrac{\partial}{\partial x}\dfrac{\partial C_i}{\partial x} + \dfrac{\partial}{\partial x}\left(\dfrac{z_iD_iFC_i}{RT}\dfrac{\partial\phi}{\partial x}\right) - v_x\dfrac{\partial C_i}{\partial x} + R_i$	For all species
$\displaystyle\sum_i z_iC_i = 0$	

Bulk boundary conditions	
$C_i = C_i^b$	
$\Phi = 0$	Arbitrary reference potential

The partial differential equations are discretized using first order Taylor's series approximations. The time integration is done explicitly, using the Euler approximation. The resulting algebraic equations can be written in a matrix format, as a tri-diagonal coefficient matrix multiplied by the unknown concentrations and solution potential. The final solution can then be obtained through different solution algorithms such as Newman's "Band-J" open-source code where it is solved by the LU decomposition method [68]. The presence of nonlinear terms, such as those in the electromigration or chemical reaction relationships, makes some of the terms in the coefficient matrix a

function of other concentrations and/or potential, i.e., they are not explicitly known. In the approach used in the present model, the final solution was obtained iteratively by using an initial guess for the unknown terms of the coefficient matrix, usually the last calculated value of the unknown term, until the desired accuracy ($R^2=10^{-12}$) was achieved.

A.2.4: Results and discussion

In general, the reduction of any weak acid in an aqueous solution, including acetic acid in the present study, is thermodynamically identical to that of hydrogen ion reduction. This can be readily shown through the reversible potential of the two reactions based on the Nernst equation, where the concentration of the weak acid and its conjugate base are defined by the chemical equilibrium of the weak acid dissociation. Therefore, the difference between the hydrogen ion reduction and the direct reduction of the weak acid resides only in the kinetics of these electrochemical reactions. The two reactions can therefore be distinguished by investigating the cathodic polarization behavior of the system at the charge transfer controlled current range.

The experimental conditions in the present study were designed so that the electrochemical activity of acetic acid as an additional oxidizing species could be properly distinguished. In these experiments, at a given solution pH the concentration of acetic acid was increased. Since the charge transfer rate from hydrogen ion reduction is constant, any increase in charge transfer controlled current densities indicates that the direct reduction of acetic acid is significant and it is occurring in parallel. In contrast, if

the charge transfer controlled current densities remain unchanged, one can conclude that the direct reduction of acetic acid is not significant.

Furthermore, all the reported polarization curves in this section show a significant increase in mass transfer limiting current as the concentration of acetic acid was increased. Nevertheless, the behavior of the mass transfer limiting current is expected to be similar whether acetic acid is directly reduced or not, thus, the variation in limiting current densities should not be used to discuss the electrochemical activity of acetic acid. This effect of acetic acid concentration on the observed limiting currents is discussed in Section A.2.4.2: .

A.2.4.1: Electrochemical activity of acetic acid

The typical polarization curves at pH 3, pH 4 and pH 5 and increasing acetic acid concentrations are reported in Figure A.2-2 to Figure A.2-4. In these graphs the anodic current densities typically consist of a linear current/potential range just above the OCP, followed by a current maximum and another linear range at more positive potentials. The cathodic currents consist of a linear current/potential range just below the OCP, associated with the hydrogen ion reduction, followed by the mass transfer limiting current and another linear range at more negative potentials associated with the water reduction reaction. The discussion below is mostly focused on the electrochemical reactions at the vicinity of the OCP. That is the anodic current densities below the anodic current maximum and cathodic current densities below the limiting current.
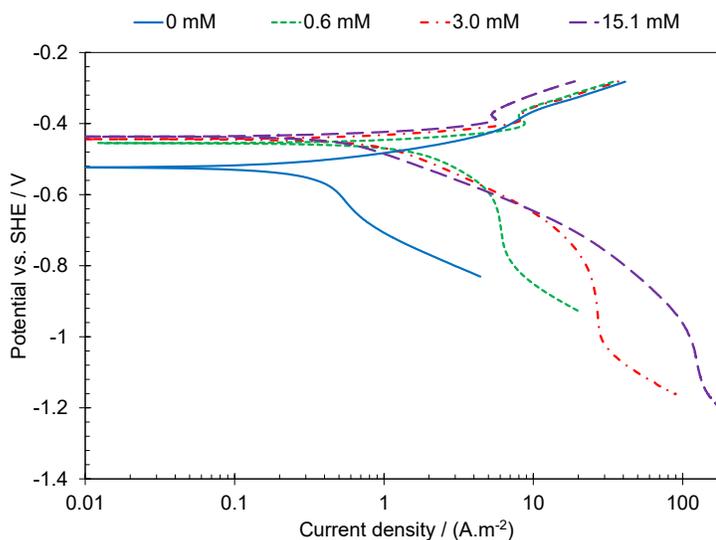
Figure A.2-2. Polarization behavior of X65 mild steel in solution of pH 5, at 30 °C, 2000 rpm, 0.1 M NaCl, and undissociated acetic acid concentrations 0 mM, 0.6 mM ($C_{t,HAc}$=1.7 mM), 3.0 mM ($C_{t,HAc}$=8.3 mM), and 15.1 mM ($C_{t,HAc}$=41.5 mM).

Figure A.2-2 shows the polarization curves obtained at pH 5, where a significant change was observed by addition of 0.60 mM undissociated acetic acid ($C_{t,HAc}$ = 1.66 mM). The shift of OCP towards more positive potentials can be explained when considering that the cathodic polarization curve was under mass transfer control in the absence of acetic acid, and the significant increase of the limiting current by addition of acetic acid leads to an increased OCP. In the presence of acetic acid, a Tafel behavior is clearly observed in the cathodic polarization curves, particularly when the acetic acid concentration was further increased. The comparison of the charge transfer controlled currents did not indicate any increase in charge transfer rates that could be associated with direct reduction of acetic acid. Actually, one can observe a slight decrease in the charge transfer rate with increasing acetic acid concentration, a behavior that will be discussed further below. The cathodic polarization curves obtained at acetic acid concentrations up to 15.1 mM ($C_{t,HAc}$ = 41.5 mM) further support these observations.

The anodic polarization curves in Figure A.2-2 show a significant change in the polarization behavior by addition of 0.60 mM undissociated acetic acid. In the presence of acetic acid, a Tafel slope of approximately 40 mV was observed, which agrees well with the typical Tafel slopes reported in the literature for anodic iron dissolution in acidic solutions [32,71]. The same 40 mV Tafel slope was obtained in the experimental data reported below for lower pH values with or without acetic acid present. However, at pH 5, as shown in Figure A.2-2, a notably different behavior with an apparent ~90 mV Tafel slope and a significantly higher rates of the anodic dissolution reaction was observed when no acetic acid was present. A similar effect has been repeatedly reported in the literature that suggests a significant change in the electrochemical behavior of the iron dissolution reaction occurs as the solution pH is increased towards neutral values (pH 5 and higher) [71–74]. This can be better understood by considering the well-known categorization of El Miligy et al. [72] who suggested that the iron dissolution in mildly acidic environments passes through four ranges as the potential is increased towards more positive values. The four ranges are characterized with different Tafel slopes and reaction orders, depending on the solution pH and the electrode potential [72]. Ordered from more negative towards more positive potentials, the authors categorized these ranges as *active dissolution*, characterized by 30 to 40 mV Tafel slope, *transition*, characterized by observation of the first current maximum, *pre-passivation*, characterized by a 120 mV Tafel slope, and *passivation* that occurs after the second current maximum [72]. The 40 mV Tafel slope observed in most conditions in the present study is a characteristic behavior of the iron oxidation in the *active dissolution* range. The increased Tafel slope at

higher pH values suggests that the iron dissolution was at the *transition / pre-passivation*

range. Nevertheless, the above discussion does not explain why the presence of acetic

acid shifts the OCP back into the active dissolution range. The complete picture can only

be seen when considering the behavior of cathodic currents as well. The comparison of

the cathodic polarization curves in Figure A.2-2, shows that at pH 5 when no acetic acid

was present, the mass transfer limited cathodic currents were extended into the potential

range well above the OCP, up to -0.425 V (vs. SHE). That means, the pH at the surface

remains significantly higher than the pH in the bulk solution even when the electrode was

polarized anodically. Therefore, the change in the electrochemical behavior of the iron

dissolution reaction with addition of acetic acid is merely a result of increased cathodic

limiting currents and consequently decreased surface pH to that of the bulk solution at

potentials equal or higher than OCP (anodic potential range).

A smaller, but notable decrease of the anodic dissolution rate was observed as the

acetic acid concentration was further increased. The anodic current densities at these

conditions were slightly retarded while the observed Tafel slopes remained unchanged,

what was observed as a slight shift of open circuit potentials toward more positive values.

This same behavior has been frequently reported in the literature, suggesting that acetic

acid slightly inhibits the iron dissolution reaction [25,35,36].

The polarization curves at pH 4 with and without acetic acid are shown in Figure

A.2-3. The Tafel behavior is clearly observed in the solutions containing acetic acid, with

charge controlled currents showing no significant increase with increasing acetic acid

concentration. The inhibiting effect on the anodic dissolution reaction can be clearly observed with the increase in acetic acid concentration.
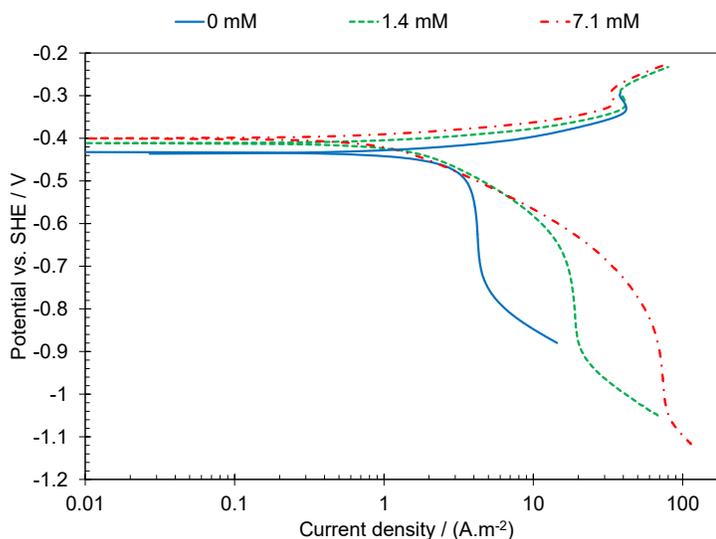
Figure A.2-3. Polarization behavior of X65 mild steel in acidic solution of pH 4, at 30 °C, RDE, 2000 rpm, 0.1 M NaCl, and undissociated acetic acid concentrations 0 mM, 1.4 mM ($C_{t,HAc}$=1.7 mM) and 7.1 ($C_{t,HAc}$=8.3 mM).

The polarization curves at pH 3 are shown in Figure A.2-4. The behavior seen at pH 3 is of particular significance, since the Tafel behavior is clearly observed in the cathodic polarization curves even when no acetic acid was present. At this condition also, increasing the acetic acid concentration did not result in any increase of the charge transfer controlled cathodic current (in the Tafel range), further supporting the argument that acetic acid is not directly reduced at the steel surface. Actually, an opposite effect was clearly observed that suggests a significant inhibiting effect of acetic acid on cathodic currents. The similar effect was noticeable at pH 5 and pH 4 as well (in Figure A.2-2 and Figure A.2-3), however, it was not as clearly discernible. The inhibitive effect

on the anodic dissolution was also observed at pH 3 similar to what was shown at higher pH values.
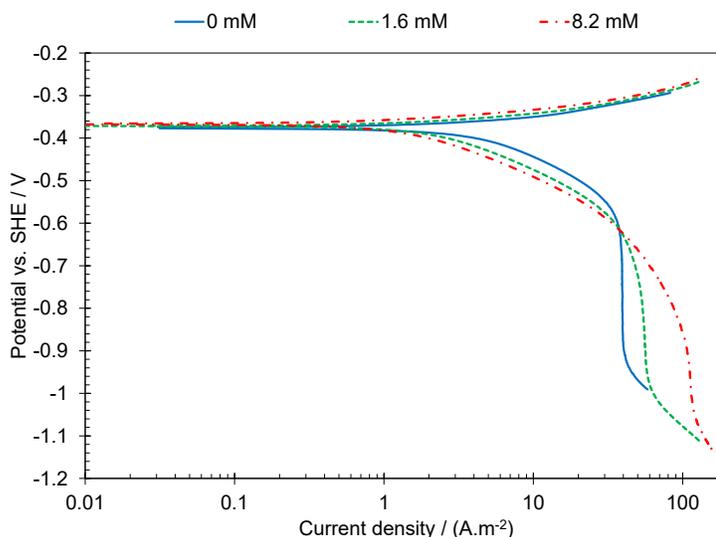
Figure A.2-4. Polarization behavior of X65 mild steel in acidic solution of pH 3, at 30 ºC, RDE, 2000 rpm, 0.1 M NaCl, and undissociated acetic acid concentrations 0 mM, 1.6 mM ($C_{t,HAc}$=1.7 mM), and 8.2 mM ($C_{t,HAc}$=8.3 mM).

Based on the polarization behavior of the studied system, it is reasonable to conclude that acetic acid is not a significant electroactive species in the conditions considered in the present study, *i.e.*, if there is any cathodic current resulting from reduction of acetic acid it is overshadowed by its inhibiting effect on the charge transfer rate of hydrogen ion reduction. Specifically, the results shown at pH 5 and 15.08 mM acetic acid, where $C_{HAc}/C_{H^+}\approx 1500$, suggest that the reaction rate constant for acetic acid direct reduction is at least three orders of magnitude lower than that of hydrogen ion reduction, considering that the over potential is identical for both reactions [55] (based on the Nernst equation with concentration terms defined by the acetic acid equilibrium). Therefore, it can be assumed that the contribution of direct acetic acid reduction in the

typical conditions encountered in the oil and gas industry would be insignificant as compared to hydrogen ion reduction. Thereby, the corrosion process of mild steel in mildly acidic solutions containing acetic acid is a result of only two electrochemical reactions: hydrogen ion reduction as the sole cathodic reaction and the iron dissolution as the sole anodic reaction. However, the polarization curves reported in Figure A.2-2 to Figure A.2-4 suggest that the presence of acetic acid may significantly affect the corrosion process, first by increasing the mass transfer limiting current and, second, by inhibiting the charge transfer rate of both the cathodic hydrogen ion reduction reaction and the anodic iron dissolution reaction. These processes are the subjects of further discussions in the following sections.

A.2.4.2: Effect of acetic acid on limiting current

The reported polarization curves in Figure A.2-2 to Figure A.2-4 showed that the limiting current density is significantly affected by acetic acid concentration. As concluded in the previous section, the hydrogen ion reduction is the only cathodic reaction in the present discussion. The limiting current is therefore a result of the depletion of hydrogen ion concentration at the metal surface. In accordance with this local change of pH at the limiting current condition, the local chemical equilibrium of acetic acid (Reaction (A.2-1)) at the surface shifts towards acetic acid dissociation. Therefore, the cathodic limiting current consists of two components:

- The mass transfer of hydrogen atoms from the bulk to the metal surface followed by their reduction at the surface.

- The mass transfer of undissociated acetic acid followed by homogeneous dissociation to hydrogen ions and acetate ions inside the diffusion layer, succeeded by reduction of the produced hydrogen ion at the surface.

A)

B)
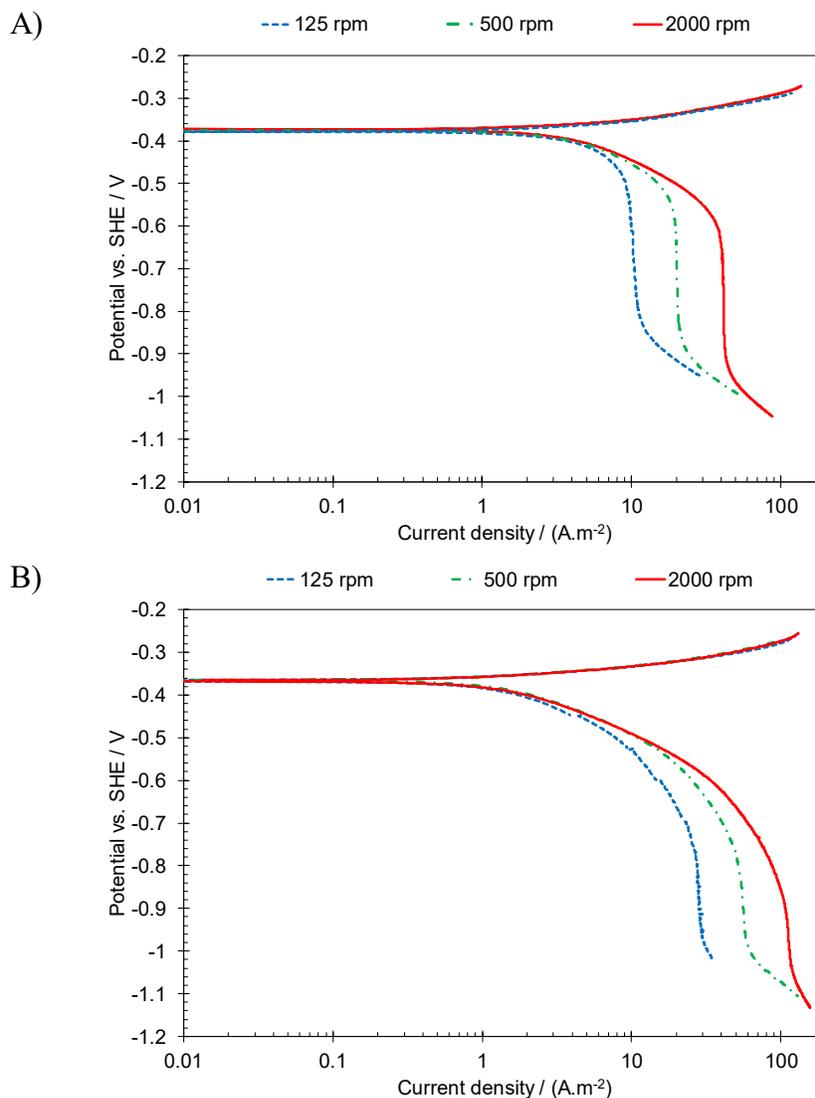
Figure A.2-5. Polarization behavior of X65 mild steel in acidic solution of pH 3, at 30 °C, 0.1 M NaCl, and various rotation speeds. A) C_{HAc}=0 mM, B) C_{HAc}=8.2 mM.

The effect of acetic acid on mass transfer rates was also studied in experiments at a fixed solution composition while the rotation speed of the RDE was varied. Figure A.2-5 shows the typical polarization curves obtained at 125, 500, and 2000 rpm at pH 3 where no acetic acid was present (Figure A.2-5.A) and when the solution contained 8.13 mM undissociated acetic acid (Figure A.2-5.B).

For the case where the hydrogen ion reduction reaction follows the acetic acid dissociation reaction, the limiting current density can be expressed through Equation (A.2-22), for a RDE flow geometry [53].

$$
i_{lim} = \frac{nFD\ (C_{H^+}^b + C_{HAc}^b)}{1.61\ D^{\frac{1}{3}}\ \omega^{-\frac{1}{2}}\ \nu^{\frac{1}{6}} + (\frac{D}{(k_{f,HAc} + k_{b,HAc})})^{\frac{1}{2}}\ /K_{HAc})}
\qquad \text{(A.2-22)}
$$

In the absence of acetic acid, the second term in the denominator of Equation (A.2-22) as well as the acetic acid concentration term disappear. Hence, Equation (A.2-22) reduces to the well-known Levich equation where the limiting current is proportional to $\omega^{0.5}$. The results obtained in the absence of acetic acid at pH 3 were found to agree well with this expected trend, as shown in Figure A.2-6.
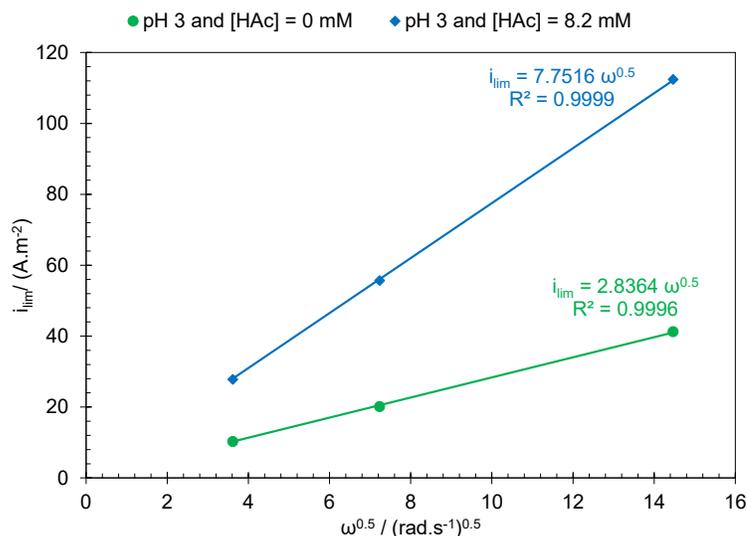
Figure A.2-6. Behavior of the limiting current density vs. square root of rotation speed in acidic solution of pH 3, at 30 °C, 0.1 M NaCl.

In the presence of acetic acid, Equation (A.2-22) suggests that the behavior of limiting current vs. $\omega^{0.5}$ would depend on the kinetics and the equilibrium constant of the acetic acid dissociation reaction as well. Nevertheless, the linear behavior obtained in the presence of acetic acid, as shown in Figure A.2-6, suggests that the flow dependent term (first term in denominator) has remained significantly larger than the chemical reaction dependent term, even at rotation speeds as high as 2000 rpm. Considering that the denominator of Equation (A.2-22) is defined only by the environmental conditions and physiochemical parameters, the limiting currents in the system studied here could therefore be represented by the superposition of hydrogen ion and acetic acid mass transfer from the bulk. That is shown to be indeed the case in Figure A.2-7, where the limiting current is presented as a function of the sum of hydrogen ion and undissociated acetic acid concentrations. The different diffusion coefficients of acetic acid and hydrogen ion, as the only species dependent parameters, should be accounted for. The

linear behavior of the trend-line and the fact that it is crossing the origin, justifies this approach. These results suggest that acetic acid is a strong buffer in the sense that the kinetics and the equilibrium of its dissociation equilibrium allows this species to readily dissociate and buffer the hydrogen ion concentration at the metal surface, whenever the hydrogen ion concentration deviates from the equilibrium. In other words, undissociated acetic acid is primarily a "carrier" for hydrogen ions and increases the effective concentration of hydrogen ions in mild steel corrosion.
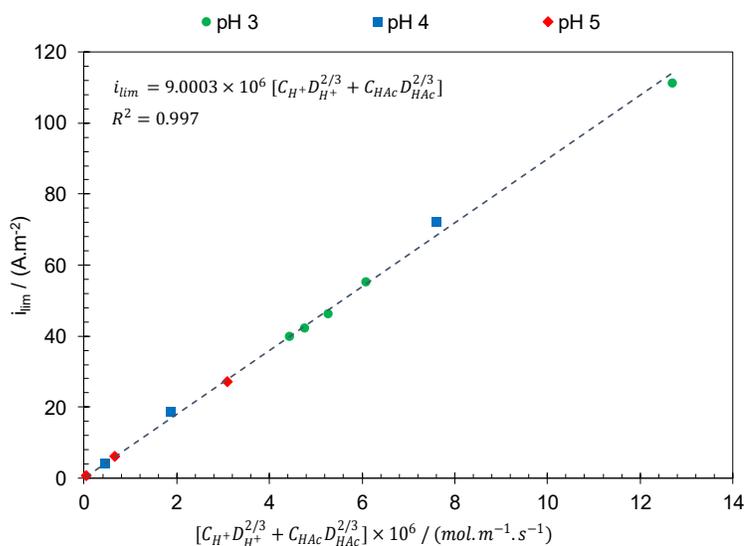
Figure A.2-7. Limiting current density at various hydrogen ion and undissociated acetic acid concentrations on X65 RDE, 2000 rpm, 30°C, 0.1 M NaCl and C_{HAc} from 0 mM to 8.2 mM.

A.2.4.3: Estimation of physiochemical parameters

The mathematical model developed in Section A.2.3.2: was used to obtain the physicochemical parameters of the studied system. This was achieved by determining appropriate values by fitting the model to the experimental data. The kinetic parameters of the electrochemical (hydrogen evolution and iron dissolution) reactions were obtained

using only the experimental data where no acetic acid was present. This step was considered necessary to assure that the estimated parameters were free of any interference due to the presence of acetic acid. Figure A.2-8 shows the comparison of the model (dotted black lines) with the experimental data at pH 3 to pH 5, using the estimated parameters shown in Table A.2-6.
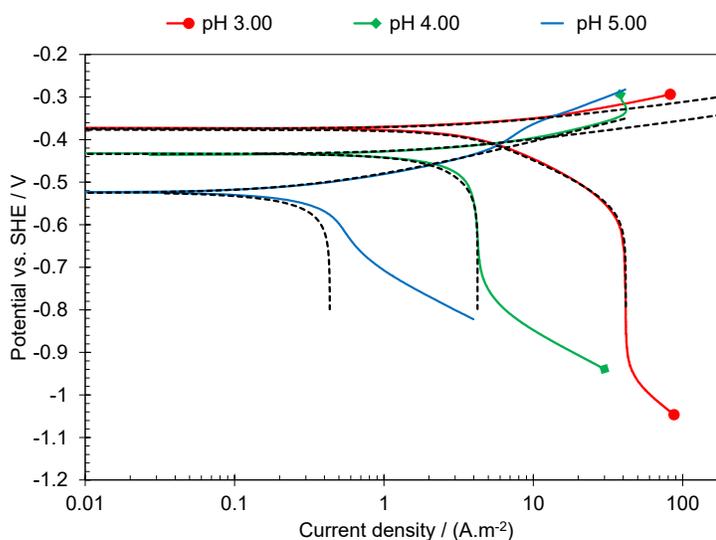
Figure A.2-8. Comparison of the experimental and calculated (dotted back lines) polarizion behavior of X65 mild steel in acidic solutions in the absence of HAc, at 30 °C, 0.1 M NaCl, RDE, 2000 rpm, and various pH values.

The transfer coefficient for the hydrogen ion reduction (0.43) was slightly lower than the commonly accepted theoretical value of 0.5, however, similar deviations have been previously reported [75,76]. The iron dissolution reaction showed a significant change in the kinetic parameters at pH 5 (compared to pH 3 and pH 4) where the Tafel slope increased from 40 mV at pH 4 to approximately 90 mV at pH 5. As discussed above, this behavior has been frequently reported in previous studies [71–74], and suggests that at these environmental conditions the mechanism of iron dissolution in the vicinity of the

corrosion potential is no longer in the active dissolution range. Based on this observation, a different charge transfer relationship was used for this particular condition (Table A.2-6). As noted in section A.2.4.1: , this behavior was only observed at pH 5 when no acetic acid was present.

Table A.2-6. Electrochemical reaction rate relationships and parameters.

Charge transfer rates	n	α	m	$E_{0,j}$ vs. SHE (V)	$k_{0j,\,ref}$	E_a (kJ/mol)
i_{c,H^+} $= -n_{H^+}Fk_{0_{H^+}}\left(C_{H^+}^s\right)^{m_{H^+}}e^{\left(\frac{-\alpha_{H^+}+n_{H^+}F(E-E_{0_{H^+}})}{RT}\right)}$	1	0.43	0.5	0.00	7.58×10^{-8}	110.6
$i_{a,Fe} = n_{Fe}Fk_{0_{Fe}}(C_{OH^-}^s)^{m_{OH^-}}e^{\left(\frac{(2-\alpha_{Fe})F(E-E_{0_{Fe}})}{RT}\right)}$ pH <5 or C_{HAc} >0	2	0.50	1	-0.44	2.27×10^1	29.5
$i_{a,Fe} = n_{Fe}Fk_{0_{Fe}}(C_{OH^-}^s)^{m_{OH^-}}e^{\left(\frac{2(1-\alpha_{Fe})F(E-E_{0_{Fe}})}{RT}\right)}$ pH = 5 and C_{HAc} =0	2	0.65	0	-0.44	2.05×10^{-5}	-

A.2.4.4: Inhibiting effect of acetic acid

Considering that direct acetic acid reduction was shown to be insignificant in the conditions of the present study, the model developed above, based solely on hydrogen ion reduction and iron dissolution reactions, should be able to describe the steady state voltammograms obtained in the presence of acetic acid. However, the inhibiting effect of undissociated acetic acid on the charge transfer rates also needs to be quantified for more accurate prediction of both the polarization curves and corrosion rates.

The inhibiting effect of acetic acid on the anodic and cathodic charge transfer rates was quantified in terms of its adsorption on the metal surface acting as a weak corrosion inhibitor that results in blockage of the active sites of the electron transfer

reactions. However, considering numerous surface active species, such as water, chloride ions, as well as anodic and cathodic reaction intermediate species and the non-uniformity of the steel surface, a detailed mechanistic description of this phenomena is well beyond the scope of the present study, hence, a semi-empirical approach was employed. The rate of electrochemical reactions in the presence of acetic acid was assumed to follow Equation (A.2-23) and Equation (A.2-24):

$$i_{H^+,HAc} = i_{H^+}(1 - \theta_c) \qquad\qquad\qquad\qquad\text{(A.2-23)}$$

$$i_{Fe,HAc} = i_{Fe}(1 - \theta_a) \qquad\qquad\qquad\qquad\text{(A.2-24)}$$

Since the reaction rate constants were known from the condition without acetic acid present, the surface coverage of acetic acid (θ) could be determined by using the model to obtain the apparent rate constants from the experimental data as shown in Equation (A.2-25). Here $k_{0,HAc}$ is the apparent reaction rate constant in the presence of acetic acid and k_0 is the reaction rate constant reported in Table A.2-6 for each reaction.

$$\frac{k_{0,HAc}}{k_0} = (1 - \theta) \qquad\qquad\qquad\qquad\text{(A.2-25)}$$

As noted in Equation (A.2-25), the calculation of θ required the k_0 where no acetic acid was present to be known explicitly. As shown in Figure A.2-2 to Figure A.2-4, pH 3 was the only condition where the pure charge transfer controlled cathodic current was observed without acetic acid being present, and the anodic polarization curve was not affected by local pH due to cathodic mass transfer limitation. Hence, the k_0 values could be obtained from the experimental data, directly. Therefore, pH 3 was selected as the base condition for the discussion on the inhibitive effect of acetic acid on the charge transfer rates. Figure A.2-9 demonstrates the values of surface coverage

obtained as described *via* Equation (A.2-25), using the experimental data at pH 3 and an

extended acetic acid concentration range.
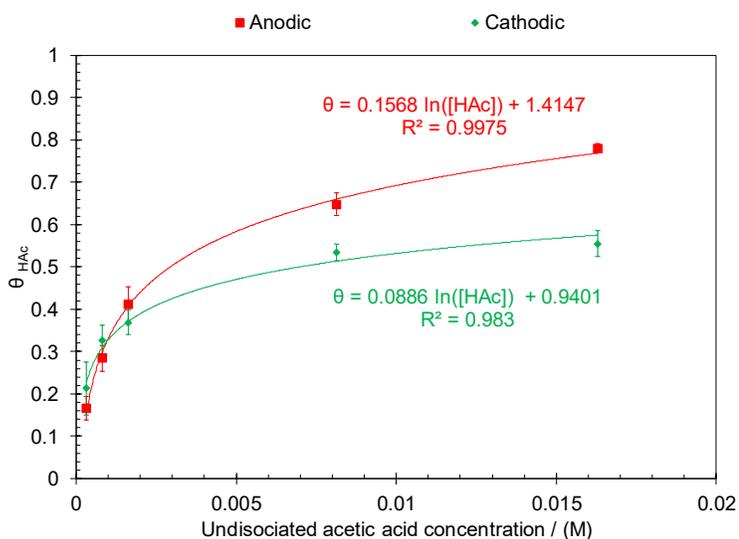
Figure A.2-9. The variation of θ, defined by Equation (A.2-25), as a function of undissocated acetic acid concentration for cathodic currents (green line) and anodic currents (red line). Error bars are based on the standard deviation of at least three repeats.

The coverage effect associated with the acetic acid adsorption shows a

logarithmic trend with the undissociated acetic acid concentration. Transforming this

functionality (Equation (A.2-26)) to Equation (A.2-27)) shows that acetic acid follows

a Temkin type adsorption isotherm.

$$\theta = A \ln(C_{Hac}) + B \qquad\qquad\qquad\qquad (\text{A.2-26})$$

$$e^{(r\theta)} = K C_{Hac} \qquad\qquad\qquad\qquad (\text{A.2-27})$$

where $K = e^{B/A}$ and $r = 1/A$. However, the observed inhibiting effect was different for

the cathodic and anodic reactions. That is due to the semi-empirical treatment of these

parameters where the effect of the numerous surface active species and non-uniform steel

surface are all lumped into the two constants of Equation (A.2-26). The difference in the observed inhibitive effect on the cathodic and anodic currents suggests a competitive adsorption scenario. At anodic currents, acetic acid is competing with electrochemical hydroxide adsorption as the reactions intermediate of the iron dissolution reaction [71,77,78], while at cathodic currents it is the electrochemical hydrogen ion adsorption in competition with acetic acid.

Figure A.2-10 is a comparison of the experimental results at pH 3 with those calculated by the model. The agreement of the results showed that the inhibitive effect of acetic acid was properly reflected through the Temkin type adsorption isotherms discussed above.
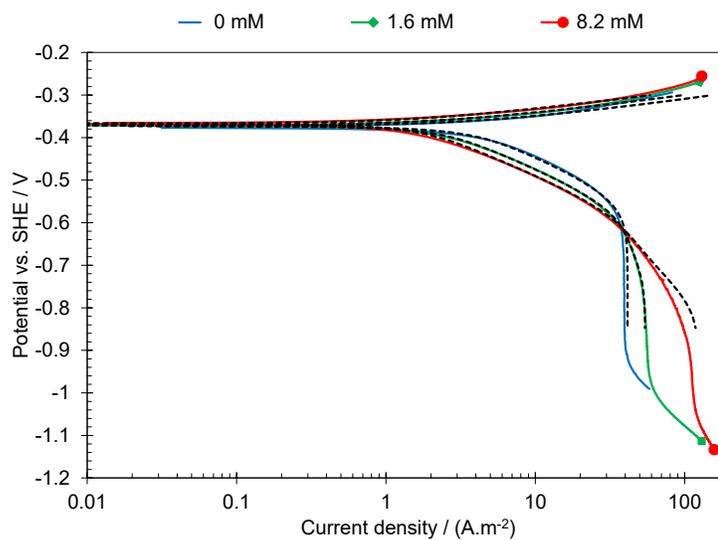
Figure A.2-10. Comparison of the experimental and calculated (dotted black lines) polarizion behavior of X65 mild steel in acidic solutions demonstrating the inhibitive effect of acetic acid of pH 3, at 30 ºC, 0.1 M NaCl, RDE, 2000 rpm.

A.2.4.5: Temperature effect

An increase in temperature affects the charge transfer and the mass transfer rates as well as the adsorption of acetic acid, and the solution speciation (as discussed in section A.2.3.2.1:). Figure A.2-11 shows the experimental polarization curves obtained at pH 3 for 30°C, 40°C and 50°C, A) in the absence and B) in the presence of acetic acid.
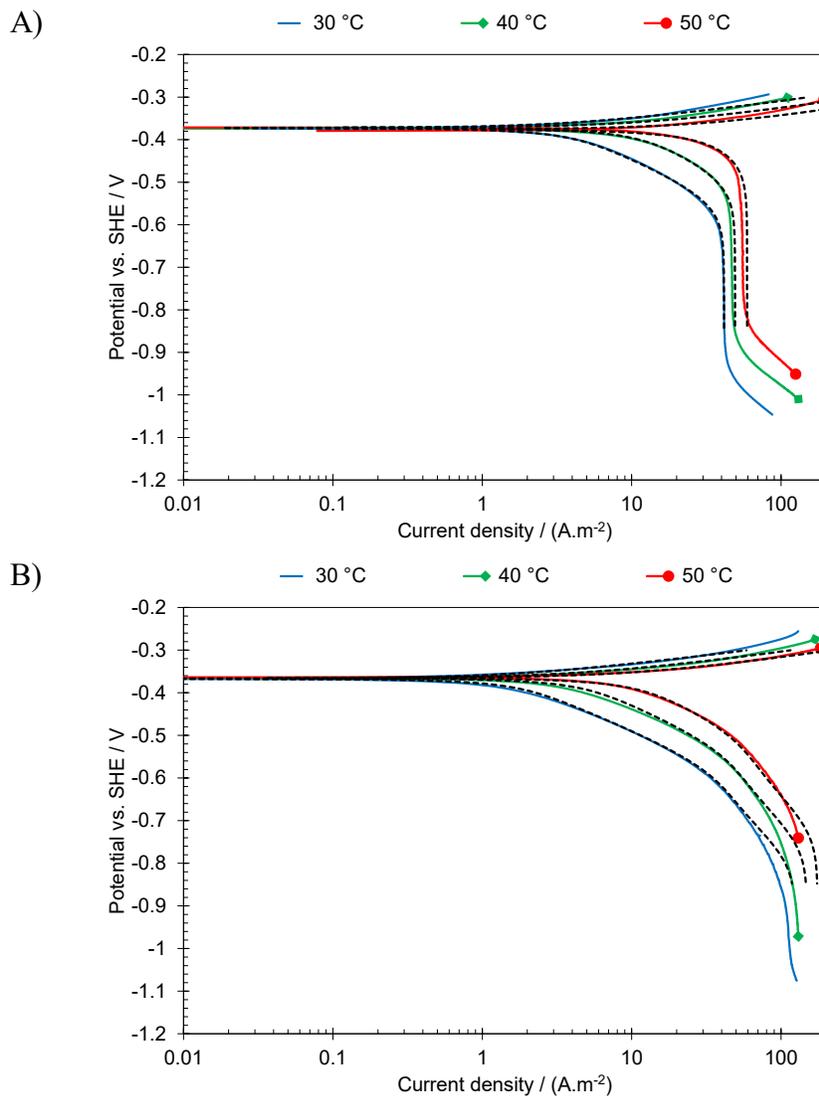
Figure A.2-11. Comparison of the experimental and calculated (dotted black lines) polarization behavior of X65 mild steel in acidic solutions demonstrating the temperature effect at pH 3, 0.1 M NaCl, 2000 rpm RDE at 30 ºC (blue line), 40 ºC (green line), and 50 ºC (red line). A) 0 ppm HAc, B) 500 ppm HAc.

The effect of temperature on mass transfer rate is through temperature dependence of the different terms of the Nernst-Planck equation, which includes the diffusion coefficients in molecular diffusion and electromigration terms. The flow velocity (v_x) in convective flow term is affected by the temperature dependence of

physical properties of water, such as viscosity and density. The temperature dependence

of these parameters are summarized in Table A.2-7.

Table A.2-7. Temperature dependence of the physiochemical properties.

Parameter	Relationship	Reference
Water density (kg/m³)	$\rho_w = 753.596 + 1.87748\,T - 0.003562\,T^2$	15
Water viscosity (cP)	$\mu = \mu_{ref}\,10^{\left(\frac{1.1709\,(T_{ref}-T)-0.001827(T_{ref}-T)^2}{(T-273.15)+89.93}\right)}$ $T_{ref} = 293.15\ K, \mu_{ref} = 1.002\ cP$	79
Diffusion coefficient	$D_i = D_{i,ref}\dfrac{T}{T_{ref}}\dfrac{\mu_{ref}}{\mu}$	68
HAc adsorption, cathodic	$\theta_c = 8.86 \times 10^2\,\dfrac{T}{303.15}\left(\ln(C_{HAc}) + 10.61 + \dfrac{-61385}{R}\left(\dfrac{1}{T} - \dfrac{1}{303.15}\right)\right)$	This study
HAc adsorption, anodic	$\theta_a = 1.57 \times 10^{-1}\,\dfrac{T}{303.15}\left(\ln(C_{HAc}) + 9.02 + \dfrac{-2248}{R}\left(\dfrac{1}{T} - \dfrac{1}{303.15}\right)\right)$	This study

The effect of temperature on charge transfer rate can be characterized by an

Arrhenius dependency and the activation energy of the electrochemical reactions. Figure

A.2-12 shows the temperature dependence of the apparent reaction rate constants, where

the slope of the trend-line represents the activation energy of a given reaction ($-E_a/R$).

Therefore, the temperature dependence of the electrochemical reactions can be expressed

through van't Hoff's law:

$$k_{0_j} = k_{0_{j,ref}}\,e^{\left(-\frac{Ea}{R}\left(\frac{1}{T} - \frac{1}{303}\right)\right)}$$

(A.2-28)
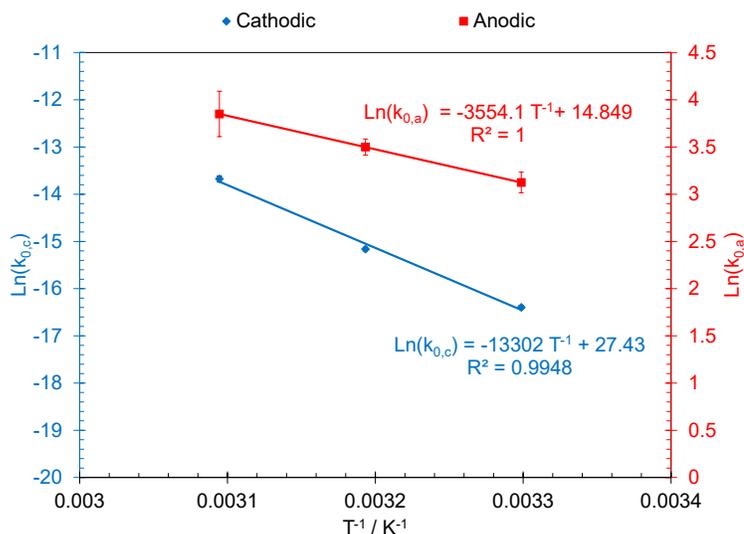
Figure A.2-12. Temperature dependence for the reaction rate constant without acetic acid present at pH 3, 0.1 M NaCl, for hydrogen ion reduction (blue line) and iron oxidation (red line). Error bars are based on the standard deviation of at least three repeats.

The effect of temperature on inhibition by acetic acid can be discussed in terms of the parameter θ as shown in Equation (A.2-27), where K is the adsorption equilibrium constant with an Arrhenius type temperature dependence ($K = K_0 e^{-Ea/RT}$) and $r = b/RT$. Therefore, Equation (A.2-26) can be restated as Equation (A.2-29) to accommodate for the temperature effect.

$$\theta = \frac{RT}{b}(\ln([HAc]) + \ln(K_0)) - \frac{E_a}{b} \qquad\qquad \text{(A.2-29)}$$

The only unknown parameter in Equation (A.2-29) is E_a, the activation energy of the acetic acid adsorption equilibrium constant. As shown in Equation (A.2-29), E_a is represented by the intercept of the trend-line ($-E_a/b$) in a θ vs. T graph as shown in Figure A.2-13. From these results, the temperature effect on the inhibition by acetic acid is expressed by the last two equations shown in Table A.2-7.
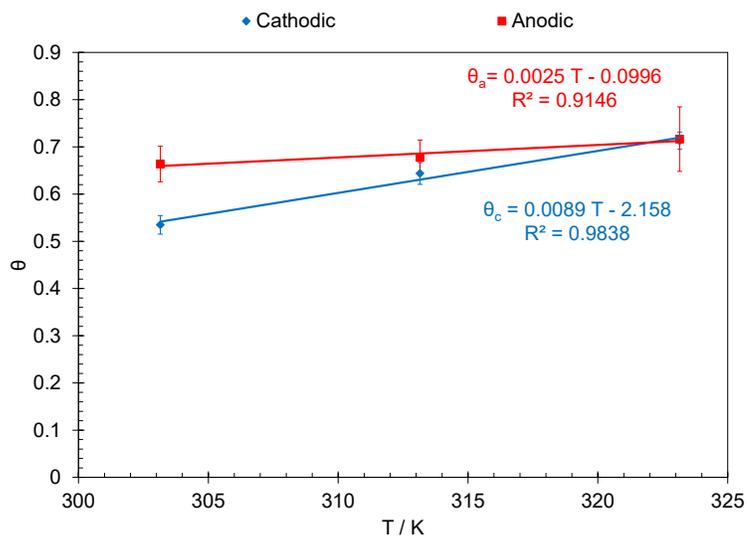
Figure A.2-13. Temperature dependence for acetic acid adsorption at pH 3, 0.1 M NaCl, and C_{HAc}=8.2 mM, for hydrogen ion reduction (blue line) and iron oxidation (red line). Error bars are based on the standard deviation of at least three repeats.

The temperature dependence of the physiochemical parameters, as summarized in Table A.2-7, were incorporated into the model and the predicted voltammograms were compared with experimental data. Figure A.2-11.A shows the comparison for the case without any acetic acid present, while the predicted voltammograms for a solution at pH 3 and 8.2 mM undissociated acetic acid concentration is shown in Figure A.2-11.B. Here again a reasonable agreement was found, while at more negative potentials close to limiting current densities, slight deviations between the predicted apparent Tafel slopes and the measurements were observed.
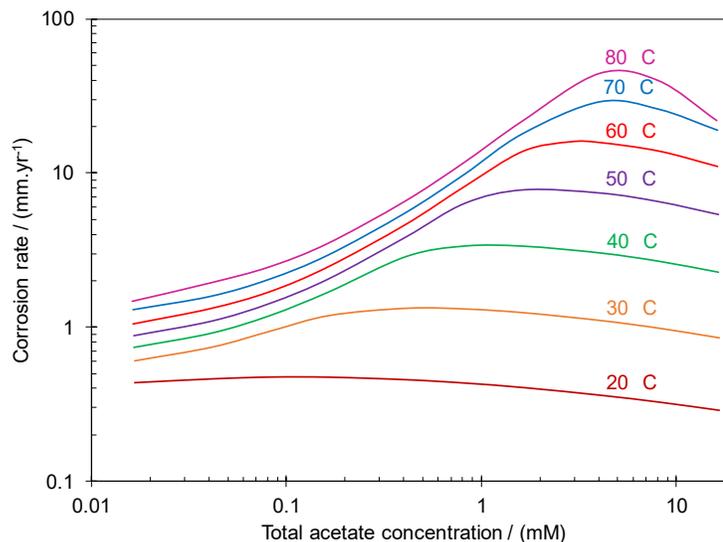
Figure A.2-14. The estimated corrosion rates for mild steel in pH 5, 0.1 M NaCl, 2000 rpm RDE with respect to temperature and total acetic acid concentration.

The effect of increased temperature in the presence of acetic acid is demonstrated in Figure A.2-14 based on the prediction of the model at pH 5. These results show a synergistic effect of temperature with undissociated acetic acid concentration on the corrosion rates that further elucidates the inconsistent and sometimes contradictory behavior of corrosion rates in the presence of acetic acid as reported in the literature (see Section A.2.1:). Figure A.2-14 shows that a maximum corrosion rate exists at each condition, which is increased at higher temperatures and is greatly influenced by acetic acid concentration. The decreasing trend of corrosion rates, observed in Figure A.2-14, is a result of acetic acid's inhibitive effect on the charge transfer cathodic and anodic currents when the corrosion current is controlled by the rate of electrochemical reactions. Whereas, the increasing effect on the corrosion rate stems from the buffering ability of acetic acid and the resulting increase in limiting currents, when the corrosion current is under mass transfer control. At elevated temperatures, the increased rate of anodic and

cathodic reactions shifts the corrosion current towards the mass transfer limiting range, as readily observed in the polarization behavior in Figure A.2-11. This combined effect leads to extremely high corrosion rates at elevated temperatures in the presence of acetic acid.

A.2.5: Corrosion rate prediction

The performance of the mathematical model developed in the previous sections was further examined with the comparison of the estimated corrosion rates with the experimental data. Figure A.2-15 is the comparison of the corrosion rate data obtained by linear polarization measurements at pH 3, pH 4, and pH 5 with and without acetic acid present. At pH 3 and pH 4 where the corrosion current is mostly under charge transfer control, increasing acetic acid concentration decreased the corrosion rates. At pH 5 and in the absence of acetic acid, the corrosion current was under mass transfer control (Figure A.2-2), therefore, by addition of 0.6 mM undissociated acetic acid, the corrosion rate was rapidly increased, but a further increase of acetic acid resulted in a slightly lower corrosion rate. The effect of acetic acid on the observed corrosion rates as shown in Figure A.2-15 was in complete agreement with the expected behavior as discussed in Sections A.2.4.1: and A.2.4.1: .
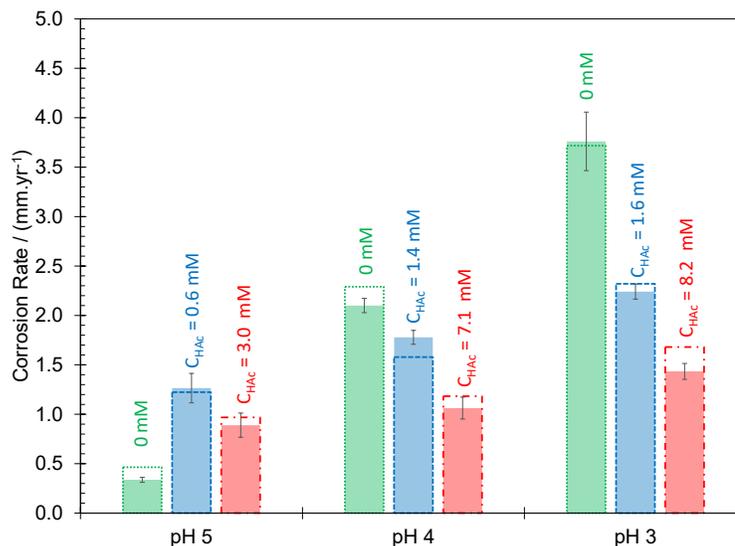
Figure A.2-15. Comparison of the experimental and calculated corrosion rates of X65 mild steel in acidic solutions, at 30 °C, 0.1 M NaCl, 2000 rpm. Green , at various pH values and $C_{t,HAc}$ values. Dashed boxed show the predicted values. Error bars are based on the standard deviation of at least three repeats.

The performance of the model was further examined in the parity plot shown in Figure A.2-16 where the experimental data was compared with the calculated corrosion rates for a wider range of environmental conditions and solution compositions (22 °C < T < 60 °C, 2 < pH < 5, 0 mM < $C_{t,HAc}$ < 16.6 mM, 125 rpm< rotation speed < 2000 rpm). Most of the calculated data points are within 20% of the measured values and in almost every case within a factor of two.
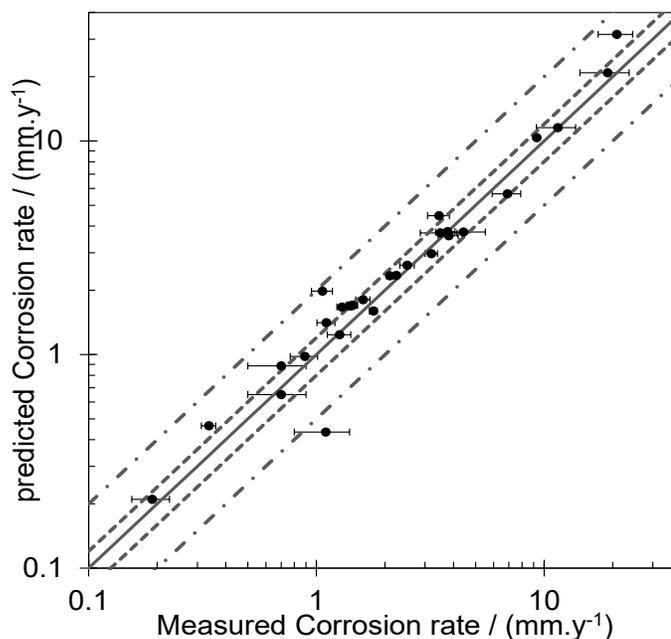
Figure A.2-16. Comparison of the predicted corrosion rates with experimental results for a wide range of parameters. 22 °C < T < 60 °C, 2 < pH < 5, 0 mM < $C_{t,HAc}$ < 16.6 mM, 125 rpm< rotation speed < 2000 rpm. Additional experimental data from Zheng et al. [13] and George et al.[32]. Dashed lines and the dotted dashed lines represent 20% and one fold deviation, respectively. Error bars are based on the standard deviation of at least three repeats.

A.2.6: Summary

- The experimental results and the quantitative analysis reported in the present study showed that the direct acetic acid reduction does not significantly contribute to the cathodic currents in acidic solutions.

- Acetic acid was shown to be a strong buffer, which was fully dissociated under mass transfer limiting conditions, meaning that the kinetics of the dissociation reaction were not rate determining.

- The inhibitive effect of acetic acid was explained through its adsorption on the metal surface, which was well defined by a Temkin type adsorption isotherm.

- Different adsorption constants over the anodic and cathodic current suggested a competitive adsorption scenario depending on the electrode potential and the dominant electron transfer reaction.

- The results reported in the present study suggest that the presence of acetic acid affects the acidic corrosion of mild steel through two mechanisms:

  - Acetic acid increases the corrosion rate through buffering the H^+ concentration at the metal surface, if the corrosion current is under mass transfer control.

  - Acetic acid decreases the corrosion rate by inhibiting the charge transfer rates, if the corrosion current is under charge transfer control.

- Elevated temperatures were shown to have a synergistic effect on acetic acid corrosion by shifting the corrosion current towards the mass transfer limiting condition, where acetic acid has a determinant effect.

Nomenclature

Symbol	Definition
A	Surface area (m^2)
C_i	Concentration of species i (M)
C_i^b	Concentration of species i at bulk (M)
C_i^s	Concentration of species i at metal surface (M)
D_i	Diffusion coefficient of species i (m^2/s)
$D_{i,ref}$	Diffusion coefficient of species i at reference temperature (m^2/s)
E	Electrode potential (V)
E_a	Activation energy (J)
E_{0j}	Standard potential of reaction j (V)
F	Faradays constant (C/mol)
ΔH_j	Enthalpy of reaction j (kJ/mol)
i_j	Current density of reaction j (A/m^2)
K_j	Equilibrium constant of reaction j
k_{0j}	Rate constant of electrochemical reaction j

$k_{0j,ref}$	Rate constant of electrochemical reaction j at reference temperature
k_f	Forward reaction rate constant
k_b	Backward reaction rate constant
m_i	Reaction order with respect to species i
n_j	Number of transferred electrons in electrochemical reaction j
n_r	Number of reacting species
n_p	Number of produced species
N_i	Flux of species i (mol/m^2.s)
r	Temkin adsorption isotherm correlation coefficient
R	Universal gas constant (J/K.mol)
R_i	Reaction rate of species i (M/s)
s_{ij}	Stoichiometric coefficient of species i in reaction j
T	temperature (K)
T_{ref}	Reference temperature (K)
t	Time (s)
u_i	Mobility of species i (m/s)
v_x	Velocity along x axis (m/s)
x	Distance from metal surface (m)
z_i	Charge of ion i
α_j	Transfer coefficient of electrochemical reaction j
δ	Diffusion layer thickness (m)
μ	Water viscosity (kg/s.m)
μ_{ref}	Water viscosity at reference temperature (kg/s.m)
θ	Surface coverage by acetic acid
ρ_w	Density of water (kg/m^3)
υ	Kinematic viscosity (m^2/s)
ϕ	Electric potential inside liquid (V)
ω	Angular velocity (rad/s)

PART B: THE CASE OF CARBON DIOXIDE

- Chapter B.1: A review on the basic mechanisms and mathematical modeling of CO_2 corrosion

- Chapter B.2: The nature of the effect of CO_2 on the cathodic currents of corrosion in aqueous acidic solutions

- Chapter B.3: The mechanism and prediction of CO_2 corrosion

- Chapter B.4: The new perspective to CO_2 corrosion of mild steel

Chapter B.1: A review on the basic mechanisms and mathematical modeling of CO_2 corrosion[4]

B.1.1: Introduction

Almost every milestone in the understanding of CO_2 corrosion coincides with development of a more inclusive mechanistic mathematical model, such that it is hard to distinguish which one was the cause and which was the result. That signifies the importance of concurrent systematic experimentation and detailed quantitative analysis, when it comes to the discussion of corrosion mechanisms. In this chapter, the state-of-the-art with regards the mechanistic understanding of uniform carbon dioxide corrosion of mild steel is reviewed and the corresponding mathematical models are presented. The existing predictive models are categorized into three groups, termed: empirical/semi-empirical, elementary mechanistic, and comprehensive mechanistic. With emphasis on mechanistic models, selected key publications are reviewed and the limits and advantages of each group of models are discussed. Furthermore, the ability of the existing models to be extended and account for more complex corrosion scenarios is discussed.

B.1.2: Background

Reliable estimation of corrosion rate is one of the key considerations for design of transmission pipelines, and related infrastructure, for oil and gas production and processing. Predicted corrosion rates directly affect major design decisions, such as

---

[4] A version of this chapter is published as: "Modeling of Uniform CO_2 Corrosion of Mild Steel in Gas Transportation Systems: A Review", Aria Kahyarian, Marc Singer, Srdjan Nesic, J. Nat. Gas Sci. Eng. 2016 (29), p. 530-549. (Reference number [43])

material selection, pipe wall thickness allowance, pipe diameter and hence velocity, etc.,
as well as operational planning such as need for corrosion mitigation, inspection and
monitoring. Underestimation of corrosion rates may therefore lead to failure, with health,
safety and environmental hazards as well as significant financial losses due to production
interruption, equipment replacement, property damage, etc. On the other hand, gross
overestimation can have a strong impact on project economics.

In oil and gas production, carbon dioxide (CO_2) is almost always present as a by-
product and, in its hydrated form (H_2CO_3), is a well-known corrosive species. Mild steel
uniform corrosion rate estimations associated with CO_2 in wet natural gas systems have
historically been done by "worst case" empirical/semi-empirical models developed in the
1980s and 1990s [80–82]. Whilst these models have been extensively used, primarily due to
their simplicity, their application is limited by the narrow range of conditions they cover.
On the other hand, increasing interest for exploration and gas production in harsher, more
corrosive environments pushes the applications of these models beyond the point where
they can be confidently used. Even though improving the models to address ever more
challenging industrial demands has been slow, advancements in the mechanistic
understanding of the underlying processes in CO_2 corrosion has provided new
opportunities for development of more robust mechanistic models, with the ability to
perform well beyond the scope covered by the previous empirical/semi-empirical models.
Having strong roots in physicochemical theory underlying the corrosion process, the
mechanistic models introduced over the past two decades have provided the flexibility

required to cover various conditions and include new processes in corrosion rate calculations.

Uniform CO_2 corrosion of mild steel can be considered as one of the most studied and well understood corrosion systems. In addition to numerous studies covering specific aspects of this corrosion system, several holistic reviews of the underlying physicochemical processes [20,28,47,83,84] as well as reviews of uniform corrosion rate prediction models [85–89] are available in the literature.

The present review is primarily focused on progress in development of mechanistic mathematical models of aqueous CO_2 corrosion of mild steel and describes the state-of-the-art. In this context, the fundamental physicochemical processes underlying uniform CO_2 corrosion are discussed and the corresponding mathematical relationships are presented. The mechanistic aspects of the chemical and electrochemical reactions, as well as mass transfer processes, are covered in some detail.

The mathematical models developed to date are categorized herein into three main groups: *(i)* empirical/semi-empirical, *(ii)* elementary mechanistic, and *(iii)* comprehensive mechanistic models. As the focus is on mechanistic models, the empirical and semi-empirical models are only briefly discussed as background/historical information. In the discussion of the mechanistic models, selected key studies are reviewed and the strength and limitations of the various modeling approaches are presented. Furthermore, the ability of the various types of models to be adapted to more complex conditions and be extended to include additional phenomena, such as those seen

in the presence of additional corrosive species (*e.g.* H₂S, carboxylic acids, etc.), corrosion product layer formation, and top of the line corrosion (TLC) is discussed.

B.1.3: Review of the fundamentals

B.1.3.1: Water chemistry in CO_2 corrosion

A comprehensive knowledge of the water composition is essential for accurate calculations of corrosion rates. Chemical equilibria relating to dissolved CO_2 and its carbonic/carbonate derivatives in bulk solution have been extensively studied [90–92]. However, reaction kinetics relating to these equilibria, particularly at the interface between the bulk fluid and the metal surface, have only been accounted for in more recent mechanistic studies [11,15,44,45].

Table B.1-1. Homogeneous chemical reactions in water/CO₂ environment.

Reaction	Equilibrium equation	
$CO_{2(g)} \leftrightharpoons CO_{2(aq)}$	$H_{CO_2} = \dfrac{[CO_{2(aq)}]}{pCO_{2(g)}}$	(B.1-1)
$CO_{2(aq)} + H_2O_{(l)} \leftrightharpoons H_2CO_{3(aq)}$	$K_{hyd} = \dfrac{k_{f,hyd}}{k_{b,hyd}} = \dfrac{[H_2CO_3]}{[CO_{2(aq)}]}$	(B.1-2)
$H_2CO_{3(aq)} \leftrightharpoons HCO_{3(aq)}^- + H^+_{(aq)}$	$K_{ca} = \dfrac{k_{f,ca}}{k_{b,ca}} = \dfrac{[HCO_3^-][H^+]}{[H_2CO_3]}$	(B.1-3)
$HCO_{3(aq)}^- \leftrightharpoons CO_{3(aq)}^{2-} + H^+_{(aq)}$	$K_{bi} = \dfrac{k_{f,bi}}{k_{b,bi}} = \dfrac{[CO_3^{2-}][H^+]}{[HCO_3^-]}$	(B.1-4)
$H_2O_{(l)} \leftrightharpoons OH^-_{(aq)} + H^+_{(aq)}$	$K_w = \dfrac{k_{f,w}}{k_{b,w}} = [OH^-][H^+]$	(B.1-5)

The main chemical reactions in CO_2 aqueous solutions, their corresponding chemical equilibria, and kinetic rate constants are presented in Table B.1-1 and Table B.1-2. The water speciation in the bulk solution can be readily calculated by

simultaneous solution of equilibrium expressions for all species along with

electroneutrality constraints [28].
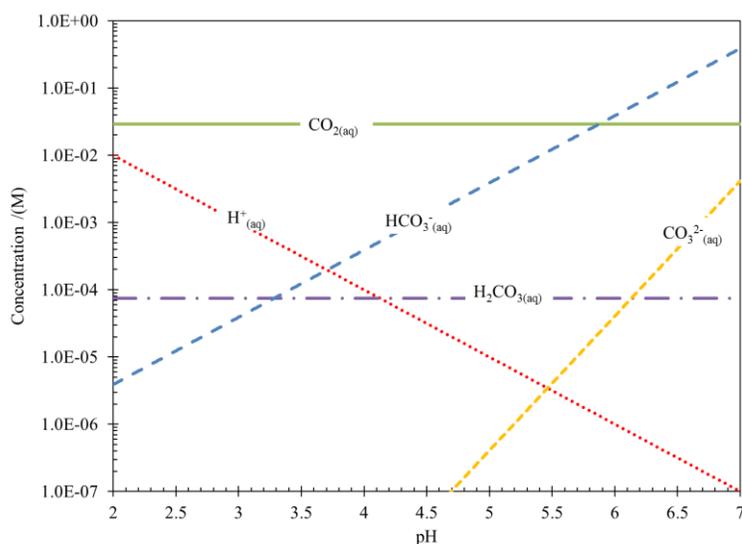
Figure B.1-1. Concentration of different species in CO_2/water equilibrium at various pH values, pCO_2= 1 bar, T=298°K, and 0.5 M NaCl in an open system with a constant CO_2 partial pressure.

An example of the results of such calculations for an open system with constant

partial pressure of 1 bar CO_2 at various pH values is shown in Figure B.1-1. The effect of

reaction kinetics on surface concentrations needs to be accounted for differently, as

discussed in detail in Section B.1.3.3: . It should be noted here that it was assumed that

the infinite dilution theory is valid, *i.e.*, the activity coefficients for all the chemical

species are assumed to be unity. This assumption is consistent with the literature

considered in the present review. While it provides a reasonable estimation of speciation

for the majority of aqueous CO_2 systems seen in gas transportation applications, it also

greatly simplifies the resulting mathematical expressions. The effect of non-ideal

behavior seen at high pressures and concentrations is discussed in Chapter B.4: . It is

important to note that the modifications required to cover this non-ideal behavior can be
readily included into the general framework of the mechanistic models discussed in the
following chapters.

Table B.1-2. Equilibrium and reaction rate constants.

Constant	Units	Ref.
$H_{CO_2} = \dfrac{1}{1.00258}\exp\left(93.4517\left(\dfrac{100}{T}\right) - 60.2409 + 23.3585\ \ln\left(\dfrac{T}{100}\right)\right.$ $\left. + \left(0.023517 - 0.023656\left(\dfrac{T}{100}\right)\right.\right.$ $\left.\left. + 0.0047036\left(\dfrac{T}{100}\right)^2\right)S\text{‰}\right)$	M.bar $^{-1}$	[91,93,94]
$K_w = \exp(\dfrac{-13847.26}{T} + 148.9652 - 23.6521\ \ln T$ $+ \left(\dfrac{118.67}{T} - 5.977 + 1.0495\ \ln T\right)S\text{‰}^{0.5} + 0.01615\ S$	M ^{2}	[91,93,95]
$k_{b,w} = 7.8 \times 10^{10}$	M $^{-1}$.s $^{-1}$	[96]
$K_{hyd} = 2.85 \times 10^{-3}$	-	[97]
$k_{f,hyd} = 10^{(329.85 - 110.541 \times \log T - \frac{17265.4}{T})}$	s $^{-1}$	[97]
$K_{ca} = 378.6\ \exp(\dfrac{-2307.1266}{T} + 2.83655 - 1.5529413\ \ln T$ $+ \left(\dfrac{-4.0484}{T} - 0.20760841\right)S\ \text{‰}^{0.5}$ $+ 0.08468345\ S\ \text{‰} - 0.00654208\ S\ \text{‰}^{1.5}$ $+\ ln(1 - 0.001005\ S\ \text{‰}))$	M	[91,93,98]
$k_{f,ca} = 10^{(5.71 + 0.0526 \times T_C - 2.94 \times 10^{-4} \times T_C^2 + 7.91 \times 10^{-7} \times T_C^3)}$	s $^{-1}$	[99]
$K_{bi} = \exp(\dfrac{-3351.6106}{T} - 9.226508 - 0.2005743\ \ln T$ $+ \left(\dfrac{-23.9722}{T} - 0.106901773\right)S\ \text{‰}^{0.5}$ $+ 0.1130822\ S\ \text{‰} - 0.00846934\ S\ \text{‰}^{1.5}$ $+\ ln(1 - 0.001005\ S\ \text{‰}))$	M	[91,93,98]
$k_{b,bi} = 5 \times 10^{10}$	s $^{-1}$	[15]*

* The value of $k_{f,bi}$ is estimated and it is not based on experimental measurements.

B.1.3.2: Electrochemical reactions in CO_2 corrosion

The cathodic and anodic reactions on the metal surface are what define the corrosion process as a heterogeneous phenomenon. Table B.1-3 summarizes the key electrochemical reactions associated with the species commonly considered electroactive in aqueous CO_2 corrosion of mild steel. Each reaction shown is an overall reaction and usually consists of a few elementary steps, which are discussed in the following sections. Reactions (B.1-6) to (B.1-9) are the possible cathodic reactions in a CO_2 containing aqueous environment. Reactions (B.1-6) and (B.1-7) are the well-known hydrogen evolution reactions from hydrogen ion and water, common for all aqueous acidic systems. Reaction (B.1-7) is the so-called "direct" reduction of carbonic acid (H_2CO_3), which has been identified by numerous authors as the main contribution of CO_2 to the enhancement of corrosion rate, when compared to strong acids [14,15,18,19]. Similarly, Reaction (B.1-8) is the reduction of bicarbonate ion which is believed to be significant at near-neutral and alkaline pH values due to high bicarbonate ion concentration, as depicted in Figure B.1-1 [100–103]. In the literature, both the reduction of carbonic acid and bicarbonate ion are known as the "direct reduction" mechanism, meaning that the undissociated acid is directly reduced at the metal surface during the corrosion process, to evolve hydrogen. An alternative mechanism known as "buffering effect" is also proposed in the literature. This mechanism suggests that the dissociation of the carbonic acid in the vicinity of the metal/solution interface replenishes the hydrogen ion concentration at the metal surface as it is consumed by the corrosion process [11,50]. It should be noted that the "direct reduction" mechanism allows for the possibility for carbonic acid (or any other

weak acid) to also act as a buffer [15,45,46], while this is not considered to be the dominant effect. On the other hand, the "buffering effect" mechanism excludes the possibility of "direct reduction" of weak acids. Therefore, the divergence of the two mechanisms, "buffering effect" and "direct reduction", is in the assumed electro-activity of the undissociated weak acid.

Similar mechanistic arguments are frequent in corrosion studies. For example, the direct reduction of water is common knowledge; it has been recently postulated that another weak acid, hydrogen sulfide, is also directly reduced [13,17]. However, the arguments on the reduction mechanism of carbonic as well as carboxylic acids are still unsettled, although now it appears that the "direct reduction" mechanism is not significant [11,12,36,50,104].

Table B.1-3. Possible electrochemical reactions in CO_2 corrosion of mild steel.

Reaction number	Electrochemical reaction	Dominant reaction type
(B.1-6)	$H^+_{(aq)} + e^- \leftrightharpoons \frac{1}{2} H_{2\,(g)}$	Cathodic
(B.1-7)	$H_2O_{(l)} + e^- \leftrightharpoons OH^-_{(aq)} + \frac{1}{2} H_{2\,(g)}$	Cathodic
(B.1-8)	$H_2CO_{3(aq)} + e^- \leftrightharpoons HCO_3^-{}_{(aq)} + \frac{1}{2} H_{2\,(g)}$	Cathodic
(B.1-9)	$HCO_3^-{}_{(aq)} + e^- \leftrightharpoons CO_3^{2-}{}_{(aq)} + \frac{1}{2} H_{2\,(g)}$	Cathodic
(B.1-10)	$Fe^{2+}{}_{(aq)} + 2e^- \leftrightharpoons Fe_{(s)}$	Anodic

B.1.3.2.1: Cathodic reactions

The exact mechanism of the cathodic reactions in the presence of weak acids in general, and carbonic acid in particular, remains open to debate. The major controversy is related to the role of undissociated carbonic acid. This protracted controversy remains

unsolved due to the intrinsic complexity of the system, especially as the weak acids are at equilibrium with hydrogen ion at all times, making it hard to distinguish the two. In aqueous solutions, based on the definition of reversible potential, it can be shown that weak acids such as carbonic acid and bicarbonate ion, are thermodynamically identical [14]. Furthermore, the fast kinetics of coupled homogeneous chemical reactions (see Table B.1-2), makes it difficult to deploy the majority of standard electroanalytical techniques in order to resolve this issue. Therefore, the main method used to study this system was through the quantitative analysis of charge transfer rates.

In the last four decades, the mechanistic understanding of CO_2 corrosion and the development of more inclusive mathematical descriptions of this system has been undergoing concurrent evolution. De Waard and Milliams were amongst the first researchers attempting to elucidate the mechanism of CO_2 corrosion [19,105]. Based on a quantitative analysis, De Waard and Milliams proposed a mechanism for CO_2 corrosion where the dominant cathodic reaction is the "direct reduction" of the undissociated carbonic acid. This mechanism was further supported by Wieckowski et al. based on their studies with cyclic voltammetry [106].

In 1977, Schmitt and Rothmann [107] proposed a mechanism for the cathodic reaction in aqueous CO_2 environments based on their study of the limiting current response to flow velocity and partial pressure of CO_2. Schmitt and Rothmann reported that the limiting current consists of both flow dependent and flow independent components. It was shown that the flow dependent part limiting current was governed by transfer of hydrogen ion and undissociated carbonic acid, while the flow independent part

was suggested to be limited by the slow reaction rate of adsorbed CO_2 to give carbonic acid, in the so called hydration step. The relevance of the adsorption in hydration of CO_2 was later challenged by Wieckowski et al. in their radiotracer study of the iron/CO_2 system [108].

The mechanism of cathodic reactions in CO_2 environments was further discussed by Gray et al. [14,103] who introduced a mathematical model for CO_2 corrosion of mild steel. Using the proposed mechanism of Schmitt and Rothmann as the basis of their model while considering the radiotracer study of Wieckowski et al.(1983b), Gray et al. suggested that the adsorption step of CO_2 introduced by Schmitt and Rothmann (1977) was unnecessary to explain the limiting currents observed in CO_2 environments. This model is based on concurrent reduction of hydrogen ions and carbonic acid, while the effect of slow hydration of carbonic acid in the bulk solution was also included. This mechanism has become the most commonly accepted mechanism of CO_2 corrosion ever since.

In more recent studies, a few attempts have been made in order to quantitatively describe the increased corrosion rates in CO_2 systems solely through the buffering effect of carbonic acid on hydrogen ion concentration. Remita et al. [11] reported a quantitative analysis of cathodic currents in CO_2 saturated solutions. The authors claimed that they could predict the cathodic currents without considering direct reduction of carbonic acid. Their model is based on the reaction rate constant of the hydrogen ion reduction obtained from experimental data in deaerated acidic solutions and the homogeneous reactions related to CO_2 equilibria. Based on the good agreement between the predicted

voltammograms and the experimental data, the authors concluded that the direct carbonic acid reduction reaction is not necessary to quantitatively explain the higher cathodic current densities observed in CO_2 systems.

Considering the limited experimental scope of the Remita et al. study (only pH 4 and 1 bar CO_2), their conclusion about the insignificant contribution of carbonic acid reduction to the cathodic current may not be readily extrapolated to conditions where carbonic acid concentration is many orders of magnitude higher than the hydrogen ion concentration (see Figure B.1-1 at pH 6 as an example). Additionally, Remita et al. compared the surface pH measurements in unbuffered acidic solution with solutions buffered with carbonic acid. The lower surface pH values obtained in carbonic acid environments was considered as additional proof for the buffering effect mechanism. However, this decreasing trend of surface pH would be expected for both mechanisms. Therefore, surface pH measurements are unable to provide conclusive arguments on the mechanism of the cathodic reaction.

In a more experimentally extensive approach, Tran et al. [50] aimed to distinguish between the direct reduction and buffering effect mechanism by studying the sensitivity of the pure charge transfer controlled cathodic currents to the concentration of undissociated acid, a similar approach to that previously used for acetic acid [12,104]. This is depicted in Figure B.1-2 by comparison of the hypothetical voltammograms of these two reaction mechanisms. Figure B.1-2.A represents the direct reduction mechanism where the net cathodic current is the summation of the current from both hydrogen ion and the undissociated weak acid (H_2CO_3) reduction. Figure B.1-2.B shows the expected behavior

of the buffering effect mechanism where the cathodic currents are only defined by hydrogen ion reduction and the weak acid is only an additional source of hydrogen ions. Here both mechanisms show identical limiting current behavior with increasing concentration of the weak acid. For the case of carbonic acid, this behavior can be explained by considering that the limiting current is the superposition of mass transfer limiting current of hydrogen ions and chemical reaction limiting current of CO_2 hydration as the rate determining steps. Therefore, the associated faster electrochemical reactions, whether in the form of direct reduction of carbonic acid, or via the buffering effect mechanism, cannot be distinguished in the potential range governed by the limiting currents.

However, at charge transfer controlled current conditions (at higher potentials), a distinctive behavior is expected. In the direct reduction mechanism (Figure B.1-2.A), both hydrogen ions and carbonic acid are reactive, therefore, at a constant pH the net current increases by rising concentrations of the weak acid. At similar conditions, in the buffering effect mechanism, when the undissociated weak acid is not reduced (Figure B.1-2.B), the charge transfer controlled current remains unchanged. Therefore, these two mechanisms can be distinguished by studying the behavior of the charge transfer controlled currents at various weak acid concentrations (carbonic acid in this case).

A)

B)
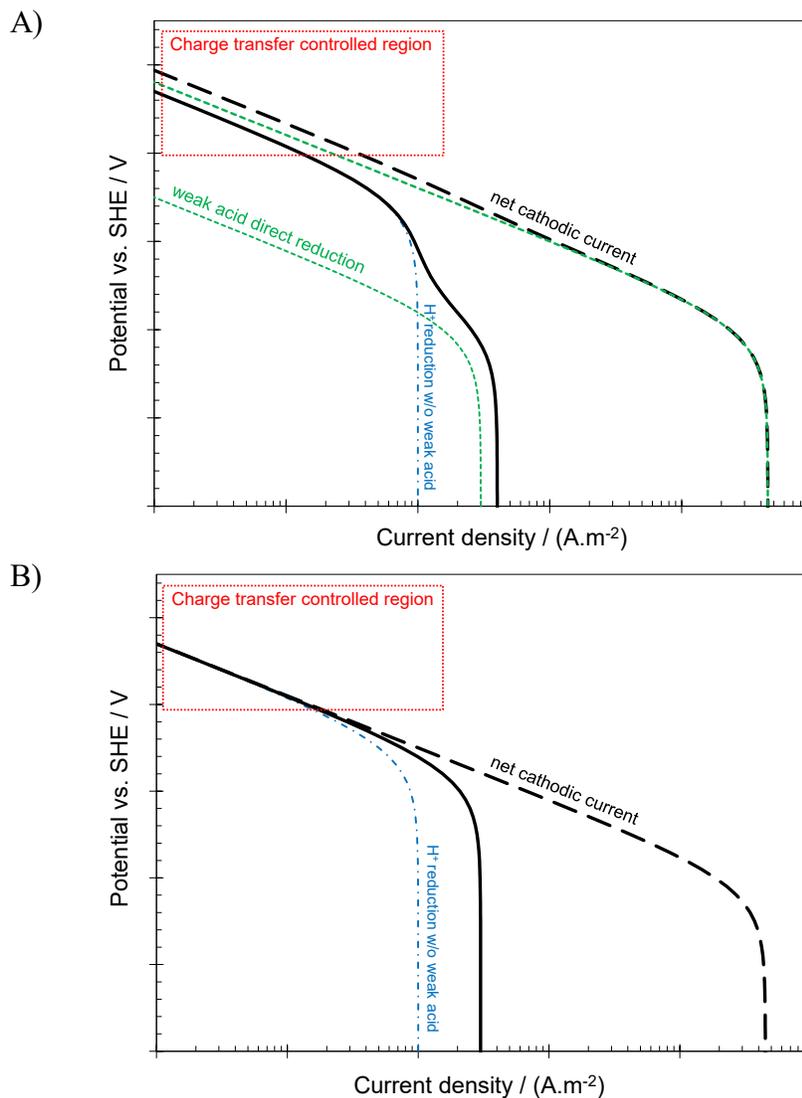
Figure B.1-2. An illustration of hypothetical polarization curves expected at a constant pH; cathodic lines for three concentrations of a weak acid (red > green > orange). Blue line represents the anodic reaction. A) direct reduction mechanism B) buffering effect mechanism.

The main difficulty in testing such a hypothesis in CO_2 environments is the lack of ability to observe the pure charge transfer cathodic current on mild steel at typical experimental conditions, due to the interference by the anodic iron dissolution reaction. Therefore, Tran et al. [50] suggested using stainless steel, being a more noble metal, where the interference by the anodic reaction is negligible for a wide range of cathodic

potentials. The polarization data reported in their work clearly show a Tafel behavior

(pure charge transfer controlled current), which appears not to respond to the change in

partial pressure of CO_2, up to 10 bar. This observation is in agreement with the behavior

expected in the buffering effect mechanism (see Figure B.1-2.B). However, the author's

suggestion that the same cathodic reaction mechanism detected on stainless steel is valid

for mild steel as well, needs to be further investigated, as the effect of alloying elements

(~ 20 wt. % Cr, and 10 wt. % Ni) and their corresponding oxide films on the

electroactivity of the metal surface could be significant. As discussed in the following

section, the sensitivity of the hydrogen evolution reactions to the state of the metal

surface is well known, which suggests that this assumption may not be acceptable

without proof.

Hydrogen evolution reaction

The hydrogen evolution reaction is one of the most widely studied

electrochemical reactions. Volmer, Heyrovsky, and Tafel steps (Reactions (B.1-11), (

B.1-12), and (B.1-13), respectively) are the most commonly accepted steps in the

hydrogen evolution mechanism [109,110], while alternative mechanisms such as the one

involving molecular hydrogen ion (H_2^+) is also proposed [111,112]. A wealth of information

is available in the literature on the mechanistic behavior and kinetic parameters for the

hydrogen evolution reaction, based on experimental results [113–116], as well as theoretical

analyses [117–124] (see Appendix I for example). A quick review of the literature readily

indicates the complex nature of this reaction, where a significant change in the kinetics

may occur with variation of the electrode material [115,125–127], surface preparation and

crystal structure [113,127], pH [114,128], overpotential [126,129], adsorbed species, and trace impurities [76,127,130,131]. This suggests that seeking universal kinetic mechanism and parameters for the hydrogen evolution reactions is neither reasonable nor possible.

$$H^+ + e^- \rightleftharpoons H_{ad} \qquad \text{Volmer acidic HER} \qquad \text{(B.1-11)}$$

$$H_{ad} + H^+ + e^- \rightleftharpoons H_2 \qquad \text{Heyrovsky acidic HER} \qquad \text{(B.1-12)}$$

$$H_{ad} + H_{ad} \rightleftharpoons H_2 \qquad \text{Tafel} \qquad \text{(B.1-13)}$$
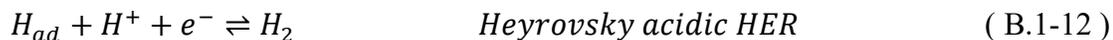
For the case of hydrogen ion reduction on iron, it is commonly considered that the reduction reaction occurs with the Volmer reaction being the rate determining step [11–13,16,17,74], generally based on the findings of Bockris et al. [75,76,115,132]. This mechanism has a theoretical value of 0.5 for the transfer coefficient (Tafel slope of b=118 mV at 25°C), and reaction order of $m = -1$ with respect to pH [118]. These parameters have been to some extent experimentally verified, with some deviations from expected theoretical values also reported in the literature (see Table B.1-4). As shown in Table B.1-4 most studies cover very acidic solutions while in less acidic solutions, *i.e.*, pH 3 and higher, the experimental verification of these parameters is limited by interference from the iron oxidation reaction.

For hydrogen evolution from water the similar elementary steps are suggested [133]. Assuming the Volmer step to be rate determining, Tafel slope of 118 mV and reaction order of zero vs. pH is expected. The reported data in the literature are generally in agreement with the expected reaction order of zero, while the reported Tafel slopes are significantly deviating from the theoretical value of 118 mV [14,54,103,116,134].

Table B.1-4. Kinetic parameters of hydrogen ion reduction on iron.

Reference	Electrolyte	b [mV]	m vs. pH
[54]	1 N [SO_4^{2-}], 0.5 N [Fe^{2+}], pH: 2.0 – 4.0	116 ± 7	-1
[115]	0.5 N HCl	133 ± 4	NA
[135]	1 N [Cl^-], [H^+]: 0.2 - 2.96	120 ± 10	-1
[134]	1 N [Cl^-], 0.1 < pH < 3	117	-1
[136]	1 N [Cl^-], 0.0 < pH < 1.8	115	-1
[137]	1 N [Cl^-], 0.07 < pH < 2.92	123-155	-0.5
	1 N [SO_4^{2-}], 0.30 < pH < 3.74	120-190	-0.5
[116]	4 wt. % NaCl, 1.42 < pH < 5.26	100	-0.5

The mechanism of hydrogen evolution from other weak acids can be described by an analogy with that of the hydrogen ion reduction described above (see appendix II for example). Using a general formulation the elementary steps of the hydrogen evolution reaction are shown below by Reaction (B.1-14) to (B.1-16), where HA denotes any weak acid such as water, carbonic acid, acetic acid, hydrogen sulfide, etc. [12,36,102,108,138]. The rate determining step in the weak acid reduction mechanisms is rarely discussed in the literature.[102]. However, the commonly used expressions for exchange current density [13,15,18,100] need to assume the Volmer step being rate determining, in order to be consistent with theory.

$$HA + e^- \rightleftharpoons H_{ad} + A^- \qquad\qquad Volmer \qquad\qquad (B.1\text{-}14)$$

$$H_{ad} + HA + e^- \rightleftharpoons H_2 + A^- \qquad\qquad Heyrovsky \qquad\qquad (B.1\text{-}15)$$

$$H_{ad} + H_{ad} \rightleftharpoons H_2 \qquad\qquad Tafel \qquad\qquad (B.1\text{-}16)$$
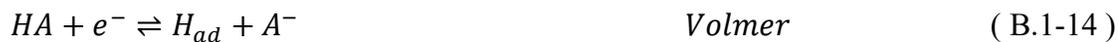
B.1.3.2.2: Anodic reaction

The most accepted mechanism for iron dissolution in CO_2-saturated acidic media, which is the main anodic reaction in mild steel corrosion, was proposed by Bockris et al. [71](BDD mechanism) as shown by Reaction (B.1-17) to (B.1-19). In the original study, the authors compared the theoretically calculated parameters from a series of possible mechanisms with their own experimentally obtained values. For their proposed mechanism, the measured Tafel slope of 40 mV agreed well with the theoretical value. The experimentally determined reaction order vs. pH of 0.9 ± 0.05 was close to the theoretical value of 1. The reaction order of ferrous ion concentration of 0.8, obtained experimentally, was also close to the theoretical value of 0.75. The authors also noted that the reaction order versus pH decreases from 1 to β/2 at pH values above 4, where β is the transfer coefficient of Reaction (B.1-17)[71]. However, in other studies a rather broad variation of these parameters has been measured (see Table B.1-5) indicating the possibility of alternative mechanisms [73].

$$Fe + OH^- \leftrightarrow Fe[OH]_{ads} + e^- \quad\quad\quad (\text{B.1-17})$$

$$Fe[OH]_{ads} \leftrightarrow Fe[OH]^+ + e^- \quad\quad\quad (\text{B.1-18})$$

$$Fe[OH]^+ \leftrightarrow Fe^{2+} + OH^- \quad\quad\quad (\text{B.1-19})$$

Table B.1-5 summarizes some of the reported kinetic parameters for iron dissolution in acidic solutions.

Table B.1-5. Kinetic parameters of iron dissolution in acidic media.

Reference	Electrolyte	b [mV]	m vs. pH	m vs. pFe
54	1 N [SO_4^{2-}], 0.5 N [Fe^{2+}] pH: 1.2 – 4.9	40	0.9±0.05	- 0.8
135	1 N [Cl^-], 0.2 < [H^+] < 2.96	65-70	0.7	NA
134	1 N [Cl^-], 0.1< pH < 3	29	1	-2
136	1 N [Cl^-], 0.0 < pH < 1.8	70	0.6	NA
137	1 N [Cl^-], 0.07 < pH < 2.92 1 N [SO_4^{2-}], 0.30 < pH < 3.74	70-44 32-25	0.83 - 1.52 1.52 - 1.43	NA

Nevertheless, the BDD mechanism has been directly used in the mathematical models of CO_2 corrosion for many years [18,19,103], while dissolved CO_2 and its associated carbonic species were shown to directly affect the anodic dissolution reaction [74,139,140]. Davis and Burstein [140] proposed an analogous reaction mechanism to the BDD mechanism by including the effect of bicarbonate ion on iron dissolution. They suggest that bicarbonate ion can act as an intermediate in the iron dissolution process in a similar way as hydroxide ion does in strong acid solutions. The direct involvement of bicarbonate ion on iron dissolution is also supported by other studies (*e.g.* Ogundele and White [101]).

In 1996, Nesic et al.[74] conducted a study of iron dissolution in CO_2 environments, illustrating the sensitivity of this reaction to pH and CO_2 partial pressure. Using

potentiodynamic sweeps and galvanostatic measurements, Nesic et al. suggested iron

dissolution in CO_2 systems has a generally different mechanism compared to the well-

known BDD mechanism. In a similar fashion as Davis and Burstein [140], Nesic et al.

assumed that the effect of carbonic species on iron dissolution is through formation of a

chemical ligand acting as a catalyst, involving CO_2 due to its high and constant

concentration at all pH values. Reaction (B.1-20) through (B.1-25) show the proposed

mechanism where CO_2 and its derivatives serve as intermediate species, in a similar role

as hydroxide ion has in the BDD mechanism. Here the rate determining step changes

from (B.1-24) at pH values below 4 to (B.1-22) at pH values of 5 and higher.

Quantitatively, the authors suggest that the effect of CO_2 is proportional to surface

coverage, so that when $pCO_2 < 0.1$ bar, the coverage is very small and the presence of

dissolved CO_2 has an insignificant effect on the anodic dissolution rate; the effect then

increases with increasing pCO_2 and at $pCO_2 > 1$ bar the metal surface coverage reaches

saturation, and the effect vanishes. The mathematical expression corresponding to this

mechanism is shown in Table B.1-6.

$$Fe + CO_2 \rightleftharpoons FeCO_{2\ ads} \tag{B.1-20}$$

$$FeCO_{2\ ads} + H_2O \rightleftharpoons FeHCO_{3\ ads} + H^+ + e^- \tag{B.1-21}$$

$$FeHCO_{3\ ads} \rightleftharpoons FeHCO_{3\ ads}^+ + e^- \tag{B.1-22}$$

$$FeHCO_{3\ ads}^+ + H_2O \rightleftharpoons FeOH_2CO_{3\ ads} + H^+ \tag{B.1-23}$$

$$FeOH_2CO_{3\ ads} \rightleftharpoons FeOH_2CO_{3\ sol} \tag{B.1-24}$$

$$FeOH_2CO_{3\ sol} + 2H^+ \rightleftharpoons Fe^{2+} + CO_2 + 2\ H_2O \tag{B.1-25}$$
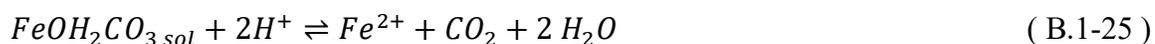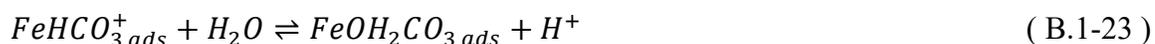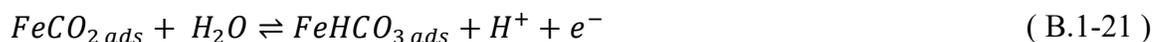
The abovementioned mechanisms proposed by Davis and Burstein [140] and also

Nesic et al. (1996b) are in conflict with the findings of Wiekowski et al.[108] where their

radiotracer study in CO_2 saturated solution showed no detectable adsorption of labeled

carbon on the metal surface. Additionally, in a more recent study by Almedia et al.[141] it

was shown that the electrochemical impedance spectra of iron in hydrochloric acid and

saturated CO_2 solution have identical characteristic loops, suggesting that the mechanism

of iron dissolution is similar in both cases and does not include any significant adsorption

of CO_2 and/or its derivatives.

B.1.3.2.3: Charge transfer rate calculations

For an elementary electrochemical reaction (Reaction (B.1-26)) the rate,

expressed in terms of current density, can be calculated using Equation (B.1-27) [53,142].

$$O + e^- \rightleftharpoons R \qquad\qquad (\text{B.1-26})$$

$$i = -i_0 \left[\frac{C_O^S}{C_O^b} e^{-\frac{\alpha F \eta}{RT}} - \frac{C_R^S}{C_R^b} e^{\frac{(1-\alpha)F\eta}{RT}} \right] \qquad\qquad (\text{B.1-27})$$

where overpotential (η) and exchange current density (i_o) are defined as follows:

$$\eta = E - E_{rev} \qquad\qquad (\text{B.1-28})$$

$$i_0 = nFK_0 C_O^{b^{1-\alpha}} C_R^{b^{\alpha}} \qquad\qquad (\text{B.1-29})$$

Considering a known exchange current density, i_0^{ref}, at reference conditions

$(C_{O,ref}^b, C_{R,ref}^b, T_{ref})$, one can use an Arrhenius type equation for the standard reaction

rate constant, $K_0 = k_0 e^{\frac{-E_a}{RT}}$, where the pre-exponential parameter (k_0) can be obtained

from Equation (B.1-29) as:

$$k_0 = \frac{i_0^{ref}}{nFC_{O,ref}^b{}^{1-\alpha} C_{R,ref}^b{}^{\alpha} e^{\frac{-E_a}{RT_{ref}}}}$$

(B.1-30)

Using Equations (B.1-29) and (B.1-30), as well as the Arrhenius' equation for standard reaction rate constants, the exchange current density at a different temperature and bulk concentration of species can be found via Equation (B.1-31).

$$i_0 = i_0^{ref} \left(\frac{C_O^b}{C_{O,ref}^b}\right)^{1-\alpha} \left(\frac{C_R^b}{C_{R,ref}^b}\right)^{\alpha} e^{\frac{-E_a}{R}\left(\frac{1}{T}-\frac{1}{T_{ref}}\right)}$$

(B.1-31)

At high values of overpotential and pure charge transfer control, (B.1-27) is simplified to the so called Tafel approximation. For example, for cathodic current it is:

$$i = -i_0 10^{\frac{-\eta}{b}}$$

(B.1-32)

where Tafel slope (b) is defined as:

$$b = -\frac{RT}{\alpha nF}$$

Assuming the rate determining (slow) step being the Volmer step for all hydrogen evolution reactions discussed previously, the exchange current densities in both Equations (B.1-27) and (B.1-32) could be calculated as shown in Table B.1-6.

Table B.1-6. Mathematical relationships describing the exchange current densities. [a]

Reaction	Exchange current density
(B.1-6)	$i_{0,H} = i_{0,H,ref} \left(\dfrac{C^b_{H^+}}{C^b_{H^+,ref}} \right)^{(1-\alpha_H)} e^{\frac{-E_a}{R}(\frac{1}{T} - \frac{1}{T_{ref}})}$
(B.1-7)	$i_{0,H_2O} = i_{0,W,ref} \left(\dfrac{C^b_{H^+}}{C^b_{H^+,ref}} \right)^{-a_W} e^{\frac{-E_a}{R}(\frac{1}{T} - \frac{1}{T_{ref}})}$
(B.1-8)	$i_{0,CA} = i_{0,CA,ref} \left(\dfrac{C^b_{H^+}}{C^b_{H^+,ref}} \right)^{-\alpha_{CA}} \left(\dfrac{C^b_{H_2CO_3}}{C^b_{H_2CO_3,ref}} \right)^{1} e^{\frac{-E_a}{R}(\frac{1}{T} - \frac{1}{T_{ref}})}$
(B.1-9)	$i_{0,BC} = i_{0,BC,ref} \left(\dfrac{C^b_{H^+}}{C^b_{H^+,ref}} \right)^{-(1+\alpha_{BC})} \left(\dfrac{C^b_{H_2CO_3}}{C^b_{H_2CO_3,ref}} \right)^{1} e^{\frac{-E_a}{R}(\frac{1}{T} - \frac{1}{T_{ref}})}$
	$i_{0,Fe} = i_{0,Fe,ref} \left(\dfrac{C^b_{H^+}}{10^{-4}} \right)^{a_1} \left(\dfrac{C^b_{CO_2}}{0.0366} \right)^{a_2} e^{\frac{-E_a}{R}(\frac{1}{T} - \frac{1}{298.15})}$
(B.1-10)[b]	$pH < 4:\ a_1 = -2\ , n\alpha_{a,Fe} = 2$ $pH > 5:\ a_1 = 0\ , n\alpha_{a,Fe} = 0.5$ $PCO_2 < 1:\ a_2 = 1$ $PCO_2 \geq 1:\ a_2 = 0$

[a] The values for activation energies, reference concentrations and exchange current densities of Reactions (B.1-6) to (B.1-8) are listed in the study of Nesic et al. [18] and for Reaction (B.1-9) in the study of Han et al. [100]. Note that the exchange current density expressions presented here are based on Equation (B.1-31) and are not necessarily similar to those shown in the references provided.
[b] The expression of exchange current density of iron dissolution reaction is the semi-empirical expression from Nesic et al. [74].

B.1.3.3: Mass transfer in corroding systems

Considering the heterogeneity of the corrosion process, mass transfer calculations are required to define the concentration of electroactive species at the reaction site, the metal surface. It has been shown that neglecting the mass transfer limitation in CO_2 corrosion rate calculation leads to significant overestimation of the corrosion rate [48,143].

In a general form, Equation (B.1-33) describes the current density of an electrochemical reaction based on the mass transfer of the reactant from the bulk solution, at steady state.

$$i = nFk_m(C^b - C^s)$$
(B.1-33)

where k_m is the mass transfer coefficient:

$$k_m = \frac{Sh\,D}{L}$$
(B.1-34)

and C^b and C^s are the concentrations of the reactant in the bulk solution and at the metal surface, respectively. The value of C^s in Equation (B.1-33) is generally unknown and defined by the kinetics of the charge transfer reaction. However, in pure mass transfer limiting conditions the surface concentration of the reactant approaches zero. Therefore, Equation (B.1-34) can be used to calculate the mass transfer limiting current density as described by Equation (B.1-35).

$$i_{lim} = nFk_mC^b$$
(B.1-35)

The mass transfer coefficient for a variety of flow conditions has been the subject of numerous studies. For example, the mass transfer limiting current for a rotating disc electrode can be derived theoretically due to laminar flow conditions, and is known as the Levich equation. For a rotating cylinder electrode, the turbulent flow correlation of Eisenberg et al. [144] is often used. The mass transfer correlation in fully developed turbulent flow through smooth, straight pipes was defined by Berger and Hau [145], where the Sherwood number (*Sh*) is correlated to the Reynolds number (*Re*) and the Schmidt number (*Sc*), as shown in Equation (B.1-36).

$$Sh = 0.0165 \, Re^{0.86} Sc^{0.33} \hspace{4cm} (\text{ B.1-36 })$$

$$8 \times 10^3 < Re < 2 \times 10^5 \, , 1000 < Sc < 6000$$

For various other flow regimes and geometries such as multiphase flow, U-bends, elbows, etc., similar correlations exist in the literature [146–150].

In the case of mixed mass transfer and charge transfer control of the cathodic reaction rate, the effect of mass transfer on net current i_{net} of an elementary electron transfer reaction can be theoretically derived, as shown by Equation (B.1-37), where the i_{ct} is the charge transfer controlled current and i_{lim} is the mass transfer limiting current defined by Equation (B.1-35).

$$\frac{1}{i_{net}} = \frac{1}{i_{ct}} + \frac{1}{i_{lim}} \hspace{4cm} (\text{B.1-37})$$

Equation (B.1-37) has been commonly used in elementary mechanistic models of CO_2 corrosion [14,18,103], as well as in semi-empirical models [48]. This approach only considers the mass transfer of one individual species based on molecular diffusion and convection, independently from other species in the solution. In a system with multiple electro-active species that are involved in chemical reactions with each other, Equations (B.1-35) to (B.1-37) fail to properly describe the mass transfer process. In that case, the mass transfer of the chemical species needs to be described by the so called Nernst-Planck equation. This is a mass conservation equation that accounts for the effect of molecular diffusion and convection as well as simultaneous interaction between different species via homogeneous chemical reactions and through forming of an electrical potential field (often referred to as electromigration, or simply migration). For an incompressible fluid and dilute solutions, the flux of species can be written as [68]:

$$N_i = -z_i u_i F C_i \nabla \phi - D_i \nabla C_i + v C_i \qquad\qquad (\text{B.1-38})$$

The Nernst-Planck equation describing mass conservation of species i in the presence of homogenous chemical reactions (R_i) is then:

$$\frac{\partial C_i}{\partial t} = -\nabla . N_i + R_i \qquad\qquad (\text{B.1-39})$$

Using the Nernst-Einstein estimation for mobility of ions for one-dimensional calculations, Equations (B.1-38) and (B.1-39) yield Equations (B.1-40) and (B.1-41), respectively, which are the building blocks of any comprehensive mechanistic model of multicomponent mass transport in reacting ionic solutions [68].

$$N_i = -D_i \frac{\partial C_i}{\partial x} - \frac{z_i D_i F C_i}{RT} \frac{\partial \phi}{\partial x} + v_x C_i \qquad\qquad (\text{B.1-40})$$

$$\frac{\partial C_i}{\partial t} = D_i \frac{\partial}{\partial x} \frac{\partial C_i}{\partial x} + \frac{\partial}{\partial x}\left(\frac{z_i D_i F C_i}{RT} \frac{\partial \phi}{\partial x}\right) - v_x \frac{\partial C_i}{\partial x} + R_i \qquad\qquad (\text{B.1-41})$$

Unlike in the simple version of the mass transfer model (Equations (B.1-35) to (B.1-37), using the Nernst-Planck equation requires knowledge of the velocity field inside the diffusion boundary layer. For the case of rotating disc electrodes, an analytical solution for the velocity profile in the form of a power series is available [68]. Neglecting the higher order terms of this power series, Equation (B.1-42) describes the velocity profile in the solution near the electrode where $a = 0.510$, and Equation (B.1-43) provides the diffusion layer thickness [68].

$$v_x = -a\Omega \left(\frac{\Omega}{v}\right)^{1/2} x^2 \qquad\qquad (\text{B.1-42})$$

$$\delta = \left(\frac{3D_{lim}}{av}\right)^{1/3} \left(\frac{\Omega}{v}\right)^{-1/2}$$
(B.1-43)

However, for practical applications such as flow in transmission gas pipelines, conditions are very different from the laminar flow case described above, primarily due to turbulent mixing. In turbulent flow, one has to rely on empirical expressions describing the level of mixing in the mass transfer boundary layer, usually through an eddy diffusivity profile [151,152].

B.1.4: The mathematical models of CO_2 corrosion

Mathematical models of CO_2 corrosion can be categorized into three main groups, based upon the extent to which they rely on theoretical foundations described above:

Empirical/semi-empirical models are based on fitting of preselected mathematical functions to experimentally obtained corrosion rate data. In purely empirical models these functions have no real meaning and are arbitrarily chosen, while with semi-empirical models these functions are at least partially rooted in the theoretical foundations of the corrosion phenomena. These types of models are strictly limited to the experimental conditions used in their calibration, with little or no extrapolation capability.

Elementary mechanistic models are also based on mathematical functions, but in this case they are rooted in physicochemical theory of the corrosion process. However, in order to maintain simplicity, these models resort to simplification and decoupling of the various processes, *e.g.*, mass transfer, chemical reactions and charge transfer phenomena. These models can be used to extrapolate predictions outside the range of experimental data used in their development, as long as the governing physicochemical processes are valid.

Comprehensive mechanistic models are deeply rooted in fundamental physicochemical laws, such as the ones described above. The underlying charge transfer, chemical, and mass transfer processes are described comprehensively and are coupled with each other. While these models are computationally and mathematically more demanding, they enable more accurate predictions, they are easier to extend by adding new physics and their extrapolation capability is superior.

B.1.4.1: Empirical/semi-empirical models

Generally, empirical/semi-empirical models are simple predictive tools developed when limited fundamental understanding is available. In some cases, the basic mathematical functions used in these models may originate from rudimentary approximations of the fundamental physicochemical processes underlying the corrosion phenomena, however, the more elaborate aspects are accounted for by introducing correction factors in the model [85,86]. In most cases, these factors are best-fit functions based on limited experimental data with no theoretical significance. This lack of theoretical meaning makes any combination of these empirical correction factors (required to cover more complex conditions) dubious, to say the least. More importantly, due to this general lack of theoretical underpinning, these models cannot be reliably extrapolated outside the conditioins used for their development. For the same reason, these models have very limited flexibility needed for further extensions to account for new data and require recalibration of the model with the entire dataset to accommodate any such extension. To date, many variations of empirical/semi-empirical models are found that address a particular application [48,80–82,105,153–155].

In an attempt to focus this review on the more recent mechanistic developments in CO_2 corrosion modeling, the discussion of empirical/semi-empirical models is limited to a brief review of the work by de Waard et al.[19,48,81,105,153,156] due to its significance in shaping the understanding of CO_2 corrosion as we know it today. However, numerous reviews on empirical and semi-empirical models are available in the literature for further reference [47,85–89,143].

de Waard and Milliams[19] based their original model on a linear pH dependence of the corrosion current obtained from equating a simple charge transfer rate expression of anodic and cathodic currents at the corrosion potential, shown as Equation (B.1-44).

$$\log i_{corr} = -A\,pH + B \qquad \text{(B.1-44)}$$

By correlating this equation with their experimental data, the constant A was obtained (A=1.3). de Waard and Milliams[19] then attempted to develop a mechanistic explanation of CO_2 corrosion by comparing the empirical value for A with the ones obtained based on a few different hypothetical mechanisms. Finally, the following "catalytic" mechanism for the cathodic reaction was proposed.

$$H_2CO_{3(aq)} + e^- \rightarrow HCO_{3\,(aq)}^- + \frac{1}{2}\,H_{2\,(g)} \qquad \text{(B.1-45)}$$

$$HCO_{3\,(aq)}^- + H_{(aq)}^+ \leftrightharpoons H_2CO_{3(aq)} \qquad \text{(B.1-46)}$$

This enabled them to derive a simple expression for the corrosion rate as a function of temperature and partial pressure of CO_2, which remained the most popular way to predict corrosion rates for decades, and is still in use today. However simplistic and questionable the approach, this was a first attempt at modeling of CO_2 corrosion in a mechanistic way using theoretical considerations. The important effects of pH, flow, and

slow CO_2 hydration on the cathodic reaction were not considered in this first attempt and were added later.

A number of new effects such as pH, flow rate, non-ideal solutions, protective scales, glycol, top of line corrosion and steel microstructure are amongst those covered in the subsequent publications of de Waard et al. [19,48,81,105,153]. These new effects were accounted for by simply introducing additional empirical correction factors as multiplicators in the original de Waard and Milliams[19] correlation. This transformed their original mechanistic approach into a semi-empirical model with all the disadvantages discussed above.

B.1.4.2: Elementary mechanistic models

Elementary mechanistic models were developed in an attempt to address the shortcomings of empirical and semi-empirical corrosion rate prediction models and to bring the well-established general understanding of electrochemistry, chemistry and mass transfer into modeling. These models also formed the necessary platform required to further improve the mechanistic modeling of CO_2 corrosion. The elementary mechanistic models are based on a decoupled description of the main physicochemical phenomena involved in the corrosion processes, *i.e.*, mass transfer, charge transfer, and chemical reactions. These models derive their strength by relying on more descriptive electroanalytical data in their development (particularly steady state voltammograms), rather than the corrosion rate data alone. With this approach, the physicochemical parameters involved in various processes could be systematically studied. Unlike the correction factors used in empirical/semi-empirical models, the parameters used in

elementary mechanistic models have a true theoretical meaning. Hence, the different elements of the model can be confidently combined in order to develop a model for more complex conditions.

The quantitative analysis of experimental results based on elementary mechanistic models provided the opportunity for deeper understanding of the underlying mechanisms. Additionally, such models for corrosion rate prediction offered flexibility for expansion to include more corrosive species, additional reactions and new physics, as well as allowing for more reliable extrapolation beyond the experimental conditions used in their development.

Gray et al. introduced one of the first and most comprehensive quantitative analyses of aqueous CO_2 corrosion of mild steel to that date, by implementing an elementary mechanistic model for charge transfer rate calculations [14,103]. Two consecutive studies were published by the authors in 1989 and 1990. The first article [14] focused on pH 4 in CO_2 saturated aqueous solution and the model is based on the direct carbonic acid reduction mechanism of de Waard and Milliams[19] as discussed above. The model developed by Gray et al. uses (B.1-32) for charge transfer calculations, and (B.1-37) to account for the mass transfer limitation. The effect of the slow preceding CO_2 hydration reaction on direct carbonic acid reduction is included with an analogy to (B.1-37) where the mass transfer limiting current is replaced with chemical reaction limiting current on rotating disk electrodes [53].

In their second publication [103], the test conditions were expanded toward more alkaline environments and higher temperatures. In that work, it was suggested that at pH

values between 6 to 10 the bicarbonate ion reacts at the metal surface, similar to the case

of carbonic acid at lower pH values. In order to extend their mathematical model to

higher temperature and pH values, including the bicarbonate reduction reaction, a similar

approach as in their previous study [14] was used. However, the effects of additional

physicochemical processes involved in these new conditions, such as formation of

protective corrosion product layers (see chapter B.1.5.2:) were not considered in their

second study.

Dayalan et al.[157] took a slightly different approach in their calculation sequence

compared to Gray et al.[14,103] by implicitly equating the mass transfer and charge transfer

rates (Equation (B.1-32)) at the metal surface in order to estimate the surface

concentration of species. However, the model proposed in that study [157] does not include

any temperature or CO_2 hydration reaction effects, and additionally suffers from

miscalculations in charge transfer rates. Despite these drawbacks, their approach was

unique in the sense that it provides the first insight into the water chemistry at the

corroding metal surface which is of significance for protective iron carbonate deposit

formation calculations [158].

Another elementary mechanistic model of CO_2 corrosion was developed in a

study published by Nesic et al. [18]. In that work the authors developed a predictive

mechanistic model based on the same elements introduced previously by Gray et al. [14,103],

while having a more practical implementation of the model for corrosion rate prediction

in practical systems. Charge transfer rates are calculated based on Equation (B.1-32),

mass transfer effect is based on Equations (B.1-35) to (B.1-37), and the CO_2 hydration

reaction was accounted for similarly to that described by Gray et al. [14,103]. Mass transfer correlations for different flow geometries were used, covering turbulent rotating cylinder flow and straight pipe flow [159]. For comparison of the results based on their model with linear sweep voltammograms, weight loss experiments was done to adjust the physicochemical parameters in the model. Additionally, a comparison of the performance of their model with the empirical/semi-empirical models of de Waard and Lotz [153] as well as Dugstad et al. [82] was provided by the authors.

Overall, the elementary mechanistic models gained general acceptance ever since, and have been widely used as the basis of mechanistic studies by many in the corrosion engineering field [100,160–163]. However, the simple approach to implementation of physicochemical theory in the elementary mechanistic models discussed here suffers from one fundamentally flawed assumption. In these models, it is assumed that species are transferred from the bulk fluid toward the metal surface and back independently from each other. In other words, the well-defined homogeneous chemical reactions as well as the ionic interaction (electromigration) between species inside the diffusion layer are ignored. While it can be argued that the latter effect can be insignificant in high conductivity solutions (aqueous brines), neglecting the chemical reactions disregards a significant process in these models. As an example, the *limiting current* in aqueous CO_2 environments was found to consist of two essential components: hydrogen ion mass transfer limiting current and CO_2 hydration reaction limiting current, which are considered to be additive in these models. While this results in a reasonable prediction of the corrosion rate as well as plausible voltamograms, it leads to inconsistent and in some

cases flawed prediction of surface water chemistry. Furthermore, this approach does not allow to account for the homogeneous carbonic acid dissociation reaction and its buffering effect, which is now known as a major process in CO_2-corrosion. This is a crucial problem when trying to model important surface phenomena, such as adsorption of species and protective corrosion product formation or when trying to make more elaborate arguments about electrochemical corrosion mechanisms.

B.1.4.3: Comprehensive mechanistic models

Comprehensive mechanistic models were developed to be more true to the fundamental physicochemical laws that describe major processes involved in a corroding system in order to address some of the shortcomings of the elementary mechanistic models mentioned above. Additionally, these models bring significant advantages such as unique insights into possible reaction pathways and accurate estimation of species concentration at the metal surface.

The word "comprehensive" refers to mathematical models based on the solution of mass conservation equation in the diffusion layer (the Nernst-Planck equation). This approach was introduced into CO_2 corrosion studies in the 1990s, while such calculations have been well established in the electrochemical engineering field in prior decades [164]. Despite the modeling approach not being novel by itself, the case of CO_2 corrosion can be considered as a rather complex application of such calculations.

The first mathematical model with this general approach was developed by Turgoose et al. [44]. In that study the authors developed a mathematical model based on the solution of the mass transfer equations and, separately, the homogeneous reaction

equilibria of carbonate species in the diffusion layer. The potential of this type of modeling to provide detailed information about concentrations of species in the diffusion layer was demonstrated. It was shown that the various corrosion mechanisms proposed previously [14,19,103,105–108] are only limited interpretations of all the possible reaction pathways in aqueous CO_2 corrosion. However, the authors ignored the charge transfer kinetics of electroactive species and the model was only used to calculate the current response at mass transfer limiting condition.

A further improvement in comprehensive mechanistic modeling was introduced by Pots [45]. The model developed by Pots is based on Equation (B.1-41) where the convective mass transfer was calculated through empirical correlation for eddy diffusivity [152]. In that work, charge transfer rates are assumed to follow the Tafel equation (Equation (B.1-32)) while the details of the parameters used in the Tafel equation was not discussed. Pots also notes the significance of homogeneous reactions on the current response, suggesting that eliminating the direct reduction reaction of carbonic acid does not significantly alter the corrosion rates estimated by the model due to the parallel dissociation reaction.

In more extensive studies, Nesic et al. and Nordsveen et al.[15,46] developed their model by implementing the Nernst-Planck equation to describe the mass transfer of species in the solution. The scope of the model was expanded beyond what was discussed in earlier works [44,45] by emphasis on the charge transfer rates calculations.

In charge transfer rate calculations used in comprehensive mechanistic models, Equation (B.1-37) is no longer applicable and the mass transfer limitation effect is

accounted for directly by calculating the surface concentration of species used in charge transfer rate expressions. In order to accommodate this, the authors described the charge transfer kinetics through the Tafel equation (Equation (B.1-32)) while the bulk concentrations in exchange current densities (Equation (B.1-31) and Table B.1-6) were replaced with surface concentrations. However, for this group of models, the proper charge transfer rate calculation should be based on Equation (B.1-27), where the surface concentrations are included in the ratio before the exponential term and the exchange current density is separately corrected for the variation in bulk concentration of active species (Table B.1-6). For example, for the case of hydrogen ion reduction, the equation used by Nesic et al.[46] and Nordsveen et al.[15] shows a factor of $([H^+]_s/[H^+]_b)^{0.5}$ difference from what is given here by Equation (B.1-27) and in Table B.1-6. Figure B.1-3 shows the ratio of hydrogen ion reduction current calculated by Nordsveen et al. [15], and the one introduced here, versus the ratio $[H^+]_s/[H^+]_b$. Here, the $[H^+]_s/[H^+]_b$ ratio of unity corresponds to pure charge transfer controlled conditions where both relationships predict the same current. However, $[H^+]_s/[H^+]_b$ deviates from unity as the mass transfer limiting conditions become significant. Consequently, the charge transfer rates calculated by the two relationships notably deviate. On the other hand, at pure mass transfer limiting conditions, where the kinetics of charge transfer is insignificant in the observed current densities, a similar limiting current would be obtained but corresponding to different surface concentrations. The deviation showed in Figure B.1-3 is therefore only significant in the mixed control region. The charge transfer rate calculation expressions similar to

those by Nordsveen et al.[15] were also used later in several subsequent studies [11,16,17,165–167].

In a more recent study, Remita et al.[11] revisited the mechanism of CO_2 corrosion, using a similar approach to quantify their experimental data. The model used in that work is the simplified steady state form of the model proposed by Nordsveen et al.[15], *i.e*, the left hand side of Equation (B.1-41) was taken to be zero. Using a steady state form of the models discussed above may be sufficient for practical purposes of corrosion rate estimation and also to compare with steady state voltammograms. This approach benefits from the comprehensive treatment of the homogeneous chemical reactions in the diffusion boundary layer and is computationally more affordable.
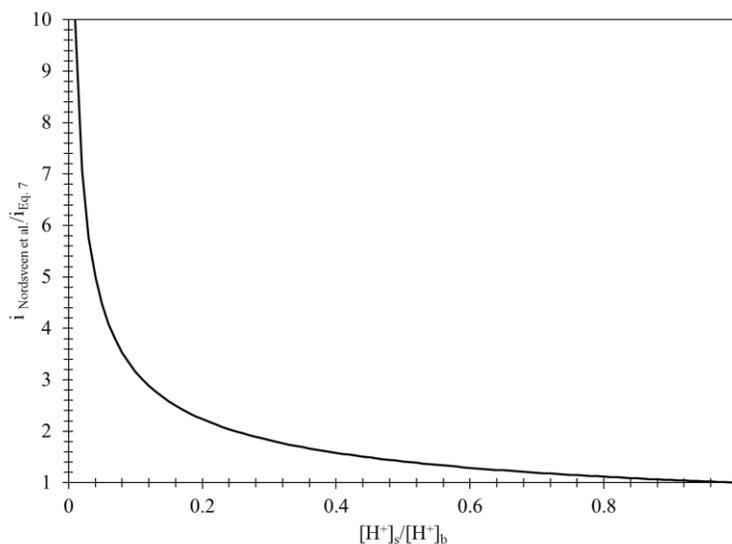
Figure B.1-3. Comparison of the current calculated from the charge transfer expression used by Nordsveen et al. [15] for hydrogen ions reduction and the relationships provided as Equation (B.1-27) and Table B.1-6 at 298 K and pH 4. The vertical axis represents normalized surface concentration of hydrogen ions.

The comprehensive mechanistic models discussed here have demonstrated their strength by depicting a more detailed and accurate picture of the processes involved in corrosion of steel in CO_2 environments. Such models are better suited to serve as a basis for further studies and a more appropriate platform for description of more complex systems and inclusion of new processes (some examples described in the section below). On the other hand, they are significantly more complicated to construct and use. Therefore, the much simpler elementary mechanistic models are still more popular with corrosion engineers, and even within the academic community, despite the known shortcomings.

B.1.5: Extension beyond basic calculations

One of the main qualities of any given corrosion modeling approach is its ability to be extended to cover more complex conditions and to have additional species and processes incorporated into the base model. The flexibility of models to include *additional corrosive species* is discussed below using the examples of acetic acid and hydrogen sulfide. The ability of the models to incorporate additional physicochemical phenomena is discussed below by using the example of *protective corrosion product film formation*. Finally, *top of the line corrosion* (TLC) encountered in wet gas pipelines is used to illustrate the flexibility of the models to be adapted for an application with very different geometry, environment, and physicochemical conditions.

B.1.5.1: Additional corrosive species

The ability of a corrosion rate predictive model to incorporate new species is of great interest for practical applications where the water chemistry is more complex

compared to laboratory experiments. Hydrogen sulfide and carboxylic acids are two main additional corrosive species commonly found in the aqueous solution alongside carbonic acid. The water chemistry associated with these weak acids can be accounted for in a similar way to what was discussed earlier for CO_2.

Reports on the significant effect of acetic acid in pipeline corrosion in the oil and gas industry are found as early as in the 1940s, where it was shown that even at concentrations as low as 300 ppm acetic acid can cause severe corrosion of pipeline steel [21]. Similar to carbonic acid corrosion, the mechanism of acetic acid corrosion has been intensely debated over the last two decades. While many studies suggest that the increased corrosion rates in the presence of acetic acid are due to its direct reduction at the metal surface [32,35,37–41], others suggest that acetic acid corrosion follows the buffering effect mechanism [12,33,36,104,155,168].

Corrosion of mild steel by aqueous hydrogen sulfide has also been extensively investigated in the last few decades. There seems to be a consensus in the literature that hydrogen sulfide follows the direct reduction mechanism based on clear observation of a distinct additional wave in cathodic sweeps [13,16,17].

In order to include the effect of additional corrosive species in empirical/semi-empirical models, extensive experimental and computational work is required, with no clear prospects of success. In order to maintain the same level of performance, the data pool on which the model was previously built needs to be extended to cover the effect of new species on the corrosion rates over the whole range of physical conditions; such as temperature, flow conditions, CO_2 partial pressures, etc. This is usually a very difficult if

not an impossible task. Additionally, the model itself and the correction factors have to be redefined to accommodate for such an expansion, without any proper theoretical guidance.

On the other hand, the elementary mechanistic models as well as the comprehensive mechanistic models easily cope with such expansions. New species are included by introducing additional charge transfer, chemical and mass transfer equations into the core model, describing the new species and processes, as appropriate. The corresponding physicochemical parameters are obtainable with a relatively small number of additional targeted experiments. In elementary mechanistic models, for each additional electroactive species, one extra equation (Equation (B.1-37)) is added to the model and solved simultaneously with the existing equations. An example of such an extension for an elementary mechanistic model is provided in Figure B.1-4 by introducing the acetic acid effect into the existing CO_2 corrosion model.

A)

B)
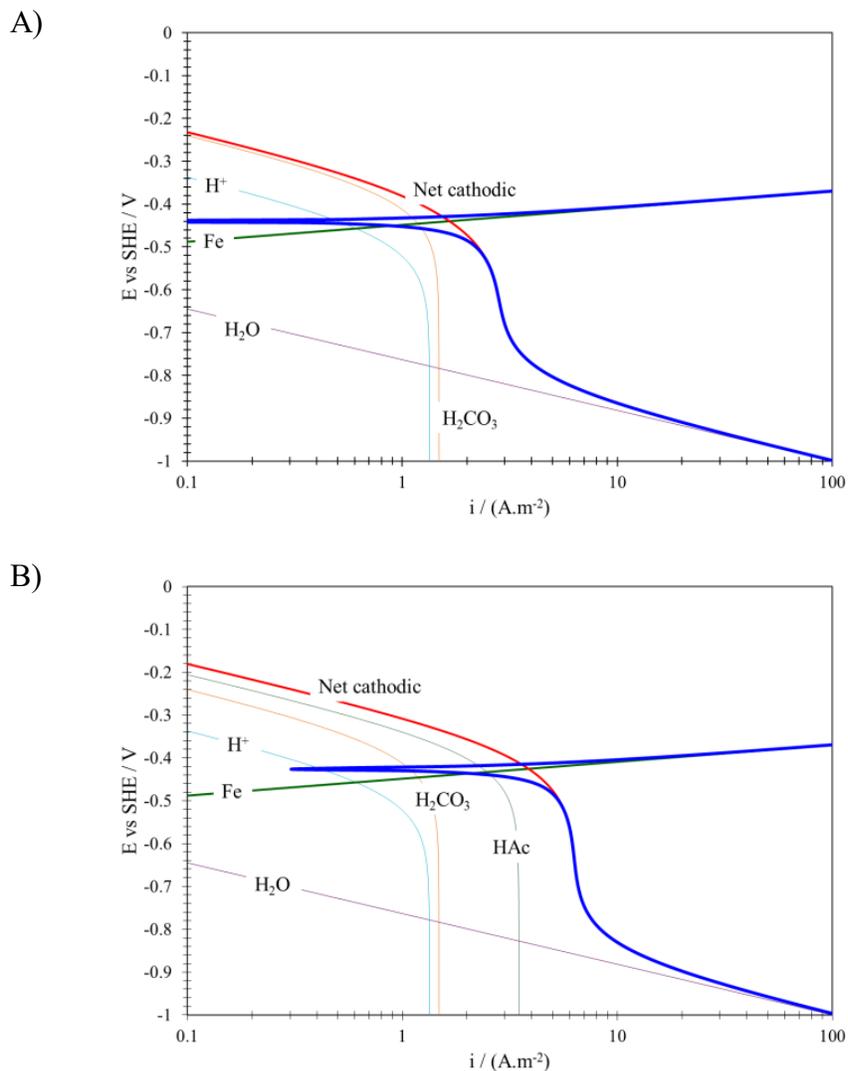
Figure B.1-4.Predicted voltammograms (solid blue line) by FREECORP [169] at pH4, 25˚ C, 1 bar CO_2, and 1 m/s flow velocity. A) 0 ppm acetic acid and B) 100 ppm acetic acid (HAc).

In the comprehensive mechanistic models, each new species is included by adding its corresponding Nernst-Planck equation (Equation (B.1-41)) into the model. If those species are involved in chemical reactions with any of the other species, this is defined via the chemical reaction term in the Nernst-Planck equation. Similar to elementary mechanistic models, additional physicochemical constants in comprehensive mechanistic

models can also be defined by a limited number of experiments. As an example, Figure B.1-5 shows the normalized concentration profiles of the active species within the diffusion layer at the corrosion potential, demonstrating the effect of acetic acid, as the additional corrosive species, when added to a comprehensive mechanistic CO_2 model.

A)

B)
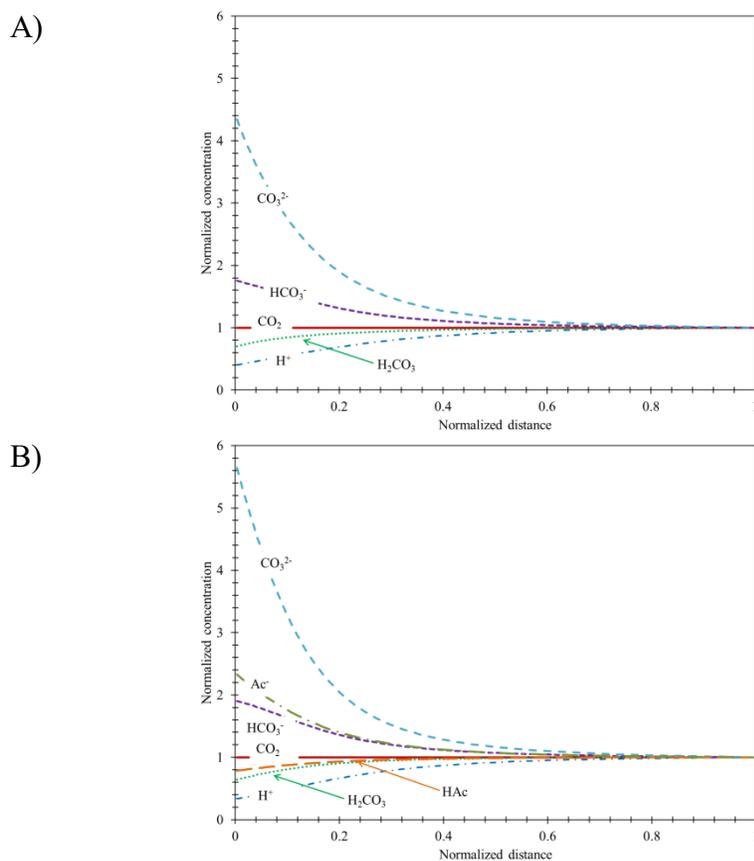
Figure B.1-5.Predicted concentration profile by MULTICORP™ at pH4, 25° C, 1 bar CO_2, and 1 m/s flow velocity. A) 0 ppm acetic acid and B) 100 ppm acetic acid (HAc).

B.1.5.2: Effect of corrosion product layer

The corrosion process is often accompanied by corrosion product layer formation at the metal surface. The protectiveness, chemical composition, as well as mechanical and physical properties of this precipitated layer are greatly affected by water chemistry,

environmental conditions such as temperature and fluid flow, steel composition and microstructure, etc. [25,34,56,140,170–174]. This may lead to complex, multi-layer corrosion product precipitates [175–179]. By limiting the discussion to CO_2 corrosion of carbon steel at conditions typical for transmission lines, one only encounters a porous iron carbonate corrosion product layer. This scenario has been incorporated in the mechanistic models [15,158,161,162,180,181].

The precipitation/dissolution of iron carbonate is described through the following heterogeneous chemical equilibrium:

$$Fe_{(aq)}^{2+} + CO_{3,(aq)}^{2-} \rightleftharpoons FeCO_{3(s)} \qquad\qquad\text{(B.1-47)}$$

If the product of the concentration of species on the left hand side exceeds the saturation limit, the formation of iron carbonate by precipitation is favored. The formation of a porous corrosion product layer on the metal surface affects the corrosion process through two main mechanisms:

- The porous iron carbonate layer acts as a barrier against transport of chemical species toward and away from the metal surface.

- The porous iron carbonate corrosion product layer blocks portions of the metal surface, making them unavailable as reaction sites.

Formation of a protective iron carbonate layer in CO_2 corrosion of steel is best discussed in the context of two general thermodynamic and kinetic criteria [170].

A thermodynamic indicator for the precipitation process is described by the extent of departure from equilibrium (Reaction (B.1-47)), termed here: the saturation value (S_{FeCO3}):

$$S_{FeCO_3} = \frac{C_{Fe^{2+}} C_{CO_3^{2-}}}{K_{sp}}$$

(B.1-48)

where K_{sp} is the iron carbonate dissolution equilibrium constant [171] for Reaction (B.1-47). A high saturation value is not the only factor leading to protective layer formation, because properties of an iron carbonate layer such as density, porosity, and adherence to the metal surface are greatly affected by kinetics of iron carbonate precipitation [170,173]. Additionally, the protectiveness of the corrosion product layer can be influenced by various chemical and mechanical removal processes [172,182,183]. However, the formation of the iron carbonate layer does not completely stop the corrosion process, this causes the existing corrosion product layer to detach from the metal surface [170,184]. This process, known as "film undermining" [180], affects the adherence, density and porosity of the corrosion product layer and ultimately its protectiveness. The role of undermining was quantified by van Hunnik et al.[170] through the introduction of a kinematic parameter called "scaling tendency", as described by equation (B.1-49). Scaling tendency can also be seen as a practical measure to assess the protectiveness and the ability to repair a damaged iron carbonate layer [34,170,185].

$$ST = \frac{R_{FeCO_{3(s)}}}{CR}$$

(B.1-49)

A scaling tendency of ST<<1 represents the case where the undermining is much faster than the formation of the corrosion product layer, therefore, a porous, often thick and non-protective layer forms, even at high saturation values. On the other hand a scaling tendency of ST>>1 suggests that the undermining is overpowered by the rapidly forming iron carbonate precipitate, creating a dense protective layer [180,185].

As for any crystalline deposits, the formation of iron carbonate should be discussed in the context of crystal nucleation and crystal growth [186]. Johnson and Tomson[187] studied the rate of iron carbonate formation using the iron count method to evaluate the iron carbonate growth rate on seed particles dispersed in the bulk solution. Based on their experimental approach of using seed particles at low saturation values (< 2), the authors by-passed the nucleation step and proposed a precipitation rate purely based on the crystal growth kinetics. Van Hunnik et al.[170] argued that the saturation values considered in Johnson and Tomson[187] precipitation rate expression do not cover an adequate range for CO_2 corrosion applications and may result in significant over estimation of precipitation rates. Van Hunnik et al. therefore used experimental data with saturation values as high as 1000, while the same indirect measurements method as Johnson and Tomson[187] was utilized to calculate the precipitation rates. In this study, authors investigated the precipitation of iron carbonate on a corroding metal surface rather than iron carbonate seeds, thus both nucleation and crystal growth steps were involved. However, the authors suggested that the crystal growth is the dominant process controlling the net precipitation rate. The ability of the expression they proposed to predict the precipitation rate, regardless of the steel microstructure, was considered as the proof of such an argument. This subject was also revisited by Sun and Nesic [185], where the previous expressions [170,174] were shown to overpredict the precipitation rate. The authors implemented a direct measurement of $FeCO_3$ precipitation rates through mass gain on steel samples. Similar to van Hunnik et al. [170], this experimental approach included both nucleation and growth mechanisms. However, the authors suggest that in

the case of iron carbonate formation on a heterogeneous mild steel substrate, the net

precipitation rate is governed by crystal growth mechanism as the rate determining step.

Despite the arguments provided by various authors [170,174,188], concerns related to changes

in saturation level over the duration of the experiments, effect of mass transfer, the

mechanism of the precipitation/dissolution reaction, and disregarding the kinetics of the

nucleation step, demand further investigations.

The precipitation rate of iron carbonate in Equation (B.1-49) can be described by

an expression in general form of (B.1-50)[186].

$$R_{FeCO_{3(s)}} = \frac{A}{V} f(T)g(S_{FeCO_3})$$

(B.1-50)

where

$$f(T) = e^{(A-\frac{B}{RT})}$$

(B.1-51)

represents the rate constant as a function of temperature based on Arrhenius' equation

where constants A and B are determined empirically. The precipitation rate dependence

on saturation value is accounted for by the $g(S_{FeCO3})$ function that is defined by the

mechanism of the precipitation/dissolution reaction. For an elementary reaction this

function can be theoretically expressed as Equation (B.1-52) [186].

$$g(S_{FeCO_3}) = K_{sp}(S_{FeCO_3} - 1)$$

(B.1-52)

This equation is similar to what was proposed by Sun and Nesic[185] indicating that

the precipitation reaction follows a first order reaction kinetics. The more elaborate forms

of the function $g(S_{FeCO3})$, such as the ones introduced by van Hunnik et al. [170] and

Johnson and Tomson[187], may suggest a more complex mechanism for this reaction (Table

B.1-7). The lack of mechanistic discussions categorizes these two precipitation rate

equations as semi-empirical expressions with all of their intrinsic limits. A summary of the expressions for precipitation rate proposed by the abovementioned references is provided in Table B.1-7.

Table B.1-7.Summary of the precipitation rate expressions.

Reference	$f(T)$	$g(S_{FeCO_3})$	K_{sp}
Johnson and Tomson [187]	$e^{(54.8 - \frac{-123000}{RT})}$	$K_{sp}(S_{FeCO_3}^{0.5} - 1)^2$	$e^{(-36.22 - \frac{-30140}{RT})}$
van Hunnik et al. [170]	$e^{(52.4 - \frac{-119800}{RT})}$	$K_{sp}(S_{FeCO_3} - 1)(1 - S_{FeCO_3}^{-1})$	Not specified
Sun and Nesic [185]	$e^{(21.3 - \frac{-64851.4}{RT})}$	$K_{sp}(S_{FeCO_3} - 1)$	[171]

In the case of elementary mechanistic models, the effect of a protective iron carbonate layer was accounted for by introducing an additional mass transfer resistance layer [158,161,162], without accounting for the surface blocking effect. A composite mass transfer resistance at a quasi-steady state condition as well as with interfacial concentrations of species can be obtained in order to calculate the corrosion rate. However, considering the aforementioned issue of the elementary mechanistic models which disregard the chemical reactions in the diffusion layer, the accuracy of this approach is questionable. Additionally, while being simple to implement, this approach further suffers from the fact that the thickness and porosity of a protective iron carbonate layer must be specified in advance of any corrosion rate calculation. As this is usually not known, an additional empirical correlation is needed, relating the properties (protectiveness) of a protective iron carbonated layer to environmental conditions.

The comprehensive mechanistic models can also be readily adapted to account for the effect of a precipitated corrosion product layer. In this case, the Nernst Planck equation is rewritten as [15,46]:

$$\frac{\partial(\varepsilon C_i)}{\partial t} = -\nabla.(\varepsilon^{3/2}N_i) + \varepsilon R_i \qquad \text{(B.1-53)}$$

in order to account for mass transfer through a porous media, with a porosity ε. In the portion of the boundary layer away from the steel surface where there is no iron carbonate layer the porosity ε is equal to one. Furthermore, all electrochemical rate expressions (current densities) are modified by multiplying with surface porosity ε, in order to account for the surface blocking effect. While these models benefit from accurate surface concentration calculations, the distribution of porosity in the precipitating iron carbonate layer still needs to be defined properly. In a simplistic approach it could be described by an empirical function in the same way as it is done for the elementary models [46].

In a more comprehensive approach, Nesic et al. presented a model for calculation of porosity distribution in the iron carbonate layer [189,190]. The authors proposed that the porosity can be calculated by writing a mass balance for the solid iron carbonate precipitate as:

$$\frac{\partial\varepsilon}{\partial t} = -\frac{M_{FeCO_3}}{\rho_{FeCO_3}}R_{FeCO_3} - CR\frac{\partial\varepsilon}{\partial x} \qquad \text{(B.1-54)}$$

where the first term is related to precipitation kinetics (Equation (B.1-50)) and the second (convective-like) term arises from the undermining effect, described above. This approach is equivalent to using the concept of scaling tendency, but one that is based on

local concentrations at the steel surface and in the porous iron carbonate layer, rather than basing it on bulk concentrations. This equation needs to be solved simultaneously with (B.1-53) for all the other species in order to provide an estimate of the porosity distribution within the corrosion product layer, and account for the effect it has on concentrations and fluxes of all other species and ultimately on the corrosion rate.

B.1.5.3: Top of the line corrosion

An example that illustrates the ability of comprehensive models to be extended relatively easily to cover quite different corrosion scenarios is the implementation for Top of the Line Corrosion (TLC) prediction.

TLC is a corrosion phenomenon occurring in pipeline transportation of wet gas when there is a significant difference of temperature between the produced fluids and the surrounding environment. If the gas/liquid flow is stratified, warm saturated water vapor condenses on the inside walls of the pipeline and forms small water droplets which become saturated with acid gases, thus leading to severe corrosion issues [29,191,192]. There is no simple mitigation method available, especially considering that the use of standard corrosion inhibitors is not feasible as they cannot readily reach the top portions of the pipeline.

TLC is very dependent on the rate of water condensation, temperature, and the solubility of corrosion products but is also linked to the presence of CO_2 and carboxylic acids. Only a limited number of sour TLC cases have been reported [193–195], these will not be discussed here. A key aspect of understanding the TLC mechanism is the interaction between condensation, corrosion, the evolution of the chemistry in the condensed water,

and formation of the corrosion product layers (iron carbonate). The size of the water droplet is controlled by the condensation rate (leading to an increase in droplet size) and by gravity and drag forces (leading to removal of droplets from the pipe wall). Corrosion products can accumulate rather quickly in the water phase leading to supersaturation with regard to iron carbonate. The formed corrosion product layer tends to block the steel surface and act as a mass transfer barrier and thus decrease the corrosion rate. However, the water in the droplet is constantly re-supplied by pure condensed water, which tends to dilute the corrosion products and decrease the saturation value. The understanding of TLC mechanisms lies in the balance between the corrosion process, which leads to supersaturation and precipitation of iron carbonate, and the condensation process, which tends to decrease the iron carbonate saturation level and lead to dissolution of the corrosion product layer [184,196].

The example of TLC is interesting for the present discussion, since there are actually no new physicochemical processes involved when compared to standard "bottom of the line" corrosion described above, other than water condensation and droplet formation. The same chemical and electrochemical processes discussed previously are valid. This is also true for the mechanism of iron carbonate precipitation. Therefore, adapting the existing mechanistic CO_2 corrosion models to the TLC environments is relatively straightforward, while this would not be the case for empirical or semi-empirical models.

Several empirical/semi-empirical approaches have been proposed to model TLC. De Waard et al.[81] were the first to propose a model for TLC based on a correction for his

widely used semi-empirical corrosion prediction equation. De Waard et al. introduced a correction factor, $F_{cond}=0.1$, in order to adapt his model to condensation conditions valid for condensation rates below an experimentally determined "critical" rate of 0.25 mL.m^{-2}.s^{-1}. In 2000, a different model was proposed by Pots and Hendriksen[184], which aimed at accounting for the competition between the iron carbonate layer precipitation rate and the condensation rate. The so called "supersaturation model" is based on the calculation of ferrous ion concentration at saturation under precipitating conditions. The steady state corrosion rate was described based on the flux of ferrous ion required to keep the condensed water supersaturated. Pots and Hendriksen emphasized the importance of correctly evaluating the condensation rate and characterizing the chemistry of the aqueous phase in order to accurately predict the corrosion rate. More recently, Nyborg and Dugstad[196] developed another semi-empirical equation for TLC prediction based on their own experimental work. It was hinged on the concept that TLC is limited by the amount of iron which can be dissolved in the thin film of condensing water. According to Nyborg and Dugstad, the TLC rate can be modeled as being proportional to the water condensation rate, the iron carbonate solubility, and supersaturation value.

All abovementioned attempts suffer from the usual shortcomings associated with empirical and semi-empirical models, *i.e.*, they have limited ability to extrapolate beyond the range of parameters they have been developed for and cannot be easily adapted to take into account additional influencing parameters, such as new species or additional types of corrosion products.

Zhang et al.[197] published the first fully comprehensive mechanistic approach to TLC modeling. The key point for this discussion is that this model was directly adapted from the mechanistic CO_2 corrosion approach developed by Nordsveen et al. [15] and Nesic et al. [46,180,189]. As mentioned before, the underlying mechanisms of corrosion (chemistry in the condensed water and the corrosion at the steel surface) have not been changed when adapting them to TLC. The only real change was the implementation of dropwise condensation rate prediction, based on heat and mass transfer theory [197]. The boundary conditions specific to the TLC scenario have also to be implemented. Zhang et al. [197] stated that, from a statistical point of view, every point on the metal surface has the same probability of being covered by liquid droplets and, consequently, it can be assumed that the entire surface is subject to uniform corrosion. This simplifies the mathematical approach from a three-dimensional situation (with semi-hemispherical droplet) to a one-dimensional geometry (in the shape of a finite liquid film). The droplet growth and loss is simulated by an increase in the liquid film with time until it reaches a calculated maximum size where the droplet disappears (falls or slides). The calculation then restarts with a minimum water film thickness (corresponding to the minimum droplet size), and the cycle is repeated, until the corrosion process reaches a steady state. Another easy adjustment of the standard "bottom of the line" corrosion model was the absence of the supporting electrolyte (aqueous salt) and ignoring the effect of flow on mass transfer within the water film.

Zhang's approach is a good example showing the adaptability of comprehensive models. The model validity range is extended by improving the physical representations

of the relevant physicochemical phenomena. Other extensions can be readily made by, for example, broadening the temperature and pressure validity ranges for kinetics or equilibrium constants, etc. New species and additional corrosion products can be easily added as the knowledge of the underlying corrosion mechanism matures.

B.1.6: Summary

Corrosion rate predictive models of mild steel in the presence of dissolved CO_2 have improved significantly since initial studies appeared in the mid 1970s. Driven by economical, safety and environmental concerns, numerous studies and mathematical models are now available pertaining to this system. In this review, mathematical models have been categorized into three main groups: empirical/semi-empirical, elementary mechanistic, and comprehensive mechanistic models. The mechanistic models show a much better potential for further development to cover more complex conditions; they offer transparency, flexibility, and extrapolation capabilities in a way that empirical/semi-empirical models cannot.

The state of the art models in CO_2 corrosion are comprehensive mechanistic models which benefit from an inclusive theoretical treatment. These models offer greatest flexibility to be adopted to cover various conditions and corrosion scenarios by adding new physics, as the knowledge of the underlying mechanisms becomes mature. Nevertheless, many challenges remain, such as improved kinetics of underlying electrochemical reactions, better understanding of protective corrosion product layer growth, extension to sour conditions, etc., which are all subject of current research efforts.

In spite of that, comprehensive mechanistic models offer the most flexible platform for inclusion of new and more complex phenomena encountered in practical applications, such as the effect of steel microstructure, effect of alloying compounds, application of inhibitors, modeling of localized attacks, etc.

Nomenclature

Symbol	Description	Units
A	Active surface area of the deposit	m^2
α_j	Transfer coefficient of electrochemical reaction j	-
b	Tafel slope	V
CR	Corrosion rate	$mm.yr^{-1}$
C_i	Concentration of species i	M
C_i^s	Concentration of species i at the electrode surface	M
C_i^b	Concentration of species i in the bulk solution	M
$C_{i,ref}^b$	Concentration of species i in the bulk solution at reference conditions	M
$C_{Fe^{2+},sat}$	Concentration of Fe^{2+} in the bulk solution at saturation with regard to $FeCO_3$	M
D	Pipe/sample diameter	m
D_i	Diffusion coefficient of species i	$m^2.s^{-1}$
$D_{i,lim}$	Diffusion coefficient of the limiting species	$m^2.s^{-1}$
δ	Diffusion layer thickness	m
E	Electrode potential	V
E^0	Standard potential	V
E_{rev}	Reversible potential	V
E_a	Activation energy	$J.mol^{-1}$
ε	Porosity	-
η	Over potential	V
F	Faraday's constant	$C.mol^{-1}$
H_{CO_2}	Henry's constant of CO_2	$M.bar^{-1}$
i	Current density	$A.m^{-2}$
$i_{0,j}$	Exchange current density of reaction j	$A.m^{-2}$

$i_{0,j,ref}$	Exchange current density of reaction j at reference conditions	A.m^{-2}
i_{lim}	Mass transfer limiting current density	A.m^{-2}
i_{ct}	Charge transfer controlled current density	A.m^{-2}
i_{net}	Net current density	A.m^{-2}
i_{corr}	Corrosion current density	A.m^{-2}
K_j	Equilibrium constant of reaction j	Varies
K_{sp}	Dissolution equilibrium constant	Varies
$K_{0,j}$	Standard reaction rate constant of electrochemical reaction j	Varies
k_0	Pre-exponent term in Arrhenius' equation	Varies
k_j	*Reaction rate constant of reaction j*	Varies
k_m	Mass transfer coefficient	m.s^{-1}
L	Characteristic length	m
m	Reaction order	-
M_i	Molecular weight of species i	g.mol^{-1}
μ	Viscosity	N.s.m^{-2}
n	Number of electrons transferred	-
N_i	Flux of species i	mol.m^{-2}.s^{-1}
υ	Kinematic viscosity	M^2.s^{-1}
Ω	Rotation speed	Rad.s^{-1}
p_i	Partial pressure of species i	bar
ϕ	Potential in the solution	V
R	Universal gas constant	j.mol^{-1}.K^{-1}
Re	Reynolds number	-
R_i	Rate of chemical reaction of species i	M.s^{-1}
ρ_i	Density of species i	kg.m^{-3}
$S\text{‰}$	Salinity	g(salt).kg^{-1}(solution)
S_{FeCO_3}	Saturation value of $FeCO_3$	-
Sh	Sherwood number	-
Sc	Schmitt number	-
ST	Scaling tendency	-
T	Temperature in kelvin	K
T_{ref}	Temperature in kelvin at reference conditions	K

T_c	Temperature in centigrade	C
t	Time	s
u_i	Mobility of species i	$m^2.V.s^{-1}$
V	Volume of the deposit	m^3
v_x	Fluid velocity along x axis	$m.s^{-1}$
WCR	Water condensation rate	$kg.m^{-2}.s^{-1}$
x	Normal distance from electrode surface	m
z_i	Electrostatic charge of species i	-

Chapter B.2: The nature of the effect of CO_2 on the cathodic currents of corrosion in aqueous acidic solutions [5]

B.2.1: Introduction

The present chapter defines the scope of the study as it relates to the mechanism of cathodic reactions in mild steel corrosion in carbon dioxide containing acidic solutions. Following the literature review in the previous chapter, the recent studies on the mechanism of cathodic reactions in CO_2-saturated acidic solutions is critically reviewed in more depth, the knowledge gap is identified, and a hypothesis is developed. It was demonstrated that the glass cell experiments are unable to provide the conditions required for testing the hypothesis. In this regards, a series of experiments were conducted in a thin channel cell test apparatus at elevated CO_2 partial pressures to determine the necessary test conditions for successful evaluation of the hypothesis. In this initial experimental study, it is shown that the direct reduction of carbonic acid is not a significant process in CO_2 corrosion. Furthermore, the effect of alloying elements was discussed in terms of their effect on the observed cathodic polarization curves.

B.2.2: Background

The mechanism of cathodic reactions involved in CO_2 corrosion, i.e., the sequence of electrochemical and chemical reactions, is a rather complex matter, in the sense that it involves a number of electroactive species that are inter-related through

---

[5] A version of this chapter is published as : "Electrochemistry of CO_2 Corrosion of Mild Steel: Effect of CO_2 on Cathodic Currents", Kahyarian, A., B. Brown, and S. Nesic, Corrosion 74 (2018): pp. 851–859 (reference number [329])

homogeneous chemical reactions. The CO_2 gas, upon dissolution in water (Reaction (B.2-1)), goes through hydration (Reaction (B.2-2)) and dissociation (Reactions (B.2-3) and (B.2-4)) reactions, forming an acidic, corrosive solution.

$$CO_{2(g)} \leftrightharpoons CO_{2(aq)} \qquad \text{(B.2-1)}$$

$$CO_{2(aq)} + H_2O_{(l)} \leftrightharpoons H_2CO_{3\,(aq)} \qquad \text{(B.2-2)}$$

$$H_2CO_{3(aq)} \leftrightharpoons HCO_{3\,(aq)}^- + H^+_{(aq)} \qquad \text{(B.2-3)}$$

$$HCO_{3\,(aq)}^- \leftrightharpoons CO_{3\,(aq)}^{2-} + H^+_{(aq)} \qquad \text{(B.2-4)}$$

CO_2 corrosion in aqueous acidic solutions is generally believed to involve numerous electrochemical reactions, as shown below [20,47,56]. The anodic partial of the reaction (B.2-5) is the cause of metal deterioration, and cathodic partial of reactions (B.2-6) through (B.2-9), provide the electron sink required for the anodic reaction to progress spontaneously. The significance of these reactions are mainly based on the studies done by de Waard and Milliams in 1975 [19,105], Schmitt and Rothmann in 1977 [107] and Gray et al. in 1989 and 1990 [14,103], as reviewed in more detail in Chapter B.1.

$$Fe^{2+}_{(aq)} + 2e^- \leftrightharpoons Fe_{(s)} \qquad \text{(B.2-5)}$$

$$H^+_{(aq)} + e^- \leftrightharpoons {}^1\!/_2\, H_{2(g)} \qquad \text{(B.2-6)}$$

$$H_2O_{(l)} + e^- \leftrightharpoons OH^-_{(aq)} + {}^1\!/_2\, H_{2(g)} \qquad \text{(B.2-7)}$$

$$H_2CO_{3(aq)} + e^- \leftrightharpoons HCO_{3\,(aq)}^- + {}^1\!/_2\, H_{2(g)} \qquad \text{(B.2-8)}$$

$$HCO_{3\,(aq)}^- + e^- \leftrightharpoons CO_{3\,(aq)}^{2-} + {}^1\!/_2\, H_{2(g)} \qquad \text{(B.2-9)}$$
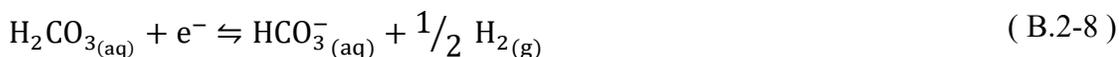
The profound effect of homogeneous reactions in CO_2 corrosion is mainly associated with the CO_2 hydration equilibrium, where only a small fraction (~0.2 %) of

$CO_{2(aq)}$ reacts to form H_2CO_3 [20]. Therefore, there is a large reservoir of $CO_{2(aq)}$ present in the solution to replenish the H_2CO_3 concentration as it is consumed by the corrosion process. The higher corrosion rates observed in aqueous CO_2 solutions, as compared to a strong acid solution (e.g., HCl) at the same pH, was therefore associated with the additional H_2CO_3 reduction and the effect of the CO_2 hydration reaction [18,55,60].

While the abovementioned mechanistic view of the cathodic reactions in CO_2 corrosion is widely accepted, the findings in more recent studies have challenged its basis [15,44–46]. In those studies, it was shown quantitatively that the limiting currents could be adequately explained even if H_2CO_3 was not considered an electroactive species [15,44–46]. This can be understood when considering the local concentration of chemical species at the metal surface, and the influence of the homogeneous chemical reactions. That is, the H_2CO_3 dissociation reaction (Reaction (B.2-3)), occurring in the vicinity of the metal surface, followed by electrochemical reduction of the produced H^+ ions (Reaction (B.2-6)), which provides a parallel reaction pathway to the direct H_2CO_3 reduction reaction. This observation carries a significant mechanistic implication as it undermines the previous commonly accepted mechanistic arguments, developed based on the analysis of cathodic polarization behavior at or close to limiting currents [14,103,107]. Therefore, to date, the evidence for direct H_2CO_3 reduction is mostly circumstantial. This was perhaps best noted by Nordsveen et al. [15] who suggested that while the cathodic limiting currents can be quantitatively explained without considering H_2CO_3 as an electroactive species, the predicted corrosion rates are in better agreement with the experimental data when this additional reaction was included in the model.

The electrochemical activity of H_2CO_3 has been discussed specifically in a few different studies. Linter and Burstein published one of the earliest articles suggesting that H_2CO_3 is not electrochemically active [198]. The authors investigated the mechanism of CO_2 corrosion on both a 13Cr stainless steel and a low alloy steel. Their arguments were developed based on the polarization curves obtained in N_2-saturated and CO_2-saturated 0.5 M NaCl solutions at pH 4.0 with additional potassium hydrogen phthalate buffer. In a nutshell, the authors were able to observe the charge transfer controlled current densities in both N_2-saturated and CO_2-saturated solutions. The results showed no significant increase in this range of current densities when comparing the two solutions, leading to the conclusion that H_2CO_3 is not electrochemically active. The findings of Linter and Burstein [198] did not gain much attention over the years, perhaps due to the concerns arising from the limited environmental conditions covered in their study, *i.e.*, the fact that at pH 4.0 the cathodic current is dominated by H^+ reduction. The concentration of H_2CO_3 at 1 bar CO_2 is about a third of H^+ at pH 4 [60]; with roughly similar exchange current densities considered for H_2CO_3 and H^+ [18], the expected contribution of H_2CO_3 falls easily within the experimental error of the measurements reported by the authors. In addition, while the use of additional buffer was an elegant way to elucidate the charge transfer cathodic currents, concerns could be raised about the secondary effects of these buffers on the electrochemical reactions.

In 2008 Remita et al. studied the electrochemical activity of H_2CO_3 using a more quantitative approach [11]. The authors conducted a series of experiments in N_2-saturated and CO_2-saturated solutions at pH~4 using a rotating disk electrode experimental

apparatus. Their arguments were based on a comprehensive mathematical model, similar to those discussed above [15,44–46]. Using the electrochemical kinetic parameters obtained for H^+ reduction in N_2-saturated solutions, the authors were able to predict the results obtained in CO_2-saturated solutions without considering H_2CO_3 as a significant species (absent in their model). Their observation led to the conclusion that H_2CO_3 is not electrochemically active, and its sole effect was claimed to be the buffering effect of H_2CO_3 on surface concentration of H^+. It is noteworthy that the arguments used in this study suffer from the same shortcomings as those in the study by Linter and Burstein[198]: the very narrow range of experimental conditions and the fact that at this condition (pH 4 and 1 bar CO_2) the cathodic currents are dominated by H^+ reduction. In fact, one may suggest that the charge transfer controlled currents were not clearly observed as compared to the study of Linter and Burstein [198], where an additional buffer was used to shift the mass transfer limiting current towards higher values. At the conditions in the study by Remita et al. [11] the observed range of cathodic currents were mostly under mixed charge transfer/mass transfer control, and the pure charge transfer controlled currents were obscured by the anodic reaction at lower currents and by the mass transfer limiting current at higher currents. That makes the distinction of the possible effect of electrochemical activity of H_2CO_3 even harder. The conclusion made by Remita et al., that H_2CO_3 acts as a buffer in this system, is in agreement with what was suggested earlier that the limiting current densities could be reasonably predicted without the direct reduction of H_2CO_3 [15,44–46]. The effect of flow velocity that was discussed extensively,

and the good agreement obtained with the model prediction, is merely a further confirmation of the buffering ability of H_2CO_3 as a weak acid.

It is important to realize that the clearly demonstrated buffering ability of H_2CO_3 (or any other weak acid) does not exclude the possibility of H_2CO_3 direct reduction, as these are two independent processes. That is the reason why, in order to distinguish them, the arguments must be based on the behavior of pure charge transfer controlled currents so that the electrochemical activity of H_2CO_3 can be separated from the chemical equilibria (buffering effect) associated with this species. This concept was not properly accounted for in the analysis of the surface pH measurements made by Remita et al [11]. Their results clearly showed that in the presence of H_2CO_3 the surface pH is lower than in a N_2-saturated solution of the same pH. While this observation further confirms the buffering ability of H_2CO_3, it provides no insight into the electrochemical activity of this species, as they claimed. In fact, considering the fast kinetics of H^+/HCO_3^- recombination as compared to CO_2 hydration [43,60], it is expected that the surface pH will be nearly identical irrespective of whether H_2CO_3 is reduced (to H_2 and HCO_3^-) or not. In brief, the study by Remita et al. is of significance as it further elucidated the possible mechanisms underlying CO_2 corrosion by explicitly focusing on the buffering ability of H_2CO_3. Nevertheless, the arguments and the experimental results did not provide sufficient evidence about electrochemical activity of H_2CO_3.

In an attempt to address the shortcomings of the previous studies, Tran et al. conducted a series of experiments at elevated pressures up to 10 bar CO_2 [50]. At such conditions the authors were able to investigate the electrochemical activity of H_2CO_3, as

the dominant chemical species, with more confidence. Nevertheless, it was noted that even at such high CO_2 partial pressures the charge transfer controlled currents could not be observed on a mild steel surface due to the interference of the anodic reaction at low current densities and the mass transfer limitation at the high current densities. Therefore, the experiments were conducted on a UNS 30400 stainless steel surface. The suppressed anodic currents on the stainless steel surface allowed the charge transfer controlled currents at the lower range to be clearly observed. The experimental results showed that the presence of H_2CO_3, even at high levels (when pCO_2=10 bar), did not result in any significant change of charge transfer controlled currents as measured on a stainless steel surface. This observation demonstrated that H_2CO_3 is not electrochemically active, at least not on the surface of stainless steel. While the experimental conditions of this study allowed a proper measurement and discussion of the electrochemical activity of H_2CO_3, one must consider the fact that the two surfaces (actively corroding mild steel vs. the passive stainless steel) are very different. The presence of a significant amount of alloying elements (i.e. ~20% Cr, 10% Ni) raises the uncertainty about whether the electrochemical mechanisms identified on stainless steel can be simply assumed to be valid for mild steel surfaces. The mechanism and the kinetics of the hydrogen evolution reaction are known to be significantly influenced by the composition of the substrate, and even by the fine differences in surface preparation procedures [115,130,199]. Additionally, the passive oxide layer formed on stainless steel may alter the kinetics and the mechanism of the hydrogen evolution reaction [125], considering that the hydrogen evolution reaction

(from H^+ or H_2CO_3) involves a series of surface dependent chemical/electrochemical adsorption/desorption steps [61,109].

The review of the existing literature clearly shows that despite many decades of research on the mechanism of CO_2 corrosion, there are still some important mechanistic aspects that have remained unresolved. Amongst them is the electrochemical activity of H_2CO_3 as one of the main chemical species in CO_2 corrosion mechanisms. However, neither of the two competing ideas about the electrochemical activity of H_2CO_3 appear to have sufficient experimental evidence, so far. As identified previously [50,62,104,200,201], the direct experimental evidence for electrochemical activity of a weak acid (such as H_2CO_3) may be obtained by investigating the behavior of pure charge transfer controlled cathodic currents. If the reduction of H_2CO_3 is significant, at a fixed pH, the charge transfer controlled currents would increase as partial pressure of CO_2 (pCO_2) increases, as a result of increased H_2CO_3 concentration and, thus, increased rate of the H_2CO_3 reduction reaction. On the other hand, if the charge transfer controlled currents remained unaffected by pCO_2, one may deduce that H^+ reduction is the dominant cathodic reaction and H_2CO_3 is not significantly electroactive.

It is apparent from the previous attempts on investigating the electrochemical activity of H_2CO_3 [11,50,198] that the main challenge in verifying these hypothetical behaviors is to create the experimental conditions required to observe the charge transfer controlled cathodic currents. In the present study, in addition to the experiments conducted in a conventional three electrode glass cell test apparatus, a thin channel flow geometry, enabling high flow velocities, was used in order to further increase the limiting

currents. This was accentuated by lowering the temperature in order to disproportionally

decrease the rates of electrochemical reactions, making them the rate determining step,

and also by increasing the pCO_2 above atmospheric pressure. Measurements in the

present study were conducted on three different surfaces: 316L stainless steel, 99.9 wt.%

pure iron and API 5L X65 mild steel. Mild steel is a typical material of choice for the

transmission pipelines in the oil and gas industry, which is a focus in the present study.

The stainless steel electrode was selected due to the same considerations as described by

Tran et al. [50] and also to provide an opportunity for the comparison with the previous

studies [50,198]. The choice of pure iron was made due to its close relevance with mild steel

(which consists of ~98 wt. % iron), when compared to stainless steel (~70 wt. % iron), in

order to provide further insight into the possible effect of alloying elements.

B.2.3: Material and methods

B.2.3.1: The Glass Cell

A series of experiments were conducted in a 1 L glass cell, using a rotating disk

(RDE), three electrode test apparatus. The experimental setup is similar to that described

for an earlier study [201]. The 0.1 M NaCl supporting electrolyte was purged with N_2 or

CO_2 gas, depending on the type of experiment. The outlet gas was monitored with an

oxygen sensor (Orbisphere 410) to assure sufficient de-oxygenation (~ 1 ppb_m dissolved

oxygen). The solution pH was then adjusted to 4.0 using a small amount of diluted NaOH

or HCl solutions. The solution pH was monitored throughout all experiments to ensure a

constant value. That was followed by further purging of the solution to maintain the

minimal amount of dissolved oxygen content. The rotating disk electrodes with a 5 mm

diameter were made of either 99.99 wt.% pure iron or API X65 5L mild steel (composition in Table B.2-1), press-fitted into a TEFLON^{TM} electrode holder (Pine instruments). The electrodes were polished and electrochemically treated according to a procedure discussed elsewhere[62].

The cathodic polarization measurements were initiated from open circuit potential (OCP) towards the more negative values after a stable OCP was observed ($<\pm 2$mV drift over 5 min). The steady state voltammograms were obtained using stair case voltammetry at 0.5 mV.s^{-1} scan rate and 1 s^{-1} sampling period. The reported results are corrected for Ohmic drop using the solution resistance obtained from electrochemical impedance spectroscopy (EIS) measurements performed after the polarization experiments (DC potential at OCP, AC potential ± 5 mV, frequency range 10kHz to 0.2 Hz at 8 points/dec). The linear polarization resistant measurements (LPR) were conducted in separate tests following the abovementioned preparation procedure. The measurements were done by sweeping the potential from 5 mV to -5 mV vs. OCP, using 0.125 mV.s^{-1} scan rate and 1 s^{-1} sampling period.

B.2.3.2: The Thin Channel Flow Cell

The thin channel flow cell (TCFC) apparatus is shown in Figure B.2-1, and described in detail elsewhere[202–207]. In the present study, the test section was slightly modified by introducing a saturated Ag/AgCl reference electrode, flush mounted on the lid, directly opposite to the working electrode, as shown in Figure B.2-2.
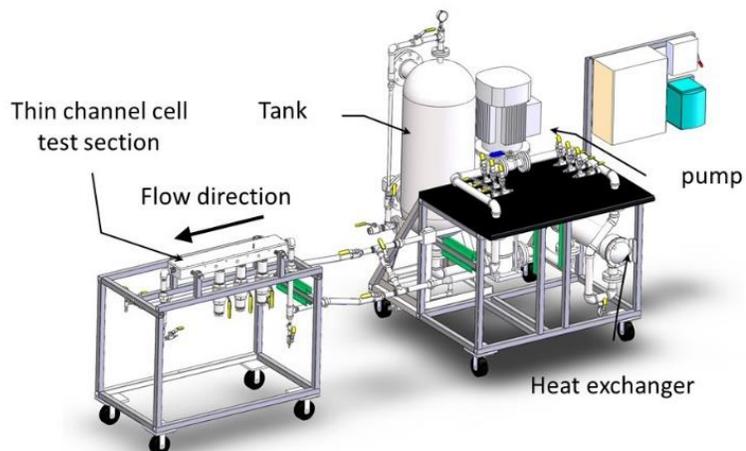
Figure B.2-1. The thin channel flow cell test apparatus.

The 0.1 M NaCl solution (110 L) was made with deionized water and analytical grade chemicals. The solution was then purged for ~3 hr, with N_2 or CO_2 gas, depending on the desired experimental conditions, while the outlet gas was monitored with an oxygen sensor (Orbisphere 410) to ensure proper deoxygenation. Maximum dissolved oxygen content, measured before initiating the experiment, was 3 ppb (typically ~1 ppb). In the high pressure experiment, after the deoxygenation step, the system was pressurized to 5 bar CO_2 and then maintained at that pressure until the solution became saturated, after at least 3 hr. As the last step, the pH (measured by an OMEGA 5431-10 in-line pH probe) was adjusted to the targeted value by gradual addition of deoxygenated HCl or NaOH solution, introduced into the system from a secondary pressurized reservoir.
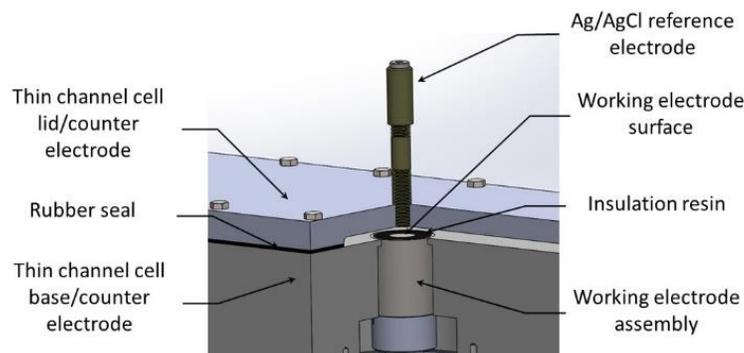
Figure B.2-2. The depiction of the three electrode cell arrangement inside the thin channel test section.

The experiments were conducted on three different substrates: 99.99 wt.% pure iron, 316L stainless steel, and API 5L X65 mild steel. The chemical composition of the stainless steel and the mild steel are shown in Table B.2-1. The working electrode assembly was built similarly to that shown in an earlier study [33], with a single disk working electrode, which was mounted into the test section as shown in Figure B.2-2.

Prior to each experiment, the working electrode was abraded with 600 grit silicon carbide paper, then rinsed and sonicated for 5 minutes using isopropanol. The working electrode was flush-mounted on the bottom of the thin channel test section, which was then closed and purged with dry CO_2 or N_2. In the case of mild steel and pure iron electrodes, after exposing the electrode to the test solution, the open circuit potential (OCP) was monitored until a steady value was reached prior to initiating polarization measurements. For the experiments on the stainless steel surface the polarization measurements were initiated 2 min after exposing the electrode to the test solution in order avoid any significant passivation of the electrode. The polarization curves were obtained using the same electrochemical measurement parameters as those in the glass cell experiments.

The solution temperature was controlled within ±0.5°C by using a jacketed immersion heater located in the tank and covered cartridge heaters used to directly heat the test section (for experiments conducted at 30°C), as well as a shell and tube heat exchanger connected to a chiller (Air-3000 FLUID CHILLERS Inc.) for experiments done at 10°C. The flow velocity inside the thin channel test section was fixed at 13 m.s^{-1} throughout the experiments.

Table B.2-1. Chemical composition of steel working electrodes in wt.%.

	S	Cu	P	V	C	Cr	Mo	Si	Ni	Mn	Co	Fe
X65	0.009	-	0.009	0.047	0.13	0.25	0.16	0.26	0.29	1.16	-	Balance
SS 316 *	0.025	0.59	0.035	0.050	0.018	16.65	2.04	0.54	10.12	1.51	0.33	Balance

*Other elements with less than 0.1 wt.% concentrations: Titanium, tin, tantalum, columbium, aluminum, boron, and vanadium.

B.2.4: Results and discussion

The steady state cathodic polarization curves obtained in glass cell experiments are presented in Figure B.2-3 and Figure B.2-4. These experiments were conducted in order to examine whether the conditions typical for glass cell experiments allow a proper discussion of the electrochemical activity of H_2CO_3. All the polarization curves reported in the present study (obtained in both the glass cell and TCFC) demonstrate the same generic trend. A steep increase in current density is seen just below the OCP, followed by the limiting current and a linearly increasing current density range at even lower potentials that is associated with the water reduction reaction.
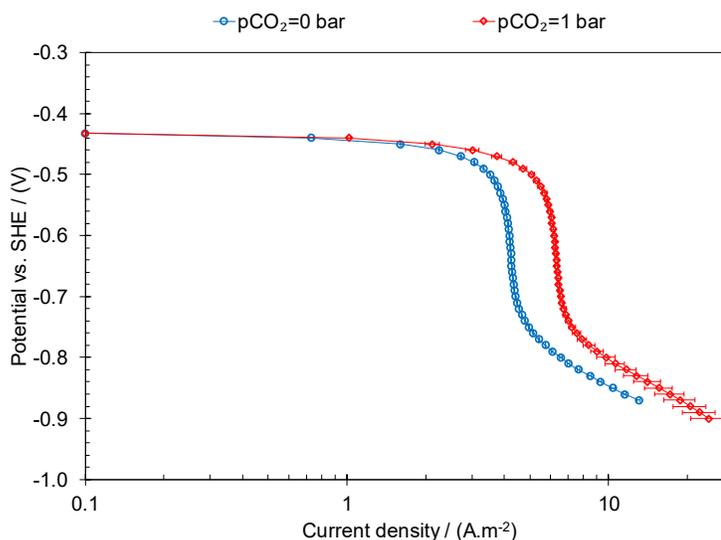
Figure B.2-3. Steady state cathodic polarization curves obtained at 30°C, pH 4.0, 2000 rpm RDE on API 5L X65 mild steel, in N_2-saturated and CO_2 saturated solutions. The error bars represent the minimum and maximum values obtained in three repeated measurements.

Figure B.2-3 shows the comparison of the cathodic polarization curves obtained in a N_2-saturated solution at pH 4.0 with a CO_2-saturated solution at the same pH. The results show a clear increase of the limiting current in CO_2-saturated solutions. As discussed above, this increase stems from the presence of carbonic acid, and the CO_2 hydration reaction, which can be readily explained irrespective of whether H_2CO_3 is electrochemically active or not. The main focus in the present study is on the charge transfer controlled cathodic currents, where the surface concentrations of species are the same as in the bulk, and the interference due to the homogeneous chemical dissociation of H_2CO_3 is not significant. At such conditions, the surface concentration of H_2CO_3 depends only on partial pressure of CO_2 and temperature. Considering the dissolution and hydration equilibria [43]:

$$[H_2CO_3] = K_{hyd}K_{dis}pCO_2 \qquad\qquad (\text{B.2-10})$$

where the brackets denote equilibrium concentration in M, and K_{hyd}=1.18×10^{-3} and K_{dis} =2.96×10^{-2} M·bar^{-1} are the equilibrium constants of the hydration reaction (Reaction (B.2-2)) and dissolution reaction (Reaction (B.2-1)) at 30°C, respectively[208,209]. Thus, for pCO$_2$=0.96 bar, the [H$_2$CO$_3$] = 3.35×10^{-5}M. At these conditions, H$^+$ is the dominant electroactive species with a three-fold higher concentration than H$_2$CO$_3$. Hence, the theoretical difference expected from the two proposed mechanisms, one with and the other without the direct reduction of H$_2$CO$_3$, is very small when compared to the typical experimental error. Furthermore, the polarization curves shown in Figure B.2-3, do not demonstrate a distinguishable charge transfer controlled current range, in neither of the solutions. Using the LPR measurement in CO$_2$ saturated solution the corrosion current is calculated to be 1.81 A·m^{-2} (based on the Stern-Geary equation with B value = 13 mV). Comparison of this value with the mass transfer limiting current of 6.34 A.m^{-2} suggests that even in CO$_2$ saturated solution the observed cathodic current polarization curve is significantly under the influence of the limiting current. Remembering that the limiting current density is identical for both mechanisms, we can make a simple comparison based on:

$$\frac{1}{i} = \frac{1}{i_{ct}} + \frac{1}{i_{lim}} \qquad\qquad (\text{B.2-11})$$

This suggests that at the mixed controle range the theoretical difference in polarization curves between the two mechanisms becomes even smaller, since the limiting current portion is identical for both cases. Therefore, the results obtained in typical glass cell experiments, which are similar to those reported previously [11,198], do not allow for a

proper mechanistic discussion of the electrochemical activity of H_2CO_3. In order to examine the electrochemical activity of H_2CO_3, the experiments were continued in the TCFC test apparatus, where more suitable experimental conditions could be achieved, as described further below.

The influence of substrate composition on the electrochemical response of the system was also examined in the glass cell experiments. The cathodic polarization curve obtained on 99.99 wt.% pure iron in N_2-saturated solution is compared with that obtained on a API 5L X65 mild steel surface in Figure B.2-4. While the reproducibility of the results obtained on a pure iron surface was slightly lower when compared to steel, the polarization curves showed that the pure iron surface is a significantly weaker catalyst for the reduction reactions, in agreement with previous reports [54,62]. Considering that the pure charge transfer controlled currents for H^+ reduction were not observed, the true difference in the electro-catalytic effect of the two surfaces cannot be properly distinguished. Nevertheless, the observed difference even in this mixed mass transfer/charge transfer controlled regime signifies the importance of the substrate composition when discussing the electrochemical mechanisms.
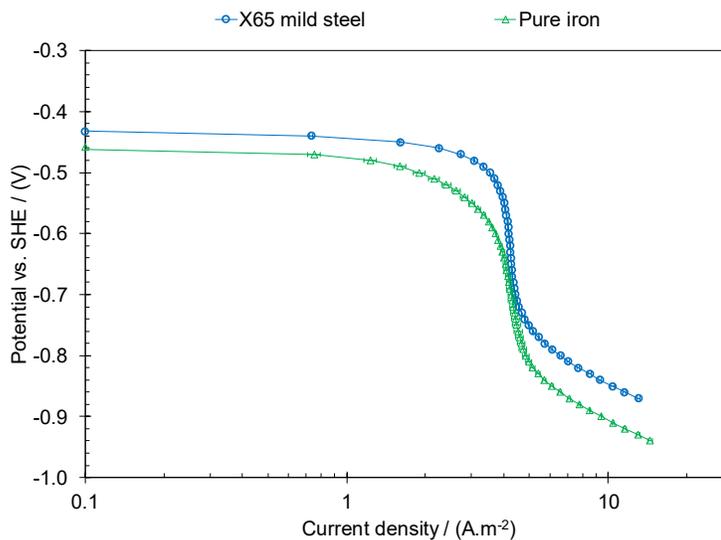
Figure B.2-4. Steady state cathodic polarization curve obtained at 30°C, pH 4.0, 2000 rpm RDE in N_2-saturated solution on API 5L X65 mild steel and 99.99 wt.% pure iron electrodes. The error bars represent the minimum and maximum values obtained in three repeated measurements.

The following experiments, conducted in the TCFC test apparatus, had two main advantages. The ability to increase the flow velocity to significantly higher values in order to increase the mass transfer limitation and the ability to conduct the experiments at elevated pCO_2 (5 bar maximum operating pressure), hence, increasing the concentration of H_2CO_3. Figure B.2-5 shows the cathodic polarization curves obtained at 30°C in the TCFC.
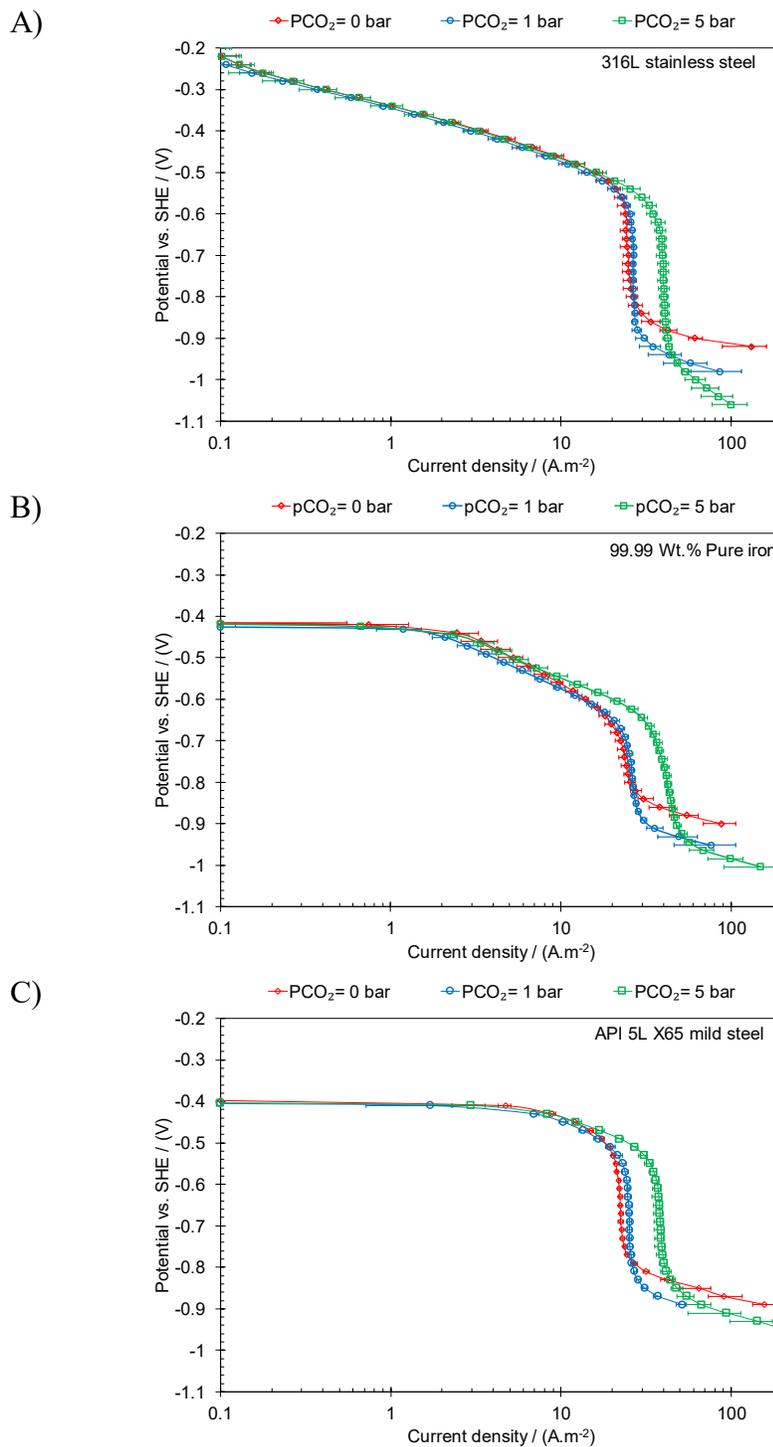
Figure B.2-5. Steady state cathodic polarization curves at pH 4, 30°C, 13 m.s^{-1} TCFC, 0.1 M NaCl, 0.5 mV.s^{-1} scan rate. A) 316 L stainless steel B) 99.99 wt.% pure iron C) API 5L X65 mild steel. Error bars represent the minimum and maximum values obtained in at least three repeated experiments.

The cathodic polarization curves obtained on 316L stainless steel electrodes are shown in Figure B.2-5.A. The results clearly demonstrate a charge transfer controlled current, in a wide potential range. This range of current densities was unaffected by increasing the pCO_2 from 0 to 5 bar and suggests that H_2CO_3 reduction on stainless steel is not significant at these conditions. Its sole effect was buffering the H^+ concentration and, hence, increasing of the limiting current. These experimental results were found to be in agreement with those reported previously [50,198]. The limiting currents in Figure B.2-5.A show an increase in the presence of CO_2. However, the increase of pCO_2 from 0 to 1 bar resulted only in a slight increase in limiting current densities, which is due to the overwhelmingly high mass transfer flux of H^+. As pCO_2 increased further to 5 bar, the concentration of H_2CO_3 increased and the effect of the CO_2 hydration reaction became more pronounced, leading to a significantly higher limiting current density.

The cathodic polarization behavior on pure iron electrodes is shown in Figure B.2-5.B. The charge transfer controlled currents were also clearly observed over an extended potential range. On the iron surface, the reproducibility of the results decreased; as indicated by the larger error bars. The charge transfer controlled cathodic currents appear to show a slight variation at different pCO_2, within the range of experimental error. Nevertheless, the comparison of the polarization curves, especially those obtained at 5 bar pCO_2 (where carbonic acid is the dominant species) with those at 0 bar CO_2, does not indicate any significant electrochemical activity of H_2CO_3.

The cathodic polarization curves obtained on an API 5L X65 mild steel surface are shown in Figure B.2-5.C. The comparison of the mass transfer limiting currents

obtained in N_2-saturated solutions with those obtained in glass cell experiments at similar conditions (Figure B.2-3) show more than a 5 fold increase (22.9 A.m^{-2} vs. 4.2 A.m^{-2}), yet the charge transfer controlled current range was still not clearly observed. With an increase of pCO_2 to 1 bar, the charge transfer controlled range gradually appeared and is seen clearly at pCO_2=5 bar. On the mild steel surface, the pure charge transfer controlled currents were observed in a rather narrow range of potentials, as compared to those on stainless steel and iron surfaces. Nevertheless, the comparison of the results at 1 and 5 bar CO_2 does not indicate significantly higher current densities in that range, favoring the arguments that H_2CO_3 is not electrochemically active on API 5L X65 mild steel either.

In order to extend the range of charge transfer controlled currents on the API 5L X65 mild steel surface and solidify the mechanistic arguments above, similar experiments were conducted at 10°C. Decreasing the temperature was expected to reduce the rates of electrochemical reactions more than the limiting currents. Such a disproportional decrease would allow the charge transfer controlled currents to be observed in a wider range. That is shown to be the case in Figure B.2-6, where the cathodic polarization curves obtained in N_2-saturated solutions at 10°C and 30°C are compared. At 10°C the rate of H^+ reduction reaction is decreased by almost an order of magnitude.
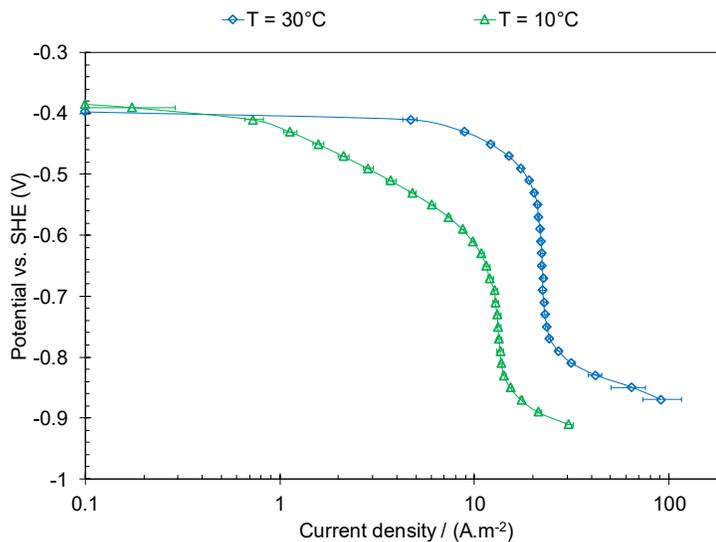
Figure B.2-6. The effect of temperature on steady state cathodic polarization curve obtained on API 5L X65 mild steel in N_2-saturated solution at pH 4.0, 13 m.s^{-1} TCFC, 0.1 M NaCl, 0.5 mV.s^{-1}. Error bars represent the minimum and maximum values obtained in at least three repeated experiments.

The effect of CO_2 partial pressure on the charge transfer controlled current densities obtained on API 5L X65 mild steel is shown in Figure B.2-7. At this condition the charge transfer controlled currents on mild steel were clearly observed and showed no significant dependence on pCO_2. The results obtained at 10°C was therefore found to further support the previous observation that the direct reduction of H_2CO_3 on a mild steel surface is insignificant.
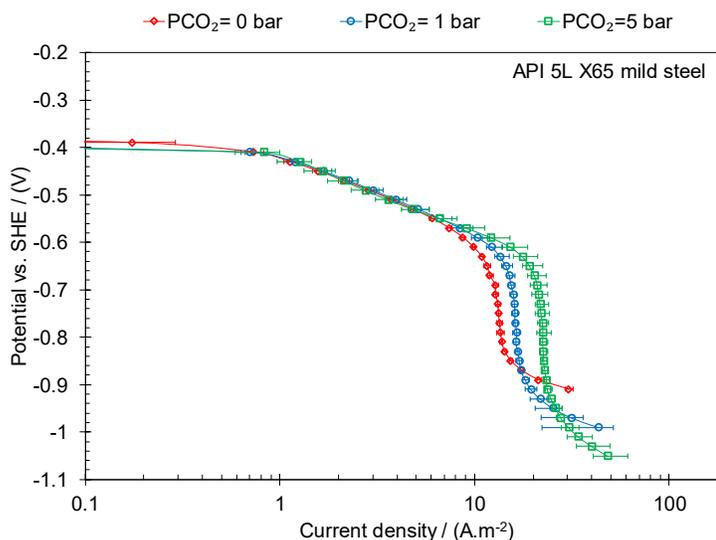
Figure B.2-7. Steady state cathodic polarization curves at pH 4.0, 10°C, 13 m.s^{-1} TCFC, 0.1 M NaCl, 0.5 mV.s^{-1} scan rate on an X65 mild steel surface. Error bars represent the minimum and maximum values obtained in at least three repeats.

The polarization curves obtained on the three different surfaces are compared in Figure B.2-8 for solutions at 5 bar CO_2 and 30°C, where the pure charge transfer controlled currents were observed on all three substrates. The results show a significant effect of the surface composition on the observed electro-catalytic activity related to H^+ reduction in the following order: mild steel > stainless steel > pure iron. Such a large difference in the electro-catalytic behavior of different substrates may result in different electrochemical mechanisms, especially considering that the investigated reactions are multi-step and include different adsorption/desorption elementary reactions. In that case, even a small change in the adsorption energies of the intermediate species may result in different behavior. Hence, while the choice of different substrates may be an appealing approach to investigate the electrochemical activity of H_2CO_3 (or any other weak acid), the complication introduced by different electro-catalytic properties requires a careful verification of the results on the substrate of interest.

In the present study, the cathodic polarization in CO_2 saturated solutions at pH 4.0 and pCO_2 up to 5 bar was investigated on pure iron, stainless steel, and mild steel surfaces. The experimental results obtained on all three substrates suggest that H_2CO_3 reduction was not significant at the conditions considered here, in support of the recent mechanistic arguments found in the literature [11,50,198]. Therefore, the cause of higher corrosion rates in CO_2-saturated brines has to be sought elsewhere. In a recent study [210], focused on the iron dissolution reaction, the presence of CO_2 was found to significantly increase the observed anodic currents for such environmental conditions. From these observations, it appeared that the underlying mechanism of CO_2 corrosion is yet to be fully established.
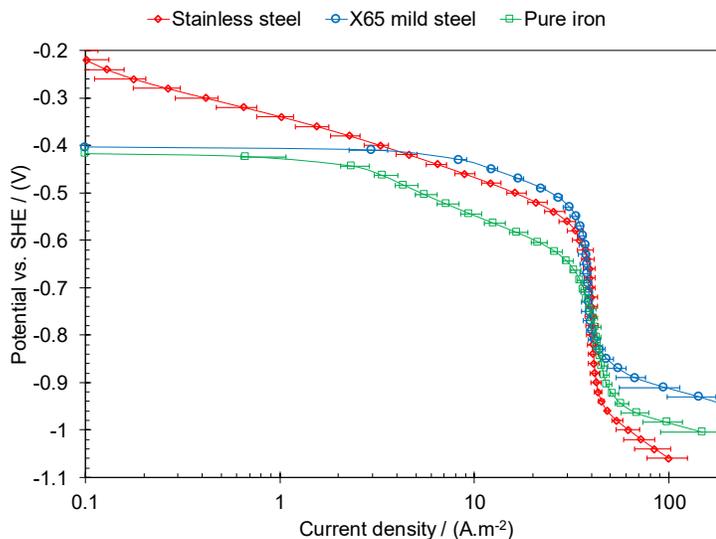
Figure B.2-8. The comparison of the steady state cathodic polarization curves obtained on API 5L X65 mild steel, 316L stainless steel, and 99.99 Wt.% pure iron at pH 4, 30°C, 13 m.s^{-1} TCFC, 0.1 M NaCl, 0.5 mV.s^{-1} scan rate. Error bars represent the minimum and maximum values obtained in at least three repeats.

B.2.5: Summary

The cathodic polarization behavior of acidic CO_2-saturated solutions at pH 4.0 was investigated on 99.99 wt.% pure iron, 316L stainless steel, and API 5L X65 mild steel surfaces, using a conventional three electrode glass cell and a thin channel flow cell. The charge transfer controlled currents were observed most clearly at high flow rates and lower temperatures achieved in the thin channel flow cell. The cathodic currents obtained on all three substrates showed no indication of direct reduction of carbonic acid up to pCO_2=5 bar. The comparison of the polarization behavior on the three substrates showed a significant difference in their electro-catalytic activity when it comes to H^+ reduction, with the API 5L X65 mild steel being most active, followed by 316L stainless steel, and with 99.99 wt.% pure iron being least active.

Chapter B.3: The mechanism and prediction of CO_2 corrosion

B.3.1: Introduction

Based on the knowledge gap and the scope of work defined in the last two chapters, this chapter expands the discussion of the CO_2 corrosion of mild steel in two directions. First, the experimental conditions were extended in order to validate the previous mechanistic findings and examine their implications on the observed corrosion rates. Second, a comprehensive mathematical model developed based on these new mechanistic findings is introduced, in order to quantitatively examine its ability to represent the experimental data and, ultimately, predict the corrosion rates in such systems.

B.3.2: Background

The mechanistic understanding of CO_2 corrosion as it relates to that observed in oil and gas production and transmission facilities has evolved significantly over the last 50 years. Amongst numerous studies in the literature, a few can be identified as milestones in our understanding of this process. The well-known studies by de Waard and Milliams are amongst the earliest that addressed the significance of CO_2 in the acidic corrosion of pipeline steel [19,105]. The authors provided mechanistic explanations for corrosion in the presence of CO_2, suggesting that corrosion in CO_2-saturated brines is defined mainly by the rate of carbonic acid (H_2CO_3) reduction as the predominant corrosive species. The authors also introduced their renowned model for prediction of corrosion rate, which gained general acceptance and is still in use to this date. Considering the current understanding of CO_2 corrosion, their proposed mechanism and

associated model suffer from many deficiencies, as discussed elsewhere [43,55,60].

Nevertheless, the reduction of carbonic acid as proposed by the authors became the center

point of the CO_2 corrosion mechanism in numerous subsequent studies.

A study by Schmitt and Rothmann published in 1977 was also a large step

forward in the understanding of CO_2 corrosion [107]. With a focus on limiting current

densities, the authors demonstrate the significance of the homogeneous CO_2 hydration

reaction. It was shown that the limiting currents in CO_2-saturated acidic solutions consist

of the mass transfer of H^+, the mass transfer of H_2CO_3, and the kinetically controlled CO_2

hydration reaction. The hydration reaction is indeed a major process that distinguishes the

CO_2 corrosion from corrosion in strong acid solution or those of other weak acids, such

as carboxylic acids and hydrogen sulfide.

The first mechanistic model of CO_2 corrosion was introduced by Gray et al. in

1989 [14]. The significance of this study was in its success in developing a corrosion rate

predictive model using a mechanistic description of the underlying electrochemical

processes. Additionally, the effect of flow and the CO_2 hydration reaction was

incorporated in the rate calculations. This study was a demonstration of how the proposed

mechanism of CO_2 corrosion could quantify the observed electrochemical and corrosion

rate behaviors. The established mechanism of CO_2 corrosion in this study has been

widely accepted ever since. In this mechanism, the iron dissolution is the anodic reaction,

and the reduction of H^+ and H_2CO_3 are the two cathodic reactions, while the concertation

of H_2CO_3 at the surface was also buffered by the CO_2 hydration reaction.

Nevertheless, it was only after the introduction of more comprehensive mathematical models [15,44–46] that the true significance of the homogeneous chemical reaction of the H_2O/CO_2 system on the electrochemical behavior and the corrosion rates was understood. In these calculations, the chemistry of the H_2O/CO_2 system is mechanistically coupled with the electrochemistry of CO_2 corrosion. These studies demonstrated the significance of homogeneous H_2CO_3 and HCO_3^- dissociation reactions. It was shown quantitatively that the cathodic limiting currents could be adequately explained, even if H_2CO_3 was not considered an electroactive species [15,45,46]. That was explained by the homogeneous dissociation of H_2CO_3 inside the diffusion boundary layer, followed by the reduction of H^+ that provides a parallel reaction pathway to the direct reduction of H_2CO_3; a process that is known as the "buffering effect" mechanism. While significant, this mechanistic observation gained little attention until recently [11,50] (see Chapter B.2:). In fact, this observation undermines the conventional CO_2 corrosion mechanism developed based on earlier works, such as those of de Waard and Milliams [19,105], Schmitt and Rothmann [107], and Gray et al.[14,103] that were based on the analysis of cathodic polarization behavior at or close to limiting currents.

In more recent years, the mechanistic role of H_2CO_3 has been further investigated. The existing ideas were distinguished by the direct reduction of carbonic acid (known as the "direct reduction mechanism") and the so-called "buffering effect mechanism" that signifies the homogeneous dissociation of H_2CO_3. It is important to note that the two above roles of H_2CO_3 are not mutually exclusive, as they are two inherently different processes. H_2CO_3 as weak acid is involved in a chemical equilibrium in an aqueous

solution, therefore at limiting current conditions where the surface pH is increased the equilibrium shifts toward dissociation in order to balance ("buffer") the H^+ ion concentration. Such a process would result in an increased limiting current, mutually occurring for all weak acids, for example, in the case of acetic acid as demonstrated previously [12,62,201]. The extent of this buffering ability is defined by the kinetics and the equilibrium properties of the individual weak acid. For the case of H_2CO_3, the relatively low equilibrium constant (pK_a=3.5) and the fast kinetics of dissociation ($k=10^8$ s^{-1}) suggest that nearly all of the H_2CO_3 could dissociate at typical experimental and industrial conditions. In addition to that, direct reduction considers H_2CO_3 to be also electrochemically active, independent from its chemical activity.

Considering the discussion above, the buffering ability of H_2CO_3 as a weak acid is definite, and the mechanistic question here is whether H_2CO_3 is also electrochemically active or not. The experimental difficulty in examination of this aspect arises from the fact that H_2CO_3 is a strong buffer, meaning that it would readily dissociate as H^+ concentration at the electrode surface decreased as compared to that in the bulk solution under mass transfer limited conditions. Hence, the current response of the system is nearly identical under mass transfer limitations, whether H_2CO_3 is electrochemically active or not, as noted in the previous studies [15,43,45,46,61]. The electrochemical activity of H_2CO_3 can only be reasonably discussed by investigating the pure charge transfer controlled cathodic current densities based on the same hypothesis as used previously [12,43,50,61]. That is, if H_2CO_3 were a significant electro-active species, the charge transfer controlled currents would increase by increasing its concentration (i.e., increasing pCO_2)

at a fixed pH where the rate of H^+ reduction was maintained constant. On the other hand, if the charge transfer controlled currents remain unchanged as the pCO_2 was increased, it can be concluded that the H_2CO_3 reduction is insignificant as compared to that of H^+ reduction. Despite the simple hypothesis and required measurement techniques, the main obstacle in verification of this hypothesis is the experimental conditions where the pure charge transfer controlled current can be observed clearly.

The electrochemical activity of H_2CO_3 has been the subject of a few studies in more recent years, as discussed in more detail in Chapter B.2: . In a study by Linter and Burstein [198], the charge transfer controlled currents at pH 4 in N_2 and CO_2 saturated solutions were observed with the aid of additional potassium hydrogen phthalate buffer. The addition of the buffer to the test solution increased the cathodic limiting current density that allowed the charge transfer controlled currents to be observed. The authors noted that no significant shift in this range of cathodic currents was observed and concluded that the H_2CO_3 is not electrochemically active. Later in 2008, Remita et al. [11] used a comprehensive mathematical model to quantify the cathodic polarization curves obtained at pH 4 and 1 bar CO_2 without considering H_2CO_3 as an electroactive species. Considering that the polarization curves were reasonably predicted by their model the authors also concluded that H_2CO_3 is not electrochemically active. Nevertheless, in both of the above mentioned studies [11,198] the limited range of the experimental results to pH 4 and 1 bar CO_2 make the generalization of the observed behavior unreasonable. At pH 4 and 1 bar CO_2, the cathodic currents are dominated with H^+ reduction and the H_2CO_3 concentration is only a fraction of that of H^+ (see Figure B.3-8), hence even if H_2CO_3 is

electrochemically active its contribution is expected to be small, which can hardly be distinguished from the typical experimental errors of the measurements. That can be also observed in the results reported previously [15,18] by the models developed based on the direct reduction of H_2CO_3, where the reduction of H_2CO_3 was shown to be only a small fraction of the total cathodic current at such conditions.

In a more experimentally extensive study Tran et al. investigated the electrochemical activity of H_2CO_3 at elevated CO_2 partial pressures up to 10 bar [50]. The authors noted that even at elevated CO_2 partial pressures the charge transfer controlled currents could not be observed in the experiments on a mild steel surface, due to the interference of the anodic iron dissolution reaction. Therefore, the experiments were carried out on a 304 stainless steel surface. With a significantly lower rate of anodic reaction on stainless steel, the authors were able to observe the charge transfer controlled currents in an extended range of current densities. This range of currents were found to be insensitive to pCO_2 up to 10 bar. Therefore, the authors concluded that the reduction of H_2CO_3 was insignificant. Although the experiments in that study were carried out in a reasonably wide range of environmental conditions, the observed mechanistic behavior on a passive stainless steel with ~ 20 wt. % Ni and ~ 10 wt. % Cr cannot be assumed to be valid on the actively corroding mild steel surface with $\sim$98 wt. % Fe, without further verifications; especially considering that the mechanism and the kinetics of the multi-step electrochemical reaction, such as the hydrogen evolution from carbonic acid, can be significantly affected by the surface properties.

In Chapter B.2: an investigation on the electrochemical activity of H_2CO_3 on 316L stainless steel, X65 mild steel and pure iron surfaces at pH 4 and CO_2 partial pressures up to 5 bar was presented. In that study, a thin channel flow cell that allowed a high flow velocity was utilized. That results in increased limiting current densities, hence, revealing the charge transfer controlled current densities. On the pure iron and stainless steel surfaces, the reported cathodic polarization curves showed a charge transfer controlled current range in an extended range of current densities, which was unaffected by increasing CO_2 partial pressures up to 5 bar. This was found to agree with the results previously reported by Tran et al. [50]. In order to examine the electrochemical activity of H_2CO_3 on an X65 mild surface directly, experiments were also conducted at 10°C that allowed the charge transfer controlled currents to be clearly observed in an extended range. The reported polarization curves showed that the charge transfer controlled current densities obtained on X65 mild steel surface were also independent from the pCO_2. Therefore, it was confirmed that the direct reduction of H_2CO_3 on a mild steel surface is insignificant for the conditions covered in that study.

The effect of CO_2 on corrosion in mildly acidic solutions is not limited to that observed in the cathodic currents. Despite decades of research dedicated to understanding of the effect of CO_2 on the cathodic currents, the effect of CO_2 on the anodic reaction has gained little attention. Nevertheless, a significant change in the behavior of the anodic iron dissolution reaction in acidic solutions has been reported in a few studies. In a study by Linter and Burstein [198], the authors reported that the rate of iron dissolution from a low alloyed steel in the transition and pre-passivation range is significantly increased in the

presence of 1 bar CO_2. In another study, Nesic et al. [74] investigated the behavior of the iron dissolution reaction in the vicinity of the corrosion potential. The authors reported a linear increase of the anodic exchange current densities with pCO_2. This effect was found to reach its maximum as pCO_2 approached 1 bar. The authors suggested that the carbonate species would enhance the rate of iron dissolution by forming a chemical ligand with the intermediate hydroxides of the iron dissolution.

As it appears from the above short review of the literature, the understanding of the mechanism of CO_2 corrosion has significantly evolved in the last few years. In order to further elucidate the mechanism of CO_2 corrosion, the present study expands on that covered in Chapter B.2: by extending the experimental conditions and also by introducing a comprehensive mathematical model based on the latest mechanistic observations. This approach allowed for a comprehensive quantitative examination of the proposed mechanisms, both as they relate to the electrochemical activity of H_2CO_3 and also the effect of CO_2 on the iron dissolution reaction. Additionally, the performance of the model to estimate the corrosion rates was examined.

B.3.3: Materials and methods

The experiments were conducted in a thin channel flow cell test apparatus similar to that used in Chapter B.2: . This test apparatus consists of a 200 L reservoir, a high power centrifugal pump, a heat exchanger, the thin channel flow test section, and a benchtop bypass flow configuration to allow pH measurement and adjustment, as shown in Figure B.3-1. All the components in this experimental apparatus are made of 316L stainless steel.
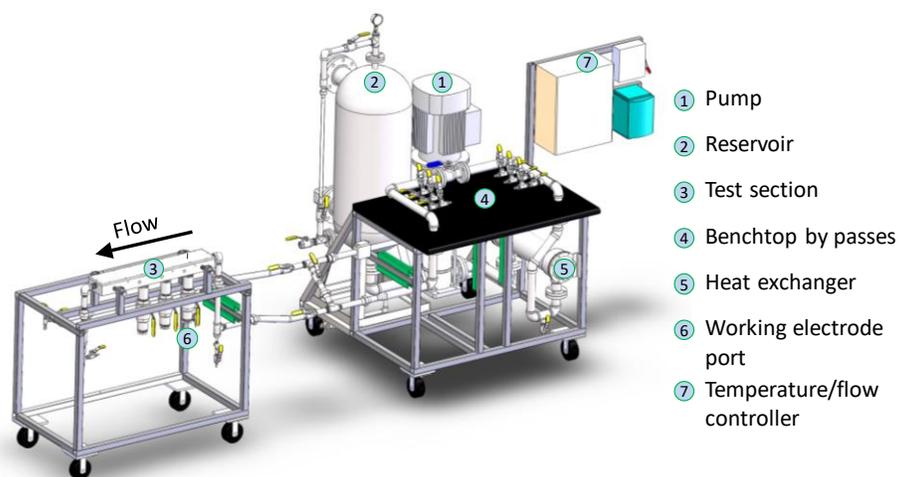
Figure B.3-1. The schematics of the thin channel flow test apparatus.

The thin channel test section has an interior height of ~3.57 mm (9/64 inch) and width of 8.89 cm (3.5 inch). The electrochemical measurements were done using a three-electrode arrangement with the cell structure serving as the counter electrode, and a house built silver/silver chloride reference electrode placed across the working electrode, as shown in Figure B.3-2. The performance of the reference electrode was examined prior to each test using a saturated calomel electrode, showing a reasonably consistent value throughout the experiments. The flow velocity inside the test section was maintained at about 12.9 m.s^{-1} in all the experiments by fixing the pump output to ~4.1 L.s^{-1} (65.0±0.5 gal.min^{-1}).
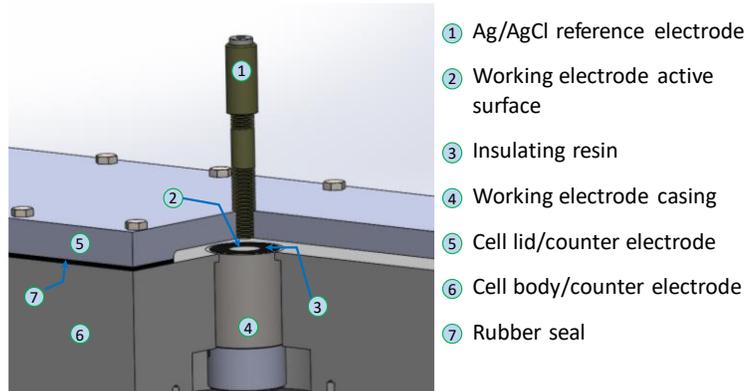
Figure B.3-2. The schematics of the electrode arrangement inside the thin channel flow cell.

The experiments were conducted using a 0.1 M NaCl supporting electrolyte (110 L) made of deionized water and analytical grade chemicals. The solution is deoxygenated prior to each test using CO_2 or N_2 gas depending on the experiments, for at least 2 hr. Meanwhile, the oxygen content of the outlet gas was monitored with an Orbisphere 410 oxygen sensor. The deoxygenation step was continued until the dissolved oxygen concentration fell below 3 ppb_m. In high-pressure experiments, this step is continued by pressurizing the system to 5 bar using CO_2 gas. The procedure was continued only after equilibrium at this high pressure was achieved. The constant pH and pCO_2 readouts were considered as the criteria for the equilibrium. This step was followed by pH adjustment, done by injection of deoxygenated HCl or NaOH solutions from a secondary 0.5 L reservoir placed on a bypass line. The pH was monitored throughout the experiments using an in-line high-pressure pH probe (Omega PHE-3431).

The working electrode assembly (shown in Figure B.3-2) was made of a disk (15.87 mm (5/8 inch) diameter) API 5L X65 mild steel specimen with the chemical composition shown in Table B.3-1. The specimen was placed inside the stainless steel

casing with epoxy resin insulation in between. Prior to each experiment, the working electrode was abraded using 600 grit silicon carbide paper, rinsed and sonicated in isopropanol, and dried using N_2 gas. The working electrode was then immediately flush mounted into the test section. After sealing, the test section was purged using CO_2 or N_2 gas, and pressurized up to the working pressure of the tank, whenever necessary. The solution temperature was controlled within ±0.5°C by using a jacketed immersion heater located in the tank and covered cartridge heaters to directly heat the test section (for experiments conducted at 30°C) as well as a shell and tube heat exchanger connected to a chiller (Air-3000 FLUID CHILLERS Inc.) for experiments done at 10°C.

Table B.3-1. Chemical composition of the X65 mild steel in wt.%.

S	P	V	C	Cr	Mo	Si	Ni	Mn	Fe
0.009	0.009	0.047	0.13	0.25	0.16	0.26	0.29	1.16	Balance

After exposing the electrode to the test solution, the open circuit potential (OCP) was monitored for 20 minutes to assure that a steady value was reached (maximum of ±2mV drift in 5 min) prior to initiating polarization measurements. The cathodic and anodic polarization curves were obtained in separate experiments by sweeping the potential from OCP towards more negative and positive values, respectively. The measurements were performed using staircase voltammetry at 0.5 mV.s^{-1} scan rate and 1 s^{-1} sampling period. The reported polarization curves were corrected for Ohmic drop with the solution resistance obtained by electrochemical impedance spectroscopy (EIS) measurements (at OCP, AC potential perturbation of 5 mV, frequency range 100kHz to

0.2 Hz at 10 points/dec) performed 15 min after polarization measurements, when a steady OCP was established. The linear polarization resistance measurements (LPR) were also performed in separate experiments following the above mentioned preparation procedure. The measurements were done in a ±5 mV vs. OCP range, using 0.125 $mV.s^{-1}$ scan rate and 1 s^{-1} sampling period.

B.3.4: Results and discussion

The experimental data was obtained in the thin channel flow cell (TCFC) described in the previous section. As compared to the conventional glass cell and also autoclave experimental apparatuses, the TCFC has two main advantages. First, it allows the experiments to be conducted under well-defined, high flow velocities. This capability allows the limiting current densities in polarization curves to be increased, thus enhancing the ability to investigate the behavior of the charge transfer controlled currents. Second, the TCFC test apparatuses used in the present study allows experiments to be conducted at up to 5 bar pCO_2. Hence, the comparison of the charge transfer controlled currents can be made not only with those obtained under N_2 atmosphere, but also with the polarization curves obtained with CO_2 present at an elevated pressure. As discussed above, one of the main challenges of the mechanistic investigation of CO_2 corrosion directly on a mild steel surface is the difficulty of obtaining reliable experimental data that clearly show the electrochemically controlled response of the system. The abovementioned advantages of the TCFC make this type of test apparatus very appealing for the purposes of this study.

The polarization curves obtained on a API 5L X65 mild steel surface at pH 4 and pH 5 are shown in Figure B.3-3.A and Figure B.3-3.B, respectively, where a significant influence of pCO_2 was observed on both the cathodic and the anodic current densities. At both pH 4 and pH 5, the presence of CO_2 linearly increased the cathodic limiting current densities, as expected. The cathodic current densities, on the other hand, have a distinct behavior for the results obtained at pH 4 as compared to those at pH 5. The cathodic polarization curves at pH 4 showed a linearly increasing range of current densities just below the OCP. That is the indication of a charge transfer controlled cathodic current range, which can be used to discuss the underlying electrochemical mechanisms. This range of current densities was found not to be significantly affected by the pCO_2. This is expected if carbonic acid is not significantly electro-active, hence increasing its concentration (by increasing pCO_2) does not affect the cathodic current when it is controlled by the rate of electrochemical reactions. This behavior was found to be in agreement with that reported previously by Tran et al. [50] on a stainless steel surface, and also in Chapter B.2: of this dissertation. However, the cathodic currents obtained at pH 5 were fully under mass transfer control even at pCO_2=5, which would not allow for verification of the mechanistic behavior observed at pH 4.
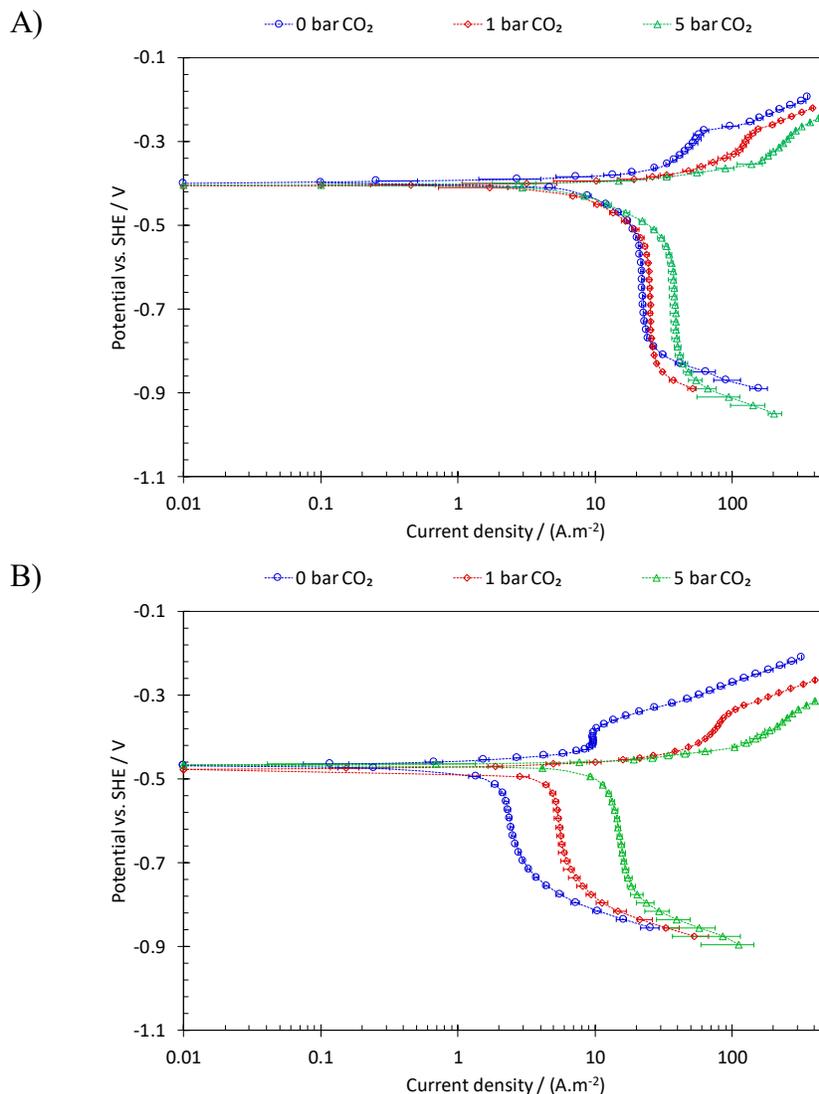
Figure B.3-3. The anodic and cathodic polarization behavior of API 5L X65 mild steel in acidic solutions, at 30°C, 12.9 m.s^{-1} flow velocity, 0.1 M NaCl, and varying pCO$_2$. A) at pH 4. B) at pH 5.

Over the anodic current range, the polarization curves showed a significant effect of pCO$_2$ on the electrochemical behavior of the iron dissolution reaction. The anodic polarization curves in neither condition shows a linear range that could be associated with the active dissolution of iron, as suggested by El Miligy et al. [72]. The observed behavior is perhaps best categorized under transition and the pre-passivation ranges[72], while the active dissolution range was covered by the cathodic currents. The transition range,

indicated by the observed current maximum in the anodic range, and the pre-passivation range, indicated by the linearly increasing current densities after the current arrest, were found to be significantly increased as pCO_2 was increased. The significance of this effect is best seen in the polarization curves obtained at pH 5. At this condition, the anodic currents were increasing hand in hand with the cathodic limiting current densities. That forces the corrosion current to remain under mass transfer limitation, even though its value is increased at elevated pCO_2.

The effect of CO_2 on the iron dissolution reaction is perhaps one of the least studied aspects of uniform CO_2 corrosion. Even in the few available studies addressing this subject, a rather inconsistent behavior was reported as discussed in more detail elsewhere [210]. The significant increase of the anodic reaction rate in the transition and pre-passivation ranges appears to be in agreement with the results reported previously by Linter and Burstein.[198] In that study, the authors suggested that the increased rate of iron dissolution was a result of the destabilization of the "passive" layer, as surface $Fe(OH)_2$ or Fe_2O_3 species, through a chemical attack by bicarbonate ion, similar to that proposed for the alkaline pH range[140,211,212]. Such an explanation may not be assumed to be valid for the conditions of the present study, considering that the formation of such a passive layer on a mild steel surface is not thermodynamically favored at the pH and potential range of interest [213].

The effect of pCO_2 on the corrosion rates at pH 4 and pH 5 is shown in Figure B.3-4. The general trend of corrosion rates vs. pCO_2 was found to agree well with the mechanistic discussion above. At pH 4, the cathodic currents were under charge transfer

control; hence, corrosion rates show only a slight increase as pCO_2 was increased from 0 to 5 bar. The slight increase of corrosion rate could, in part, be explained by the influence of CO_2 on the anodic reaction. On the other hand, at pH 5 corrosion rates were significantly influenced by pCO_2, where almost a five-fold increase was observed by increasing the pCO_2 from 0 to 5 bar. Considering the polarization curves obtained at the similar conditions (Figure B.3-3.B), the corrosion currents were significantly influenced by the limiting current densities at all conditions. Hence, the increased corrosion rates are the result of increased limiting currents, as well as the increased rate of the anodic reaction.

In our further attempt to improve the mechanistic arguments above, a set of experiments at a lower temperature (10°C) were considered in the present study. Decreasing the temperature was expected to influence the observed polarization curves by disproportionally decreasing the rate of charge transfer reactions as compared to the limiting current. Such behavior would allow the charge transfer cathodic currents and the anodic currents at the active dissolution range to be observed more clearly, hence enhancing the mechanistic arguments developed in the present study.
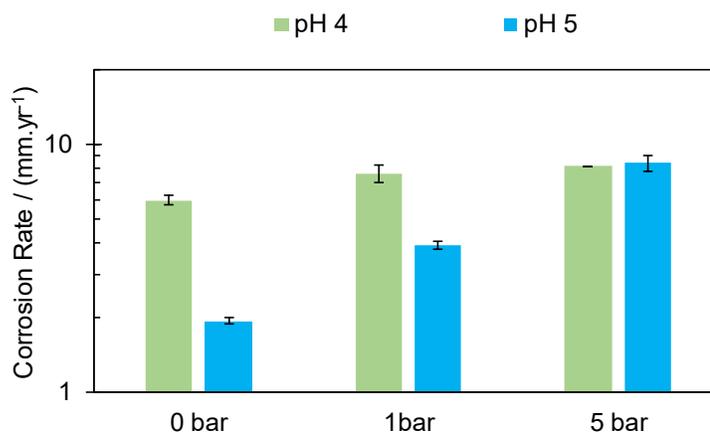
Figure B.3-4. The measured corrosion rates on API 5L X65 mild steel in acidic solutions, at 30°C, 12.9 m.s^{-1} flow velocity, 0.1 M NaCl, and varying pH and pCO$_2$.

The polarization curve obtained on X65 mild steel under a N$_2$ atmosphere at pH 4 and 10°C is compared with that obtained at 30°C, as shown in Figure B.3-5. The results were in agreement with the expected behavior, where a clear Tafel behavior observed over the cathodic currents, indicating a charge transfer controlled cathodic current range. Moreover, the anodic current densities exhibit a linear range just above the OCP, which corresponds to the active iron dissolution range. The clear separation between the cathodic and anodic currents observed at this lower temperature provides a great opportunity for better understanding of the effect of CO$_2$ on the electrochemical behavior of this system.
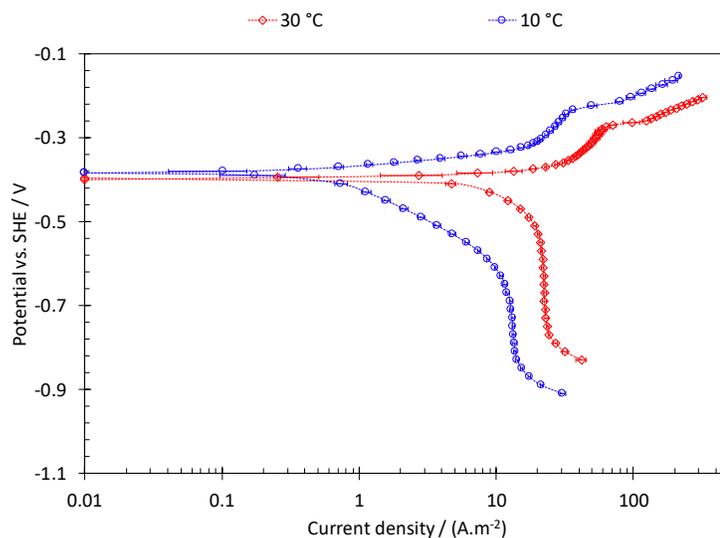
Figure B.3-5. The effect of temperature on the observed polarization behavior of API 5L X65 mild steel in N_2-saturated acidic solutions at pH 4, 12.9 m.s^{-1} flow velocity, 0.1 M NaCl.

The effect of pCO_2 on the observed polarization behavior at pH 4 and pH 5 was re-examined at 10°C, as shown in Figure B.3-6. At pH 4, the charge transfer controlled cathodic currents were observed clearly at an extended potential range. The behavior of cathodic currents with pCO_2 was in complete agreement with that observed at 30°C in Figure B.3-3.A. The experimental data obtained at pH 5 also showed a similar range of current densities that was not significantly affected by increasing the pCO_2 from 1 to 5 bar. This observation further solidifies the abovementioned mechanistic arguments that carbonic acid is not a significantly electroactive-species. It is noteworthy that at pH 5 and 5 bar CO_2 the concentration of carbonic acid is about 40 fold higher than that of H^+.

A)

B)
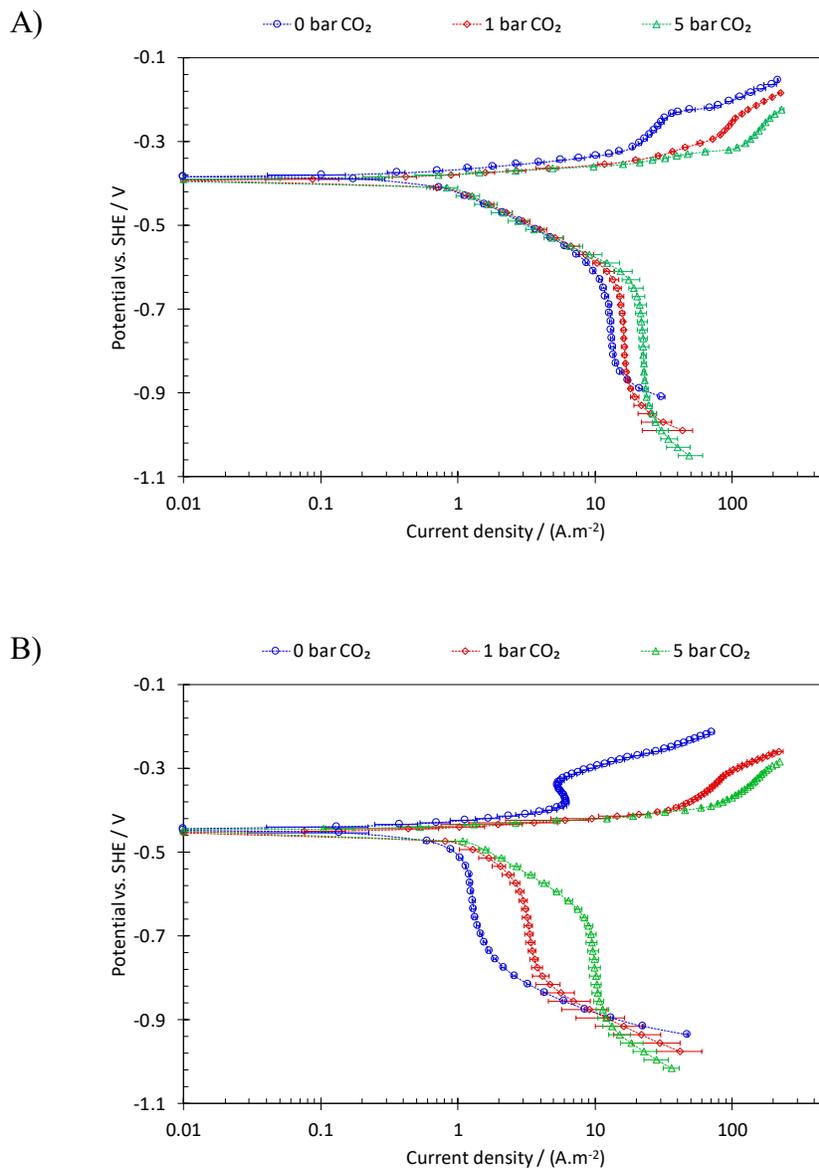
Figure B.3-6. The anodic and cathodic polarization behavior of API 5L X65 mild steel in acidic solutions, at $10^{o}C$, 12.9 m.s^{-1} flow velocity, 0.1 M NaCl, and varying pCO_2. A) at pH 4. B) at pH 5.

Over the anodic current range, the polarization curves obtained at $10^{o}C$ clearly demonstrate a range of linearly increasing anodic currents associated with the active dissolution range, in addition to the transition and pre-passivation ranges. The electrochemical behavior at the pre-passivation range is similar to that observed at $30^{o}C$. In the active dissolution range, the presence of CO_2 led to observation of a slightly

decreased Tafel slope, when compared to the polarization curves obtained under a N_2 atmosphere at the same pH. The decrease in the Tafel slope in this range was not intensified at higher CO_2 partial pressures.

The observed influence of CO_2 on the anodic reaction in the active dissolution range was found to partially agree with the results reported by Nesic et al. [74]. In that study [74] the authors investigated the effect of CO_2 on the anodic polarization curves in a narrow potential range (~100 mV) above the corrosion potential. The proposed mechanism by Nesic et al. [74] suggests that CO_2 is actively engaged in the electrochemistry of iron dissolution by directly adsorbing onto the metal surface in a chemical ligand replacement interaction that replaced the ferrous hydroxide intermediate species. The authors suggest that the presence of CO_2 increased the exchange current densities, increasing with a linear proportionality to pCO_2 up to 1 bar. Furthermore, it was noted that as pCO_2 approached 1 bar, the effect of CO_2 reaches its maximum and the rate of the anodic reaction was not further increased with increasing pCO_2. The trend in the present study also suggests that the presence of CO_2 resulted in an increased rate of reaction which was not further intensified at pCO_2 greater than 1 bar. However, in the present study the effect appears to be in the form of a slight decrease in the apparent Tafel slope.

The corrosion rates obtained for pH 4 and pH 5 at 10°C are shown in Figure B.3-7. These values are generally about an order of magnitude smaller than those obtained at 30°C. The corrosion rates reported here show only a small dependence of pCO_2. As is clearly observed in the polarization curves of Figure B.3-6, at 10°C the cathodic currents are under charge transfer control; hence increasing pCO_2 does not result

in higher cathodic currents, as expected based on the mechanistic arguments above. Additionally, the anodic reaction in the vicinity of OCP was under the active dissolution range, which was only slightly affected by pCO_2. Considering this behavior, the observed trend of corrosion rates vs. pCO_2 in Figure B.3-7 was found to be consistent with what is expected. Unlike those observed at 30°C for pH 5, at 10°C the corrosion rates were also found to be mostly insensitive to pCO_2, due to the absence of the direct H_2CO_3 reduction reaction.
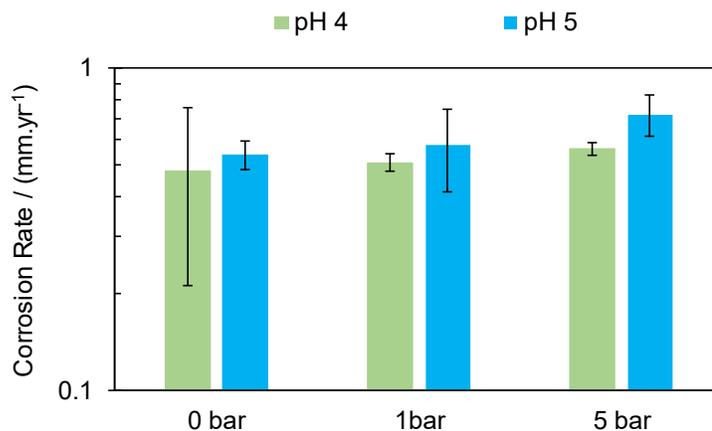
Figure B.3-7. The measured corrosion rates on API 5L X65 mild steel in acidic solutions, at 10°C, 12.9 m.s^{-1} flow velocity, 0.1 M NaCl, and varying pH and pCO_2.

B.3.5: Quantitative analysis

B.3.5.1: Solution speciation

The calculation of the solution composition is a primary step in mathematical modeling of CO_2 corrosion and the estimation of corrosion rates. The primary objective in such a calculation is to determine the solution speciation, as dictated by the equilibria associated with H_2O/CO_2 system. The water/CO_2 equilibria includes the steps from CO_2

dissolution, hydration and dissociation reactions as well as water dissociation as shown

by Reactions (B.3-1) through (B.3-5).

$$CO_{2(g)} \leftrightharpoons CO_{2(aq)} \qquad\qquad\qquad\qquad\qquad\qquad\qquad\text{(B.3-1)}$$

$$CO_{2(aq)} + H_2O_{(l)} \leftrightharpoons H_2CO_{3\,(aq)} \qquad\qquad\qquad\qquad\qquad\text{(B.3-2)}$$

$$H_2CO_{3(aq)} \leftrightharpoons HCO_{3\,(aq)}^- + H^+_{(aq)} \qquad\qquad\qquad\qquad\text{(B.3-3)}$$

$$HCO_{3\,(aq)}^- \leftrightharpoons CO_{3\,(aq)}^{2-} + H^+_{(aq)} \qquad\qquad\qquad\qquad\text{(B.3-4)}$$

$$H_2O_{(l)} \leftrightharpoons OH^-_{(aq)} + H^+_{(aq)} \qquad\qquad\qquad\qquad\qquad\text{(B.3-5)}$$

In a generic formulation, the single phase chemical equilibrium for any reaction j,

with n_r reactants (R) and n_p products (P), in the form of:

$$\sum_{m=1}^{n_r} R_m \rightleftharpoons \sum_{n=1}^{n_p} P_n \qquad\qquad\qquad\qquad\qquad\qquad\text{(B.3-6)}$$

is expressed as Equation (B.3-7) for an ideal solutions:

$$\frac{\prod_{n=1}^{n_p} c_{P_n}}{\prod_{m=1}^{n_r} c_{R_m}} = \frac{k_{f,j}}{k_{b,j}} = K_j \qquad\qquad\qquad\qquad\qquad\text{(B.3-7)}$$

where c_i is the concentration of the chemical species i, K_j is the equilibrium constant of

reaction j, and $k_{f,j}$ and $k_{b,j}$ are the kinetic rate constants associated with the forward and

backward reactions involved in each equilibrium. Equation (B.3-7) can be used to

represent the equilibrium of Reactions (B.3-1) to (B.3-5).

The phase equilibrium of CO_2 dissolution in water (Reaction (B.3-1)) can be

expressed based on Henry's law, assuming an ideal solution:

$$\frac{\phi_{CO_2} p_{CO_2}}{c_{CO_2}} = K_{H,CO_2} \qquad\qquad\qquad\qquad\qquad\text{(B.3-8)}$$

where ϕ_{CO_2} and p_{CO_2} are fugacity coefficient and partial pressure of CO_2, respectively,

and K_{H,CO_2} is the Henry's constant. The fugacity coefficient of CO_2 can be obtained using

the empirical equations reported by Duan et al.[214] as shown in Table B.3-2. This

expression was shown to agree well with the iterative fugacity calculations based on a

fifth order virial equation of state[214,215], and it allows for simple, explicit calculation of

this parameter. In the conditions of this study the partial pressure of CO_2 in the CO_2/H_2O

gas phase is $P_{CO_2} = P_{tot} - P_{ws}$, with P_{tot} being the total pressure of the system and P_{ws}

being the saturation pressure of water that was obtained from the empirical relationship

shown in Table B.3-2.

In the literature on the equilibrium and speciation of the CO_2/H_2O system it is

customary to lump the concentration of the dissolved CO_2 with carbonic acid to define

$C_{CO_{2(aq)}^*} = C_{CO_{2(aq)}} + C_{H_2CO_{3(aq)}}$. Therefore, the equilibria is discussed in term of

Reaction (B.3-9) and Reaction (B.3-10), where carbonic acid is not considered

explicitly.

$$CO_{2(g)} \rightleftharpoons CO_{2(aq)}^* \qquad\qquad\qquad\qquad (\text{ B.3-9 })$$

$$CO_{2(aq)}^* + H_2O_{(l)} \rightleftharpoons HCO_{3\ (aq)}^- + H^+_{\ (aq)} \qquad\qquad\qquad\qquad (\text{ B.3-10 })$$

The corresponding reported equilibrium constants (denoted by asterisk) are therefore

expressed as:

$$K_{H,CO_2^*}^* = \frac{\phi_{CO_2} p_{CO_2}}{c_{CO_2^*}} \qquad\qquad\qquad\qquad (\text{ B.3-11 })$$

$$K_{Ca}^* = \frac{c_{HCO_{3\ (aq)}^-} c_{H^+(aq)}}{c_{CO_{2(aq)}^*}} \qquad\qquad\qquad\qquad (\text{ B.3-12 })$$

However, the effect of hydration reaction can be readily incorporated into these expressions in order to obtain the true equilibrium constants, required for the water chemistry calculation in the CO_2 corrosion context. The relationship between the K^* values and the true equilibrium constants can be obtained with a simple mathematical manipulation:

$$K_{H,CO_2} = \left(1 + K_{hyd}\right) K^*_{H,CO_2^*} \qquad\qquad (\text{B.3-13})$$

$$K_{Ca} = (1 + {1}/{K_{hyd}}) K^*_{Ca} \qquad\qquad (\text{B.3-14})$$

The Henry's constant as well as the equilibrium constants for carbonic acid, bicarbonate ion and water dissociation reactions are listed in Table B.3-2. The Equilibrium constant of the CO_2 hydration (Reaction (B.3-2)), K_{hyd}, is perhaps the one constant that is known with the least confidence. There have been a number of different studies addressing this parameter [90,97,208,216–218]. The early literature on this parameter was reviewed by Kern[217] with reported values being shown to be scattered in a rather wide range. The commonly used value of $K_{hyd} = 2.58 \times 10^{-3}$ [15,219,220] is, in fact, at the higher end of the reported values range. The reason could be that it was obtained based on the value of pKca=3.76 (see Equation (B.3-14)) reported by Wissbrun in 1954[221]. Recent studies[208,222,223] suggest that the pKca (= 3.40 – 3.50) is significantly lower than that reported by Wissbrun[221]. The discrepancies of reported pKca values, and hence the K_{hyd}, are mostly due to the strong influence of solution non-idealities, in addition to the inherent measurement uncertainties. However, the K_{hyd} can also be obtained from the forward and backward kinetic rate constants of the hydration reaction. Since this reaction only involves neutral species, the effect of having a non-ideal solution is minimal; hence,

the reported values are in that sense more reliable. In the present study a relationship

(Table B.3-2) based on a kinetic model by Wang et al. [218] was used and found to agree

reasonably well with our experimental results.

Table B.3-2. The equilibrium parameters for CO_2/H_2O system.[*]

Param.	K^*_{H,CO_2^*} † [209]	φ_{CO_2} †† [214]	K_{hyd} ††† [218]	K^*_{ca} [224] ♮	K_{bi} [224] ♮	K_w [64] ♮♮	P_{ws} [225,226] ♭
a_1[**]	1.3000 E1	1.0000	1.02E4	233.51593	-151.1815	-4.098	1.167 E3
a_2	-1.3341 E-2	4.7587 E-3	-55.7	0.0000	-0.0887	-3245.2	-7.242 E5
a_3	-5.5898 E2	-3.3570 E-6	NA	-11974.3835	-1362.2591	2.2362	-1.707 E1
a_4	-4.2258 E5	0.0000	NA	0.0000	0.0000	-3.984 E7	1.202 E5
a_5	NA	-1.3179	NA	-36.5063	27.7980	13.957	-3.233 E6
a_6	NA	-3.8389 E-6	NA	-450.8005	-29.5145	8.5641 E5	1.492 E1
a_7	NA	0.0000	NA	21313.1885	1389.0154	NA	-4.823 E3
a_8	NA	2.2815 E-3	NA	67.1427	4.4196	NA	4.051 E5
a_9	NA	0.0000	NA	0.0084	0.0032	NA	-2.386 E-1
a_{10}	NA	0.0000	NA	-0.4015	-0.1644	NA	6.502 E2
a_{11}	NA	0.0000	NA	-0.0012	-0.0005	NA	NA

*   The Equilibrium constants are based on molal concentrations. Appropriate unit conversion should be considered if necessary.

**   The a_i values are rounded to four digits after the decimal.

† $\ln\left(K^*_{H,CO_2^*}\right) = a_1 + a_2 T + \dfrac{a_3}{T} + \dfrac{a_4}{T^2}$

†† $\phi_{CO_2} = a_1 + \left[a_2 + a_3 T + \dfrac{a_4}{T} + \dfrac{a_5}{T-150}\right] P + \left[a_6 + a_7 T + \dfrac{a_8}{T}\right] P^2$

††† $K_{hyd} = 55.6\ exp(\dfrac{-a_1 + a_2\,T}{RT})$

♮ $\ln(par.) = a_1 + a_2\,T + \dfrac{a_3}{T} + \dfrac{a_4}{T^2} + a_5\,\ln(T) + \left(\dfrac{a_6}{T} + \dfrac{a_7}{T^2} + \dfrac{a_8}{T}\ lnT\right)$
$\qquad + \left(\dfrac{a_9}{T} + \dfrac{a_{10}}{T^2} + \dfrac{a_{11}}{T}\ lnT\right)(p - p_s)^2$

P$_s$=1 if T<373.15, P$_s$=P$_{ws}$ if T>373.15.

♮♮ $-\log(K_w) = a_1 + \dfrac{a_2}{T} + \dfrac{a_3}{T^2} + \dfrac{a_4}{T^3} + \left(a_5 + \dfrac{a_6}{T} + \dfrac{a_7}{T^2}\right)\log(10^{-3}\rho_w)$

♭ $P_{ws} = 10\left[\dfrac{2C}{-B + (B^2 - 4AC)^{0.5}}\right]^4$

$A = \theta^2 + a_1\theta + a_2\ ;\ B = a_3\theta^2 + a_4\theta + a_5\ ;\ C = a_6\theta^2 + a_7\theta + a_8;\ \theta = T + \dfrac{a_9}{T-a_{10}}$

In addition to the equilibrium relationships of the CO_2/H_2O system, in the absence of an electric field, the concentration of ions must also satisfy the charge balance as shown by Equation (B.3-15).

$$\sum_i z_i C_i = 0 \qquad\qquad (\text{B.3-15})$$

In the case of the present study, where the solution pH and the pCO$_2$ are known, the solution speciation can be obtained from the relationships describing the chemical equilibria and the electroneutrality equation. This system of equations can be expressed in matrix format in the form of Equation (B.3-16), so that the solution speciation can be directly obtained by calculating the inverse of the coefficient matrix (Equation (B.3-17)).

$$[A].[C] = [S] \qquad\qquad (\text{B.3-16})$$

$$[C] = inv([A]).[S] \qquad\qquad (\text{B.3-17})$$

An example of one such calculations is shown in Equation (B.3-18) which, on top of NaCl, also includes the concentration of NaOH that is required to reach the specified pH. Figure B.3-8 illustrates the solution speciation obtained following the above procedure at 1 bar and 5 bar CO$_2$.

$$
\begin{bmatrix}
1 & 0 & 0 & 0 & 0 & 0 & 0 & 0 & 0 & 0 \\
0 & 0 & 1 & 0 & 0 & 0 & 0 & 0 & 0 & 0 \\
1 & -K_{H,CO_2} & 0 & 0 & 0 & 0 & 0 & 0 & 0 & 0 \\
0 & -K_{hyd} & 0 & 1 & 0 & 0 & 0 & 0 & 0 & 0 \\
0 & 0 & 0 & -K_{ca} & 10^{-pH} & 0 & 0 & 0 & 0 & 0 \\
0 & 0 & 0 & 0 & -K_{bi} & 10^{-pH} & 0 & 0 & 0 & 0 \\
0 & 0 & 0 & 0 & 0 & 0 & 10^{-pH} & 0 & 0 & 0 \\
0 & 0 & 1 & 0 & -1 & -2 & -1 & -1 & 1 & 0 \\
0 & 0 & 0 & 0 & 0 & 0 & 0 & 1 & 0 & 0 \\
0 & 0 & 0 & 0 & 0 & 0 & 0 & 0 & 1 & -1
\end{bmatrix}
\cdot
\begin{bmatrix}
f_{CO_2} \\
c_{CO_{2(aq)}} \\
c_{H^+_{(aq)}} \\
c_{H_2CO_{3(aq)}} \\
c_{HCO_3^-{}_{(aq)}} \\
c_{CO_3^{2-}{}_{(aq)}} \\
c_{OH^-{}_{(aq)}} \\
c_{Cl^-{}_{(aq)}} \\
c_{Na^+{}_{(aq)}} \\
c_{NaOH_{(aq)}}
\end{bmatrix}
=
\begin{bmatrix}
p_{CO_2}\phi_{CO_2} \\
10^{-pH} \\
0 \\
0 \\
0 \\
0 \\
a_{H_2O}K_w \\
0 \\
c_{NaCl_{(aq)}} \\
c_{NaCl_{(aq)}}
\end{bmatrix}
\qquad (\text{B.3-18})
$$
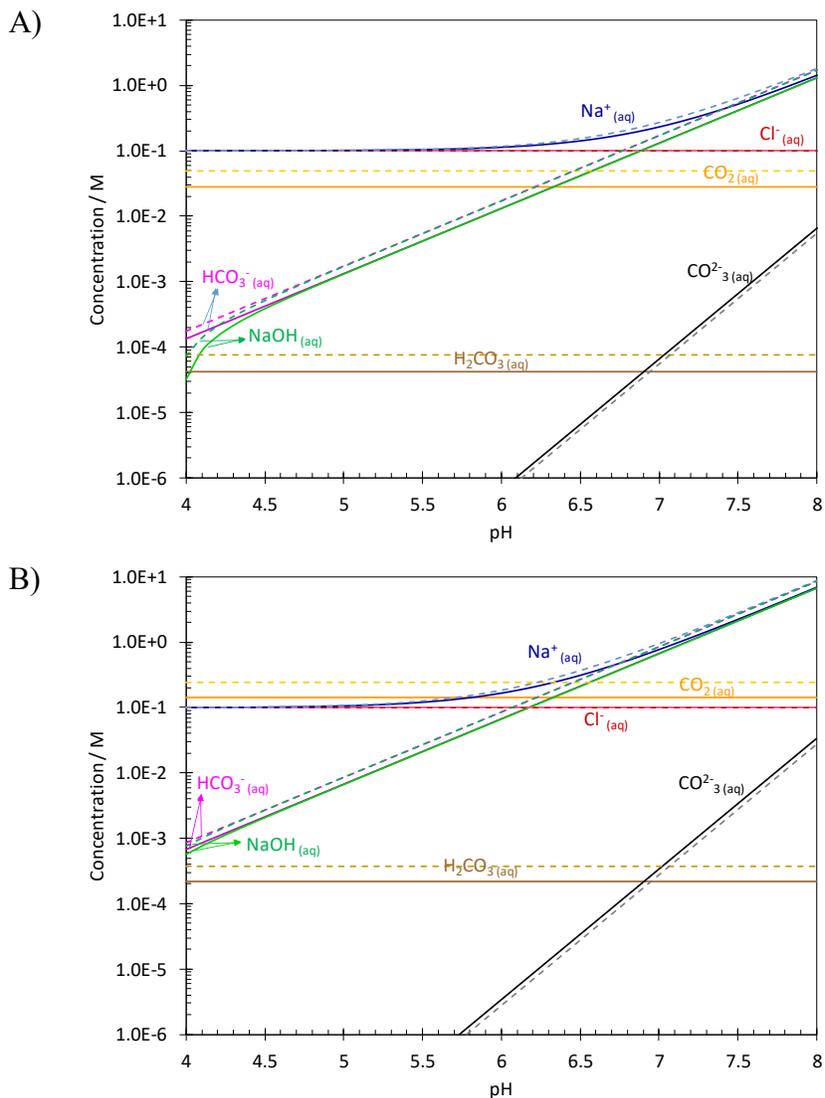
Figure B.3-8. The pH dependence of the solution speciation at 1 bar CO$_2$ (solid lines) and 5 bar CO$_2$ (dashed lines), at A) 30°C. B) 10°C. The concentration of the alkalinity required at any pH value is included in the form of NaOH.

B.3.5.2: The rate of electrochemical reactions

The present mathematical model is a quantitative approach to verify the conclusions made based on the experimental results presented above, and ultimately to use the current mechanistic understanding of CO$_2$ corrosion for estimating the corrosion rates. Hence, direct reduction of carbonic acid, as proposed in the conventional

mechanism of CO_2 corrosion, is not included in the present model. Also, the reduction of water occurs at significantly lower potentials, and it is only significant at near-neutral pH values. Therefore, the reduction of H^+ is the only cathodic reaction considered in the present model. The rate of this reaction is expressed as shown below, where $k_{0_{H^+}}$ and m_{H^+} are the reaction rate constant and the reaction order, respectively, which are estimated based on the experimental data as further discussed in the following sections.

$$i_{c,H^+} = -n_{H^+}Fk_{0_{H^+}}C_{H^+}^{S\,m_{H^+}}e^{\left(\frac{-\alpha_{H^+}F\left(E-E_{0_{H^+}}\right)}{RT}\right)} \qquad (\text{B.3-19})$$

Considering the fact that the concentration of H_2 in the solution is negligible, and also the potential range of interest in the present study, the hydrogen oxidation reaction was assumed to be insignificant and Equation (B.3-19) only represents the cathodic half reaction of the H^+/H_2 redox couple.

The rate of the anodic iron dissolution reaction in CO_2-saturated solutions is commonly expressed in terms of a simple electron transfer reaction as a single, straight anodic line [15,18,166,227]. That treatment practically presumes that the iron dissolution reaction always occurs at the active dissolution range. Considering the observed behavior in Figure B.3-3, and also those reported in the previous studies, this assumption is an oversimplification[72,74,210,228]. While it has been reported previously [74,198], the effect of CO_2 on the rate of anodic reaction is not well quantified. In a study be Nesic et al. [74], the authors proposed a series of electrochemical parameters in terms of a simple electron transfer reaction that described the rate of anodic reaction in CO_2-saturated solutions; each valid only at a certain pH range. This approach was latter used in the development of a corrosion rate predictive model by the authors [15,189,229].

The mechanism of the iron dissolution reaction in acidic solution can now be considered as one of the classic subject areas of electrochemical mechanism studies, which has been studied extensively over the last several decades [71,72,135,228,230–234]. An extensive review of the literature is beyond the scope of this study, however, interested readers can find a wealth of information in reviews dedicated to this subject [73,78]. In the classical view, iron dissolution was believed to occur either through the so-called "catalytic mechanism" or "consecutive mechanism", depending on the surface activity and microstructure of the metal substrate [71,73,78,232,234,235]. Further mechanistic studies suggest that the iron dissolution reaction occurs through a series of parallel reactions and, depending on the rate determining step, the observed behavior can be associated with either of the previously proposed mechanisms [73,228,236]. More recent studies also provide further mechanistic insights into the transition and the pre-passivation ranges of anodic iron dissolution, suggesting that the active dissolution range is followed by higher order oxidation of surface intermediate species[73,228,234,236].

Despite the advancements in the understanding of the iron dissolution mechanism, its inherent complexity has left some mechanistic aspects of this reaction controversial, more specifically when it comes to the interpretation of the observed behavior to electrochemical steps. While it is shown that the models based on the uniform surface chemistry mechanisms [71] are unable to reasonably explain the observed EIS measurements [78,228,236], the proposed alternative self-catalytic, two-electron transfer step of the "catalytic mechanism", has also been criticized [71]. This latter reaction is suggested to occur on self-reproducing "kink" sites [78,230], while their nature, and a quantitative

measure of the potential and pH dependence of their surface concentration, which are of great significant in determining the reaction rate, requires further elucidation. In a more recent publication, Lorenz et al.[234] offered some explanations in this regards that is based on the surface morphology and low dimension systems concepts.

Aside from these lingering controversies, considering the inherent complexity of the iron dissolution reaction with numerous elementary steps and intermediate species, a fully mechanistic micro-kinetic description of this process is a significant undertaking that is beyond the scope of the corrosion rate predictive model considered in the present study. Additionally, the effect of the solution composition and the presence of various anions are known to influence not only the kinetics but also the mechanism of the iron dissolution reaction[73,201,233,237]. In CO_2 solutions, the lack of a mechanistic understanding of the effect of carbonate species on the mechanism of this reaction, compounded by the non-uniformity of the steel surface and are some of the additional complexities. On the other hand, the experimental data reported in the present study in Figure B.3-5, or those in Figure B.3-3.B and Figure B.3-6.B, suggest that the corrosion current can be either in the active dissolution range or in a transition and possibly pre-passivation range. In addition to the solution pH, as discussed in part by Nesic et al. [74], that is also defined by other environmental conditions (in this case temperature). Therefore, in corrosion rate predictive models it is critical to include a mechanism that reasonably predicts the behavior of the anodic reaction and also provides a smooth transition between different anodic dissolution mechanisms.

In an attempt to quantify the observed behavior for the active dissolution, as well as those in the pre-passivation and the transition ranges, the rate of the iron dissolution reaction is expressed using a semi-empirical approach in the present study. In this approach, while the major components of the iron dissolution mechanism are accounted for, some details of the underlying mechanism are inevitably disregarded. At a high level, the iron dissolution from the active to the pre-passive range can be seen to consists of four main elements that are common in most proposed mechanisms[73,78,228,233,238]. These are: two linear ranges corresponding to active dissolution and the pre-passivation, the presence of a current maximum in the transition range, and its gradual disappearance with change in solution pH. The linearly increasing current density in the active dissolution range and that in the pre-passivation range were also clearly observed in the experimental results shown above in Figure B.3-6. Regardless of the physical explanations, the current density from these reactions (j) can be expressed as follows, considering the electrochemical nature of the reactions.

$$i_{a,j} = F k_{0,j} C_{H^+}^{s}{}^{m_{H^+,j}} e^{\left(\frac{\alpha_j FE}{RT}\right)} \hspace{3cm} (\text{ B.3-20 })$$

where kj is the kinetic rate constant, E is the potential, and α_j is the transfer coefficient (including the symmetry factor and number of the electrons in the reaction sequence), $C_{H^+}^{s}$ is the surface concentration of H^+ to represent the pH dependence of the iron dissolution with the apparent reaction order of $m_{H^+,j}$. It should be noted that Equation (B.3-20) does not represent the current/potential dependence of a single elementary reaction, rather it represents the response of a sequence of reaction steps, and the kinetic parameters are representing the apparent values.

There is an agreement in the literature that the pre-passivation range is a result of the oxidation of an existing intermediate species to higher orders [73,228,234,236]. Such processes commonly exhibit Tafel slopes lower than 2RT/nF (similar to that observed in the active dissolution range), unless the surface coverage of the oxidized intermediate species (θ) is not potential dependent, i.e., when $\theta \rightarrow 1$. The observation of a ~120 mV Tafel slope in the pre-passivation range also supports such a scenario. The concentration of this intermediate can be expressed using a generic Langmuir isotherm for an electrochemical process as Equation (B.3-21). Furthermore, such a process suggests that the 120mV range is only observed when $\theta \rightarrow 1$, where the rate of other electrochemical reactions are inevitably halted due to lack of available reaction sites. Therefore, as the third main element of the anodic polarization curve, the accumulation of this intermediate species on the surface is responsible for the "S-shaped" behavior observed in the transient range. In order to reflect the effect of this surface species, the rate of all electrochemical reactions are multiplied by (1-θ) to represent the available reactions sites for those reactions. The consistent observation of this behavior in the transition range suggests that the potential and concentration dependence of this passivating process are likely to be similar to those in the active dissolution range.

$$\theta = \frac{K_\theta C_{H^+}^{s}{}^{m_{H^+,\theta}} e^{(\frac{\alpha_\theta FE}{RT})}}{1 + K_\theta C_{H^+}^{s}{}^{m_{H^+,\theta}} e^{(\frac{\alpha_\theta FE}{RT})}} \qquad\qquad \text{(B.3-21)}$$

Nevertheless, the "S-shaped" behavior, resulting into the observed current maximum, is only present in a narrow pH range and disappears at more acidic and also in more alkaline environments. In the acidic solutions purged with N_2, the reported

experimental results above show about a 0.5 order dependence on H^+ concentration, which was found to agree well with that reported in the literature [72,234,238]. On the other hand, in the CO_2-saturated solutions the current maxima does not exhibit any significant pH dependence (Figure B.3-3 and Figure B.3-6), yet the previously reported results showed that this current maxima no longer exists at higher pH values[74].

Based on such observations, one can conclude that the active dissolution range and the current maximum, in addition to what was discussed above, is also affected by a secondary process with a rate rapidly decreasing with increasing pH. The process can be in the form of the change in the rate determining step, as noted previously [71,73,228], that reduces the rate of reaction in the active dissolution range. Hence, its corresponding rate can also be essentially expressed in the same generic form of Equation (B.3-20). The observed net rate at the active dissolution range resulting from these two processes can be estimated based on the harmonic average of both reaction rates in order to reflect the consecutive nature of these reactions. The net anodic current can therefore be expressed as Equation (B.3-22).

$$i_a = (\frac{1}{(1-\theta)i_1} + \frac{1}{(1-\theta)i_2})^{-1} + \theta i_3 \qquad \text{(B.3-22)}$$

Figure B.3-3 demonstrates the results of a mathematical simulation of the anodic polarization curve based on the above mentioned considerations for the results obtained in N_2 saturated solution, while the performance of the complete model is further discussed in the following sections. The anodic current density at the active dissolution range obtained using the harmonic average of an electrochemical process, expressed as Equation (B.3-20), with $m_{H^+,1} = -2$ and $\alpha_1 = 2$, and another with $m_{H^+,2} = 1$ and

$\alpha_2 = 1$. The Langmuir isotherm in the form of Equation (B.3-21) is represented with

$m_{H^+,\theta} = -2$ and $\alpha_\theta = 2$. And, finally, the current densities in the pre-passivation range

were obtained using $m_{H^+,3} = 0$ and $\alpha_3 = 0.5$.
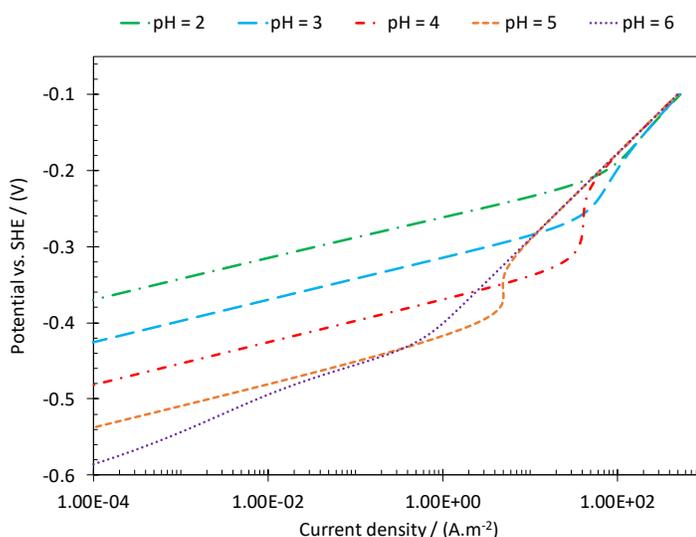
Figure B.3-9. The calculated anodic polarization curve in N_2-saturated acidic solutions at 10°C.

As shown in Figure B.3-9, the semi-empirical calculation of the anodic current

density following the abovementioned considerations is able to reflect the observed

potential and pH dependence at both the lower and higher current densities with a

reasonably predicted transition state in between. Nevertheless, some deviations,

especially in the transition state, would be expected due to the simplified mechanistic

considerations behind these calculations, which disregards the reaction steps and the

intermediate species of relatively lesser significance.

Considering that the general behavior of the anodic polarization curves are similar

in both N_2 and CO_2 saturated solutions, the anodic current density for the latter case was

also calculated using the same approach, while the observed differences, including the dependence on CO_2 concentration and the slightly lower Tafel slope in the active dissolution range was included here. The expressions for electrochemical reactions and the Langmuir isotherm were reworked for the case of CO_2-saturated solutions:

$$i_{a,j} = Fk_{0,j}{C_{H^+}^S}^{m_{H^+,j}}{C_{CO_2}^S}^{m_{CO_2,j}}e^{(\frac{\alpha_j FE}{RT})} \qquad (B.3\text{-}23)$$

$$\theta = \frac{K_\theta {C_{H^+}^S}^{m_{H^+,\theta}}{C_{CO_2}^S}^{m_{CO_2,\theta}}e^{(\frac{\alpha_\theta FE}{RT})}}{1 + K_\theta {C_{H^+}^S}^{m_{H^+,\theta}}{C_{CO_2}^S}^{m_{CO_2,\theta}}e^{(\frac{\alpha_\theta FE}{RT})}} \qquad (B.3\text{-}24)$$

Figure B.3-10 shows the results of a mathematical simulation of the anodic polarization curve for the results obtained in CO_2 saturated solutions, while the performance of the complete model is further discussed in the following sections. The current density at the active dissolution range obtained using the harmonic average of an electrochemical process with $m_{H^+,1} = -2.5$, $m_{CO_2,1} = 0$ and $\alpha_1 = 2.5$, and another with $m_{H^+,2} = 1$, $m_{CO_2,2} = 0.5$ and $\alpha_2 = 2$. The Langmuir isotherm in the form of Equation (B.3-24) is represented with $m_{H^+,\theta} = -2.5$, $m_{CO_2,\theta} = -0.5$ and $\alpha_\theta = 2.5$. And, finally, the current densities in the pre-passivation range were obtained using $m_{H^+,3} = -0.5$, $m_{CO_2,3} = 0.5$ and $\alpha_3 = 0.5$. Figure B.3-10 demonstrates the performance of the present semi-empirical approach with the change in pH and partial pressure of CO_2, as it relates to the conditions of the present study. The case of iron dissolution in CO_2-saturated solution is even more complex than that in N_2-saturated solution, with many major aspects yet to be understood. While the anodic polarization behavior is significantly influenced in the presence of CO_2, the carbonate species (CO_2, H_2CO_3, HCO_3^-, and CO_3^{2-}) responsible for such an effect cannot be explicitly identified. Due to the lack of a better

understanding, the rate expressions were represented in terms of the dissolved CO_2 concentration (Equation (B.3-23)). However, the fractional dependence and as well as the increased pH dependence may suggest that multiple carbonate species are involved. That involvement may also be through multiple (thermodynamically identical) parallel steps depending on the reactive carbonate species.

Nevertheless, the results obtained in this fashion were able to reasonably represent the general behavior observed at the conditions of the present study. The elements used in the present calculations can be modified to incorporate the new mechanistic understanding of this reaction as it becomes available, in order to improve the range of validity of the results.
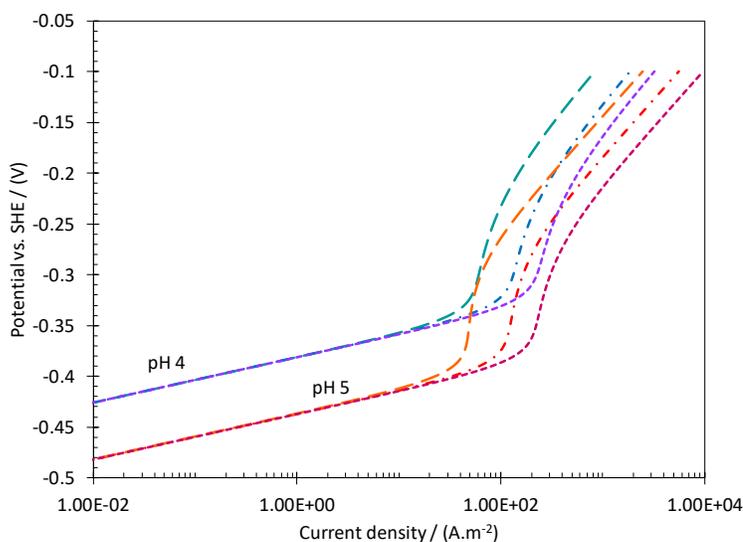
Figure B.3-10. The calculated anodic polarization curve, in CO_2-saturated acidic solutions at 10^oC, at pH 4 and 5, pCO_2=1 bar (long dashed lines), pCO_2=5 bar (dotted-dashed lines), and pCO_2=15 bar (dashed lines).

The mathematical model below is built based on only two electrochemical reactions, H^+ reduction and Fe oxidation. The rate of these reactions in aqueous acidic

solutions can be obtained as discussed above. Considering the heterogeneity of the corrosion process and the underlying electrochemical reactions, these reactions are occurring at the metal surface. These expression are therefore included in the model as the metal surface boundary condition, where the flux of the species (N_i as discussed in detail in section B.3.5.3:) at the electrode is defined by the rate of these electrochemical reactions. That can be mathematically expressed as:

$$N_i|_{x=0} = -\frac{s_{ij}i_j}{n_jF} \hspace{4cm} (\text{B.3-25})$$

Equation (B.3-25) relates the current density of reaction j (H^+ reduction or Fe oxidation) to the flux of the involved electroactive species at the metal surface, where s_{ij} is the stoichiometric coefficient of species i in reaction j, and n_j is the number of transferred electrons in reaction j. The negative sign is to compensate for the sign convention where anodic currents are represented with positive values and cathodic currents with negative values. For the chemical species that are not involved in electrochemical reactions the flux at the metal surface is zero:

$$N_i|_{x=0} = 0 \hspace{4cm} (\text{B.3-26})$$

The kinetic parameters of the H^+ reduction reaction expressed in the form of Equation (B.3-20) were obtained by finding the best fit of the model with the experimental data, with the temperature effect expressed in term of the van't Hoff equation. The values of $k_{0_{H^+}} = 2E-8$, $m_{H^+} = 0.5$, $q_{H^+} = 0.43$, and the reaction enthalpy of $\Delta H = 100.3\ kj$ at $T_{ref} = 283^o K$ were obtained, which were found to be in reasonable agreement with those obtained on a mild steel with the same composition in glass cell experiments during an earlier study [201].

In a similar fashion, the kinetic parameters of the iron dissolution were obtained as listed in Table B.3-3. The rate of this reaction, and its pH and pCO$_2$ dependence, was characterized as discussed above. Despite there being four parameters involved, each was obtained with a reasonable confidence based on its corresponding feature in the polarization curves. Considering the significantly different apparent Tafel slopes and pH dependence observed in N$_2$-saturated and CO$_2$-saturated solutions, two sets of kinetic parameters were inevitably used to represent the rate of this reaction in each case.

Table B.3-3. Kinetic parameters of the iron dissolution reaction in acidic solutions.

	N$_2$-saturated environment		CO$_2$-saturated environment	
	$k_{0,ref}$	$\Delta H\ (kj)\ at\ T_{ref} = 283$	$k_{0,ref}$	$\Delta H\ (kj)\ at\ T_{ref} = 283$
k_1	1.5E6	42.9	3.0E9	42.9
k_2	4.0E5	12.1	1E13	6.1
k_3	5.0E-2	39.2	4.5E-3	30.2
K_θ	1.5E10	10.2	4.0E13	24.7

B.3.5.3: Mass transfer and the buffering effect in the boundary layer

In order to calculate the rate of electrochemical reactions, as discussed in the previous section, the surface concentration of the electro-active species are required to be known. The surface concentrations can be calculated in terms of mass conservation inside the diffusion layer that is stretching from the metal surface to the bulk solution with the known solution speciation (as discussed in section B.3.5.2:). The mass conservation inside the diffusion layer of electrochemical systems is described via the Nernst-Planck Equation as:

$$\frac{\partial C_i}{\partial t} = -\nabla . N_i + R_i \qquad\qquad (\text{B.3-27})$$

Where N_i is the flux of species i and R_i is the rate of its production/consumption via chemical reactions that incorporate the effect of the CO_2 hydration reaction and the carbonic acid buffering effect. The flux is typically expressed as:

$$N_i = -z_i u_i F C_i \nabla \phi - D_i \nabla C_i + v C_i \qquad \text{(B.3-28)}$$

The first term in Equation (B.3-28) is the contribution of electro-migration for the ionic species i in the presence of an electric field ($\nabla \phi$) with charge of z_i and mobility of u_i, where F is Faraday's constant. The second term is the molecular diffusion arising from the concentration gradient, with D_i being the diffusion coefficient. The last term represents the effect of convective flow with the velocity of v.

In the fully developed turbulent flow regime, such as the one inside the thin channel cell of the present study, the convective flow term in Equation (B.3-28) is no longer applicable and the effect of flow is represented by the concept of eddy diffusivity. That suggests, unlike laminar flow that moves the bulk of the fluid towards a certain direction, the eddies in turbulent flow mix the solution at a microscale. Therefore, the effect of turbulent flow is represented with an analogy to molecular diffusion, with D_e representing eddy diffusivity. Hence Equation (B.3-28) in turbulent flow is restated as:

$$N_i = -z_i u_i F C_i \nabla \phi - (D_i + D_e) \nabla C_i \qquad \text{(B.3-29)}$$

Considering the symmetry of the electrode, the tangential and radial components of Equations (B.3-27) and (B.3-29) have no practical significance. Furthermore, assuming an ideal solution, the ionic mobility can be expressed via the Nernst-Einstein relationship ($u_i = D_i/RT$). Therefore, Equations (B.3-27) and (B.3-29) can be simplified for a one dimensional semi-infinite domain normal to the electrode surface:

$$N_i = -(D_i + D_e)\frac{\partial C_i}{\partial x} - \frac{z_i D_i F C_i}{RT}\frac{\partial \phi}{\partial x}$$

(B.3-30)

$$\frac{\partial C_i}{\partial t} = \frac{\partial}{\partial x}\left((D_i + D_e)\frac{\partial C_i}{\partial x}\right) + \frac{z_i D_i F}{RT}\frac{\partial}{\partial x}\left(C_i\frac{\partial \phi}{\partial x}\right) + R_i$$

(B.3-31)

The diffusion coefficients appearing in Equations (B.3-30) and (B.3-31) for the species of significance in the present study are listed in Table B.3-4. The temperature dependence of molecular diffusivity (D_i) can be expressed on the basis of the well-known Stokes-Einstein relationship as:

$$\frac{D_{i,T}}{D_{i,298}} = \frac{T}{298}\frac{\mu_{298}}{\mu_T}$$

(B.3-32)

where T is the temperature in degrees Kelvin and μ_T is the water viscosity at T.

Table B.3-4. Reference diffusion coefficients at 25 ºC.

Species	Diffusion coefficient in water $\times 10^9$ (m²/s)	Reference
CO_2	1.92	150
H_2CO_3	1.75	estimated
HCO_3^-	1.185	70
CO_3^{2-}	0.923	70
H^+	9.312	68
OH^-	5.273	70
Na^+	1.334	68
Cl^-	2.032	68,70
Fe^{2+}	0.72	68

The eddy diffusivity distribution throughout the boundary layer of a fully developed turbulent flow can be obtained from the empirical equation suggested by Arvanith[151]:

$$D_e = \nu \frac{0.0007\, x^{+3}}{\left[1 + 0.00405 x^{+2}\right]^{1/2}}$$

(B.3-33)

where ν is the kinematic viscosity and x^+ is the dimensionless distance from the wall defined as:

$$x^+ = \frac{x\left(\tau_w/\rho\right)^{1/2}}{\nu}$$

(B.3-34)

Equation (B.3-33) is valid for $x^+ < 30$ and is universal for all turbulent flow when appropriate dimensionless parameters are used. The influence of the geometry of channel flow appears in the wall shear stress term (τ_w) of Equation (B.3-34). Where τ_w is defined as a function of Fanning friction factor (C_f) as shown in Equation (B.3-35), and the Fanning friction factor itself is a function of the Reynolds number (Re). The Reynolds number carries the geometry specific information in this set of equations.

$$\tau_w = {}^1\!/_2\, \rho C_f V^2$$

(B.3-35)

In Equation (B.3-35), V is the average flow velocity (m.s^{-1}), and ρ is the fluid density (kg.m^{-3}). There are a few different empirical relationships proposed for calculating the friction factor in a turbulent flow regime. In the present study, the correlation of Swamee and Jain[239] for Darcy friction factor ($C_d = 4C_f$) was used (Equation (B.3-36)), which is essentially an explicit derivation of the well-known Colebrook-White correlation[240]. The Reynolds number (Re$= V.D_{eq}/\nu$) was calculated based on the equivalent characteristic diameter: $D_{eq} = 4A/P$, where A and P are the cross-section area and the interior perimeter of the thin channel.

$$C_d = 0.25 \left[\log \left(\frac{\varepsilon/D_{eq}}{3.7} + \frac{5.74}{Re^{0.9}} \right) \right]^{-2}$$

(B.3-36)

The first term in the logarithm in Equation (B.3-36) accounts for the effect of

wall roughness (ε) on the friction factor.

The wall shear stress calculated using Equations (B.3-35) and (B.3-36) is

compared with the experimental data for the thin channel flow cell used in the present

study in Figure B.3-11. The experimental results shown in Figure B.3-11 are recalculated

from the data obtained in earlier studies in the same thin channel flow cell [204,206,241,242].

The experimental data was obtained via pressure drop measurements and also with a wall

shear stress probe (Lenterra Inc.), as described in detail in the original studies [204,206,241,242].
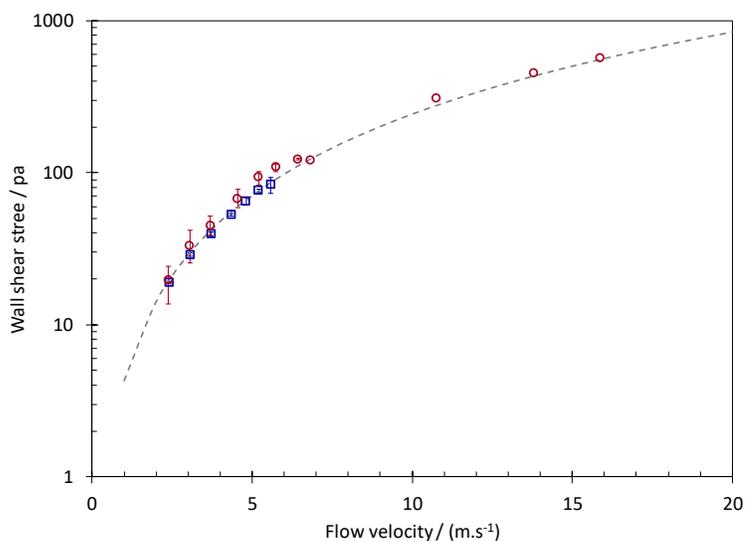
Figure B.3-11. The comparison of the calculated and measured wall shear stress in the thin channel flow cell used in the present study. Experimental data from Li [204] and Akeer [241].

The R_i term in Equation (B.3-31) represents the effect of the homogeneous

reactions as the source/sink of the chemical species. The rate of each chemical reaction j

in the general form of Reaction (B.3-37) can be calculated as shown in Equation (B.3-38).

$$\sum_{r=1}^{n_r} C_r \rightleftharpoons \sum_{p=1}^{n_p} C_p$$

(B.3-37)

$$R_j = k_{f,j} \prod_{r=1}^{n_r} C_r - k_{b,j} \prod_{p=1}^{n_p} C_p$$

(B.3-38)

The rate of production (or consumption) of every species i (R_i) for j chemical reactions shown as Reactions (B.3-2) to (B.3-5) may be expressed in a matrix format as Equation (B.3-39), where the fluid inside the boundary layer is assumed to be a single liquid phased saturated with CO_2. The kinetic rate constant of the chemical reactions can be found in Table B.3-5.

(B.3-39)

$$\begin{bmatrix} R_{CO_{2(aq)}} \\ R_{H^+_{(aq)}} \\ R_{H_2CO_{3(aq)}} \\ R_{HCO^-_{3(aq)}} \\ R_{CO^{2-}_{3(aq)}} \\ R_{OH^-_{(aq)}} \end{bmatrix} = \begin{bmatrix} -1 & 0 & 0 & 0 \\ 0 & 1 & 1 & 1 \\ 1 & -1 & 0 & 0 \\ 0 & 1 & -1 & 0 \\ 0 & 0 & 1 & 0 \\ 0 & 0 & 0 & 1 \end{bmatrix} \times \begin{bmatrix} R_{hyd} \\ R_{ca} \\ R_{bi} \\ R_w \end{bmatrix}$$

Table B.3-5. Kinetic rate constants of Reactions (B.3-2) to (B.3-5). k_f denotes the reaction progress from left to right and $K=k_f/k_b$.

Reaction #	Reaction rate constant	reference
(B.3-2)	$k_{f,hyd} = 1.28 \times 10^{11} \, e^{(\frac{81200}{RT})} \, (1/s)$	218
(B.3-3)	$k_{b,ca} = 4.7 \times 10^{10} \quad (1/M.s)$	66,91,243
(B.3-4)	$k_{b,bi} = 5.0 \times 10^{10} \quad (1/M.s)$	91,243
(B.3-5)	$k_{b,w} = 1.4 \times 10^{11} \quad (1/M.s)$	66,67

Considering the discussion above, Equation (B.3-31) can be used to describe the concentration distribution of the involved chemical species inside the boundary layer. The potential inside the boundary layer can also be specified with the aid of the electro-neutrality Equation (B.3-15). The electro-neutrality equation applied in the diffusion boundary layer is, in fact, derived from the more theoretically valid Poisson's equation [60]. This derivation is based on fact that in common aqueous electrochemical systems the potential gradient is too small to result in any significant change in the charge density (charge density=0 as shown in Equation (B.3-15))[60]. In the typical conditions of CO_2 corrosion, especially when significant amounts of ionic species are present, this assumption generally remains valid.

B.3.5.4: Mathematical methods

The mathematical equations as described in section B.3.5.3: form a set of non-linear, coupled, partial differential equations. The following set of dimensionless variables were defined to replace distance (x), concentration (C_i), and potential (E and ϕ).

$$X = \frac{x}{\delta} \qquad \xi_i = \frac{C_i}{C_i^b} \qquad \Phi = \frac{F\phi}{RT} \qquad \psi = \frac{FE}{RT}$$

The resulting set of differential equations can be solved numerically. With the simple one-dimensional geometry spanning from the metal surface towards the bulk solution, the finite difference method can be used to solve the equations. This method is commonplace in mathematical modeling of electrochemical systems [244–246], and has been discussed in detail elsewhere [68,247].

Considering the heterogeneous nature of the metallic CO_2 corrosion and the fast kinetics of the involved homogenous chemical reactions, the concentration gradients for the solution in the vicinity of the metal surface can be large. In order to capture the effect of homogeneous chemical reactions, it is necessary to have sufficient resolution inside the reaction boundary layer. That can be achieved simply by increasing the number of spatial nodes in a uniform grid, but leads to increased memory requirements and slower computations. The alternative approach used in the present study is to employ a non-uniform grid with a fine resolution close to the metal surface and more coarse increments as the bulk solution is approached. The latter method can significantly shorten the computational time. The partial differential equations are discretized using second order, non-uniform, Taylor's series approximations, resulting in a set of linear algebraic equations. In the present model the grid size was allowed to grow linearly with a factor of 1.1 from the initial value of $X=1.0\times10^{-4}$. The non-uniform grid derivative approximations used in the present study are shown in Table B.3-6 for a function $f(x)$, where $\Delta x_j = x_j - x_{j-1}$ is the distance between the two adjacent nodes.

The discretized equations can further be transformed into a matrix format for convenience. The final solution can then be obtained through various solution algorithms such as Newman's "Band-J" open source code where the coefficient matrix is developed and further solved by the LU decomposition method [68,247]. The temporal derivation was expressed using Euler's approximation in the present study. Considering that the equations are non-linear, the solution at each time step was obtained iteratively, using an explicit approach.

Table B.3-6. Derivative approximation for a non-uniform grid.

First order derivative, central approximation	$f'(x_i) = a_i f(x_{i-1}) + b_i f(x_i) + c_i f(x_{i+1})$	
$a_i = -\dfrac{\Delta x_{i+1}}{\Delta x_i(\Delta x_i + \Delta x_{i+1})}$	$b_i = \dfrac{\Delta x_{i+1} - \Delta x_i}{\Delta x_i \Delta x_{i+1}}$	$c_i = \dfrac{\Delta x_i}{\Delta x_{i+1}(\Delta x_i + \Delta x_{i+1})}$
First order derivative, three point forward approximation	$f'(x_i) = a_i f(x_i) + b_i f(x_{i+1}) + c_i f(x_{i+2})$	
$a_i = -\dfrac{2\Delta x_{i+1} + \Delta x_{i+2}}{\Delta x_{i+1}(\Delta x_{i+1} + \Delta x_{i+2})}$	$b_i = \dfrac{\Delta x_{i+1} + \Delta x_{i+2}}{\Delta x_{i+1} \Delta x_{i+2}}$	$c_i = -\dfrac{\Delta x_{i+1}}{\Delta x_{i+2}(\Delta x_{i+1} + \Delta x_{i+2})}$
Second order derivative, central approximation	$f''(x_i) = a_i f(x_{i-1}) + b_i f(x_i) + c_i f(x_{i+1})$	
$a_i = \dfrac{2}{\Delta x_i(\Delta x_i + \Delta x_{i+1})}$	$b_i = -\dfrac{2}{\Delta x_i \Delta x_{i+1}}$	$c_i = \dfrac{2}{\Delta x_{i+1}(\Delta x_i + \Delta x_{i+1})}$

B.3.5.5: Model verification

The performance of the calculations is examined against the experimental data as shown in Figure B.3-12 to Figure B.3-14. Figure B.3-12 demonstrates the results obtained at 10°C, which is of particular interest in the present study. At this condition the charge transfer controlled current densities were clearly observed, and found not to be affected by the partial pressure of CO_2. It was based on this observation that the direct

reduction of H_2CO_3 was considered insignificant. The quantitative analysis of the results showed that both the charge transfer controlled cathodic currents and the limiting current densities can be adequately estimated considering only the H^+ reduction while the homogeneous chemical reactions are properly incorporated in the model. The estimated anodic current densities were also in good agreement with the experimental data, with the effect of CO_2 being reasonably incorporated into the model.
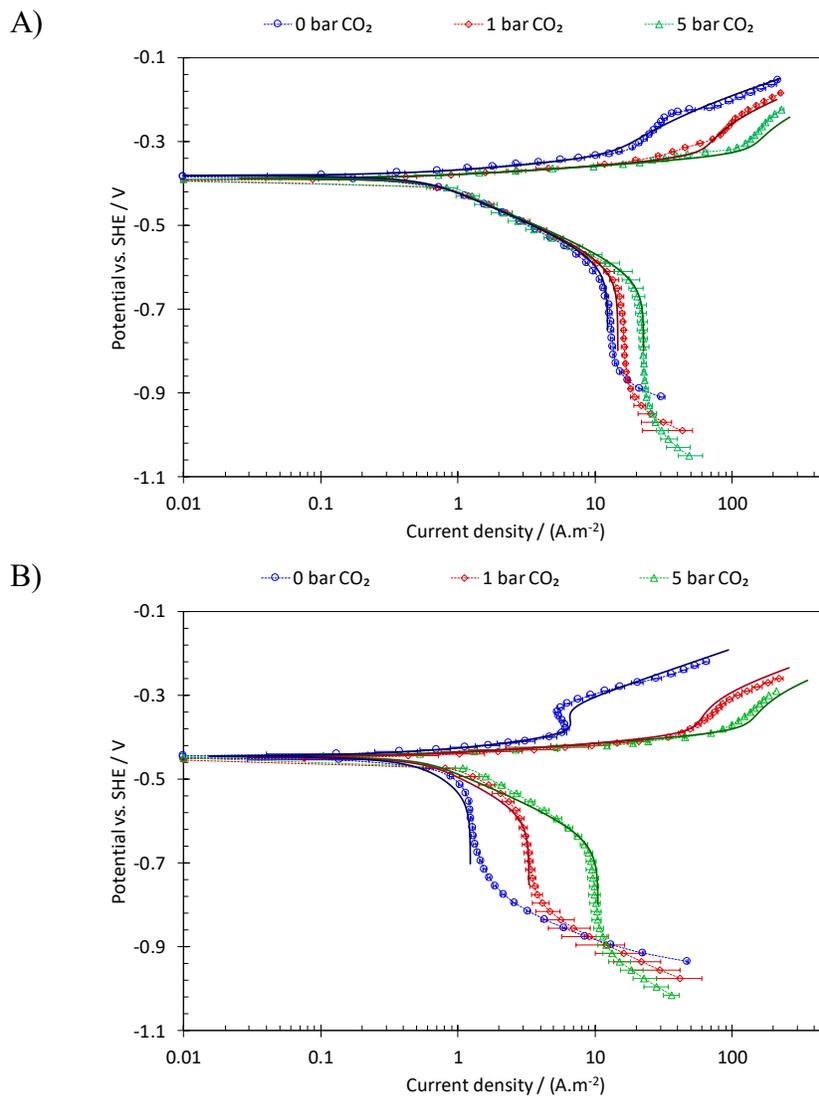
Figure B.3-12. The comparison of the simulated polarization curves with the experimental data obtained on API 5L X65 mild steel in acidic solutions, at 10°C, 12.9 m.s^{-1} flow velocity, 0.1 M NaCl, and varying pCO$_2$. A) at pH 4. B) at pH 5.

The effect of temperature on the polarization curves at 5 bar CO$_2$ is shown in Figure B.3-13, where the results from 10°C and 30°C measurements were compared at pH 4 and pH 5. The effect of temperature on the cathodic limiting current density is accounted for through the physical properties of water and also the chemical equilibrium associated with the CO$_2$/H$_2$O system, which were estimated well at both conditions. The

change in electrochemical reaction rate constants are calculated through the van't Hoff

equation as discussed in section B.3.5.2: .

A)

B)
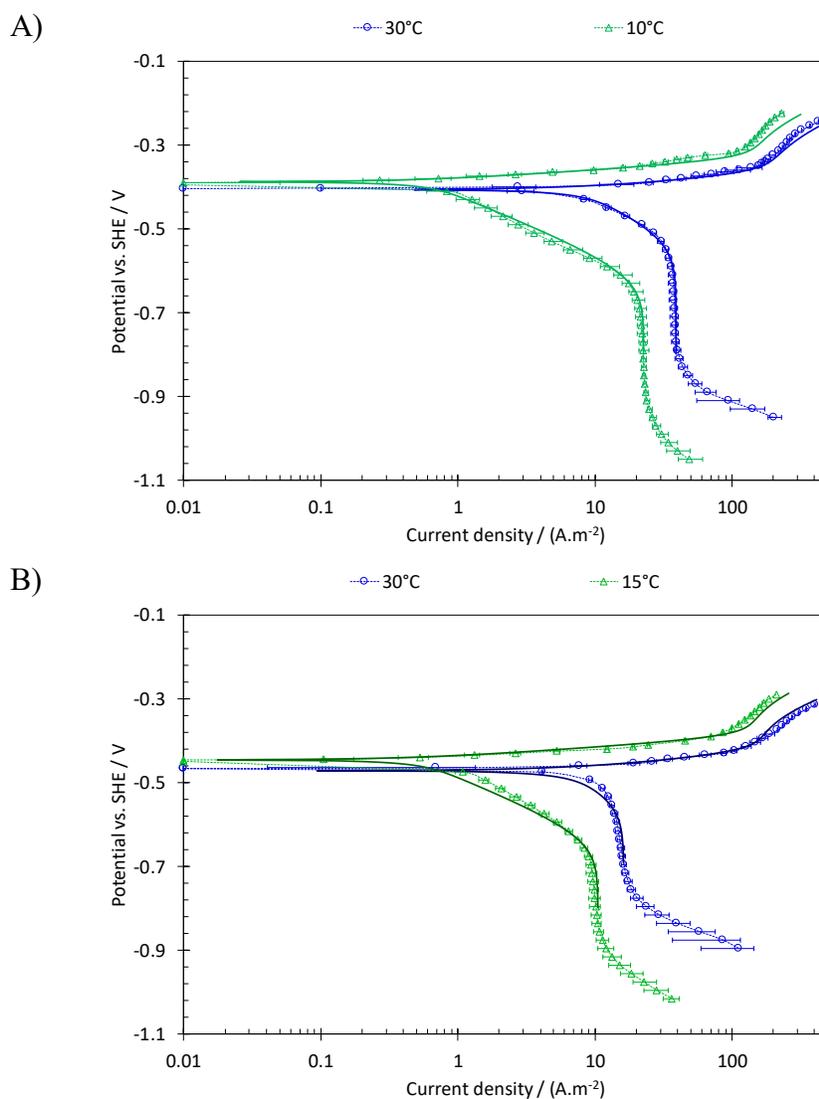
Figure B.3-13. The comparison of the simulated polarization curves with the experimental data obtained on API 5L X65 mild steel in acidic solutions, 12.9 m.s^{-1} flow velocity, 0.1 M NaCl, 5 bar pCO_2. A) at pH 4. B) at pH 5.

Ultimately, the mathematical model developed above was used to estimate the

corrosion rates as shown in Figure B.3-14 to Figure B.3-16. Figure B.3-14 is the

comparison of the estimated corrosion rates with those obtained experimentally for the conditions of the present study. The model was found to successfully predict the corrosion rates with reasonable accuracy. Also, the transition from the charge transfer controlled corrosion scenario that is the predominant corrosion mechanism in low temperatures to the mass transfer controlled corrosion mechanism observed at higher temperatures was properly reflected in the estimated corrosion rates. The significance of this behavior is further demonstrated in Figure B.3-15, where the estimated corrosion rates at pH 5 and various pCO$_2$ values is demonstrated as a function of temperature.
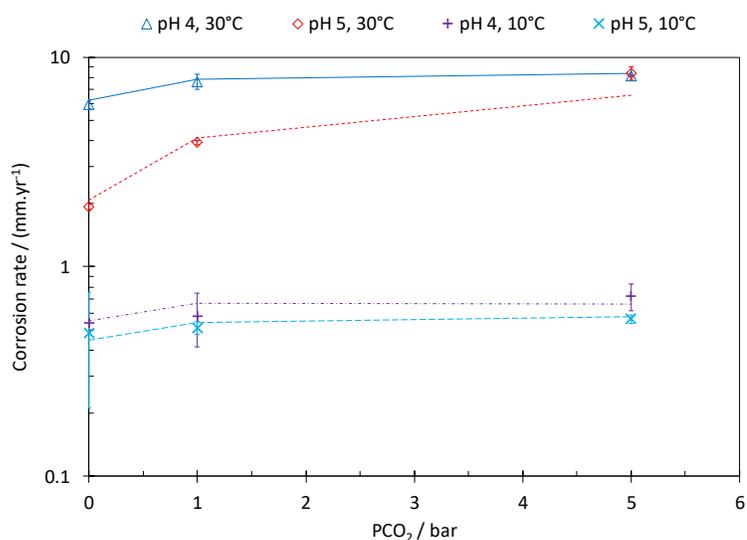
Figure B.3-14. The comparison of the experimental and estimated corrosion rates on API 5L X65 mils steel, in 0.1 M NaCl solutions and 12.9 m.s^{-1} flow velocity.

As is apparent in Figure B.3-15, the corrosion at low temperatures is under charge transfer control at nearly all pCO$_2$ values; hence, the corrosion rate does not show any significant dependence on pCO$_2$. As the temperature is increased, the corrosion rates at lower pCO$_2$ values become mass transfer limited, which is indicated by the rapidly

increasing rates as the pCO_2 is increased; as a result of the buffering effect of CO_2 and H_2CO_3. The pCO_2 threshold where the corrosion gets into the charge transfer controlled range is strongly dependent on environmental conditions such as temperature, as shown in Figure B.3-15, or other parameters such as flow velocity and the presence of other buffering species (e.g., carboxylic acids). In the conditions considered here the charge transfer controlled condition at the corrosion current are reached at approximately 5 bar CO_2 at 30°C, while at 60 and 90°C the transition is not clearly observed even at pCO_2 as high as 50 bar.
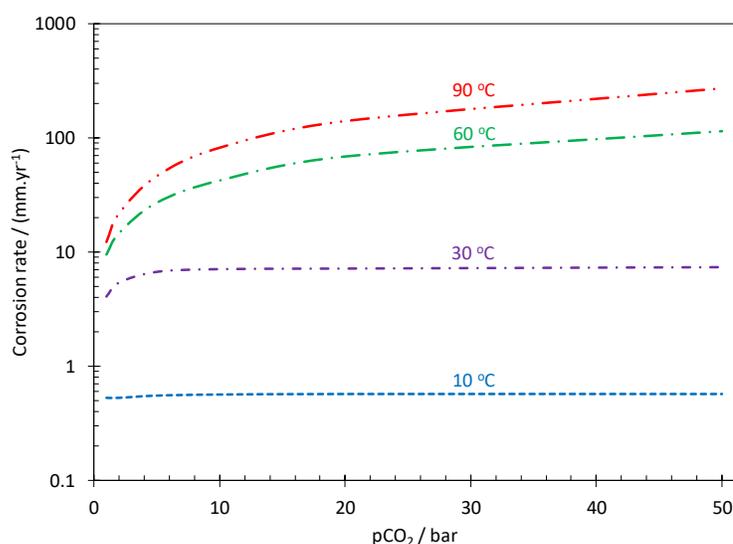
Figure B.3-15. The effect of temperature on the predicted corrosion rates at pH 5, 0.1 M NaCl and 12.9 m.s^{-1} flow velocity.

The effect of pH on the transition from charge transfer controlled corrosion to mass transfer controlled scenario is shown in Figure B.3-16. While at lower pH values the corrosion rates are generally higher, they are less affected by the pCO_2. That is because the corrosion is under charge transfer control. However, increasing the

temperature eventually shifts the corrosion potential into the mass transfe controlled

range which is significantly affected by pCO_2. The transition from charge transfer to

mass transfer controlled corrosion at higher pH values occurs at lower temperatures as

shown in Figure B.3-16. That leads to the observation of higher influence of pCO_2 on the

observed corrosion rates at higher pH values.

A significant effect of H_2CO_3 on the corrosion rate is observed at higher

temperatures and pCO_2 values. This behavior leads to a more practically important

conclusion. Even though the direct reduction of carbonic acid is shown to be

insignificant, the presence of CO_2 would remain one of the main parameters in corrosion

rate prediction in typical environmental conditions. The elevated temperatures and near

neutral pH values are very common conditions in oil and gas production and transmission

facilities. At such conditions, the cathodic current is significantly influenced by the mass

transfer, and the anodic current is most likely at the transition/pre-passivation range; both

of which are significantly affected by the presence of CO_2. Hence, although H_2CO_3 is not

electrochemically active, the corrosion rates are expected to be still significantly

influenced by pCO_2. That also signifies the importance of proper accounting of the

chemical reactions inside the diffusion layer when calculating the corrosion rates. That

can be achieved using the available comprehensive mathematical models, similar to the

one developed in the present study. The earlier, more simplistic, modeling approach

[14,18,103] does not allow for proper description of the buffering effect as discussed in more

detail elsewhere [43,60].
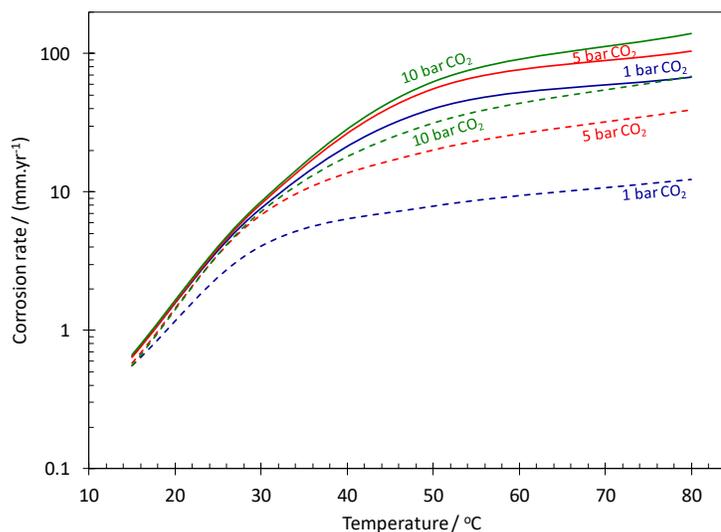
Figure B.3-16. The effect of temperature on the predicted corrosion rates at pH 4 (solid lines) and pH 5 (dashed lines), at 0.1 M NaCl and 12.9 m.s^{-1} flow velocity.

B.3.6: Summary

The electrochemical activity of H_2CO_3 reduction was investigated on the basis of the charge transfer controlled range of the cathodic polarization curves in CO_2-saturated solutions on a mild steel surface. The experimental results did not indicate that H_2CO_3 is a significant electro-active species. The effect of CO_2 on the anodic polarization curves, especially that observed in the transition and pre-passivation ranges, were confirmed by the experimental results of the present study. These mechanistic observations were used in development of a comprehensive mathematical model, in order to provide further quantitative support. The simulated polarization curves and the estimated corrosion rates were found to agree well with those obtained experimentally. The significance of these mechanistic observations were further discussed based on the estimated corrosion rates of the model. The pCO$_2$ dependence of the corrosion rates were shown to be strongly temperature dependent. At low temperatures, corrosion rates are not significantly

influenced by pCO$_2$ since the anodic dissolution is in the active dissolution range and the cathodic current is under charge transfer control. On the other hand, at elevated temperature a linear pCO$_2$ dependence of the corrosion rate is expected. That is the result of the shift of corrosion current into the transition/pre-passivation range of the iron dissolution reaction and, at the same time, the shift of the corrosion current into the mass transfer controlled cathodic current, both of which were found to be significantly increased in the presence of CO$_2$.

Nomenclature

Symbol	Definition
C_i	Concentration of species i (M)
C_i^b	Concentration of species i at bulk (M)
C_i^s	Concentration of species i at metal surface (M)
C_f	Fanning friction factor
D_i	Diffusion coefficient of species i (m^2/s)
D_e	Eddy diffusivity (m^2/s)
D_{eq}	Equivalent characteristic diameter (m) $D_{eq} = 4A/P$
$D_{i,ref}$	Diffusion coefficient of species i at reference temperature (m^2/s)
E	Electrode potential (V)
E_{0j}	Standard potential of reaction j (V)
F	Faradays constant (C/mol)
ΔH_j	Enthalpy of reaction j (kJ/mol)
i_j	Current density of reaction j (A/m^2)
i_{app}	Applied current density (A/m^2)
K_j	Equilibrium constant of reaction j
k_{0j}	Rate constant of electrochemical reaction j
$k_{0j,ref}$	Rate constant of electrochemical reaction j at reference temperature
K_H^0	Henry's constant at water saturation pressure (m/bar)
k_f	Forward reaction rate constant
k_b	Backward reaction rate constant
m_i	Reaction order with respect to species i
n_j	Number of transferred electrons in electrochemical reaction j
N_i	Flux of species i (mol/m^2.s)
R	Universal gas constant (J/K.mol)

$P_{CO_{2(g)}}$	Partial pressure of CO_2 (bar)
P_{tot}	Total pressure (bar)
P	Pressure (bar)
$P_{CO_2 S}$	Saturation pressure of CO_2 (bar)
P_{ws}	Saturation pressure of water (bar)
R_i	Reaction rate of species i (M/s)
Re	Reynolds number
s_{ij}	Stoichiometric coefficient of species i in reaction j
T	Temperature (K)
T_{ref}	Reference temperature (K)
t	Time (s)
τ_w	Wall shear stress (pa)
θ	Surface coverage by the intermediate species
u_i	Mobility of species i (m/s)
V	Average flow velocity (m/s)
v_x	Velocity along x axis (m/s)
x	Distance from metal surface (m)
z_i	Charge of ion i
α_j	Transfer coefficient of electrochemical reaction j
ε	Surface roughness (m)
μ	Water viscosity (kg/s.m)
μ_{ref}	Water viscosity at reference temperature (kg/s.m)
ρ_{Fe}	Density of iron (kg/m^3)
ρ_w	Density of water (kg/m^3)
υ	Kinematic viscosity (m^2/s)
ϕ	Electric potential inside liquid (V)
φ_{CO_2}	Fugacity coefficient of $CO_{2(g)}$

Chapter B.4: The new perspective of CO_2 corrosion of mild steel

B.4.1: Introduction

In order to recast the mechanistic findings of the previous chapters into a generic mechanism of CO_2 corrosion of mild steel as seen in the oil and gas industry, the environmental conditions are further extended, so it could be assumed that they are a reasonably representative of those seen in a majority of industrial applications. That included the increase of CO_2 partial pressure to 15 bar and the studied pH up to 6. Similar to the previous chapters, a comprehensive mathematical model was developed for simulation of polarization curves, and prediction of corrosion rates. Considering that at these extended conditions the ideal solution assumption is not necessarily valid, the non-ideal solution properties were included in the model in the context of moderately concentrated solutions. For this purpose, a Pitzer's specific interaction model was developed for water chemistry calculations and further coupled with the electrochemical model. The mechanistic finding in this chapter were found to agree with the previous ones. That is, the fact that carbonic acid is not reduced directly dutring the corrosion process. Additionally, extending the environmental conditions revealed the effect of the bicarbonate ion. It was found that this effect is a result of the bicarbonate ion dissociation reaction (i.e., another buffering effect), and that the bicarbonate ion is not reduced at the metal surface, just like carbonic acid.

B.4.2: Background

The mechanism of carbon dioxide (CO_2) corrosion of mild steel has been a controversial subject for decades, perhaps due to the complexities arising from the

presence of numerous chemically and (what was assumed) electrochemically active

species in an aqueous acidic CO_2/H_2O system. In conventional understanding of CO_2

corrosion, the corrosion is a result of a series of chemical (Reactions (B.4-1) to (B.4-5

)) and electrochemical (Reactions (B.4-6) to (B.4-10)) processes. The chemical

reactions are associated with the CO_2/H_2O equilibria in acidic solutions. The complexities

of this chemical system alone has made it the subject of numerous studies over many

decades, while some aspects remain the subject of recent investigations [91,218,222,223,243,248–

250]. Upon dissolution in water (Reaction (B.4-1)), the dissolved CO_2 undergoes a series

of chemical reactions, starting with the hydration reaction to produce carbonic acid

(H_2CO_3). H_2CO_3, as a diprotic weak acid, is partially dissociated to form hydrogen (H^+)

and bicarbonate (HCO_3^-) ions and further to carbonate ion (CO_3^{2-}) as shown in Reactions

(B.4-3) and (B.4-4) .Water, present as the solvent, can also dissociate according to

Reaction (B.4-5).

$$CO_{2(g)} \leftrightharpoons CO_{2(aq)} \qquad\qquad\qquad (\text{B.4-1})$$

$$CO_{2(aq)} + H_2O_{(l)} \leftrightharpoons H_2CO_{3(aq)} \qquad\qquad\qquad (\text{B.4-2})$$

$$H_2CO_{3(aq)} \leftrightharpoons HCO_3^-{}_{(aq)} + H^+{}_{(aq)} \qquad\qquad\qquad (\text{B.4-3})$$

$$HCO_3^-{}_{(aq)} \leftrightharpoons CO_3^{2-}{}_{(aq)} + H^+{}_{(aq)} \qquad\qquad\qquad (\text{B.4-4})$$

$$H_2O_{(l)} \leftrightharpoons OH^-{}_{(aq)} + H^+{}_{(aq)} \qquad\qquad\qquad (\text{B.4-5})$$

The electrochemistry of CO_2 corrosion has also been conventionally believed to

be an equally complicated system. While iron dissolution (anodic partial of Reaction (

B.4-6)) is the main anodic reaction, the cathodic reactions (cathodic partial of Reactions

(B.4-7) to (B.4-10)) include the H^+ reduction as well as the direct reduction of other weak acids present in the system, e.g. H_2CO_3, HCO_3^- and water.

$$Fe^{2+}_{(aq)} + 2e^- \leftrightharpoons Fe_{(s)} \qquad\qquad (\text{B.4-6})$$

$$H^+_{(aq)} + e^- \leftrightharpoons {}^1\!/_2\, H_{2\,(g)} \qquad\qquad (\text{B.4-7})$$

$$H_2O_{(l)} + e^- \leftrightharpoons OH^-_{(aq)} + {}^1\!/_2\, H_{2\,(g)} \qquad\qquad (\text{B.4-8})$$

$$H_2CO_{3(aq)} + e^- \leftrightharpoons HCO_{3\,(aq)}^- + {}^1\!/_2\, H_{2\,(g)} \qquad\qquad (\text{B.4-9})$$

$$HCO_{3\,(aq)}^- + e^- \leftrightharpoons CO_{3\,(aq)}^{2-} + {}^1\!/_2\, H_{2\,(g)} \qquad\qquad (\text{B.4-10})$$
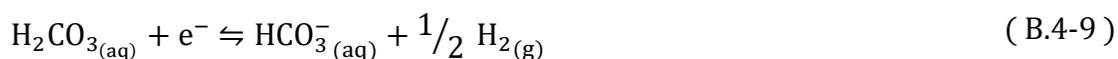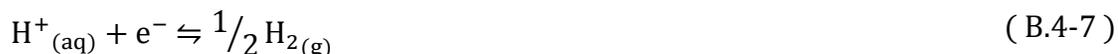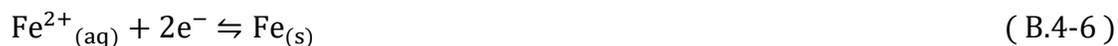
This mechanistic view has been developed gradually from the 1970s to the early 2000s. The earliest publications that suggest a significant role for carbonic acid in CO_2 corrosion are those of de Waard and Millimas [19,105]. The authors suggest that in CO_2-saturated acidic solutions, the direct reduction of carbonic acid is the dominant cathodic reaction. Considering the pCO_2 dependence of H_2CO_3 concentration as defined by Reaction (B.4-2), the authors proposed their well-known relationship between the corrosion rate and pCO_2. The mechanism of cathodic reactions as suggested in this study consists of the direct reduction of H_2CO_3, followed by the association reaction of HCO_3^- with H^+. It is easy to recognize the evolution of understanding of the mechanism of CO_2 corrosion, as described above, compared to what was proposed by de Waard and Milliams in those early studies [19,105]. Nevertheless, the results approach in their work was what initiated a series of investigation that resulted in the mechanistic view of CO_2 corrosion, as we know it today.

The significance of the chemical reactions of CO_2-H_2O was only recognized after the study by Schmitt and Rothmann on the limiting current densities of CO_2-saturated solutions [107]. In particular, in that study the authors demonstrated the significance of the CO_2 hydration reaction. The authors showed that the limiting current in such a system, in addition to the mass transfer of H^+ and H_2CO_3 from the bulk solution, also consists of the slow chemical CO_2 hydration reaction, which reproduces H_2CO_3 in the vicinity of the metal surface when its concentration is reduced from the equilibrium values as a result of the corrosion process. In fact, this reaction is now known as a characteristic process unique to CO_2 corrosion, that differentiates CO_2 corrosion not only from corrosion in strong acid solutions but also from the corrosion in the presence of other weak acids such as carboxylic acids and hydrogen sulfide. Considering the low equilibrium constant of the hydration reaction, only a small fraction of dissolved CO_2 reacts to form H_2CO_3. Therefore, there is large reservoir of dissolved CO_2 available in the solution, and immediately at the corroding metal surface, to replenish the concentration of the weak acid itself as it is consumed in the corrosion process.

In studies conducted by Gray et al. [14,103], the mechanistic understanding of CO_2 corrosion was significantly improved. Full recognition of CO_2 corrosion as an electrochemical process and the mechanistic treatment of the underlying processes is perhaps the main contribution in these studies. Gray et al. used a mechanistic approach to represent the reduction of H^+ as well as the direct reduction of H_2CO_3 and HCO_3^-, while incorporating the effect of mass transfer and CO_2 hydration reactions as a homogeneous reaction occurring in the vicinity of the electrode surface. These publications are, in a

sense, the collection of the mechanistic knowledge at that time, and the demonstration of the ability of mechanistic models to explain the observed behavior of the system.

The mechanistic view of CO_2 corrosion as described in this dissertation is the result of further developments stemming from the introduction of more comprehensive mathematical models in the late 1990s and 2000s [15,44–46]. These models allowed the chemical and electrochemical aspects of CO_2 corrosion to be coupled properly. It was only after this step that the significance of the homogeneous dissociation reactions (Reactions (B.4-3) and (B.4-4)) were understood. This type of model was introduced into CO_2 corrosion by the studies of Turgoose et al.[44] and Pots [45], and further developed by Nesic et al.[15,46]. The quantitative analysis in these studies allowed the observation of the now well understood fact that the limiting currents in CO_2-saturated solutions can be properly quantified without considering the direct reduction of H_2CO_3 and HCO_3^- [15,44–46]. That was justified by the possibility of a parallel reaction pathway through the homogeneous dissociation of the weak acid (Reactions (B.4-3) and (B.4-4) for H_2CO_3 and HCO_3^-), followed by the reduction of H^+ at the metal surface; considering that at the limiting current conditions the increasing surface pH shifts the chemical equilibrium towards the dissociation reaction. This observation is of great mechanistic significance as it questions the basis of the basic mechanism of CO_2 corrosion developed in the previous studies.

For example, in the study by Gray et al. [14,103], the mathematical model used to investigate the reaction mechanism does not allow the dissociation reactions to be introduced in calculations, as further discussed elsewhere [43,60]. Therefore, the limiting

currents could only be explained if H_2CO_3 (and HCO_3^-) were considered to be directly reduced at the metal surface. However, considering the possibility of this parallel reaction pathway through the dissociation reaction, the previous mechanistic argument now appears to lack sufficient experimental evidence as its support. Nonetheless, this mechanistic inconsistency did not gain much attention and the direct reduction reactions remained a part of the accepted mechanism of CO_2 corrosion until 2008.

In 2008, Remita et al. [11] published a study with the dissociation reaction of H_2CO_3 and its "buffering" ability as the center point of their discussion. The authors emphasized the fact that the cathodic currents can be explained for the most part without considering H_2CO_3 as an electroactive species. That led the authors to conclude that this reaction does not occur in CO_2 corrosion of mild steel. This study is of particular significance for the mechanistic understanding of CO_2 corrosion, despite the fact that with a very narrow range of environmental conditions it does not provide the necessary experimental evidence to conclude that H_2CO_3 is not electrochemically active (see Chapter B.2:). This publication indeed initiated a series for more targeted studies on the electrochemical activity of H_2CO_3 [50], including the present investigation. At the same time, other studies on the significance of the electrochemical activity of acetic acid on mild steel corrosion was going through similar mechanistic discussions [12,32,42,62,168,201].

Similar to the case of H_2CO_3 reduction, acetic acid was also conventionally presumed to be directly reduced during the corrosion process. However, there now seems to be a consensus in the literature that the direct reduction of acetic acid is insignificant and its main contribution is through homogeneous dissociation at the vicinity of the

electrode surface that buffers the surface concertation of H^+ [12,62,168,201]. The similarity between these cases further signified the importance of a similar mechanistic investigation for the case of CO_2 corrosion.

As recognized before [12,62], since the limiting currents behave similarly whether the weak acid is directly reduced or not, the electrochemical activity of a weak acid can be studied by the behavior of the charge transfer controlled cathodic currents. In this approach, at a fixed pH where the rate of H^+ reduction is constant, if the weak acid was electrochemically active the charge transfer controlled current would increase in response to the increasing concentration of the weak acid. At similar conditions if the weak acid is not electrochemically active, the charge transfer controlled current densities are not affected by the concentration of weak acid. In this argument, since the H^+ reduction always occurs in acidic solutions, the electrochemical activity of the weak acid can only be obtained if it is the dominant reaction. Therefore, the experiments should cover a sufficiently high ratio of the weak acid concentration to the H^+ concentration before the direct reduction of weak acid can be ruled out with a reasonable confidence.

While both corrosion scenarios, the case of acetic acid and that of CO_2, include the same mechanistic aspects, the difficulty in experimentation made the investigation of the mechanism of CO_2 corrosion a more challenging subject. In the case of acetic acid, the experiments in a typical glass cell under atmospheric conditions provide a sufficiently wide range of conditions required for a proper investigation of the electrochemical activity of the weak acid [12,62,201]. On the other hand, similar conditions for the case of carbonic acid can only be achieved in the experiments at elevated pressures. Even at

elevated pressures up to 10 bar CO_2, Tran et al.[50] noted that the charge transfer controlled current densities cannot be observed clearly on a X65 mild steel surface, and the abovementioned hypothesis cannot be verified. In the case of mild steel, the charge transfer controlled currents are covered by the anodic iron dissolution in the low current density range, and by the limiting current in the high current density range. The authors therefore investigated the mechanism of CO_2 corrosion on a stainless steel surface instead [50]. The decreased rate of anodic reaction on the stainless steel surface allowed the charge transfer controlled current densities to be observed in a reasonably extended range. Tran et al. showed that this range of current densities remain insensitive to the partial pressure of CO_2 up to 10 bar [50]. Therefore, the authors provided the experimental evidence that carbonic acid was not a significant electroactive species on a stainless steel surface. Nevertheless, considering the different surface properties of the passive stainless steel with a singificant amount of alloying elements (~20% Ni and ~10 % Cr) and the actively corroding mild steel, the mechanistic observations on one surface cannot be presumed to be valid on the other.

The studies in Chapter B.2: and Chapter B.3: were aimed to address this deficiency, where the same hypothesis was examined directly on a X65 mild steel. The experiments were performed using a thin channel flow cell at high flow velocities and CO_2 partial pressures up to 5 bar. The reported experimental data, particularly those obtained at 10°C, showed charge transfer controlled currents in an extended range of potentials. The charge transfer controlled currents were found to remain unaffected in pCO_2 ranging from 0 to 5 bar, hence the direct reduction of carbonic acid was shown to

be insignificant on the mild steel surface as well. In Chapter B.3: this mechanism was incorporated in a comprehensive mathematical model in order to provide further quantitative evidence for this mechanistic view. The agreement of the results from the model both at the charge transfer controlled range and for the limiting current was considered as further evidence for the validity of the mechanistic observations that the direct reduction of carbonic acid is not significant in CO_2 corrosion. As expected, the presence of H_2CO_3 only increases the magnitude of the limiting current as a result of homogeneous H_2CO_3 dissociation and CO_2 hydration at the vicinity of the metal surface. The reported experimental and estimated corrosion rates as a function of pCO_2 were also found to agree well with this mechanistic view. It was shown that when the cathodic currents are under charge transfer control increasing the partial pressure of CO_2 has no significant effect on corrosion rates, whereas, when the corrosion was under the influence of the limiting current, increasing the pCO_2 increased the corrosion rates almost linearly.

The results below expands on the previous studies both in terms of the range of the experimental conditions and also the mathematical modeling of CO_2 corrosion of mild steel. In the present case, the experiments were conducted in a high-pressure thin channel flow cell in order to allow for relatively high flow velocities. The conditions cover the pCO_2 range from 1 to 15 bar and the pH range from 4 to 6, in order to further examine the range of validity of the above mentioned mechanistic view. As is discussed further below, no indication of the direct reduction of carbonic acid was observed over this whole range of studied conditions. The experiments at higher pH and pCO_2 also provided the opportunity to investigate the effect of HCO_3^-, where it was also found to be

able to buffer the surface pH and, hence, increase the observed limiting current in the same fashion that H_2CO_3 does. Additionally, in the conditions of the present study no indication of the direct reduction of HCO_3^- was observed either, despite its presence at rather high concentrations.

At the elevated partial pressures and the presence of a high amount of alkalinity at higher pH values, the behavior of the system deviates significantly from the ideal conditions, assumed in previous studies [15,166,167], and in Chapter B.3: . The mathematical model in the present study was therefore extended into the moderately concentrated solutions range. The water chemistry calculations, as it concerns CO_2 corrosion, is discussed in term of activities of the species using the Pitzer specific interaction model. Furthermore, the comprehensive mechanistic electrochemical model was coupled with the Pitzer model in order to incorporate the effect of non-idealities into the transfer processes as well the homogeneous chemical reaction.

B.4.3: Experimental procedures

The experiments were carried out in the high pressure thin channel flow cell (HPTCFC) as depicted in Figure B.4-1. The whole test apparatus structure was made of 316L stainless steel. The experimental setup consists of a mixing tank used for pH measurement and pH adjustment, a heat exchanger used for temperature control, a high-pressure electric motor to generate the required flow, and the test section. In the present study the heat exchanger was connected to an industrial chiller (AIR 3000 from Coolant Chillers, Inc.) in order to remove the heat generated by the pump and allow the experiments to be conducted below room temperature. The temperature was monitored

using a thermocouple placed inside the tank. The test section (thin channel cell) with 76 cm flow length, allows the fluid flow through a 0.478 mm high, and 63.5 mm wide channel. The pump (Leeson G131510.00 series with 7.5 hp) output was adjusted to provide the required flow velocity that was measured using a turbine flow meter (Omega FTB-1308).
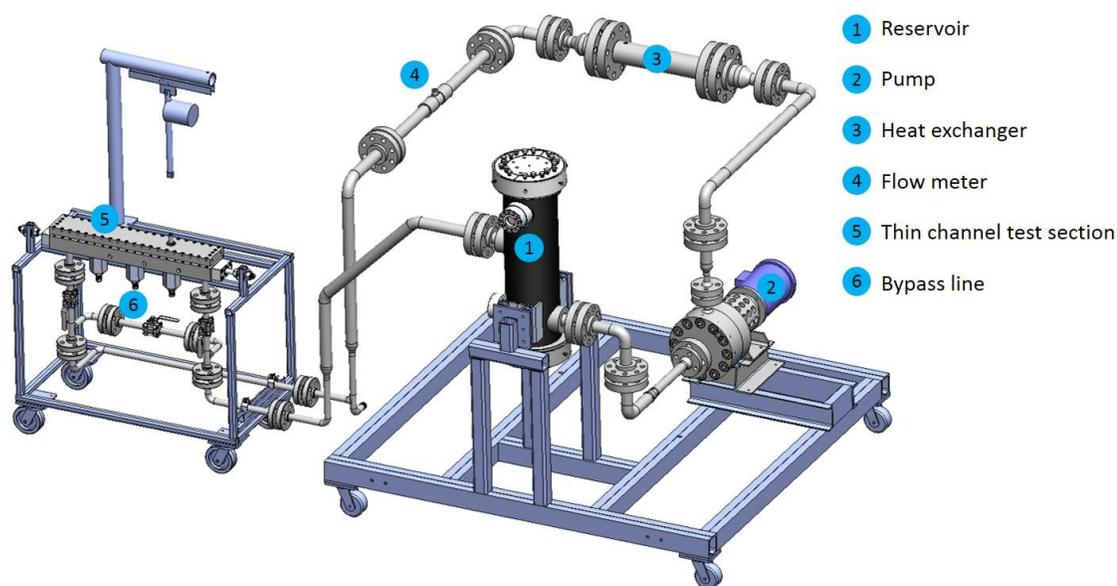
Figure B.4-1. Schematics of the high pressure thin channel flow cell.

The typical experimental procedure started with filling the test apparatus with 50 L deionized water, followed by addition of 292 grams of NaCl, to make 0.1 M NaCl solution. The solution was then deoxygenated using pure CO_2 gas flowed through a muffler installed at the interior bottom of the tank. In order to ensure proper deoxygenation, the gas output was monitored using an oxygen sensor (Orbisphere). The maximum dissolved oxygen gas at the end of the deoxygenation step was 2 ppb_m through

all experiments, achieved typically after ~2 hr of continuous purging. In the experiments at elevated pressures, after the deoxygenation step, the output gas flow was shut off and the system was pressurized to the targeted value. The pressure was monitored with a digital pressure gauge (Honeywell FPG1Dl) with ± 0.1 % accuracy. A constant pressure and pH readout over 30 minutes was considered as the criteria that the system has reached chemical equilibrium (usually after about ~4 hr). The pH of the solution was measured using a high pressure glass pH probe (Corr Instruments, Inc.). This procedure is followed by pH adjustment to the targeted value by gradually injecting a deoxygenated, concentrated NaOH solution into the tank. In a few cases where a large quantity of sodium ions were required to achieve the targeted pH (e.g. 15 bar CO_2 at pH 6) the required amount of sodium was pre-calculated and added into the solution during the deoxygenation step in the form of sodium bicarbonate. All the chemicals used in the present study were research grade (Fisher Scientific).

1 Reference electrode housing
2 Reference electrode
3 Working electrode surface
4 Working electrode assembly
5 Thin channel lid
6 Thin channel base
7 Flow area

Figure B.4-2. The schematics of the thin channel test section and electrode arrangement.

The test section in the present study allows a three electrode arrangement where the channel structure serves as the counter electrode. An in-house built Ag/AgCl reference electrode was mounted onto the cell lid across from the working electrode, as shown in Figure B.4-2. The working electrodes were made of either API 5L X65 mild steel or 316L stainless steel with the chemical composition shown in Table B.4-1. The working electrode assembly was made with a 316L stainless steel casing, with the disk shaped working electrode at the center located across from the reference electrode. The working electrode was isolated from the structure and the casing using an epoxy resin (LOCTITE Stycast 2850FT). Prior to each measurement, the electrode was abraded using 600 grit silicon carbide paper, rinsed and sonicated in isopropanol alcohol, and dried using nitrogen gas. The electrode was then flush mounted to the bottom of the test section just before initiating the electrochemical measurement. The test section is immediately purged and pressurized to the same level as of the tank. The solution, prepared following the procedure above, was then introduced into the test section. The experimental conditions of the present study are summarized in Table B.4-2.

Table B.4-1. Chemical composition of the working electrodes in wt.%.

	S	Cu	P	V	C	Cr	Mo	Si	Ni	Mn	Co	Fe
X65	0.009	-	0.009	0.047	0.13	0.14	0.16	0.26	0.36	1.16	-	Balance
SS 316 *	0.025	0.59	0.035	0.05	0.018	16.65	2.04	0.54	10.12	1.51	0.33	Balance

*Other elements with less than 0.1 wt.% concentrations: titanium, tin, tantalum, columbium, aluminum, boron, vanadium.

The electrochemical measurements for the API 5L X65 mild steel electrode were done using a Gamry Reference 600 potentiostat in the following order: 15 min monitoring of the open circuit potential (OCP), linear polarization resistance (LPR)

measurement, 5 min at OCP, potentiodynamic measurement, 5 min at OPC,

electrochemical impedance spectroscopy measurement. The OCP measurements showed

a steady final potential at all experimental conditions covered in the present study. The

LPR measurements were done using a 0.125 mV.s^{-1} scan rate and 1 s^{-1} sampling period at

the potential range of ±5mV vs. OCP. No significant change in OCP was observed before

and after LPR measurements. The steady state polarization measurements were done

using staircase voltammetry with a scan rate of 0.5 mV.s^{-1} and sampling period of 2 s^{-1}.

The catholic and anodic polarization curves were obtained in separate experiments by

scanning the potential from OCP towards more negative and more positive potentials,

respectively. The EIS measurements, used to obtain the solution resistance, were

conducted at OCP with 5 mV AC voltage perturbation, at the frequency range of 10 kHz

to 0.2 Hz and 10 points/decade.

Table B.4-2.Experimental conditions.

Test apparatus	Thin channel flow, three electrode arrangement
Flow velocity	4.6 m.s^{-1}
Materials	API X65 5L Mild steel 316L stainless steel
Temperature	10ºC to 40ºC (±0.5)
pH	3.0 to 6.0 (±0.02)
pCO_2	0 to 15 bar (± 0.1%)
Supporting electrolyte	0.1 M NaCl

For the experiments on 316L stainless steel, in order to avoid the formation of any passive layer, the initial OCP monitoring was inevitably minimized to 2 minutes. That step was followed by the potentiodynamic measurement, 5 minutes at OCP, and the EIS measurement. The electrochemical measurement parameters were identical to those used for the X65 mild steel surface. The good reproducibility of the potentiodynamic measurements (discussed further below) and the absence of any unexplained variations in the obtained polarization curves, was taken as confirmation that the formation of the passive layer was circumvented.

B.4.4: Results and Discussion

The polarization behavior in CO_2-saturated mildly acidic solutions was experimentally investigated on 316L stainless steel and API 5L X65 mild steel surfaces. The experiments were done in the pH range of 4 to 6 at CO_2 partial pressures from 1 to 15 bar. In view of the findings in Chapter B.2: and Chapter B.3: , the present experiments were conducted mostly at 10°C, in order to allow for proper investigation of the polarization behavior of the system. However, the effect of temperature is discussed in a separate set of experiments, as discussed in more detail in the following sections.

The cathodic polarization curves obtained for the 316L stainless steel surface are shown in Figure B.4-3. The polarization curves reported here all consist of a linearly increasing range at low current densities, followed by the observation of mass transfer limiting current, and a secondary linearly increasing range of current densities at more negative potential, associated with the reduction of water. Nevertheless, at pH 6, while similar characteristic ranges are present, they are not as easily distinguishable due to the

smaller gap between the H^+ reduction line at less negative potentials and the water reduction line that occurs at more negative potentials.

The first linear section at low current density range is of particular interest in the present discussion, as it represents the charge transfer controlled cathodic current density. As discussed above, this range of current densities are expected to reveal the electrochemical activity of the involved carbonate species. The reported polarization curves with increasing pCO_2 values clearly show that, at a given pH, the cathodic currents in that range are insensitive to pCO_2. This observation indicated that H_2CO_3 is not a significant electro-active species and the cathodic currents are only the result of H^+ reduction. More specifically, considering the results obtained at pH 6 and 15 bar CO_2, where the concentration of H_2CO_3 is 700 times higher than that of H^+ (see Figure B.4-7.A), suggests that the H^+ reduction reaction is the dominating cathodic reaction. This observation is found to agree well with those in Chapter B.2: and Chapter B.3: , suggesting that H_2CO_3 is not directly reduced on the steel surface.

The limiting current densities are, on the other hand, significantly influenced by pCO_2, as expected. The presence of CO_2 and H_2CO_3 are known to increase the limiting current via two processes:

- H_2CO_3 as weak acid with a relatively high equilibrium constant (pKa=3.5) and fast kinetics of dissociation ($k=10^8$ s^{-1}), it also is an effective buffer. When present in the solution H_2CO_3 readily dissociates as the surface pH is increased at limiting current condition, in order to maintain its chemical equilibrium. This process acts

as an additional source of H^+ ions inside the boundary layer, hence results in increased limiting current densities.

- H_2CO_3 is also involved in the CO_2 hydration equilibrium. Considering the low equilibrium constant of this reaction, only a small fraction (~0.2 %) of $CO_2(aq)$ reacts to form H_2CO_3. Therefore, there is a large reservoir of $CO_{2(aq)}$ present in the solution to replenish the H_2CO_3 concentration as it is consumed by the dissociation reaction. In that sense, the concentration of H_2CO_3 itself is also buffered by the hydration reaction while, unlike H_2CO_3 dissociation, this reaction is limited by slow kinetics.
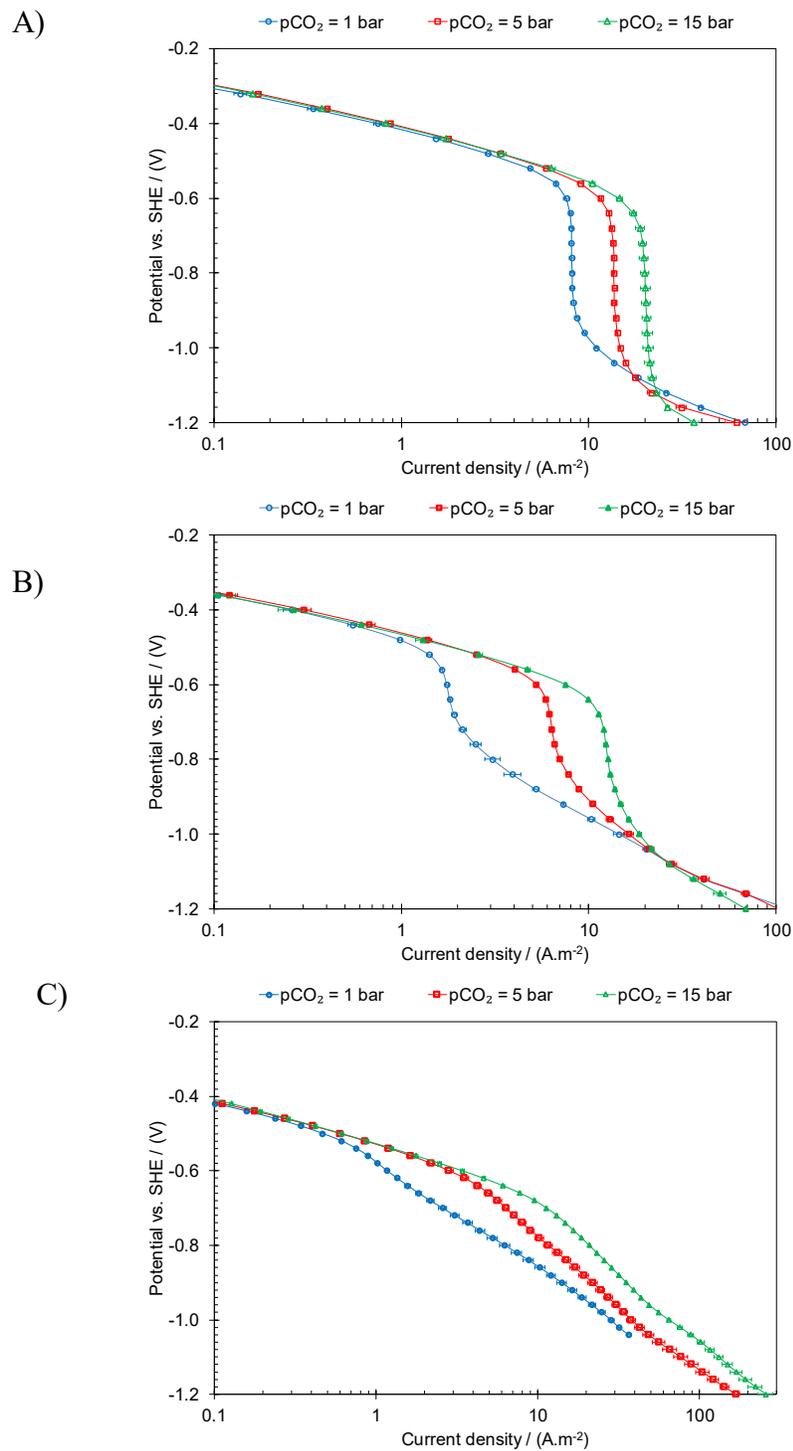
Figure B.4-3. The steady state cathodic polarization curves obtained on 316 L stainless steel at 10°C, 0.1 M NaCl, 4.6 m.s⁻¹ flow velocity, at pCO_2 of 1, 5, and 15 bar. A) pH 4. B) pH 5. C) pH 6. The error bars show the standard deviation for at least three repeated experiments.

The linear range of current densities observed at potentials more negative than those where the limiting current is seen, associated with the water reduction reaction, shows some variation with pCO_2. As is apparent from Figure B.4-3, this effect is more pronounced as the bulk pH was increased. Similar behavior was also reported previously in CO_2-saturated solutions as well as in solutions containing acetic acid [198,201]. Such an influence can be associated with secondary effects relating to CO_2 or carbonate species on the surface (e.g., adsorption) or the extreme surface pH values that are reached at such negative potentials. Nevertheless, the exact mechanism behind this behavior is not clearly understood.

The polarization behavior of the API 5L X65 mild steel in CO_2-saturated solutions in the pH range from 4 to 6 and pCO_2 from 1 to 15 bar is shown in Figure B.4-4. At pH 4, the cathodic polarizations curves show the charge transfer controlled cathodic currents in an extended range as seen in Figure B.4-4.A; where increasing the pCO_2 from 1 to 15 bar did not result in any appreciable change in the current densities of that range. This was found to be in agreement with that observed on the stainless steel surface in Figure B.4-3 and those reported earlier in Chapter B.2: and Chapter B.3: . This behavior indicates that the direct reduction of H_2CO_3 is insignificant on a mild steel surface. On the other hand, the cathodic limiting current densities were significantly influenced by pCO_2, as discussed above.

The anodic polarization curves in Figure B.4-4.A demonstrate a linearly increasing range at the potentials just above the OCP, which is associated with the active dissolution range of the iron oxidation reaction. At higher potentials, an abrupt increase

of the Tafel slope was observed. This range of current densities is categorized as the transition range, which is expected to be followed by another linear range of current densities observed in the pre-passivation range [72,210]. Similar behavior was reported previously for iron dissolution from mild steel in CO_2-saturated solutions [210]. In the results reported here, the electrochemical response in the active dissolution range was insensitive to pCO_2, while a significant influence of pCO_2 on the magnitude of the current maximum in the transition range was observed. The pre-passivation range was not observed clearly in the experimental data obtained at this condition due to practical measurement limitations at those extreme current densities. The observed behavior of the anodic polarization curve was in reasonable agreement with those in the previous studies [198,210]. The pCO_2 independent active dissolution range as well as the strong pCO_2 dependence of the current maximum in the transition range has been reported in Chapter B.3: and also in previous studies [198,210].
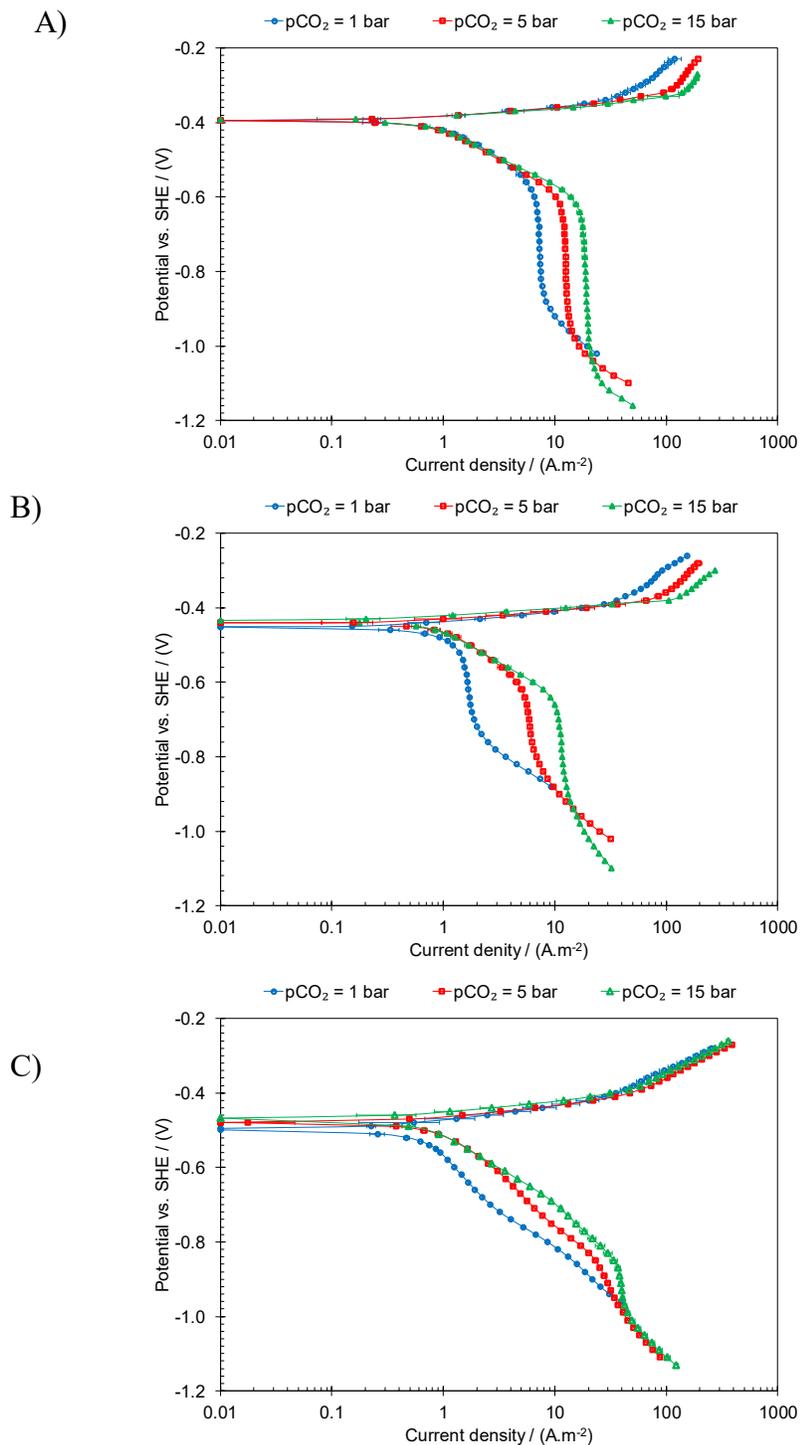
Figure B.4-4. The steady state cathodic polarization curves obtained on API 5L X65 mild steel at 10°C, 0.1 M NaCl, 4.6 m.s^{-1} flow velocity, at pCO$_2$ of 1, 5, and 15 bar. A) pH 4. B) pH 5. C) pH 6. The Error bars show the standard deviation of at least three repeated experiments.

The experimental data obtained at pH 5 were found to be in agreement with those for pH 4, as shown in Figure B.4-4.B. However, at 1 bar CO_2, the cathodic currents were to some degree under mass transfer influence. That would result in some increase of the surface pH at the vicinity of OCP. The small deviations in the active dissolution range on anodic currents can be associated with this effect. Besides that, the charge transfer controlled cathodic currents observed at 5 and 15 bar CO_2 did not show any influence that could be associated with the direct reduction of H_2CO_3. The significant influence of pCO_2 on the anodic current maximum of the transition range was observed at pH 5, similar to that seen at pH 4.

At pH 6, the polarization data showed some significantly different characteristic behaviors, as shown in Figure B.4-4.C. At pH values of 4 and 5, a single limiting current was observed at about -0.6 V (vs. SHE) which was associated with the mass transfer of H^+ and H_2CO_3 and the kinetically limited CO_2 hydration reaction. At pH 6, in addition to that, a secondary limiting current at about -0.9 V (vs. SHE) was observed. The magnitude of the first limiting current observed at pH 6 was found to be nearly similar to that observed at pH 4 and pH 5. Considering the high pCO_2 (in the case of 5 and 15 bar) and the high flow velocity, pH effect on the limiting current density is expected to be small. That can be seen when comparing the limiting current at 15 bar CO_2 at pH 4 (19 $A.m^{-2}$) with that observed at pH 5 (12 $A.m^{-2}$). Therefore, the first limiting current observed at pH 6 can be associated with the same process. That is, H^+ reduction buffered by the H_2CO_3 dissociation reaction.

At 1 bar CO_2, the cathodic current is completely controlled by the limiting current. However, at 5 and 15 bar CO_2 the linear range of cathodic currents just below the OCP and before the first limiting current indicates a charge transfer controlled range. This range of cathodic current was also found to be insensitive to pCO_2, as expected when H_2CO_3 is not electrochemically active. This observation is of importance since it significantly extends the range of validity of the previous arguments on the electrochemical activity of H_2CO_3 on the mild steel surface, similar to that discussed for the case of stainless steel.

The cathodic currents observed below the first limiting current can therefore be associated with the effect of HCO_3^-. Similarly to H_2CO_3, the conventional mechanistic view of CO_2 corrosion assumes that HCO_3^- is also electrochemically active [20,28,43,55,100,103]. This reaction was believed to be only significant at a near neutral pH range such as for the conditions associated with Figure B.4-4.C. Similar to the case of H_2CO_3, arguments for the electrochemical activity of HCO_3^- and its ability to buffer the H^+ concentration as a weak acid can be put forward. In the mechanistic studies of corrosion in the presence of weak acids it is common to readily associate the observation of a secondary limiting current with the direct reduction of the weak acid, i.e., the arguments used for the case of H_2S [13,16,17] or sulfurous acid [251]. On the other hand, even though the current densities after the first limiting current is significantly increased when comparing the polarization curves at pCO_2 of 5 and 15, the charge transfer controlled range before the first limiting current is not affected. That may suggest the appearance of this secondary wave is not an electrochemical process. It appears that a secondary

buffering process due to the dissociation of HCO_3^- is initiated as a result of high surface pH at such conditions. This behavior is further examined quantitatively in the following sections.

The anodic polarization at pH 6 was also found to behave differently from those observed at pH 4 and 5. The most significant aspect is the absence of the transition range and its corresponding current maximum. Beside the slight deviation at 1 bar CO_2 caused by the change in surface pH as a result of mass transfer limited current densities, the pCO_2 dependence observed at pH 6 was somewhat lower than that observed in the results obtained at pH 4 and 5. That includes the current densities associated with the pre-passivation range at higher potentials, identified by the higher Tafel slope. These observations suggest a rather significant change of the iron dissolution mechanism with pH.

The experimentally obtained corrosion rates are shown in Figure B.4-5. The trends in corrosion rates were found to be in good agreement with that expected from the polarization measurements in Figure B.4-4. At these conditions, in the vicinity of the corrosion potential, the cathodic current was mostly under charge transfer control and the anodic current was in the active dissolution range. As discussed above, in the absence of the direct reduction of H_2CO_3, neither the cathodic nor the anodic currents have a significant dependence on pCO_2. That is also reflected in the measured corrosion rates, which further supports the aforementioned mechanistic arguments.
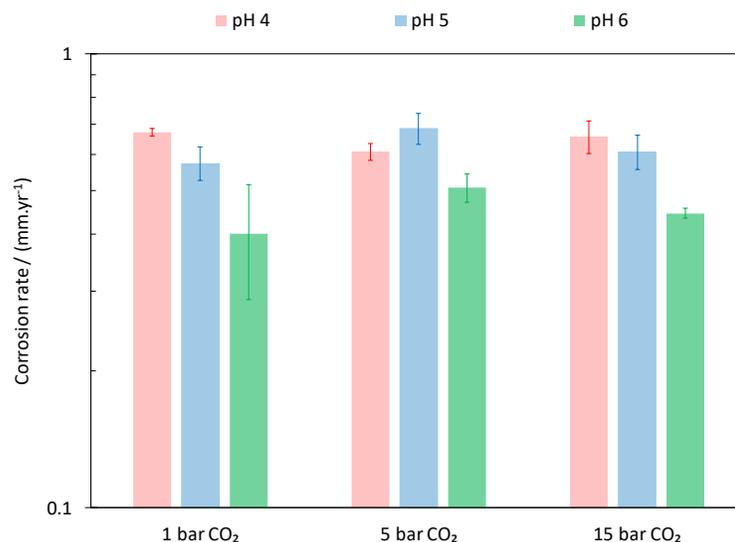
Figure B.4-5. The measured corrosion rates at 10ºC, 4.6 m.s^{-1} TCFC flow, and 0.1 M NaCl on a API 5L X65 mild steel. Error bars represent the standar devation of at least three seperate measurements.

B.4.5: Model development

B.4.5.1: Water chemistry calculation

As the first step in a quantitative discussion of the polarization curves and corrosion rate data, the solution speciation has to be obtained. That is essential to determine the concentration of the involved chemical species, in order to establish their chemical and electrochemical contributions to the overall process. The reactions associated with the chemical equilibria of a H_2O/CO_2 system in an acidic solution were shown above via Reactions (B.4-1) through (B.4-5). The solution speciation can be obtained by finding the concentrations that satisfy all the equilibrium expressions associated with these homogeneous chemical reactions. Reactions (B.4-1) to (B.4-4) describe CO_2 dissolution, hydration and dissociation in acidic environments, and Reaction (B.4-5) is water dissociation.

Carbon dioxide's dissolution equilibrium, Reaction (B.4-1), can be quantified in terms of a modified Henry's law based on the Kriechevsky-Kasarnovsky treatment[252], which has been frequently used to assess CO_2 solubility in water [249,253,254]:

$$\frac{f_{CO_2}}{a_{CO_2}} = K_{H,CO_2} e^{\left(\int_{P_{ws}}^{P} \frac{\overline{V}_{m,CO_2}}{RT} dP\right)} \qquad (\text{ B.4-11 })$$

where, on the left hand side, the numerator is the fugacity of CO_2 (bar) in the gas phase ($f_{CO_2} = p_{CO_2}\varphi_{CO_2}$), where p_{CO_2} is the partial pressure of CO_2 (bar), and the denominator is the activity of CO_2 in the solution ($a_{CO_2} = m_{CO_2}\gamma_{CO_2}$), where m is the molal concentration of CO_2. It should be noted that the water chemistry calculations in CO_2/H_2O systems have been conventionally done on molal concentration basis, which is followed in this discussion as well. In order to couple this calculation with the electrochemical model that is conventionally developed on the molar based concentrations, the proper unit conversion should be considered.

On the right hand side, K_{H,CO_2} is the Henry's constant at saturation pressure of water as shown below in Equation (B.4-14), and the exponential term in Equation (B.4-11) is the so-called Poynting pressure correction factor that essentially accounts for the change of Henry's constant with pressure. The integral domain in Equation (B.4-11) is from water saturation pressure (P_{ws} defined in Table B.4-7) to the total pressure of the system (in bar), suggesting that this parameter is significant only at high pressures. The partial molar volume of CO_2 in the aqueous phase, $\overline{V}_{m,CO_2}$ in m^3/mol, appearing in Equation (B.4-11) was determined by Garcia et al.[255] and it is reworked to be expressed in terms of Kelvin temperature as shown in Table B.4-7. For a binary H_2O/CO_2 system,

carbon dioxide partial pressure is $P_{CO_2} = P_{tot} - P_{ws}$, with P_{tot} being the total pressure of

the system and P_{ws} being the saturation pressure of water (bar).

In the literature on the equilibrium and speciation of the CO_2/H_2O system, it is

customary to lump the concentration of the dissolved CO_2 with carbonic acid to define

$C_{CO_2^*(aq)} = C_{CO_2(aq)} + C_{H_2CO_3(aq)}$. Therefore, the equilibria is discussed in terms of

Reaction (B.4-12) and Reaction (B.4-13), where carbonic acid is not explicitly

considered.

$$CO_{2(g)} \rightleftharpoons CO_{2(aq)}^* \qquad\qquad\qquad (\text{B.4-12})$$

$$CO_{2(aq)}^* + H_2O_{(l)} \rightleftharpoons HCO_3^-{}_{(aq)} + H^+{}_{(aq)} \qquad\qquad\qquad (\text{B.4-13})$$

Fortunately, incorporating the effect of the hydration step (Reaction (B.4-2)) and

carbonic acid into existing equilibrium constants based on CO_2^* (denoted by asterisk in

the discussion below) is a matter of simple mathematical manipulation. It can be shown

that:

$$K_{H,CO_2^*}^* e^{\left(\int_{P_{ws}}^{P} \frac{\overline{V}_{m,CO_2}}{RT} dP\right)} = \frac{f_{CO_2}}{a_{CO_2^*}} = \frac{f_{CO_2}}{a_{CO_2} + a_{H_2CO_3}} = \frac{f_{CO_2}}{a_{CO_2}(1 + K_{hyd})}$$

Hence:

$$K_{H,CO_2} = \left(1 + K_{hyd}\right) K_{H,CO_2^*}^* \qquad\qquad\qquad (\text{B.4-14})$$

The $K_{H,CO_2^*}^*$ term in Equation (B.4-14) is the Henry's constant at water saturation

pressure on the basis of CO_2^* concentration, which can be obtained using the expression

developed by Li and Duan [209], shown in Table B.4-7.

The fugacity coefficient of $CO_{2(g)}$, ϕ_{CO_2}, required in Equation (B.4-11) was

calculated based on the empirical expression proposed by Duan et al. [214], which was

shown to agree well with the more complex iterative calculations of the fifth order virial equation of state used in their earlier study [250]. The empirical relationship provided in Table B.4-7 is valid for pressures up to CO_2 saturation pressure (P_{CO_2S} in Table B.4-3) when $T<305$ and, at $305<T<405$ up to $P= 75+(T-305)\times1.25$.

Table B.4-3. Temperature dependence of the physiochemical properties.

Parameter	Relationship	Reference
Water density (kg/m³)	$\rho_w = 753.596 + 1.87748\,T - 0.003562\,T^2$	15
Water viscosity (cP)	$\mu = \mu_{ref}10^{\left(\frac{1.1709\,(T_{ref}-T)-0.001827(T_{ref}-T)^2}{(T-273.15)+89.93}\right)}$ $T_{ref} = 293.15\,K, \mu_{ref} = 1.002\,cP$	79
Diffusion coefficient *	$D_i = D_{i,ref}\dfrac{T}{T_{ref}}\dfrac{\mu_{ref}}{\mu}$	
Saturation pressure of CO_2 (mm Hg)	$\log(P_{CO_2S}) = 7.58828 - \dfrac{861.82}{(T-273.15)+271.883}$	256

* Reference values are listed in Table B.4-9.

Following the dissolution step, the dissolved CO_2 is involved in a series of homogeneous reactions as shown via Reactions (B.4-2) through (B.4-5). Using a generic notation, the single phase chemical equilibrium for any reaction j, with n_r reactants and n_p products takes the form of:

$$\sum_{m=1}^{n_r} R_m \rightleftharpoons \sum_{n=1}^{n_p} P_n \qquad\qquad\text{(B.4-15)}$$

and can be further expressed as:

$$\frac{\prod_{n=1}^{n_p} a_{P_n}}{\prod_{m=1}^{n_r} a_{R_m}} = \frac{k_{f,j}}{k_{b,j}} = K_j \qquad\qquad\text{(B.4-16)}$$

On the basis of Equation (B.4-15), the mathematical relationships as it relates to CO_2/H_2O equilibria, Reactions (B.4-2) through (B.4-5), are listed in Table B.4-7.

These relationships are expressions in terms of chemical activity of the involved species, where: $a_i = m_i\gamma_i$. In the solutions with low ionic strength, where an ideal solution approximation is valid, the activity coefficients may be assumed to be unity ($\gamma_i \to 1$), hence the activity terms could be assumed equal to the corresponding concentrations. On the other hand, in concentrated solutions, the activity coefficients may significantly deviate from unity, making an explicit calculation of this parameter inevitable. The latter case is discussed in Section B.4.5.1.1: below.

Table B.4-4. Equilibrium relationships for the CO_2/H_2O system.

Reaction (B.4-2)	$\dfrac{a_{H_2CO_{3(aq)}}}{a_{CO_{2(aq)}} a_{H_2O}} = K_{hyd}$	(B.4-17)
Reaction (B.4-3)	$\dfrac{a_{HCO_3^-{}_{(aq)}} a_{H^+{}_{(aq)}}}{a_{H_2CO_{3(aq)}}} = K_{ca}$	(B.4-18)
Reaction (B.4-4)	$\dfrac{a_{CO_3^{2-}{}_{(aq)}} a_{H^+{}_{(aq)}}}{a_{HCO_3^-{}_{(aq)}}} = K_{bi}$	(B.4-19)
Reaction (B.4-5)	$\dfrac{a_{OH^-{}_{(aq)}} a_{H^+{}_{(aq)}}}{a_{H_2O}} = K_w$	(B.4-20)
Reaction (B.4-50)	$\dfrac{a_{HCO_3^-{}_{(aq)}}}{a_{CO_{2(aq)}} a_{OH^-{}_{(aq)}}}$ $= K_{ca} \times K_{hyd}/K_w$	(B.4-21)
Reaction (B.4-51)	$\dfrac{a_{CO_3^{2-}{}_{(aq)}} a_{H_2O}}{a_{HCO_3^-{}_{(aq)}} a_{OH^-{}_{(aq)}}} = K_{bi}/K_w$	(B.4-22)

The CO_2 hydration reaction and its equilibrium constant, K_{hyd}, have been discussed in a number of different studies over the past few decades [90,97,208,216–218]. However, the value of this parameter is known with the least certainty amongst all equilibrium constants in the CO_2/H_2O system, perhaps due to the experimental difficulty

of distinguishing carbonic acid from the dissolved CO_2. On the other hand, the equilibrium constant of the dissociation reaction in terms of CO_2^* (Reaction (B.4-13)) is well known. A simple mathematical manipulation based on the definition of equilibrium constants reveals the relationship between K_{Ca}^*, K_{hyd}, and K_{Ca} , where K_{Ca}^* , is the equilibrium constant of Reaction (B.4-13)(B.3-10), and K_{Ca} is the true dissociation constant of carbonic acid as shown via Reaction (B.4-3).

$$K_{Ca}^* = \frac{a_{HCO_3^-{}_{(aq)}} a_{H^+{}_{(aq)}}}{a_{CO_2^*{}_{(aq)}}} = \frac{a_{HCO_3^-{}_{(aq)}} a_{H^+{}_{(aq)}}}{a_{CO_2{}_{(aq)}} + a_{H_2CO_3{}_{(aq)}}} = \frac{a_{HCO_3^-{}_{(aq)}} a_{H^+{}_{(aq)}}}{a_{H_2CO_3{}_{(aq)}} \left(1 + {}^{1}\!/\!{K_{hyd}}\right)}$$

Hence:

$$K_{Ca} = \left(1 + {}^{1}\!/\!{K_{hyd}}\right) K_{Ca}^* \qquad\qquad (\text{B.4-23})$$

Equation (B.4-23) shows that the known value of either K_{Ca} or K_{hyd} alongside with the known K_{Ca}^* that can be used to obtain the third parameter.

A number of experimental measurements of pK_{Ca} reported in the literature are collected in Table B.4-5, earlier studies on this are reviewed by Kern [217] and are omitted from this table. The reported pK_{Ca} values show a rather significant scattering, especially those obtained in earlier studies as compared to the more recent reported values. In addition to inherent uncertainties of equilibrium constant measurements, the fact that carbonic acid dissociation is greatly affected by the non-ideal solution chemistry can be the source of the observed scattering. The calculation of activity coefficients at 25°C for 0.1 and 0.5 m NaCl concentrations shows a factor of 1.4 and 2 difference (0.15 and 0.3 pK units) between the apparent equilibrium constant and that at infinitely dilute solution, respectively (see Section B.4.5.1.1: for a detailed discussion). In order to determine the

pK_{Ca} values from indirect methods (e.g. spectroscopic pH measurements), a rather extensive water chemistry calculation (similar to the subject of this section) is usually required in the data analysis [208,218,222]. Hence, values can only be obtained with sufficient confidence if the non-ideal behavior is meticulously accounted for in data analysis. Knowing that when the indirect methods are in use, the post correction of the final results may not necessarily provide the correct estimation of pK_{Ca} at infinite dilution.

Table B.4-5. Reported values of carbonic acid dissociation constant (K_{Ca}) at 25°C.

Reference	pK_{Ca}
Pines et al. (2016) [222]	3.49
Wang et al. (2010) [218]	3.70[a]
	3.53[b]
Adamczyk et al. (2009) [223]	3.45
Soli and Byrne (2002) [208]	3.42[c]
Wissbrun et al. (1954) [221]	3.76
Roughton (1941) [257]	3.60
This study	3.49

[a] originally reported values based on unspecified reference of K_{Ca}^*.
[b] recalculated based of reported K_{hyd} and K_{Ca}^* from Duan and Li [249].
[c] authors calculated this value from measured $pK_{Ca} = 3.04$ at 0.65 m NaCl, using the correction for activities from Harned and Bonner [258].

If the K_{hyd} is obtained from K_{Ca} values through Equation (B.4-23), the above mentioned uncertainties are carried over into this estimated value. In fact, the value of $K_{hyd} = 2.58\text{E-}3$ that is commonly used in the literature [15,28,97,163,219,259] is based on the pK_{Ca} reported by Wissbrun et al. [221]. That value is placed at the higher end of the reported range of equilibrium constants, as shown in Table B.4-5. Other reported pK_{Ca}

values would result in significantly different K_{hyd}. For example, the $pK_{Ca} = 3.42$, reported by Soli and Byrne [208] results in $K_{hyd} = 1.15E\text{-}3$.

A)

B)
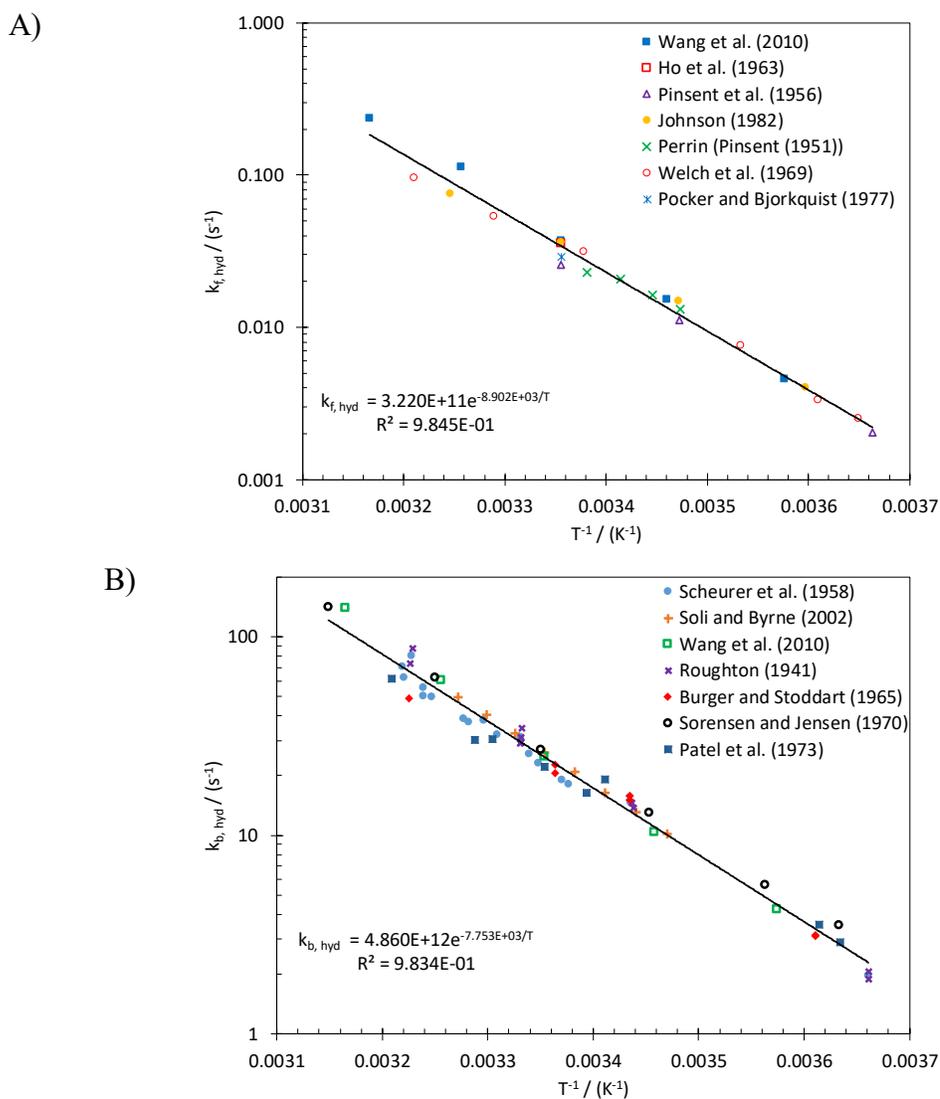
Figure B.4-6. Experimental values of A) $k_{f,hyd}$ from Wang et al. [218], Ho and Sturtevant [260], Pinsent et al. [261], Johnson [262], Perrin [263], Welch et al. [264], and Pocker and Bjorkquist [265]. B) $k_{b,hyd}$ from Scheurer et al. [266], Soli and Byrne [208], Wang et al. [218], Roughton [257], Burger and Stoddart [267], Sorensen and Jensen [268], and Patel et al. [269].

The value of K_{hyd} can also be obtained from the kinetic rate constants of the forward and backward CO_2 hydration reaction based on $K_{hyd} = k_{f,hyd}/k_{bhyd}$. Unlike K_{Ca},

K_{hyd} is not significantly influenced by non-ideal chemistry of the solution. As is apparent

from Equation (B.4-17), K_{hyd} is a function of the activity of the neutral species, CO_2,

H_2CO_3, and H_2O, none of which is profoundly affected by the non-ideality of the

solution. Therefore, one can conclude that the values obtained from $K_{hyd}=k_{f,hyd}/k_{bhyd}$ are

more reliable, at least as far as it concerns the effect of non-idealities.

In the present study, the kinetic rate constants are re-evaluated from a number of

experimental data sources previously reported in the literature, excluding those where

K_{Ca} was used in data analysis. As shown in Figure B.4-6.A and Figure B.4-6.B, the

temperature dependence correlation for the rate constants were obtained based on the

Arrhenius law:

$$k = A_0 e^{(-\frac{E_a}{RT})}$$
(B.4-24)

A_0, the pre-exponent parameter, and E_a, the activation energy in Equation (B.4-24), for

$k_{f,hyd}$, k_{bhyd}, and K_{hyd} are listed in Table B.4-6. These results show that K_{hyd} is a weak

function of temperature when comparing the activation energy with those of the forward

and backward rate constants. That is in accord with what is reported in the literature. [97,208]

Table B.4-6. The Arrhenius parameters for the kinetics rate constants and the equilibrium constant of CO_2 hydration reaction (from 0 to 45 °C).

Parameter	A_0 (s^{-1})	E_a (kJ)
$k_{f,hyd}$ (s^{-1})	3.22E11	74.011
$k_{b,hyd}$ (s^{-1})	4.86E12	64.485
K_{hyd}	6.633E-2	9.526

The value of K_{hyd} obtained in the present study (Table B.4-6), alongside with K_{Ca}^*

from Duan and Li [209,249] (shown in Table B.4-7) was used to obtain the K_{Ca} at an

extended temperature and pressure range. Considering the small effect of non-ideality

and temperature on K_{hyd}, the resulting values can be considered to reasonably represent

the true equilibrium constant of carbonic acid dissociation. As shown in Table B.4-5, this

procedure results in an estimated $K_{ca} = 3.49$ at 25 °C, which is in a reasonable

agreement with the values obtained in the more recent studies [218,222,223].

The temperature-pressure dependence relationship developed by Li and Duan

[209,249], describing the equilibrium constant of carbonic acid dissociation on the basis of

CO_2^* concentration (K_{ca}^*), was used in the present study and is shown in Table B.4-7. A

similar relationship was developed by the authors to describe the temperature-pressure

dependence of the bicarbonate ion dissociation equilibrium constant (K_{bi}) [209,224] (Table

B.4-7), which was used in the present study according to Equation (B.4-19).

The water dissociation equilibrium, Reaction (B.4-5), is mathematically

described by Equation (B.4-20), where a_{H_2O} is the activity of water that can be assumed

to be unity in ideal solutions. The values for the equilibrium constant (K_w) can be

obtained from the formulation introduced by Marshall and Frank [64], as shown in Table

B.4-7.

In addition to the abovementioned mathematical expressions that represent the

CO_2/H_2O equilibria, in the absence of an electric field, the concentration of ions must

also satisfy the charge balance as shown by Equation (B.4-25). The equation is

commonly known as the electro-neutrality constraint and it is of fundamental importance

in defining the solution speciation in the presence of ionic species.

$$\sum_i z_i m_i = 0 \qquad\qquad (\text{B.4-25})$$

Table B.4-7. The parameters of the CO_2/H_2O Equilibrium calculation.*

Param.	$\bar{V}_{m,CO_2}$ ** [209] (cm³.mol⁻¹)	K^*_{H,CO_2^*} † [209] (bar.m⁻¹)	φ_{CO_2} †† [214]	K^*_{ca} [224] ♮ (m)	K^*_{bi} [224] ♮ (m)	K_w [64] ♮♮ (m²)	P_{ws} [270] ♭ (bar)
a_1	139.181	1.3000 E1	1.0000	233.51593	-151.1815	-4.098	1.167 E3
a_2	-6.8622 E-1	-1.3341 E-2	4.7587 E-3	0.0000	-0.0887	-3245.2	-7.242 E5
a_3	1.2873 E-3	-5.5898 E2	-3.3570 E-6	-11974.3835	-1362.2591	2.2362	-1.707 E1
a_4	-5.044 E-7	-4.2258 E5	0.0000	0.0000	0.0000	-3.984 E7	1.202 E5
a_5	NA	NA	-1.3179	-36.5063	27.7980	13.957	-3.233 E6
a_6	NA	NA	-3.8389 E-6	-450.8005	-29.5145	8.5641 E5	1.492 E1
a_7	NA	NA	0.0000	21313.1885	1389.0154	NA	-4.823 E3
a_8	NA	NA	2.2815 E-3	67.1427	4.4196	NA	4.051 E5
a_9	NA	NA	0.0000	0.0084	0.0032	NA	-2.386 E-1
a_{10}	NA	NA	0.0000	-0.4015	-0.1644	NA	6.502 E2
a_{11}	NA	NA	0.0000	-0.0012	-0.0005	NA	NA

*   The a_i values are rounded to four digits after the decimal.

** $\bar{V}_{m,CO_2} = a_1 + a_2\,T + a_3\,T^2 + a_4\,T^3$

† $\ln\left(K^*_{H,CO_2^*}\right) = a_1 + a_2 T + \dfrac{a_3}{T} + \dfrac{a_4}{T^2}$

†† $\phi_{CO_2} = a_1 + \left[a_2 + a_3 T + \dfrac{a_4}{T} + \dfrac{a_5}{T-150}\right]P + \left[a_6 + a_7 T + \dfrac{a_8}{T}\right]P^2$

♮ $\ln(par.) = a_1 + a_2\,T + \dfrac{a_3}{T} + \dfrac{a_4}{T^2} + a_5\,\ln(T) + \left(\dfrac{a_6}{T} + \dfrac{a_7}{T^2} + \dfrac{a_8}{T}\ln T\right)$

         $+ \left(\dfrac{a_9}{T} + \dfrac{a_{10}}{T^2} + \dfrac{a_{11}}{T}\ln T\right)(p - p_s)^2$

     $P_s=1$ if $T<373.15$, $P_s=P_{ws}$ if $T>373.15$.

♮♮ $-\log(K_w) = a_1 + \dfrac{a_2}{T} + \dfrac{a_3}{T^2} + \dfrac{a_4}{T^3} + \left(a_5 + \dfrac{a_6}{T} + \dfrac{a_7}{T^2}\right)\log(10^{-3}\rho_w)$

♭ $P_{ws} = 10\left[\dfrac{2C}{-B + (B^2 - 4AC)^{0.5}}\right]^4$

     $A = \theta^2 + a_1\theta + a_2$; $B = a_3\theta^2 + a_4\theta + a_5$; $C = a_6\theta^2 + a_7\theta + a_8$; $\theta = T + \dfrac{a_9}{T - a_{10}}$

The additional cations and anions in the solution may alter the speciation from the

"natural" state of a pure H_2O/CO_2 system. This can be due to the change in activity

coefficients in the presence of a significant amount of any dissolved species, as discussed below in section B.4.5.1.1: . The effect of natural salts such as chloride salts (e.g. NaCl, KCl) on the solution speciation is an example of such scenario. In addition to the effect on activity coefficients, the presence of ions may change the speciation by altering the charge balance in the solution, as described by the electroneutrality equation. This is the case when the additional species consists of an ion that is involved in the chemical equilibrium of the system, coupled with a "conserved" ion. The conserved ions are not involved in chemical equilibrium and their concentration is not directly affected by the environmental conditions, pCO_2 and the solution pH. Such chemical compounds can be grouped as either strong acids (e.g. hydrochloric acid), strong bases (e.g. sodium hydroxide), or non-neutral salts (e.g. carbonate, and bicarbonate salts). It is worthwhile to notice their difference with neutral salts (e.g. sodium chloride) where the corresponding terms for the cation and the anion concentrations always cancel out in the electro-neutrality equation. As a generic rule, the concentration of the ions involved in the chemical equilibria are bound to compensate for any charge imbalance of the conserved ions. This criteria is used to determine the solution speciation in the presence of various ionic species, as discussed further in the following sections.

B.4.5.1.1: Non-ideal aqueous phase

In dilute solutions, it can be assumed that the activity coefficients are close to unity, however, as the concentration of dissolved species increases, this assumption may result in significant miscalculation of the equilibrium speciation. In the latter case, the activity coefficients should be determined and included in water chemistry calculations.

In the present study, the activity coefficients are obtained using the well-known specific interaction Pitzer equations. This approach is commonplace in calculation of activity coefficients of complex electrolytes with high ionic strength, and has been used extensively for H_2O/CO_2 systems containing various ionic species. Based on Pitzer equations, the activity coefficients of cations (M), anions (X), and neutral species (N) can be calculated via Equations (B.4-26) to (B.4-28), respectively.

$$ln(\gamma_M) = z_M^2 F + \sum_{a=1}^{N_a} m_a \left(2B_{Ma} + ZC_{Ma}\right) + \sum_{c=1}^{N_c} m_c \left(2\Phi_{Mc} + \sum_{a=1}^{N_a} m_a \psi_{Mca}\right)$$
$$+ \sum_{a=1}^{N_a-1} \sum_{a'=a+1}^{N_a} m_a m_{a'} \psi_{aa'M} + |z_M| \sum_{c=1}^{N_c} \sum_{a=1}^{N_a} m_c m_a C_{ca} + \sum_{n=1}^{N_n} 2m_n \lambda_{nM}$$

(B.4-26)

$$ln(\gamma_X) = z_X^2 F + \sum_{c=1}^{N_c} m_c \left(2B_{cX} + ZC_{cX}\right) + \sum_{a=1}^{N_a} m_a \left(2\Phi_{Xa} + \sum_{c=1}^{N_c} m_c \psi_{Xac}\right)$$
$$+ \sum_{c=1}^{N_c-1} \sum_{c'=c+1}^{N_c} m_c m_{c'} \psi_{cc'X} + |z_X| \sum_{c=1}^{N_c} \sum_{a=1}^{N_a} m_c m_a C_{ca} + \sum_{n=1}^{N_n} 2m_n \lambda_{nX}$$

(B.4-27)

$$ln(\gamma_N) = \sum_{n=1}^{N_n} 2m_n \lambda_{Nn} + \sum_{c=1}^{N_c} 2m_c \lambda_{Nc} + \sum_{a=1}^{N_a} 2m_a \lambda_{Na} + \sum_{c=1}^{N_c} \sum_{a=1}^{N_a} m_c m_a \xi_{Nca}$$

(B.4-28)

Furthermore, the activity of water, as the solvent, is defined via:

$$ln\left(a_{H_2O}\right) = -\frac{MW_{H_2O}\, \phi}{1000} \sum_i m_i$$

(B.4-29)

with molecular weight of water, $MW_{H_2O} = 18.015$, and the osmotic pressure (ϕ) obtained through Equation (B.4-30):

$$(\phi - 1) = \frac{2}{\Sigma_i m_i} \left(-\frac{A^\phi I^{3/2}}{1 + b\, I^{1/2}} \right) \left[\sum_{c=1}^{N_c} \sum_{a=1}^{N_a} m_c m_a \left(B_{ca}^\varphi + Z C_{ca} \right) \right.$$

$$+ \sum_{c=1}^{N_c - 1} \sum_{c'=c+1}^{N_c} m_c m_{c'} \left(\Phi_{cc'}^\varphi + \sum_{a=1}^{N_a} m_a \psi_{cc'a} \right)$$

$$+ \sum_{a=1}^{N_a - 1} \sum_{a'=a+1}^{N_a} m_a m_{a'} \left(\Phi_{aa'}^\varphi + \sum_{c=1}^{N_c} m_c \psi_{aa'c} \right)$$

$$+ \sum_{n=1}^{N_n} \sum_{a=1}^{N_a} m_n m_a \lambda_{na} + \sum_{n=1}^{N_n} \sum_{c=1}^{N_c} m_n m_c \lambda_{nc} + \left. \sum_{n=1}^{N_n} \sum_{c=1}^{N_c} \sum_{a=1}^{N_a} m_n m_c m_a \xi_{nca} \right]$$

(B.4-30)

The parameters F, C_{MX}, and Z appearing in Equations (B.4-26), (B.4-27), and (B.4-30) are defined as:

$$F = -A^\phi \left(\frac{I^{1/2}}{1 + b\, I^{1/2}} + \frac{2}{b} \ln \left(1 + b\, I^{1/2} \right) \right) + \sum_{c=1}^{N_c} \sum_{a=1}^{N_a} m_c m_a B_{ca}' + \sum_{c=1}^{N_c - 1} \sum_{c'=c+1}^{N_c} m_c m_{c'} \Phi_{cc}'$$

$$+ \sum_{a=1}^{N_a - 1} \sum_{a'=a+1}^{N_a} m_a m_{a'} \Phi_{aa}'$$

(B.4-31)

$$Z = \sum_i |z_i| m_i$$

(B.4-32)

where A^ϕ is one third of the Dubye-Huckel limiting slope with value of 0.392 at 25°C. A^ϕ is discussed in detail by Pitzer [271] and it was shown to have a -3/2 order temperature dependence, hence:

$$A^\phi = 0.392 \left(\frac{298.15}{T} \right)^{3/2}$$

(B.4-33)

The parameter B appearing in Equations (B.4-26) and (B.4-27), B^ϕ in Equation (B.4-30), and B' in Equation (B.4-31), are the second virial coefficients representing the interaction of opposite charge ions, which are obtained via the following ionic strength (I) dependent relationships:

$$B_{MX}^\phi = \beta_{MX}^{(0)} + \beta_{MX}^{(1)} e^{-a_{MX}\sqrt{I}} + \beta_{MX}^{(2)} e^{-12\sqrt{I}} \qquad\qquad (\text{ B.4-34 })$$

$$B_{MX} = \beta_{MX}^{(0)} + \beta_{MX}^{(1)} g(a_{MX}\sqrt{I}) + \beta_{MX}^{(2)} g(12\sqrt{I}) \qquad\qquad (\text{ B.4-35 })$$

$$B_{MX}' = \beta_{MX}^{(1)} g'(a_{MX}\sqrt{I})/I + \beta_{MX}^{(2)} g'(12\sqrt{I})/I \qquad\qquad (\text{ B.4-36 })$$

Where $\beta^{(0)}$, $\beta^{(1)}$, and $\beta^{(2)}$ are the parameters obtained experimentally, $a_{MX} = 2.0$ when M

or X is a univalent ion, or $a_{MX} = 1.4$ when X and M are 2-2 or higher valance couple.

The functions g (x) and g' (x) are defined as:

$$g(x) = 2(1 - (1 + x)e^{-x})/x^2 \qquad\qquad (\text{ B.4-37 })$$

$$g'(x) = -2\left(1 - \left(1 + x + \frac{x^2}{2}\right)e^{-x}\right)/x^2 \qquad\qquad (\text{ B.4-38 })$$

The second virial coefficients, Φ, Φ^ϕ, and Φ', appearing in Equations (B.4-26), (

B.4-27), (B.4-30), and (B.4-31), represent the interaction of same charged ions, and

they can be obtained via:

$$\Phi_{ij}^\phi = \theta_{ij} + E_{\theta_{ij}}(I) + I\, E'_{\theta_{ij}}(I) \qquad\qquad (\text{ B.4-39 })$$

$$\Phi_{ij} = \theta_{ij} + E_{\theta_{ij}}(I) \qquad\qquad (\text{ B.4-40 })$$

$$\Phi'_{ij} = E'_{\theta_{ij}}(I) \qquad\qquad (\text{ B.4-41 })$$

The functions $E_{\theta_{ij}}$ and $E'_{\theta_{ij}}$ are defined via Equations (B.4-42) and (B.4-43),

respectively.

$$E_{\theta_{ij}} = \left(\frac{z_i z_j}{4I}\right)\left[J(x_{ij}) - \frac{1}{2}J(x_{ii}) - \frac{1}{2}J(x_{jj})\right] \qquad\qquad (\text{ B.4-42 })$$

$$E'_{\theta_{ij}} = -\left(\frac{E_{\theta_{ij}}}{I}\right) + \left(\frac{z_i z_j}{8I^2}\right)\left[x_{ij}J'(x_{ij}) - \frac{1}{2}x_{ii}J'(x_{ii}) - \frac{1}{2}x_{jj}J'(x_{jj})\right] \quad (\text{ B.4-43 })$$

The value of the function J, and its derivative $J'=dJ/dx$, were evaluated by Pitzer and shown to be reasonably represented with the empirical Equation (B.4-44), with $C_1=4.118$, $C_2=7.247$, $C_3=-4.408$, $C_4=1.837$, $C_5=-0.251$, $C_6=0.0164$.

$$J = 1/6x^2\ln(x)e^{-10x^2} + \left(\sum_{k=1}^{6} C_k x^{-k}\right)^{-1}$$ (B.4-44)

The second virial coefficients, λ_{ni}, appearing in equations (B.4-26), (B.4-27), (B.4-28), and (B.4-30), represent the interaction of a neutral species, and it is obtained experimentally similar to parameters θ and β.

The parameters C, ψ, ζ, appearing in Equations (B.4-26), (B.4-27), (B.4-28), and (B.4-30), are the third virial coefficients. C_{MX}, representing the single electrolyte interaction, can be obtained via Equation (B.4-45):

$$C_{MX} = \frac{1}{2} C_{MX}^{\phi} |z_M z_X|^{1/2}$$ (B.4-45)

The parameters, ψ and ζ , are the triple ion interaction, and ion-ion-neutral interaction, respectively. The values of these trinary interaction parameters are generally small and they are multiplied with three concentration terms. In the present study, since the concentration terms are usually well below unity, the trinary interaction term are assumed to be negligible, and were not included in calculations.

The parameters of the second and third virial coefficients required for calculation of the activity coefficients were extracted from the literature and are listed in Appendix III. As noted above, most equations are functions of species concentrations and the ionic strength that are not initially known. Hence, an iterative scheme is necessary for such calculations. In the present study, the solution speciation in an ideal solution at the same

environmental conditions is used as the first guess. The relevant Pitzer parameters were then calculated based on the ideal values and further refined by an iterative scheme until a reasonable accuracy was achieved.

B.4.5.1.2: Case I: solution speciation for known pCO_2 and pH

This is a common scenario in a laboratory setting where the fugacity of CO_2 in the gas phase is known from its partial pressure and environmental conditions, and the pH of the solution is directly measured. The experimental procedure of the present study is an example of this case, where the pH of the CO_2-saturated solution is adjusted to a certain value by addition of sodium hydroxide or sodium bicarbonate, to increase the pH from its natural value, or hydrochloric acid to decrease the pH from its natural value.

The calculations in this case are based on the equilibrium equations shown in Table B.4-4, along with the electroneutrality constraint and the known pH and pCO_2. These equations form a set of non-linear, coupled algebraic equations that can be expressed using matrix notation in the form of Equation (B.4-46), where [A] is a square coefficient matrix, [C] is a vector of the unknown concentrations, and S is the vector of the source terms. The unknown concentration vector ([C]) can then be obtained by calculating the inverse coefficient matrix as shown in Equation (B.4-47).

$$[A].[C] = [S] \qquad\qquad\qquad (B.4\text{-}46)$$

$$[C] = inv([A]).[S] \qquad\qquad\qquad (B.4\text{-}47)$$

An example of one such calculation is shown in Equation (B.4-48), where Na^+ and Cl^- are the only two conserved ions present in the solution. Here the parameter "CI" with concentration units is introduced to represent the charge imbalance required to reach

the specified pH and, in this case, it is assumed to be in the form of Na^+ ions (i.e., the addition of NaOH or $NaHCO_3$ into the solution). If the specified pH is below that autogeneously expected for the natural H_2O/CO_2 system, CI represents the Cl^- ion (addition of HCl into the solution), thus the last two rows in the coefficient matrix of Equation (B.4-48) must be reworked accordingly. This concentration of the conserved ion is in addition to that from neutral salts such as NaCl, that is assumed to be present in the solution ($c_{NaCl_{(aq)}}$).

It is worthwhile to note that calculations in Equation (B.4-48) are done on the basis of pH as the activity of hydrogen ion (not concertation). It is also important to distinguish where activity coefficients should be used. For example, the chemical reactions with chemical potential as their driving force should be represented in terms of activities if applicable, while the electroneutrality and mass balance equations are based on the concentration of involved species, and must be expressed accordingly.

If an ideal solution is assumed, all the activity and activity coefficients in Equation (B.4-48) reduce to unity, and the solution speciation can then be readily obtained. For the case of non-ideal solutions, the coefficient matrix ([A]) contains the activity coefficients, which are functions of the unknown concentrations. Therefore, an iterative calculation scheme is necessary, where a first guess (e.g., the solution speciation with ideal solution assumption) is used to obtain the activity coefficients, and the coefficient matrix. The solution speciation and the parameter "CI" is then obtained by further iterations.

$$\begin{bmatrix}
1 & 0 & 0 & 0 & 0 & 0 & 0 & 0 & 0 & 0 \\
0 & 0 & \gamma_{H^+} & 0 & 0 & 0 & 0 & 0 & 0 & 0 \\
1 & -\gamma_{CO_2}K_{H,CO_2}e^{\left(\int_{P_{ws}}^{P}\frac{\bar{V}_{m,CO_2}}{RT}dP\right)} & 0 & 0 & 0 & 0 & 0 & 0 & 0 & 0 \\
0 & -a_{H_2O}\gamma_{CO_2}K_{hyd} & 0 & \gamma_{H_2CO_3} & 0 & 0 & 0 & 0 & 0 & 0 \\
0 & 0 & 0 & -\gamma_{H_2CO_3}K_{ca} & \gamma_{HCO_3^-}10^{-pH} & 0 & 0 & 0 & 0 & 0 \\
0 & 0 & 0 & 0 & -\gamma_{HCO_3^-}K_{bi} & \gamma_{CO_3^{2-}}10^{-pH} & 0 & 0 & 0 & 0 \\
0 & 0 & 0 & 0 & 0 & 0 & \gamma_{OH^-}10^{-pH} & 0 & 0 & 0 \\
0 & 0 & 1 & 0 & -1 & -2 & -1 & -1 & 1 & 0 \\
0 & 0 & 0 & 0 & 0 & 0 & 0 & 1 & 0 & 0 \\
0 & 0 & 0 & 0 & 0 & 0 & 0 & 0 & 1 & -1
\end{bmatrix}$$

$$\cdot\begin{bmatrix}
f_{CO_2} \\
c_{CO_{2(aq)}} \\
c_{H^+_{(aq)}} \\
c_{H_2CO_{3(aq)}} \\
c_{HCO_{3(aq)}^-} \\
c_{CO_{3(aq)}^{2-}} \\
c_{OH^-_{(aq)}} \\
c_{Cl^-_{(aq)}} \\
c_{Na^+_{(aq)}} \\
CI
\end{bmatrix} = \begin{bmatrix}
p_{CO_2}\phi_{CO_2} \\
10^{-pH} \\
0 \\
0 \\
0 \\
0 \\
0 \\
a_{H_2O}K_w \\
c_{NaCl_{(aq)}} \\
c_{NaCl_{(aq)}}
\end{bmatrix}$$

$$(\text{B.4-48})$$

An example of the solution speciation and the activity coefficients from such calculations are shown in Figure B.4-7. Figure B.4-7.A demonstrates the solution speciation of the carbonate species at 10°C for CO_2 partial pressures of 1 and 15 bar. At 1 bar CO_2, the solution speciation for all species show a nearly linear trend with the solution pH, suggesting that the effect of non-idealities is rather small. That is also seen on the calculated activity coefficients in Figure B.4-7.B, where the obtained values show only a small variation with pH. On the other hand, at 15 bar CO_2, the effect of non-ideal solution becomes significant at pH values about 5. That effect is readily observed by the non-linear behavior in Figure B.4-7.A. At the same time the calculated activity coefficients shown in Figure B.4-7.B demonstrated a radical change in their values at the same pH range. It should be noted that the main cause of the non-ideal behavior in the present discussion is the Na^+ ions present in the solution as represented by the calculated charge imbalance "CI" in Figure B.4-7.A . In these conditions, this parameter can be associated with the concentration of $NaOH$ or $NaHCO_3$ required to reach each specific pH. Another valuable observation in Figure B.4-7.A is that in most conditions the

parameter CI is equal to the concentration of HCO_3^-, that shows the alkalinity of the solution is for the most part is in the form of HCO_3^-.

As shown in Figure B.4-7.B, the effect of non-idealities is not the same for all species; even a reverse influence on the activity coefficients could be observed. That is one of the main properties that is unique to the Pitzer's specific interaction model, and it is not properly reflected in more simplistic approaches based on the initial Debye–Hückel theory, like Davies' equation. Additionally, such simplistic approaches suggest the neutral species are not affected significantly by the non-ideal solution, while the calculation of the specific interaction showed that in the present case the activity coefficient of the dissolved CO_2 is increased by about threefold in the pH range considered here.

A)

B)
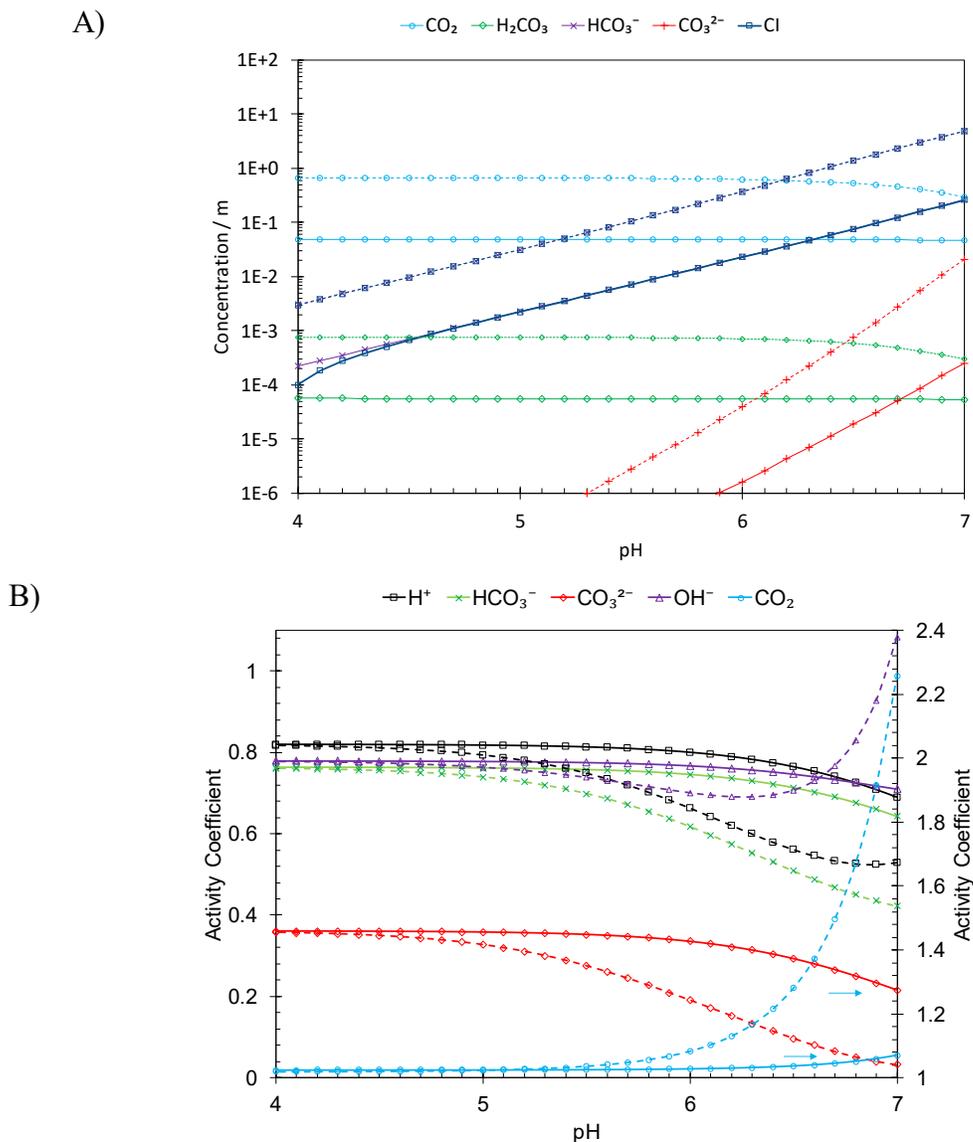
Figure B.4-7. The water chemistry calculation at 10°C and 0.1 M NaCl at pCO$_2$ of 1 bar (solid lines) and 15 bar (dashed lines). A) The calculated concentration of carbonate species and the charge imbalanace (CI) as a function of pH. B) the calculated activity coefficients as a function of pH.

B.4.5.1.3: Case II: solution speciation for known pCO$_2$ at unknown pH

This scenario is common in field operations where in situ pH measurements are not usually available, while the concentration of dissolved species is provided by laboratory analysis. In this case, the fugacity of CO$_2$ in the gas phase is known from its

partial pressure and the environmental conditions. The solution speciation, including the pH, can be obtained for a given (known) concentration of conserved ions.

The solution algorithm is fairly similar to that discussed above, however, in this case the coefficient matrix, [A], is undefined as it includes the unknown solution pH. Hence, the calculations are to be done iteratively. In an ideal solution, the inverse of the coefficient matrix can be calculated based on a first guess for pH, and be used to obtain the concentration of species as shown in Equation (B.4-48). This process needs to be coupled with an optimization algorithm (e.g. fzero function in MATLAB) in order to find the final answer iteratively, with a reasonable accuracy.

In non-ideal calculations, the iterative calculations for pH are done in series with iterative calculations required for non-ideal condition as discussed for Case I. The first guess for pH is used to obtain the speciation with ideal solution assumption. These values were then used as the input to obtain the activity coefficients and the coefficient matrix in order to find the non-ideal solution speciation through iterative calculations. The whole process is then repeated to optimize the value of pH with a reasonable accuracy.

An example of such calculations is shown in Equation (B.4-49). In a general view, the coefficient matrix is similar to that in Equation (B.4-48). The main differences are one less equation that specified the solution pH, and the predefined total concentration of the conserved ions in the source vector. The parameter "CI" defined for Case I, is no longer applicable since the charge imbalance is explicitly known in the present scenario.

$$
\begin{bmatrix}
1 & 0 & 0 & 0 & 0 & 0 & 0 & 0 & 0 \\
1 & -\gamma_{CO_2}K_{H,CO_2}e^{\left(\int_{P_{ws}}^{P}\frac{\bar{V}_{m,CO_2}}{RT}dP\right)} & 0 & 0 & 0 & 0 & 0 & 0 & 0 \\
0 & -a_{H_2O}\gamma_{CO_2}K_{hyd} & 0 & \gamma_{H_2CO_3} & 0 & 0 & 0 & 0 & 0 \\
0 & 0 & 0 & -\gamma_{H_2CO_3}K_{ca} & \gamma_{HCO_3^-}10^{-pH} & 0 & 0 & 0 & 0 \\
0 & 0 & 0 & 0 & -\gamma_{HCO_3^-}K_{bi} & \gamma_{CO_3^{2-}}10^{-pH} & 0 & 0 & 0 \\
0 & 0 & 0 & 0 & 0 & 0 & \gamma_{OH^-}10^{-pH} & 0 & 0 \\
0 & 0 & 1 & 0 & -1 & -2 & -1 & -1 & 1 \\
0 & 0 & 0 & 0 & 0 & 0 & 0 & 1 & 0 \\
0 & 0 & 0 & 0 & 0 & 0 & 0 & 0 & 1
\end{bmatrix}
$$

$$
\cdot
\begin{bmatrix}
f_{CO_2} \\
c_{CO_{2(aq)}} \\
c_{H^+_{(aq)}} \\
c_{H_2CO_{3(aq)}} \\
c_{HCO_3^-_{(aq)}} \\
c_{CO_3^{2-}_{(aq)}} \\
c_{OH^-_{(aq)}} \\
c_{Cl^-_{(aq)}} \\
c_{Na^+_{(aq)}}
\end{bmatrix}
=
\begin{bmatrix}
p_{CO_2}\phi_{CO_2} \\
0 \\
0 \\
0 \\
0 \\
0 \\
a_{H_2O}\,K_w \\
c_{Cl^-_{(aq)}} \\
c_{Na^+_{(aq)}}
\end{bmatrix}
$$

(B.4-49)

Figure B.4-8 to Figure B.4-10 demonstrated the results of such calculations as compared to the experimental data reported in the literature. Figure B.4-8 shows the calculated pH at various partial pressures of CO_2 up to 60 bar where no additional salts were present in the solution. At such conditions, while a reasonable agreement with the experimentally measured values of Meyssami et al.[272] was obtained, at elevated pressures some deviations are observed.
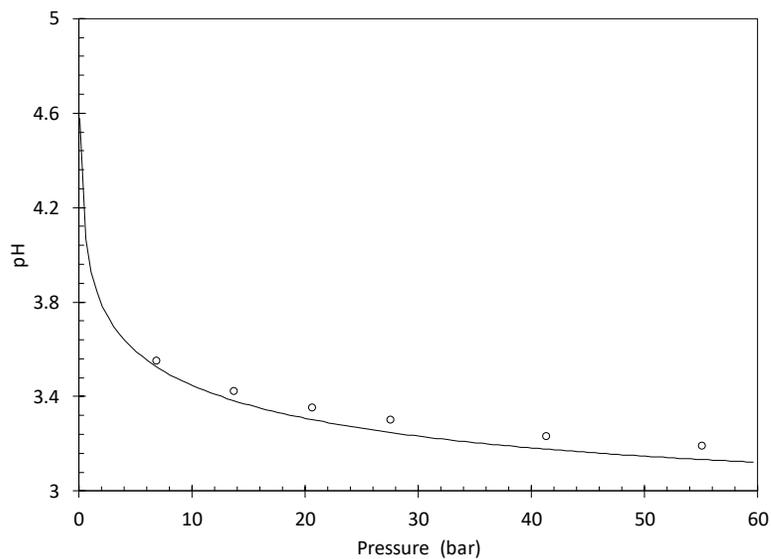
Figure B.4-8. The comparison of the calculated solution pH under pure CO_2 atmosphere with the experimental data taken from Meyssami et al.[272], at 32ºC, in the absence of any additional salts.

The performance of the non-ideal water chemistry calculations is further examined in the case of solutions containing a significant amount of additional NaCl. Figure B.4-9 shows the variation in pH as a function of pCO_2 in the solutions containing 0.5 M NaCl, at 26ºC, 50ºC, and 74ºC . The experimental data was taken from a study by Crolet and Bonis.[273], and found to reasonably agree with the calculated value, while at high temperatures some deviations are observed.
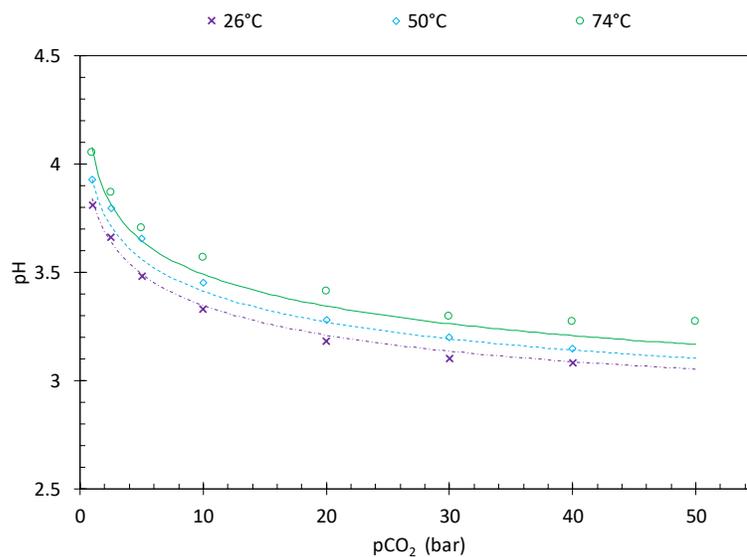
Figure B.4-9. The change in pH as a function of pCO_2 for a 0.5 M NaCl solution. The lines represent the calculated values, and the points are the experimental data taken from Crolet and Bonis.[273].

The effect of NaCl concentration is further examined in Figure B.4-10. At the NaCl concentrations below 1 M, the solution pH was predicted with a fairly good accuracy. However, at higher salt concentration the degree of agreement decreased, where at 3.5 M NaCl the predicted solution pH was about 0.15 pH units higher that the values reported by Crolet and Bonis.[273].
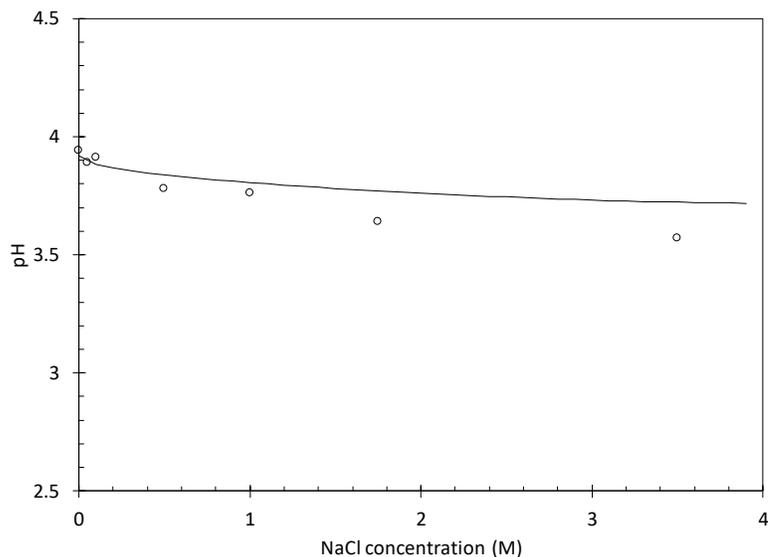
Figure B.4-10. The effect of NaCl concentration on the solution pH, at 25°C, 1 bar CO_2. The solid line shows the calculated values, and the open circles show the experimental data taken from Crolet and Bonis.[273].

B.4.5.2: Chemical kinetics of the H_2O/CO_2 system

The discussion so far in this section covers the calculations required to obtain the speciation at equilibrium in the bulk of solution. In the discussion of internal pipeline corrosion, the solution speciation in the vicinity of the metal surface may deviate from that in the bulk, under the influence of heterogeneous reactions occurring at the pipeline wall. The heterogeneous reactions include both the electrochemical reactions causing the metal deterioration and the chemical reactions, such as corrosion product layer formation. The concentration of the species at the metal surface defines (in part) the rate of electrochemical reactions and, hence, it is essential for determining the corrosion rate. Such calculations require the explicit knowledge of the kinetics of the involved homogeneous chemical reactions.

The homogeneous chemical reactions in the acidic CO_2/H_2O system are listed above as Reactions (B.4-2) through (B.4-5). However, the hydroxylation reactions of the carbonate species as shown via Reactions (B.4-50) and (B.4-51) may also become significant in near-neutral and alkaline environments. It is worthwhile to note that Reactions (B.4-50) and (B.4-51) are the equivalents of Reactions (B.4-2) and (B.4-4) with addition of water dissociation, hence, if the conditions for the equilibrium for those reactions are satisfied, Reactions (B.4-50) and (B.4-51) are also at equilibrium. In other words the relationships describing the equilibrium of Reactions (B.4-50) and (B.4-51) are not independent equations from the set describing the CO_2 speciation in acidic solutions, as shown in Table B.4-4. Hence, they are not included in equilibrium water chemistry calculation. Nevertheless, these "alkaline" reactions are of significance in terms of the reaction kinetics and are discussed in more detail in the following paragraphs.

$$CO_{2(aq)} + OH^-_{(aq)} \leftrightharpoons HCO^-_{3\,(aq)} \qquad\qquad\qquad\qquad \text{(B.4-50)}$$

$$HCO^-_{3\,(aq)} + OH^-_{(aq)} \leftrightharpoons CO^{2-}_{3\,(aq)} + H_2O_{(l)} \qquad\qquad\qquad \text{(B.4-51)}$$

The rate of production or consumption of each species can be calculated by considering the forward and backward rates of all the homogeneous reactions. The bulk solution is assumed to be a single liquid phase saturated with CO_2, hence the kinetics of the CO_2 dissolution reaction is not included in the present discussion. The rate of each chemical reaction j involved in the generic Reaction (B.4-52) can be calculated as shown in Equation (B.4-53).

$$\sum_{r=1}^{n_r} C_r \rightleftharpoons \sum_{p=1}^{n_p} C_p \qquad \text{(B.4-52)}$$

$$R_j = k_{f,j} \prod_{r=1}^{n_r} C_r - k_{b,j} \prod_{p=1}^{n_p} C_p \qquad \text{(B.4-53)}$$

The reaction rate of chemical species i involved in the aforementioned chemical reactions can be represented in a matrix format as shown in Equation (B.4-54). Where the coefficient matrix has the size of $i \times j$, i being the number of chemical species and j being the number of chemical reactions.

$$\begin{bmatrix} R_{CO_{2(aq)}} \\ R_{H^+_{(aq)}} \\ R_{H_2CO_{3(aq)}} \\ R_{HCO^-_{3(aq)}} \\ R_{CO^{2-}_{3(aq)}} \\ R_{OH^-_{(aq)}} \end{bmatrix} = \begin{bmatrix} -1 & 0 & 0 & 0 & -1 & 0 \\ 0 & 1 & 1 & 1 & 0 & 0 \\ 1 & -1 & 0 & 0 & 0 & 0 \\ 0 & 1 & -1 & 0 & 1 & -1 \\ 0 & 0 & 1 & 0 & 0 & 1 \\ 0 & 0 & 0 & 1 & -1 & -1 \end{bmatrix}$$

$$\times \begin{bmatrix} k_{f,hyd}\, a_{CO_2} a_{H_2O} - k_{b,hyd}\, a_{H_2CO_3} \\ k_{f,ca}\, a_{H_2CO_3} - k_{b,ca}\, a_{H^+} a_{HCO_3^-} \\ k_{f,bi}\, a_{HCO_3^-} - k_{b,bi}\, a_{H^+} a_{CO_3^{2-}} \\ k_{f,w}\, a_{H_2O} - k_{b,w}\, a_{H^+} a_{OH^-} \\ k_{f,hyd,OH}\, a_{CO_2} a_{OH^-} - k_{b,hyd,OH}\, a_{HCO_3^-} \\ k_{f,bi,OH}\, a_{HCO_3^-} a_{OH^-} - k_{b,bi,OH}\, a_{CO_3^{2-}} a_{H_2O} \end{bmatrix}$$

(B.4-54)

The kinetic rate constants of the chemical reactions of CO_2/H_2O system, used in Equation(B.4-54), are listed in Table B.4-8. The forward and backward rate constants are related to the equilibrium constant as shown in Equation (B.4-16), thus, with a known equilibrium constant only one of the forward or the backward rate constants needs to be specified. This was the basis of discussion on the equilibrium constant of the

hydration reaction. The kinetics of CO_2 hydration reaction is described based on the same equations obtained previously (Table B.4-6) as shown in Table B.4-8.

Eigen categorized the protonation reactions of bicarbonate, carbonate and hydroxide ion as "diffusion limited" reactions [67,274], meaning that these reactions are instantaneous when the hydrogen ion and each of these ions are encountered. The value of 4.7E10 ($M^{-1}.s^{-1}$) suggested for bicarbonate protonation, and the pK_a=3.49 for carbonic acid dissociation, shows that the carbonic acid dissociation rate constant is of the order of 10^7 (s^{-1}). Such a large kinetic rate constant suggests that the kinetics of carbonic acid dissociation is not rate limiting in the typical conditions encountered in CO_2 corrosion scenarios. On the other hand, water dissociation with pK_a of 14, and protonation rate constant of 1.4E11, has a kinetic rate constant of the order of 10^{-3}, suggesting that this reaction is not of much significance in the environmental conditions of CO_2 corrosion. The rate constant for bicarbonate dissociation is estimated to be 179 at 25°C (s^{-1}) in the present study (more details in Section B.4.6.3:), which places the kinetics of this reaction in between the water and carbonic acid dissociation. The estimated value suggests that the kinetics of this reaction can become the determinant factor in corrosion rate prediction at certain conditions. The author was unable to find any experimental measurements of this parameter in the literature for further confirmation. Nevertheless, Zeebe and Wolf-Gladrow reported an estimated value of 5E10 ($M^{-1}.s^{-1}$) for carbonate ion protonation, which by considering the pK_a of 10.32 for bicarbonate ion [91] results in a dissociation rate constant of 2.3 (s^{-1}) that is about two orders of magnitude smaller than the value estimated in the present study.

Table B.4-8. Kinetic rate constants for reactions involved in CO_2/H_2O system. k_f denotes the reaction progress from left to right.

Reaction #	Reaction rate constant	Reference
(B.4-2)	$k_{b,hyd} = 4.86E12 \ e^{(\frac{-64485}{RT})} \ (s^{-1})$	This study
(B.4-3)	$k_{b,ca} = 4.7E10 \ (M^{-1}.s^{-1})$	274
(B.4-4)	$k_{f,bi} = 13.14E07 \ e^{(\frac{-33452}{RT})} \ (s^{-1})$	This study
(B.4-5)	$k_{b,w} = 1.12 \times 10^{11} \ (M^{-1}.s^{-1})$	275
(B.4-50)	$k_{f,hyd,OH} = 4.2E13 \ e^{(\frac{-55438}{RT})} \ (M^{-1}s^{-1})$	261
(B.4-51)	$k_{f,bi,OH} = 6E9 \ (M^{-1}.s^{-1})$	274

Reactions (B.4-50) and (B.4-51), as noted above, are significant only in near-neutral and alkaline solutions. As mentioned before, these two reactions can be obtained by a linear combination of other reactions in acidic solutions (see Table B.4-4), hence, it is not necessary to include them in equilibrium water chemistry calculations. However, when discussing the homogeneous chemical reaction kinetics these two reaction should be accounted for as they may provide parallel pathways for consumption or production of the involved chemical species.

The reaction of CO_2 with OH^- (Reaction (B.4-50)) occurs in parallel to the CO_2 hydration reaction (Reaction (B.4-2)). The rate constant for Reaction (B.4-50) has been determined by Pinsent et al. [261] as noted in Table B.4-8, and was shown to agree reasonably well with the results obtained from other independent studies [217,262]. At 25°C the rate constant of the reaction between CO_2 and OH^- is 8.04E3 ($M^{-1}.s^{-1}$). At the same condition, the rate constant of CO_2 combination with water is 3.33E-2 (s^{-1}). The

comparison of the rate of these reactions suggest that the crossover occurs at pH=8.62, assuming an ideal solution:

$$k_{f,hyd} \, c_{CO_2} = k_{f,hyd,OH} \, c_{CO_2} c_{OH^-}$$

$$pH = 14 - \log\left(\frac{k_{f,hyd}}{k_{f,hyd,OH}}\right) = 8.62$$

This suggests that at pH values about 8 both reactions are of significance and should be included in calculations. Note that while CO_2 corrosion is generally defined in acidic solutions, even in acidic solutions such pH values can be reached at the vicinity of the metal surface when the corrosion current is under mass transfer control. That is particularly the case when the bulk solution has a pH $\geq$ 6.

The hydroxylation of bicarbonate ion, forward partial of Reaction (B.4-51), is also categorized as "diffusion limited" by Eigen, with the reported reaction rate of 6E9 ($M^{-1}.s^{-1}$) [274] at 25°C. The comparison of the rate of this reaction with that of bicarbonate dissociation, shows that the crossover of the rate of these two reactions is at ~pH=5, suggesting that these reactions are of kinetically equal significance at nearly all typical conditions encountered in industrial CO_2 corrosion scenarios.

$$k_{f,bi,OH} \, c_{HCO_3^-} c_{OH^-} = k_{f,bi} \, c_{HCO_3^-}$$

$$pH = 14 - \log\left(\frac{k_{f,bi,OH}}{k_{f,bi}}\right) = 5.12$$

B.4.5.3: Electrochemical reactions

The rate of electrochemical reactions at the metal surface were expressed in the same fashion as discussed in Chapter B.3: . Here, the carbonate species were not considered to be electrochemically active. Also, the water reduction reaction, considering

that it occurs only at more negative potentials, is not considered to be significant in the vicinity of the corrosion potential. The sole cathodic reaction in the present model is the H^+ reduction expressed via Equation (B.4-55).

$$i_c = -Fk_{0_{H^+}} a_{H^+}^{s\ m_{H^+}} e^{(\frac{\alpha FE}{RT})} \qquad \text{(B.4-55)}$$

where i is the current density in A.m^2, a^s is the surface activity, m is the apparent reaction order, and other parameters have their common electrochemical meaning. The kinetic parameters of the H^+ reduction reaction were obtained by the best fit of the model with the experimental data as $k_{0_{H^+}} = 2E - 8$, $m_{H^+} = 0.5$, $\alpha_{H^+} = 0.43$, as shown below in Section B.4.6: .

As discussed in Chapter B.3: , the rate of the iron oxidation reaction in the active dissolution, transition, and pre-passivation ranges can be obtained as the combination of three different rate determining steps considering the surface coverage of an intermediate species θ, according to Equations (B.4-56), (B.4-57), and (B.4-58).

$$i_a = (\frac{1}{(1 - \theta)i_1} + \frac{1}{(1 - \theta)i_2})^{-1} + \theta i_3 \qquad \text{(B.4-56)}$$

$$i_{a,j} = Fk_{0,j} a_{H^+}^{s\ m_{H^+,j}} a_{CO_2}^{s\ m_{CO2,j}} e^{(\frac{\alpha_j FE}{RT})} \qquad \text{(B.4-57)}$$

$$\theta = \frac{K_\theta a_{H^+}^{s\ m_{H^+,\theta}} a_{CO_2}^{s\ m_{CO2,\theta}} e^{(\frac{\alpha_\theta FE}{RT})}}{1 + K_\theta a_{H^+}^{s\ m_{H^+,\theta}} a_{CO_2}^{s\ m_{CO2,\theta}} e^{(\frac{\alpha_\theta FE}{RT})}} \qquad \text{(B.4-58)}$$

The kinetic parameters for these reactions were also obtained based on the apparent Tafel slopes and reaction orders of the experimental data as shown below:

$a,1$: $k_{0,1} = 4.0E09$; $m_{H^+,1} = -2.5$; $m_{CO_2,1} = 0$; $q_1 = 2.5$.

$a,2$: $k_{0,2} = 1.0E13$; $m_{H^+,2} = 1$; $m_{CO_2,2} = 0.5$; $q_2 = 2$.

$a,3:$ $k_{0,3} = 09E - 03$; $m_{H^+,3} = -0.5$; $m_{CO_2,3} = 0.5$; $q_3 = 0.5$.

$\theta:$ $K_\theta = 7.0E13$; $m_{H^+,\theta} = -2.5$; $m_{CO_2,\theta} = -0.5$; $q_\theta = 2.5$.

B.4.5.4: The diffusion boundary layer

The rate of electrochemical reactions and consequently the corrosion rate can only

be determined if the surface concertation of the involved electroactive species is known.

These values, however and in a practical sense, are not directly measurable. Nevertheless,

with a known speciation in the bulk solution the values of the surface concentrations can

be calculated by constructing a detailed account of their transfer through the diffusion

boundary layer.

The flux of chemical species inside the diffusion boundary layer can be described

as Equation (B.4-59). The mathematical model developed in the present study considers

the non-ideal solution properties in the context of moderately dilute solutions, hence, the

flux of species, N_i (mol.m^{-3}.s^{-1}), is expressed in terms of chemical potential as shown in

Equation (B.4-59).

$$N_i = -u_i C_i \nabla \mu_i + C_i v \qquad\qquad (\text{B.4-59})$$

where C_i is concentration (mol.m^{-3}), u_i is mobility (m^2.s^{-1}.V^{-1}), v (m.s^{-1}) in the second

term represents the convective flow due to the movement of the bulk fluid, and μ_i (j.mol^{-1}

) is the (electro)chemical potential of the (ionic) species, which can be split in two

independent "chemical" and "electrostatic" parts [68]:

$$\mu_i = RT \ln(\gamma_i C_i) + F z_i \phi \qquad\qquad (\text{B.4-60})$$

where ϕ is the potential inside the solution (V). The combination of Equations (B.4-59)

and (B.4-60), assuming that the Nernst-Einstein relationship ($D_i = RTu_i$) gives the flux

relationship for non-ideal condition in moderately dilute solutions, yields:

$$N_i = -D_i \nabla C_i - D_i C_i \nabla \ln(\gamma_i) - \frac{FD_i C_i z_i}{RT} \nabla\phi + C_i v \qquad \text{(B.4-61)}$$

At ideal solution conditions where γ_i approaches 1 the second term in Equation (B.4-61)

is equal to zero and the flux relationship of an infinitely diluted solution is established [68].

In Equation (B.4-61), the bulk movement of the fluid is accounted for in the

convective flow term ($v\,C$), where v describes the local velocity inside the boundary

layer. However, in the turbulent flow regime of the thin channel flow cell, the dominant

mass transfer mechanism is in the form of turbulent mixing, hence the convective flow

term cannot be readily calculated. The turbulent mixing decays as the solid wall is

approached, in the diffusion boundary layer, and turbulent convection can be quantified

in terms of an eddy diffusivity (D_e in $m^2.s^{-1}$) changing within the diffusion boundary

layer. Considering the analogy with the Fick's law used to represent turbulent mixing,

Equations (B.4-61) for a turbulent flow becomes:

$$N_i = -(D_i + D_e)\nabla C_i - D_i C_i \nabla \ln(\gamma_i) - \frac{FD_i C_i z_i}{RT} \nabla\phi \qquad \text{(B.4-62)}$$

The concentration of each chemical species for an elementary volume of the

solution can be defined in terms of the mass conservation law, using the flux relationship

(Equation (B.4-62)). The change in concentration of species i over the time interval of

Δt is defined by the change in its flux over Δx, in addition to the rate of

consumption/production of species i through homogeneous chemical reactions, R_i

(mol.m^{-3}.s^{-1}). This is mathematically expressed *via* Equation (A.2-10) :

$$\frac{\partial C_i}{\partial t} = -\nabla . N_i + R_i \qquad \text{(B.4-63)}$$

For most practical applications, the tangential and radial components of Equation

(B.4-62) and Equation (B.4-63) are not of any significance. Therefore, for a one-

dimensional semi-infinite geometry in the direction x normal to the metal surface,

Equation (B.4-62) and Equation (B.4-63) can be simplified to Equation (B.4-64) and

Equation (B.4-65) , respectively.

$$N_i = -(D_i + D_e)\frac{\partial C_i}{\partial x} - D_i C_i \frac{\partial \ln(\gamma_i)}{\partial x} - \frac{z_i D_i F C_i}{RT}\frac{\partial \phi}{\partial x} \qquad \text{(B.4-64)}$$

$$\frac{\partial C_i}{\partial t} = \frac{\partial}{\partial x}\left((D_i + D_e)\frac{\partial C_i}{\partial x}\right) + \frac{\partial}{\partial x}\left(D_i C_i \frac{\partial \ln(\gamma_i)}{\partial x}\right) + \frac{\partial}{\partial x}\left(\frac{z_i D_i F C_i}{RT}\frac{\partial \phi}{\partial x}\right) \qquad \text{(B.4-65)}$$
$$+ R_i$$

The non-ideal solution effect on mass transfer and mass conservation calculations

are accounted for as shown in Equation (B.4-64) and Equation (B.4-65). The activity

coefficient term appearing in Equation (B.4-65) was calculated using Pitzer's model as

described in the previous section, while the local concentration of the chemical species

are used in calculations. In order to do so, the Pitzer model developed in section

B.4.5.1.1: was coupled with the electrochemical model of the present discussion.

The effect of homogeneous chemical reactions, expressed by the R_i term in

Equation (B.4-65), is also significantly influenced by the non-ideal solution properties.

The term R_i, including the effect of activity coefficients, is calculated according to the

discussion in Section B.4.5.2: . An accurate account of the homogeneous chemical

reactions involved in the complex water chemistry of CO_2 saturated solutions is essential for calculating the concentration of the chemical species inside the boundary layer and also at the metal surface. This is of significance, since the dissociation reactions associated with weak acids such as carbonic acid, carboxylic acids, and hydrogen sulfide may act as an additional source (or sink) for the chemical species as their concentrations depart from equilibrium values in the bulk solution. The buffering effect of carbonic acid and bicarbonate ion on the electrochemical response of the system is reflected by this term.

The effect of molecular diffusion induced by the concentration gradient of the chemical species inside the boundary layer is accounted for in the first terms of Equations (B.4-64) and (B.4-65). The diffusion coefficients for the chemical species included in the present model can be found in Table B.4-9. The temperature dependence of the diffusion coefficient are estimated based on the Einstein-Stocks relationship as shown in Table B.4-3.

Table B.4-9. Reference diffusion coefficients at 25 ºC (77˚F).

Species	Diffusion coefficient in water $\times 10^9$ (m²/s)	Reference
CO_2	1.92	150
H_2CO_3	1.75	Estimated
HCO_3^-	1.185	70
CO_3^{2-}	0.923	70
H^+	9.312	68
OH^-	5.273	70
Na^+	1.334	68
Cl^-	2.032	68,70
Fe^{2+}	0.72	68

The effect of turbulent flow in terms of the eddy diffusivity profile in the boundary layer for a fully developed turbulent flow can be expressed via Equation (B.3-33), as discussed in more detail in Chapter B.3: .

$$D_e = \nu \frac{0.0007\, x^{+3}}{\left[1 + 0.00405 x^{+2}\right]^{1/2}}$$ (B.4-66)

where ν is the kinematic viscosity (m^2.s^{-1}), and x^+ is the dimensionless distance from the wall defined as:

$$x^+ = \frac{x\left(\tau_w/\rho\right)^{1/2}}{\nu}$$ (B.4-67)

Equation (B.4-67) is valid for x^+<30, and is universal for all turbulent flow regimes when appropriate dimensionless parameters are used. The wall shear stress, τ_w in Pa, appearing in Equation (B.4-67) is mathematically expressed as :

$$\tau_w = \frac{1}{2}\rho C_f V^2$$ (B.4-68)

with water density ρ (kg.m^{-3}) and the average fluid velocity of V (m.s^{-1}). The term C_f in Equation (B.4-68) is the Fanning friction factor, which can be calculated based on the explicit relationship reported by Swamee and Jain[239] for Darcy friction factor (C_d), considering C_d=$4C_f$.

$$C_d = 0.25\left[\log\left(\frac{\varepsilon/D_{eq}}{3.7} + \frac{5.74}{Re^{0.9}}\right)\right]^{-2}$$ (B.4-69)

where ε (m) is the surface roughness, the Reynolds number (Re= $V.D_{eq}/\nu$) was calculated based on the equivalent characteristic diameter: D_{eq}= $4A/P$ (m), with A and P

being the cross section area and the interior perimeter of the thin channel. Equation (

B.4-69) is merely an explicit derivation of the well-known Colebrook-White correlation

[240].

The effect of electromigration on the flux of ionic species away/towards the metal

surface is accounted for by the third term of Equations (B.4-64) and (B.4-65). While its

contribution to the surface concentration of electroactive species in the brines with high

ionic strength is negligibly small, in certain corrosion scenarios it cannot be neglected.

For example, in the case of corrosion in condensed water such as for Top of the Line

Corrosion (TLC) or corrosion inside "dry" gas lines, the liquid phase does not include

any significant amount of dissolved salts (e.g. NaCl). The calculation of the electro-

migration effect requires the potential inside the boundary layer to be specified. In its

simplest form, this parameter can be specified by including the electro-neutrality equation

(Equation (B.4-70)) in calculations to satisfy the number of required relationships.

$$\sum_i z_i C_i = 0$$
(B.4-70)

It is worthwhile to note that the electroneutrality equation does not suggest that

the potential gradient is zero. It can be calculated from Poisson's equation, which relates

the electric potential (V) in a medium with a uniform dielectric constant to a given charge

distribution [68]:

$$\nabla^2 \phi = -\frac{F}{\varepsilon} \sum_i z_i C_i$$
(B.4-71)

where F is Faraday's constant and ε ($C.V^{-1}.m^{-1}$) is the dielectric constant of the medium.

Considering the large values of the correlation coefficient (F/ε), in typical aqueous

solutions [60], Equation (B.4-71) suggest that any significant charge imbalance inside the boundary layer requires an extremely large potential gradient, which is not commonly the case in aqueous electrochemical systems. By moving the correlation coefficient to the left side of Equation (B.4-71), its value becomes negligibly small for all practical purposes. Therefore, the charge density at each element of the solution can be approximated using Equation (B.4-70).

B.4.5.5: Initial and boundary conditions

Since Equation (B.4-65) is a transient partial differential equation one needs to define initial and boundary conditions in order to solve it. At the initial time (t=0) it can be assumed that the well mixed solution comes into contact with the metal surface. Hence, the concentrations of chemical species throughout the diffusion layer are constant, known values, defined by the chemical equilibria of the solution as discussed in section B.4.5.1: .

In the bulk solution ($x=\delta$) the concentration of chemical species remains unchanged at all times (t$\geq$0). Therefore, the boundary condition can be defined for the bulk solution based on the known concentration of species identical to the initial conditions.

The boundary condition at the metal/solution interface is based on the known fluxes, and includes all the electrochemical reaction rate calculations. For an electroactive chemical species, the flux at the metal/solution boundary is equal to the rate of the corresponding electrochemical reactions. For an electroactive species i involved in

electrochemical reaction j, the flux, at the metal surface can be described through equation (B.4-72):

$$N_i|_{x=0} = -\frac{s_{ij} i_j}{n_j F} \qquad \text{(B.4-72)}$$

The negative sign in Equation (B.4-72) represents a sign convention where cathodic currents are presumed negative and anodic currents are positive. Additionally, the reactants are represented with a negative stoichiometric coefficient (s_{ij}) and the products with positive numbers.

For non-electroactive species the flux at the metal surface is zero:

$$N_i|_{x=0} = 0 \qquad \text{(B.4-73)}$$

Equation (B.4-72) and Equation (B.4-73) can be applied to describe the mass transfer for all chemical species at the metal surface. The electric potential inside the solution may also be specified through the electroneutrality constraint *via* Equation (B.4-70) (or Poisson's equation) similar to that in the governing equations.

Considering the governing equations, the initial conditions, and the boundary conditions discussed above, this system of equations is fully specified if the potential at the metal surface (E_{app}) is known so that the rate of electrochemical reactions can be calculated. That is a common case in electroanalytical measurements (e.g. potentiodynamic sweeps) where electrode potential is the controlled parameter. However, in corrosion rate predictions this parameter (E_{app} = corrosion potential) is generally not known a priori. In that case, an additional relationship is required: the charge conservation at the metal surface. All the cathodic (reduction) currents are balanced by the anodic (oxidation currents), meaning that the net current resulting from all j

electrochemical reactions is equal to zero (i.e., there is no need for an externally

"applied" current i_{app}). The charge conservation can be mathematically expressed as

Equation (B.4-74).

$$i_{app} = 0 = \sum_j i_j \qquad\qquad\text{(B.4-74)}$$

B.4.5.6: Mathematical methods

The mathematical equations as summarized in Table B.4-10 form a set of non-

linear, coupled, partial differential equations to be solved numerically. The solution was

obtained using the finite difference method on a non-uniform grid and Newman's

"Band-J" open source code [68,247], similar to that described in Chapter B.3: .

Table B.4-10. Summary of equations used in the comprehensive mathematical model.

Electrode surface boundary

$N_i = -\sum_j \dfrac{s_{ij} i_j}{n_j F}$	*for all electroactive species*
$N_i = 0$	*for all non − electroactive species*
$\sum_i z_i C_i = 0$	
$i_{app} = 0 = \sum_j i_j$	*for unknown electrode potential case*

Diffusion layer

$$\frac{\partial C_i}{\partial t} = \frac{\partial}{\partial x}\left((D_i + D_e)\frac{\partial C_i}{\partial x}\right) + \frac{\partial}{\partial x}\left(D_i C_i \frac{\partial \ln(\gamma_i)}{\partial x}\right) + \frac{\partial}{\partial x}\left(\frac{z_i D_i F C_i}{RT}\frac{\partial \phi}{\partial x}\right) + R_i$$

$$\sum_i z_i C_i = 0$$

Bulk boundary and Initial condition

$C_i = C_i^b$	*for all species*
$\Phi = 0$	

In the present study, the electrochemical model as described above is coupled with the water chemistry Pitzer model in order to include the effect of non-ideal solutions in a computationally reasonable time. The inputs of the model include the solution pH, NaCl concentration, temperature, CO_2 partial pressure, flow velocity, hydrodynamic length, the number of spatial and temporal nodes, and the potential range, if applicable. As the first step the solution speciation is obtained based of the water chemistry model. The results are used to specify the initial and the bulk boundary condition of the electrochemical model. Considering the non-linear equations in the electrochemical model, and also in the coupled Pitzer model, the solution was obtained using an iterative calculation approach. The concentrations and activity coefficients for the bulk solution

was used as the first guess to solve the equations at the first temporal node and all spatial nodes. The results were then used as input for the Pitzer model to obtain a new set of local activity coefficients. The process was iterated until convergence with a reasonable accuracy is achieved. At the end of this process, the concentrations and the activity coefficients at all spatial nodes is specified. The same process is repeated for the following time steps, using the last set of concentrations and activity coefficients as the initial guess.

B.4.6: A quantitative discussion

B.4.6.1: Flow effect

The effect of flow in CO_2 corrosion is reflected in the magnitude of the limiting current density. In many practical scenarios, especially those at higher temperatures, the corrosion rate is under mass transfer control, and is defined by the cathodic limiting current density. As discussed above, the mass transfer of H^+ and H_2CO_3 from the bulk are major components of limiting current, in addition to the effect of CO_2 chemical hydration and HCO_3^- dissociation reactions at the vicinity of the metal surface.

In the present mode the mass transfer for turbulent flow regimes is incorporated in terms of eddy diffusivity as described via Equation (B.4-65). Despite the current application in the thin channel flow cell, the law of wall suggests that this expression remains valid for all fully developed turbulent flow regimes, including that of pipeline flow. In order to examine the performance of this empirical equation in determining the limiting currents, a series of experiments with flow velocity as a variable was considered here. The experiments were conducted at pH 3 in N_2-saturated and CO_2-saturated

solutions, where the limiting current could be observed clearly under atmospheric conditions. Figure B.4-11 demonstrates the comparison of the limiting current densities predicted by the model with those obtained experimentally. At pH 3, considering the high concentration of H^+, no significant effect from the presence of CO_2 was expected since the overwhelmingly high mass transfer of H^+ from the bulk solution overshadows the buffering reactions associated with the presence of this species. The results of the model showed less than a 1% difference in CO_2 saturated and N_2 saturated solutions at the conditions considered here, and hence are not shown in Figure B.4-11. That was also seen in the experimental data. While some variations were observed, the difference is marginally within the experimental error. Over all, the agreement of the model with the measured limiting current densities was found to be satisfactory.
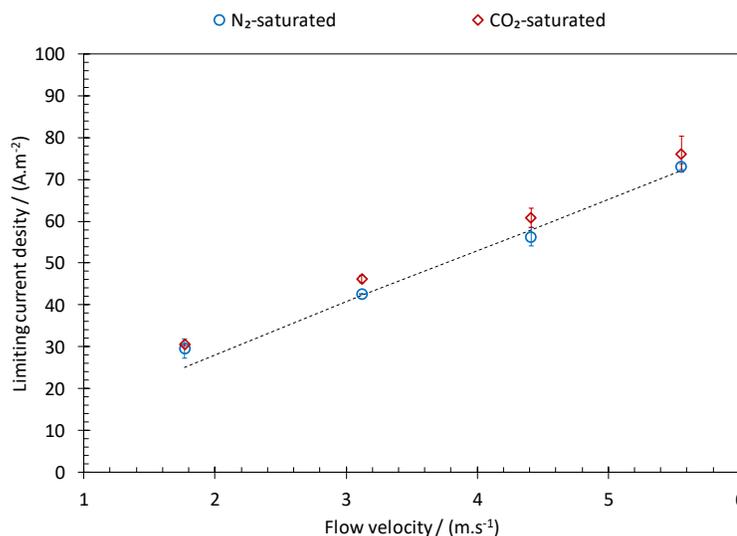
Figure B.4-11. The comparison of the calculated limiting current density at pH 3, 10 °C, 0.1 M NaCl, $pCO_2=0$, with experimental data obtained at similar conditions (blue circles) and in solutions with $pCO_2=1$ bar (red diamonds).

B.4.6.2: Effect of pH and pCO_2

The performance of the mathematical model developed in the present study was examined using the experimental data. Figure B.4-12 demonstrates the comparison of the simulated polarization curves with those obtained experimentally. The model was found to be able to capture most mechanistic features of the studied system. At pH 4 and pH 5 the cathodic polarization curves, including the limiting current, were successfully predicted without considering the direct reduction of carbonic acid. This agreement is a further verification of the mechanistic arguments for the mechanism of cathodic currents. At the same time, the anodic dissolution in the active range as well as the transition to the pre-passivation range, including their dependence on pCO_2, was predicted with a fairly reasonable accuracy; knowing that some deviations are naturally expected due to the simplified approach used to quantify such a complex reaction. This extends the range of validity of the incorporated semi-empirical model of iron dissolution to pCO_2 as high as 15 bar.

The results at pH 6 are perhaps of more significance, where the model was found to successfully predict the seemingly different governing mechanisms; both in the cathodic and anodic ranges. At pH 6, a secondary limiting current was observed at more negative polarization potentials. In the conventional view of the mechanism of CO_2 corrosion, that was believed to be the sign of the direct reduction of HCO_3^- to hydrogen. Yet, in the present model, the only electroactive cathodic species is H^+ and the predicted secondary limiting current is a result of the homogeneous HCO_3^- dissociation that is favored at the high surface pH in such conditions. It is also important to note that the

magnitude of this limiting current is determined by the slow rate of the HCO_3^- dissociation reaction. Therefore, the first limiting current is a result of the kinetically limited CO_2 hydration reaction and the second limiting current is the result of kinetically limited HCO_3^- dissociation. Figure B.4-13 illustrates the calculated normalized surface concentration of the involved carbonate species (vs. bulk concentration) as a function of the calculated surface pH, on primary axes. The current potential response of the model is also demonstrated in secondary axes. The simulation results show that by the gradual decrease of the potential, the surface pH gradually increases from the bulk value, which is at the same time accompanied by the decrease of H_2CO_3 surface concentration through its chemical dissociation. This trend is continued until the first limiting current is reached (at ~ -0.61 V), where the surface H_2CO_3 concentration approaches zero. The further decrease of the potential, and therefore increasing surface pH, favors the dissociation of HCO_3^- as seen by its depleting surface concentration and increased current densities. At more negative potentials, where the rate of HCO_3^- dissociation reaches it maximum, the second limiting current is observed. Throughout this potential range, while the surface H^+ and H_2CO_3 concentrations are dramatically decreased, the concentration of CO_2 and HCO_3^- are only slightly changed, due to their corresponding slow kinetics. The buffering ability of H_2CO_3 and HCO_3^- may be distinguished in this regards. H_2CO_3 can be considered a strong buffer in the sense that its equilibrium and kinetics allow this species to readily dissociate as the surface pH is increased; this is the same behavior as observed for the case of carboxylic acids[62,201]. On the other hand, HCO_3^- can be regarded as a weak buffer,

due to its low pKa that limits its dissociation to the relatively high pH values, and also it's slow reaction kinetics.
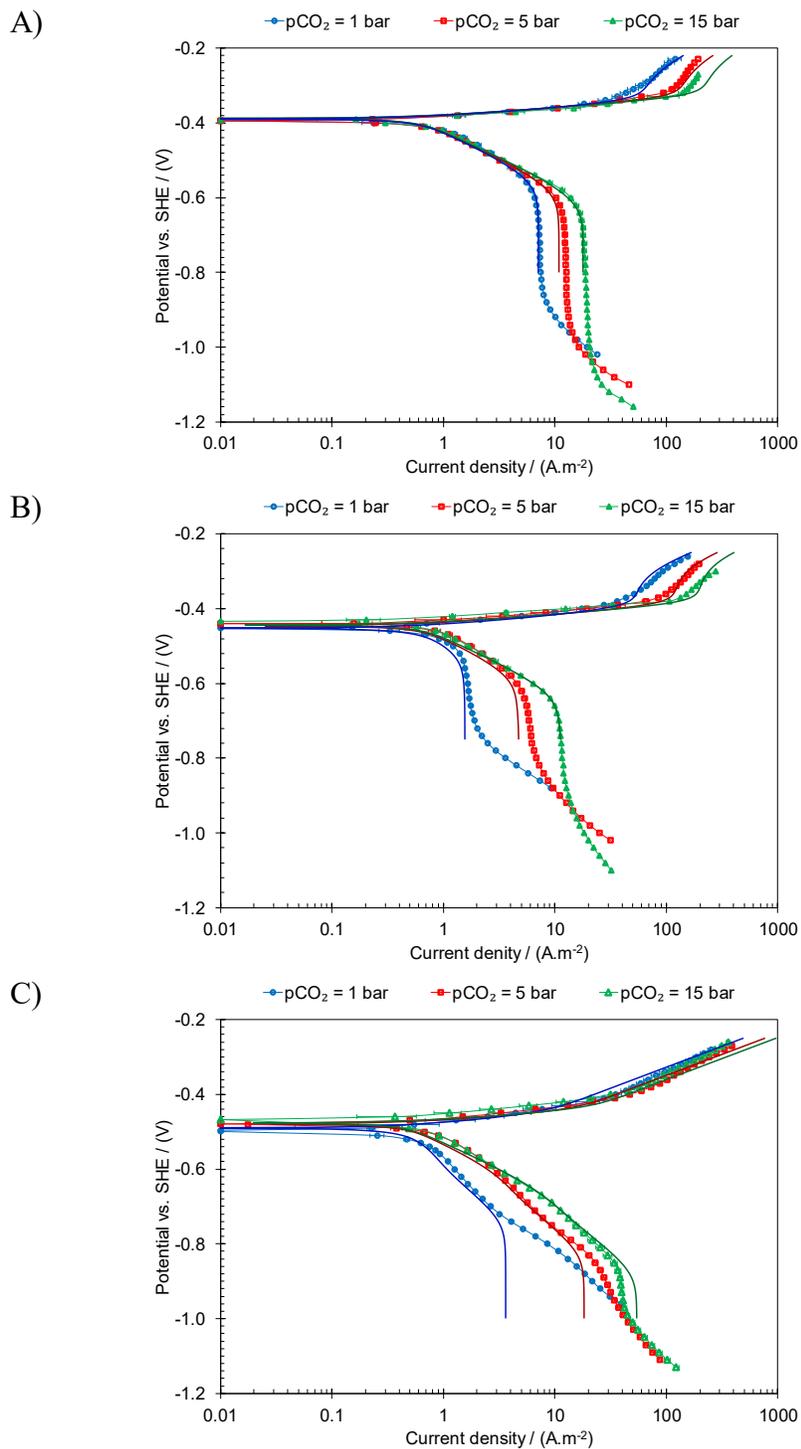
Figure B.4-12. The comparison of the simulated and the experimental polarization curves obtained on API 5L X65 mild steel at 10°C, 0.1 M NaCl, 4.6 m.s^{-1} flow velocity, at pCO_2 of 1, 5, and 15 bar. A) pH 4. B) pH 5. C) pH 6. The Error bars show the standard deviation of at least three repeated experiments.

Furthermore, the secondary limiting current becomes less visible at elevated CO_2 partial pressures, and is only observed as a change in the apparent slope of the cathodic currents. That behavior was also predicted by the model via the buffering effect of HCO_3^-. It should be noted that the current density range in between the two limiting currents are no longer under pure charge transfer control, but controlled by the surface concentration of H^+ that is provided by the slow HCO_3^- dissociation reaction. Therefore, this range of current densities are pCO_2 dependent through the pCO_2 dependence of HCO_3^-, a behavior that is seen in Figure B.4-12.
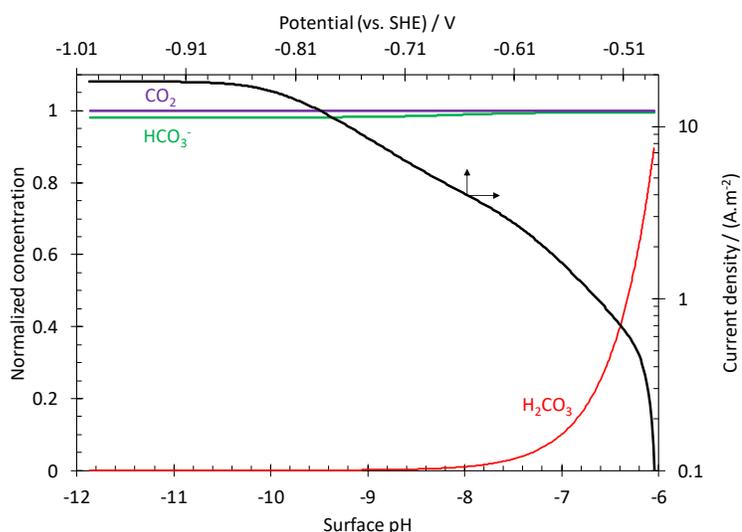
Figure B.4-13. The illustration of the calculated surface concentration of CO_2, H_2CO_3, and HCO_3^- versus the calculated surface pH, on primary axes. The calculated current/potential response at the same conditions, on the secondary axes. Conditions: pH 6, 5 bar CO_2, 10°C, 4.6 m.s^{-1} TCFC flow.

The electrochemical activity of HCO_3^- has to be discussed in relation to its effect on the pure charge transfer controlled range that is observed prior to the first limiting current. At pH 6 and 15 bar CO_2, where the concentration of HCO_3^- is about 3×10^5 higher than H^+, no significant change of current densities was observed in that range. This indicates that in acidic CO_2 corrosion neither H_2CO_3 nor HCO_3^- are directly reduced at

the metal surface, and the higher corrosion rates in CO_2-saturated environments are the results of the complex set of homogeneous chemical reactions associated with the H_2O/CO_2 system. That also highlights the capability and the necessity of the comprehensive mathematical models for incorporating the surface chemistry in corrosion rate estimations.

On the anodic current range, the transition range was no longer observed at pH 6. The simulated results where found to be able to capture this behavior. The results from the model at pH 6 suggests that, differently to what is seen in lower pH, the active dissolution range is no longer observed. The observed anodic currents were dominated by the reaction associated with the pre-passivation range. The observed different Tafel slopes at lower and higher current densities are the result of the dependence of this reaction on the surface coverage of the intermediate species (θ), where at low coverages, when θ is potential dependent as described by Equation (B.4-58), a lower Tafel slope is observed. As θ approaches 1 and is no longer increased with increasing potentials, the second range of current densities with an increased Tafel slope is observed. Considering the experimental errors, the simulated behavior of the anodic current was in reasonable agreement with the experimental data, however, the pCO_2 dependence as well as the Tafel slope appear to be slightly lower that that seen at lower pH values.

B.4.6.3: Effect of Temperature

Temperature has a significant known effect on almost all aspects of CO_2 corrosion. As shown in Figure B.4-14, increasing temperature results in an enhancement of both the charge transfer processes and the limiting currents. The effect of temperature

in the latter case is, for the most part, due to the kinetics and equilibria of the CO_2/H_2O system; discussed in detail in section B.4.5.1: . Some less significant effects resulting from the change in the physical properties of water (e.g., water density and viscosity) and the diffusivity of the species was also expected. These effects are incorporated in the present calculations, and as shown in Figure B.4-14 the predicted limiting currents are found to be in reasonable agreement with the experimental data.
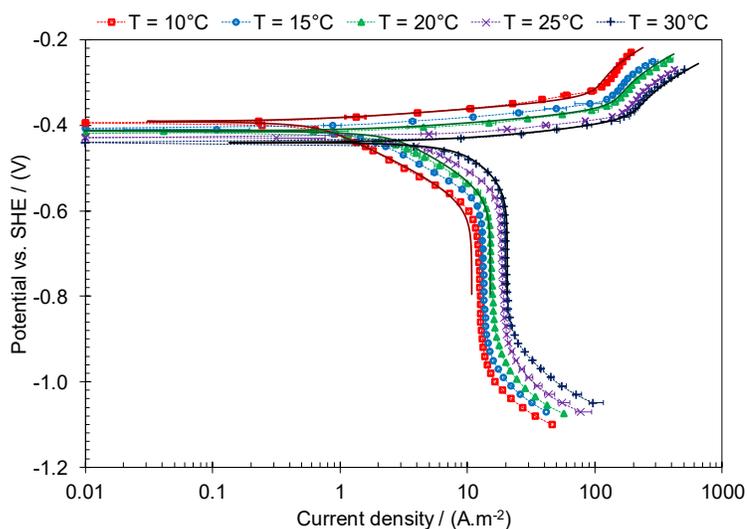
Figure B.4-14. The steady state polarization curves obtained at pH 4, 5 bar pCO2, 4.6 m.s^{-1} TCFC flow, and 0.1 M NaCl on a API 5L X65 mild steel at various temperatures. The solid lines show the calculated polarization curves at selected temperatures.

The two main reactions of interest in the present discussion are the H^+ reduction and iron oxidation in the active dissolution range, occurring at the vicinity of the corrosion potential. The temperature dependence of these two reactions can be discussed best at the conditions where the cathodic currents are clearly observed and the anodic currents show the active dissolution range in a rather extended range. For this reason, the temperature dependence of these reaction was investigated at pH 5 and 5 bar CO_2. Even

at such conditions, the results shown in Figure B.4-14 suggest both reactions have rather a high temperature dependence where at temperatures about 30°C the effect of mass transfer limitation becomes significant at the corrosion potential, distorting the charge transfer controlled range of both the cathodic and anodic currents. Therefore, the temperature dependence of these reactions are inevitably investigated in the lower temperature range.

The temperature dependence of the electrochemical reactions were obtained based on Arrhenius plots as shown in Figure B.4-15 and Figure B.4-16. Figure B.4-15 shows the temperature dependence of the H^+ reduction reaction, where the natural log of the apparent reaction rate constant, as obtained by the best fit of the model to the average data of Figure B.4-14, is plotted as a function of $1/T$. The slope of the trend line is equal to $-E_a/R$. Considering these results, the apparent activation energy of H^+ reduction was found to be 83.2 kJ.
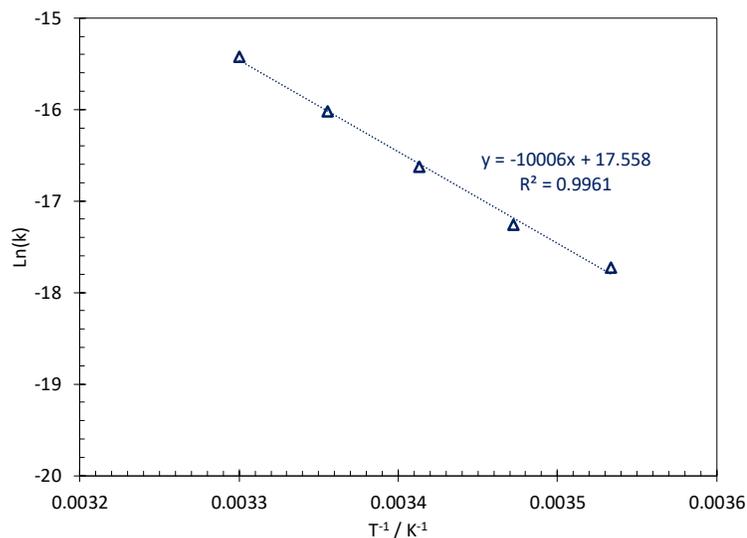
Figure B.4-15. The Arrhenius plot for the temperature dependence of the H$^+$ reduction kinetic rate constant.

The temperature dependence of the oxidative iron dissolution reaction was obtained in a similar fashion. As discussed earlier, the iron dissolution was expressed as a combination of four components. Figure B.4-15 shows the temperature dependence of k_1, k_3, and K_θ, for the reactions at the active dissolution range, pre-passivation range and the equilibrium constant of its associated intermediate species, respectively. Similar to the cathodic reaction, the iron dissolution reaction also shows a rather significant temperature dependence, especially at the active dissolution range. The activation energies for k_1, k_3, and K_θ were estimated to be 126.8 kJ, 63.0 kJ, and 95.8 kJ, respectively.

It should be noted that the second reaction at the active dissolution range with rate constant of k_2 is not observed at this pH and pCO$_2$ range. In fact, as discussed in Chapter B.3: , that reaction only becomes viable in a narrow range of condition at pH values somewhere between 5 and 6, and as it becomes rate determining, it diminishes the whole active dissolution range (see Figure B.4-12), where the anodic currents would be

dominated by the reaction of the pre-passivation range. Its transitional nature in a narrow range of conditions makes the exact determination of its value and temperature dependence subject to extensive experimentation, while for the same reason, for corrosion rate prediction in CO_2 system it is practically insignificant. Therefore, it is established that the temperature dependence of this parameter has no significant influence on the practical performance of the model. The temperature dependences obtained herein were incorporated into the model. An example of the estimated polarization curves is shown in Figure B.4-14, where a good agreement was found with the experimental data.
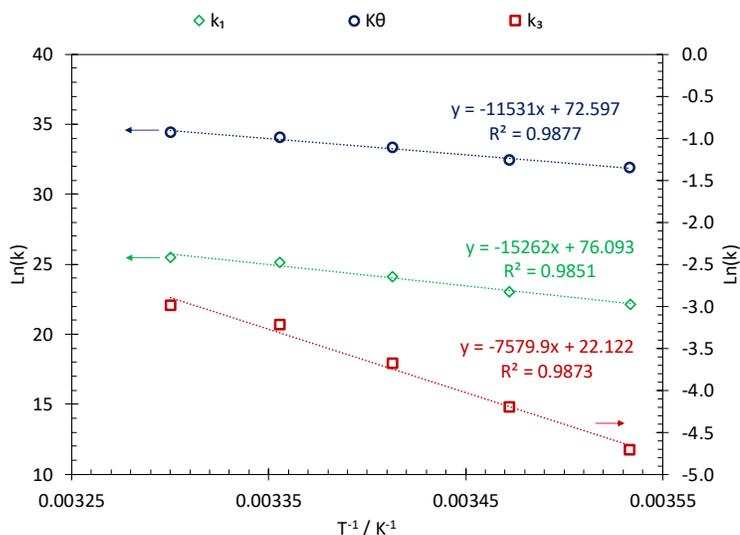
Figure B.4-16. The Arrhenius plot for the temperature dependence of the kinetic rate constant of the components of the iron dissolution reaction.

The temperature dependence of the kinetics of homogeneous chemical reactions are worthy of a further discussion. As noted above, the CO_2 corrosion involves a series of reactions with extreme rate constants, which are referred to as "diffusion controlled" reactions; meaning that these reactions are almost instantaneous as their rates are defined

by the rate at which the ions meet. The association of carbonic acid, bicarbonate ion are examples of such reactions, as discussed in previous sections. In the present discussion the dissociation rate of carbonic acid and bicarbonate ion and their temperature dependences is of particular interest. For the case of carbonic acid, considering the reported rates of the backward reaction is of the order of 10^{10} and the equilibrium constant of the order of 10^{-3}, this suggests that the rate of this reaction at room temperature is of the order of 10^7. With such a high kinetic rate this reaction is not expected to be rate limiting even at most extreme conditions encountered in CO_2 corrosion scenarios. Therefore, the temperature dependence of the rate of this reaction is not of any significance and can be treated as a constant value, for any practical purpose, in the present discussion. On the other hand, for the case of bicarbonate dissociation, even though the association reaction is also categorized as "diffusion controlled", the equilibrium constant of the order of 10^{-10} suggests that the dissociation reaction is rather slow at room temperatures. This was observed in the polarization curves reported in Figure B.4-12, where the limiting current densities were associated with the buffering effect of bicarbonate, and are limited by the rate of that reaction. To the best of the author's knowledge, no direct measurements for the rate of this reaction and its temperature dependence have been reported.

In the present study, the rate constant of the bicarbonate ion dissociation and its temperature dependence was estimated based on the limiting current densities obtained at pH 6 and pCO_2 of 5 bar. As shown in Figure B.4-12, the second limiting current observed at -0.85 V (vs. SHE) is associated with the rate of the bicarbonate dissociation reaction.

Figure B.4-17 shows the limiting current densities at this range that were measured at

temperatures from 10 ℃ to 40 ℃, and corrected for the interference of water reduction.

The measurements showed increased scattering with increased temperatures, as indicated

by the larger error bars at higher temperatures. The measured limiting currents do not

have a simple relationship with the bicarbonate dissociation rate constant since they also

include the effects of mass transfer of H^+, H_2CO_3, and HCO_3^-, in addition to effects

associated with the CO_2 hydration reaction. In order to obtain reasonably confident

estimations, the model was used to find the HCO_3^- dissociation rate constant associated

with the average values of the measured limiting currents. By doing so, all the above-

mentioned components of the limiting current are properly accounted for. The results

obtained in this fashion are shown in the primary axes of Figure B.4-17, and the rate

constant of bicarbonate ion dissociation was expressed as shown in Table B.4-8.
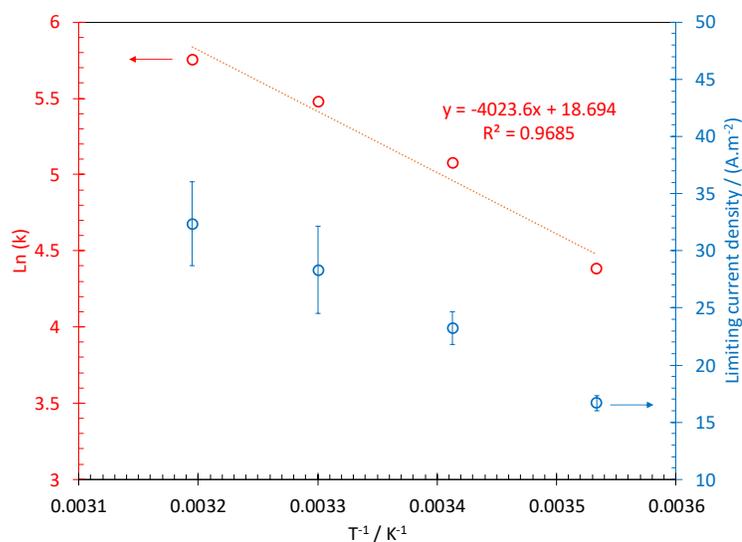
Figure B.4-17. The Arrhenius plot for the kinetic rate constant of the bicarbonate ion dissociation.

B.4.6.4: Corrosion rates

The estimated corrosion rates by the model are compared with the experimental data in this section. Figure B.4-18 shows the results obtained at $10^{\circ}C$ corresponding to the polarization curves shown in Figure B.4-4. In this graph the dashed bars show the estimated corrosion rates. At such conditions neither the cathodic currents nor the anodic currents were expected to be significantly influenced by the partial pressure of CO_2. That behavior was properly reflected by the predicted results. However, slight deviations, especially in the corrosion rates at pH 6, were observed.
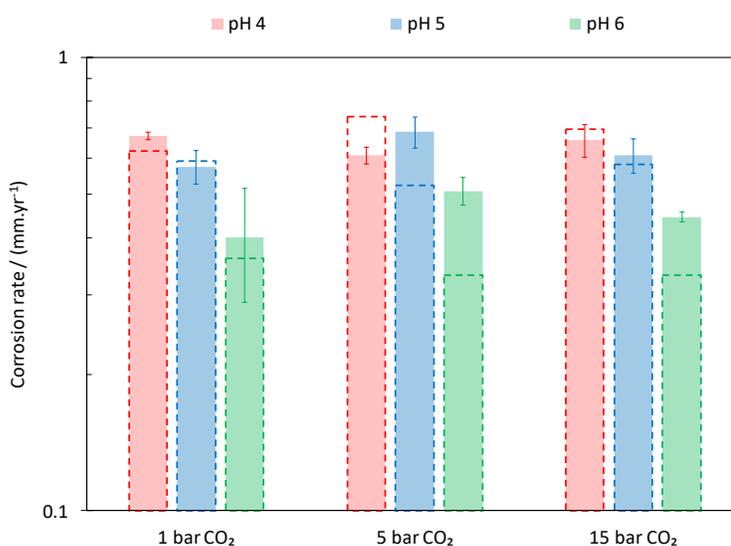
Figure B.4-18. The comparison of the estimated and the measured corrosion rates at $10^{\circ}C$, 4.6 m.s^{-1} TCFC flow, and 0.1 M NaCl on a API 5L X65 mild steel.

The effect of temperature on the models ability to estimate the corrosion rates is shown in Figure B.4-19, for pH 4 and pH 6, at 5 bar pCO_2. As expected, the increasing temperatures results in significantly higher corrosion rates. The estimated corrosion rates were found to agree reasonably well with those obtained experimentally, demonstrating

the capabilities of the model in capturing the effect of temperature. Furthermore, the estimated corrosion rates at 5 bar pCO_2 for various pH values and two temperatures, 10°C and 40°C, are compared with the experimental data in Figure B.4-20.
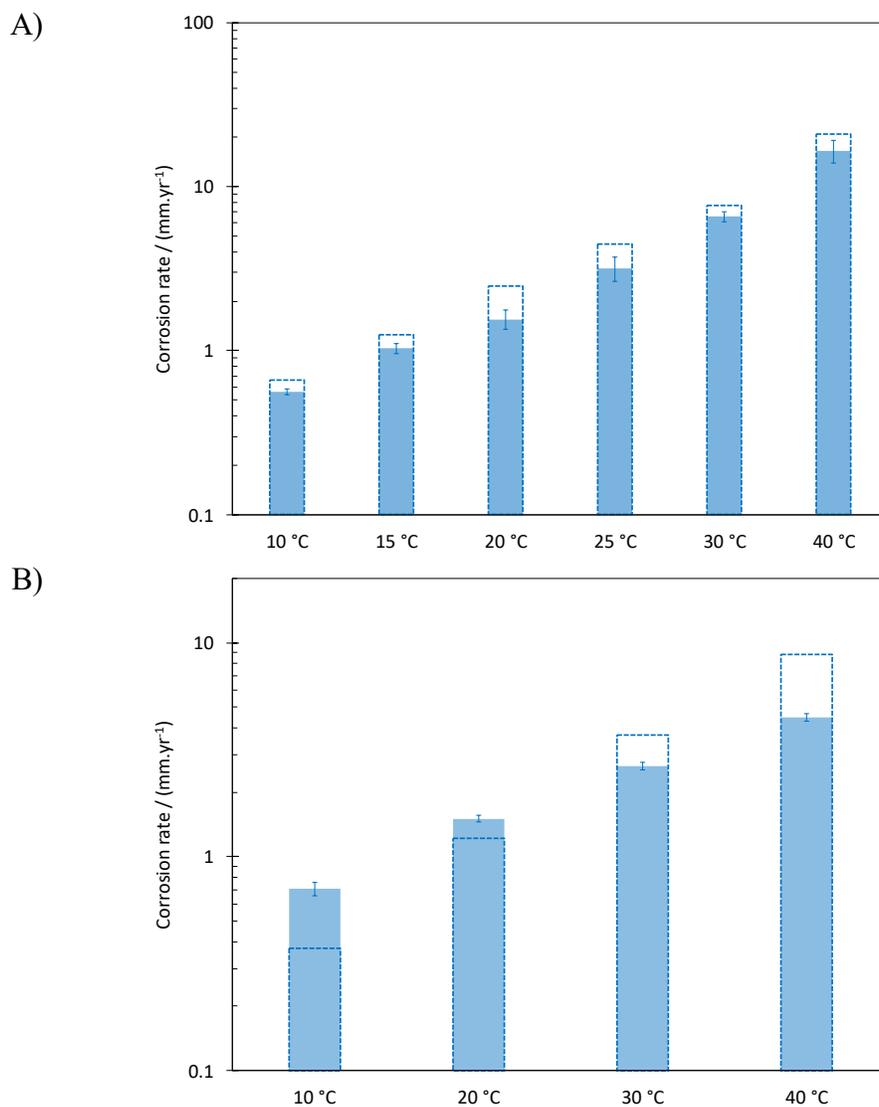
Figure B.4-19. The comparison of the estimated and measured corrosion rates at 5 bar pCO_2, 4.6 m.s^{-1} TCFC flow, and 0.1 M NaCl on a API 5L X65 mild steel at various temperatures. A) pH 4. B) pH 6.
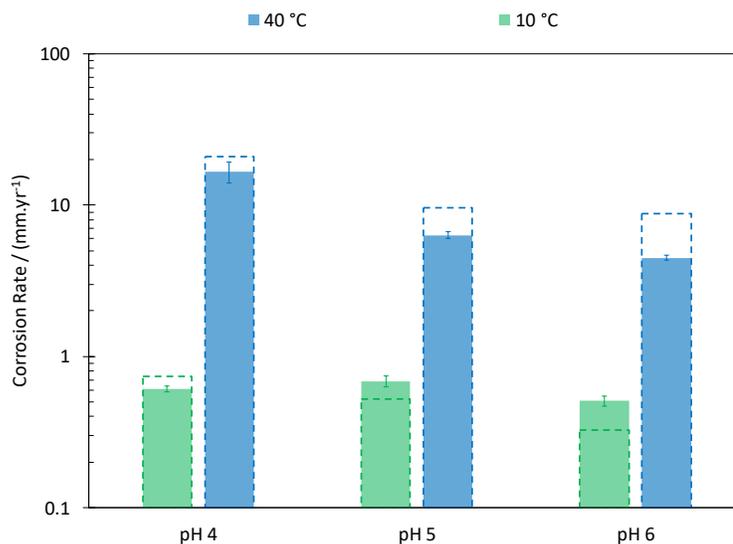
Figure B.4-20. The comparison of the estimated and the measured corrosion rates at 10°C and 40°C, 4.6 m.s^{-1} TCFC flow, 0.1 M NaCl, 5 bar pCO$_2$, and pH values from 4.0 to 6.0, on a API 5L X65 mild steel.

Ultimately, in order to examine the overall performance of the model, the estimated corrosion rates are compared with the experimental data in the parity graph of Figure B.4-20, for the environmental condition range of: 0<pCO$_2$<15 bar, 4.0 < pH < 6.0, 10°C<T<40°C , flow= 4.6 m.s^{-1} and 12.9 m.s^{-1}. The experimental data in Figure B.4-20 include the data obtained both in the present study and those in Chapter B.3: . The results demonstrated the ability of the model to reasonably estimate the corrosion rates in a reasonably wide range of experimental conditions, where almost all data points fall within 50% error from the estimated values.
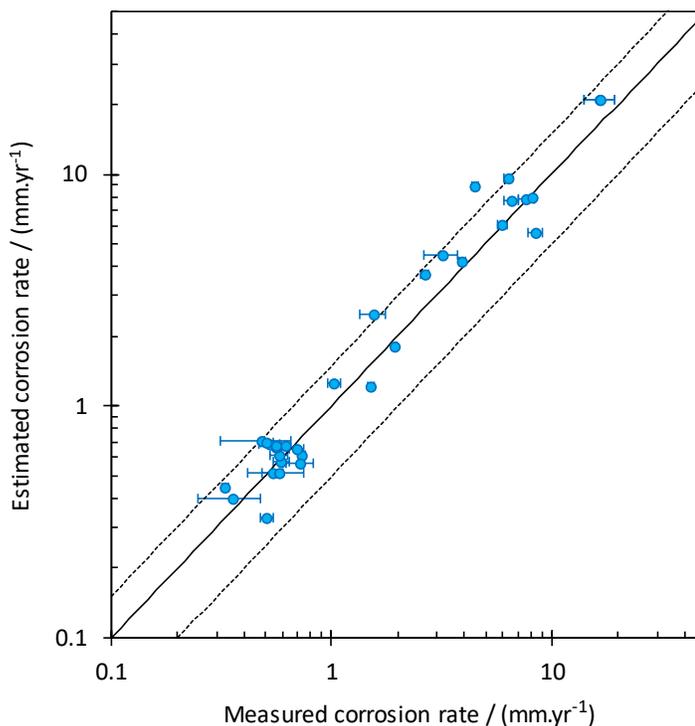
Figure B.4-21. Parity graph of the corrosion rate data and the estimated values at $0<pCO_2<15$ bar, $4.0 < pH < 6.0$, $10^oC<T<40^oC$, flow= $4.6 m.s^{-1}$ and 12.9 $m.s^{-1}$.

B.4.7: Summary

The electrochemical behavior of CO_2-saturated acid solutions on API 5L X65 mild steel was investigated experimentally and theoretically in the pH range of 4 to 6 and for CO_2 partial pressures from 1 to 15 bar. The theoretical investigation of the system was done based on a comprehensive mechanistic mathematical model that was coupled with a Pitzer-type specific interaction model, in order to account for the non-ideal behavior of the system. The results showed that:

- The direct reduction of H_2CO_3 is insignificant, in agreement with previous findings. The increased limiting currents were readily explained by the buffering effect of H_2CO_3 through its dissociation reaction and the CO_2 hydration reaction.

- The rate of the iron dissolution reaction in the transition and pre-passivation ranges is increased significantly with increasing CO_2 partial pressures. However, this effect was reduced at higher pH values.

- The effect of bicarbonate ion was observed at pH 6 and elevated CO_2 partial pressures. Quantitative analysis of the data suggests that the direct reduction of HCO_3^- is also insignificant, and the observed influences associated with this species can be readily explained by it's buffering ability as a weak acid.

- The corrosion rates estimated using the present model were found to be able to represent the values obtained experimentally well.

PART C: THE CASE OF HYDROGEN SULFIDE

- Chapter C.1: The buffering effect as the main contribution of H_2S in mild steel corrosion

Chapter C.1: The buffering effect as the main contribution of H_2S in mild steel corrosion[6]

C.1.1: Introduction

In the context of H_2S corrosion of mild steel, the direct reduction of H_2S is currently believed to be the main contribuor of this species to the cathodic currents. This is perhaps due to the distinct behavior of the cathodic currents in the presence of H_2S, as compared to that of other weak acids such as carboxylic acids and carbonic acid. In the presence of H_2S, the cathodic currents readily show a "double wave" shape that is widely considered to be the result of direct reduction of this species. In this chapter, with the focus on the buffering ability of H_2S, the mechanism of the cathodic reactions in H_2S containing solutions is theoretically investigated. It is shown that all characteristic behaviors of the cathodic currents that were previously associated with the direct reduction of H_2S, including the "double wave" shape, can be explained in terms of the H_2S dissociation reaction and its buffering effect as a weak acid.

C.1.2: Background

In the presence of an aqueous medium, hydrogen sulfide (H_2S) in the gas phase can dissolve and dissociate according to equilibrium Reactions (C.1-1) to (C.1-3). As a weak acid, H_2S is only partially dissociated in the aqueous phase, establishing its own set of chemical equilibria. The presence of these sulfide species in the solution is believed to dramatically influence the corrosion process, both in terms of their electrochemical

---

[6] A version of this chapter is under revew for publication as : "H_2S Corrosion of Mild Steel: A Quantitative Analysis of the Mechanism of the Cathodic Reaction", Kahyarian, A., and S. Nesic, Electrochimica Acta, 2019

tendencies and, perhaps more importantly, due to their contributions to the formation of a corrosion product layer.

$$H_2S_{(g)} \rightleftharpoons H_2S_{(aq)} \qquad \text{(C.1-1)}$$

$$H_2S_{(aq)} \rightleftharpoons HS^-{}_{(aq)} + H^+_{(aq)} \qquad \text{(C.1-2)}$$

$$HS^-{}_{(aq)} \rightleftharpoons S^{2-}_{(aq)} + H^+_{(aq)} \qquad \text{(C.1-3)}$$

The present study is focused on the mechanistic fundamentals of the H_2S contribution to the cathodic currents during the corrosion process. The acidic corrosion of steel in the presence of H_2S is believed to be the result of electrochemical dissolution of iron (Reaction (C.1-4)) as the main anodic reaction, accompanied by a series of cathodic hydrogen evolving reactions as shown via Reactions (C.1-5) to (C.1-8). These include hydrogen ion (H^+) and water (H_2O) reduction (Reactions (C.1-4) and (C.1-5), respectively), which are well-known processes in metallic corrosion in deaerated aqueous acidic systems. Furthermore, in the context of the present study, the hydrogen-evolving reactions associated with the direct reduction of H_2S and HS⁻ (Reactions (C.1-6) and (C.1-7), respectively) are comonly presumed to contribute to cathodic currents[13,16,17,276–282]. The relative significance of these cathodic reactions is thought to be defined mainly by the solution pH and H_2S partial pressure, that specifies the concentration of the involved electroactive species.

$$Fe^{2+} + 2e^- \rightleftharpoons Fe \qquad \text{(C.1-4)}$$

$$H^+_{(aq)} + e^- \rightleftharpoons {}^1\!/_2\, H_{2,(g)} \qquad \text{(C.1-5)}$$

$$H_2S_{(aq)} + e^- \rightleftharpoons {}^1\!/_2\, H_{2,(g)} + HS^-{}_{(aq)} \qquad \text{(C.1-6)}$$

$$HS^-_{(aq)} + e^- \rightleftharpoons {}^1/_2\, H_{2,(g)} + S^{2-}_{(aq)} \qquad\qquad (\text{C.1-7})$$

$$H_2O_{(aq)} + e^- \rightleftharpoons {}^1/_2\, H_{2,(g)} + OH^-_{(aq)} \qquad\qquad (\text{C.1-8})$$

Qualitative arguments associated with the electrochemical contribution of H_2S to the cathodic currents can be found in studies from as early as 1965, as reported by Bolmer[276]. The same direct H_2S reduction reaction was also considered to contribute to the observed polarization cathodic currents obtained in rotating disk experiments by Morris, et al.[277]. In that study, the authors noted that in the presence of H_2S, the H^+ reduction limiting current is significantly increased, while the behavior of the charge transfer controlled range of currents remained unaffected. That behavior was attributed to the direct reduction of H_2S. Such observations made the proposed electrochemical activity of the H_2S an accepted mechanism of corrosion in H_2S systems in subsequent studies [278–282]. Nevertheless, a systematic investigation of this mechanistic aspect was not done until more recently. In 2013, Kittel, et al., investigated the cathodic polarization curves of a H_2S containing solution on a stainless steel surface [17]. The previous reports of the significant effect of H_2S on the limiting current was confirmed in that study. Furthermore, the authors showed that in certain conditions a "double wave" shape appears in the polarization curves; an observation that was considered as a solid proof for the direct H_2S reduction reaction. The observed double wave was associated with the existence of two electrochemical reactions and their corresponding limiting currents, one being the H^+ and other being the H_2S reduction reaction. The experimental findings of this study were further used to developed a mathematical model for cathodic polarization behavior in H_2S containing solutions [16]. The model proposed in that study included both

the H^+ and H_2S cathodic reactions and also the homogeneous chemical reactions

associated with the H_2S/H_2O system.

In a paralel study[13] , Zheng, et al., investigated the mechanism of mild steel

corrosion in the presence of H_2S, in a wider range of experimental conditions. The effect

of H_2S on the limiting current, and the existence of two limiting currents (i.e., the "double

wave") was also reported in that study. The authors noted that both limiting currents,

associated with the H^+ and H_2S reduction reactions, are the result of mass transfer

limitations of the involved reactants. These observations led the authors to conclude that

in H_2S containing solutions, the direct reduction of H_2S is a significant cathodic process.

Zheng, et al., also developed an elementary mechanistic model [43] based on these findings,

where a reasonable agreement with the experimental data was reported. The scope of this

study was later extended to the case of corrosion under CO_2/H_2S mixed atmospheres [259].

The mechanistic findings in the latter case were found to agree with those of their

original N_2/H_2S system[13]. In 2017, Esmaeely, et al., reported a set of experimental

polarization data at pH_2S of 1 bar [283] on a mild steel surface. The reported polarization

curves were found to behave similarly to those obtained at lower H_2S partial pressures in

earlier studies [13,259]. The authors used the same model as that proposed by Zheng, et al., [13]

to compare with their experimental data, reporting good agreement.

Looking at the study of mild steel corrosion in the presence of weak acids in its

entirety, the findings of the last 15 years have revolutionized the classic mechanistic

understanding of this process [11,12,15,62,189,200,201,210]. The main leap in the mechanistic

understanding over recent years was a result of the introduction of comprehensive

mechanistic mathematical models [15,45,166,167,227], as reviewed elsewhere [43,60]. These models allowed the complex water chemistry, typical of solutions containing CO_2, carboxylic acid, and also H_2S, to be coupled with mass transfer and surface electrochemical processes. The quantitative results obtained from these models highlighted the effect of homogeneous chemical reactions on corrosion, particularly the rate of cathodic reactions [11,15,45,46,210]. It was based on such analyses, and well targeted experiments, that recent studies demonstrated that direct reduction of weak acids such as acetic acid and carbonic acid, previously considered an essential part of the corrosion mechanism, are in fact insignificant [11,12,50,62,201]. The contribution of these species is now known to be mainly a result of their natural buffering ability as weak acids [11,12,50,62,201].

In typical environmental conditions of corroding systems, weak acids such as acetic acid and carbonic acid with pKa values below 4 have favorable conditions to readily dissociate and buffer the surface pH. With this property, the cathodic limiting currents in the presence of these weak acids is significantly increased, since the dissociation reaction acts as an additional source of H^+ at the electrode surface. That, in turn, results in increased corrosion rates if controlled by the limiting current.

At the other end of the spectrum, a weak acid such as water, with a pKa of 14, has no significant buffering ability, as its dissociation is only favored at extreme pH values. Interestingly, the case of H_2S with pKa of about 7 falls at the mid-range of this spectrum. Therefore, one may expect H_2S to also exhibit a significant buffering ability, at least in a certain range of environmental conditions. Nevertheless, this aspect has largely remained neglected in mechanistic studies of H_2S corrosion. This may be partially due to the fact

that elementary mechanistic models commonly used to quantify the experimental data, such as that developed by Zheng, et al.[13,259], are not able to properly represent the complex solution chemistry in the vicinity of the metal surface [43,60].

In the present study, the effect of homogeneous dissociation of H_2S inside the diffusion boundary layer on the polarization response of the system was investigated theoretically. For that purpose, a comprehensive mathematical model was developed in order to incorporate the effect of the homogeneous reactions and the transport processes on the surface concentration of H^+. As discussed further in the following sections, the results showed that the buffering effect of H_2S is indeed significant in nearly all typically encountered conditions. The increased limiting currents and the observed "double wave" were readily explained by the homogeneous H_2S dissociation reaction, without considering the direct reduction of H_2S. The simulated polarization curves were also compared to the recent experimental data reported in the literature, and a reasonable agreement was found.

C.1.3: Mathematical model

C.1.3.1: Water chemistry

The water chemistry calculation is the first step in a quantitative analysis of any corroding system, which is essentially done to obtain the concentration of the involved chemical species. Upon dissolution in water, the dissolved H_2S, as a diprotic weak acid, partially dissociates to form HS^- and H^+. HS^- itself can further dissociate to form another H^+ and S^{2-}. This reaction sequence is described according to the chemical Reactions (

C.1-1) to (C.1-3), above. In an aqueous solution the dissociation of water, as the solvent, also occurs as shown by Reaction (C.1-9).

$$H_2O_{(l)} \rightleftharpoons OH^-_{(aq)} + H^+_{(aq)} \hspace{4cm} (\text{C.1-9})$$

The dissolution of H_2S in water (equilibrium Reactions (C.1-1)) can be described according to Henry's law, assuming ideal conditions:

$$\frac{C_{H_2S_{(aq)}}}{p_{H_2S_{(g)}}} = K_{H,H_2S} \hspace{4cm} (\text{C.1-10})$$

where $C_{H_2S_{(aq)}}$ (M) is the concentration of the dissolved H_2S, $p_{H_2S_{(g)}}$ is the partial pressure of H_2S (bar), and K_{H,H_2S} is Henry's constant, as shown in Table C.1-1.

The chemical equilibria of the dissociation Reactions (C.1-2) and (C.1-3) can be expressed mathematically via Equations (C.1-11) and (C.1-12), with K_{H_2S} and K_{HS^-} being the equilibrium constants of the H_2S and HS⁻ dissociation reactions, respectively, as shown in Table C.1-1.

$$\frac{C_{HS^-_{(aq)}} C_{H^+_{(aq)}}}{C_{H_2S_{(aq)}}} = K_{H_2S} \hspace{4cm} (\text{C.1-11})$$

$$\frac{C_{S^{2-}_{(aq)}} C_{H^+_{(aq)}}}{C_{HS^-_{(aq)}}} = K_{HS^-} \hspace{4cm} (\text{C.1-12})$$

The water dissociation reaction, ionic product of K_w (see Table C.1-1), can also be expressed as:

$$C_{OH^-_{(aq)}} C_{H^+_{(aq)}} = K_w \hspace{4cm} (\text{C.1-13})$$

Table C.1-1. Equilibrium and kinetic rate constants of the H$_2$S/H$_2$O system.

Parameter	Reference
$K_w = (10^{-3}\rho_w)^2 \; 10^{-\left(a1+\frac{a2}{T}+\frac{a3}{T^2}+\frac{a4}{T^3}+\left(a5+\frac{a6}{T}+\frac{a7}{T^2}\right)log\left(10^{-3}\rho_w\right)\right)}$ (M ^{2}) a_1= -4.098, a_2= -3245.2, a_3= 2.2362, a_4= -3984E7, a_5= 13.957, a_6= -1262.3, a_7= 8.5641E5	64
$K_{H,H_2S} = (10^{-3}\rho_w) \; 10^{\left(b_1+b_2\,T+b_3\,T^2+{}^{b_4}/_T+b_5\,log(T)\right)}$ (M.bar^{-1}) b_1= 6.343E2 , b_2= 2.709 E-1, b_3= -1.113E-4, b_4= -1.672E4, b_5=-2.619E2	284
$K_{H_2S} = (10^{-3}\rho_w) \; 10^{\left(c_1+c_2\,T+c_3\,T^2+{}^{C_4}/_T+c_5\,\ln(T)\right)}$ (M) c_1=7.824E2, c_2= 3.613E-1, c_3= -1.672E-4, c_4= - 2.057E4, c_5= - 1.427E2	285
$K_{HS^-} = 10^{-17.4}$ (M)	286
$k_{b,H_2S} = 7.5 \times 10^{10}$ (M^{-1}.s^{-1})	274
$k_{b,HS^-} = 8 \times 10^{10}$ (M^{-1}.s^{-1})	Estimated
$k_{b,w} = 1.4 \times 10^{11}$ (M^{-1}.s^{-1})	66,67

At a known solution pH and partial pressure of H$_2$S, the solution speciation can be readily obtained based on Equations (C.1-10) to (C.1-13). In addition to the species above, the solution usually contains other ions such as Na$^+$ and Cl$^-$ as dissolved neutral salts (i.e., NaCl), with a known concentration that can be directly specified. However, a charge imbalance in the conserved ions, the ions that are not involved in the equilibria, e.g., Na$^+$ and Cl$^-$, would result in a shift in the solution pH. In fact, commonly in both experimental and practical scenarios, such ions are introduced into the solution as acid, base, or acidic/basic salts, e.g., HCl, NaOH, etc. At a given pH the charge imbalance can be obtained via electroneutrality constraints, shown as Equation (C.1-14). In a simple case, such as that in laboratory conditions, where the charge imbalance is a result of a single species, this parameter can be readily translated to the concentration of that species.

$$\sum_i z_i C_i = 0 \qquad \text{(C.1-14)}$$

Figure C.1-1 demonstrates the results of such calculations for an open system at 0.1 and 1 bar H_2S partial pressures for a range of pH values.
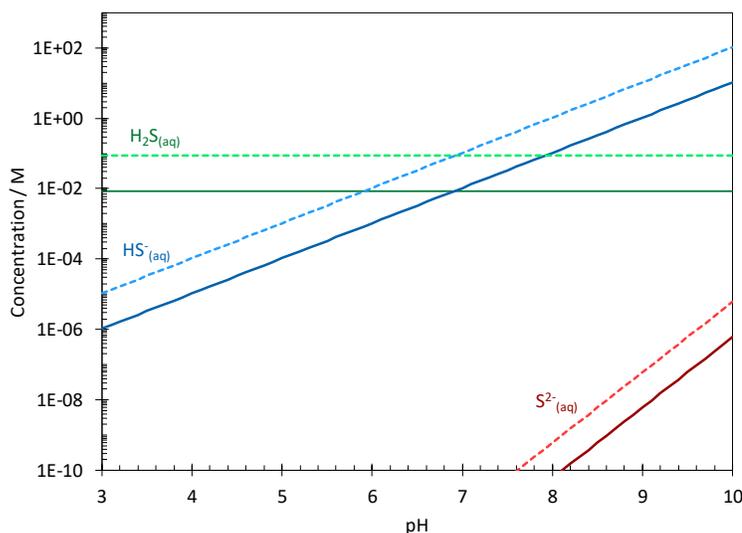
Figure C.1-1. The calculated solution speciation of H_2S/H_2O system at 30°C, for 0.1 bar H_2S (solid lines), and 1 bar H_2S (dashed lines).

C.1.3.2: Governing equations inside the diffusion boundary layer

The electrochemical response of a system, such as the one considered in the present study, can be obtained by solving the mass conservation law in the diffusion boundary layer. That is a necessary step considering the heterogeneous nature of the electrochemical reactions, and the fact that their rates are defined based on the surface concentration of the active species; which are not explicitly known. Such calculations allow these concentrations to be obtained based on the known bulk concentrations, when the appropriate relationships governing their concentration distribution inside the

diffusion layer and at the electrode surface are used. The mass conservation law inside the diffusion boundary layer is described as Equation (C.1-15), which is also known as the Nernst-Planck Equation.

$$\frac{\partial C_i}{\partial t} = -\nabla . N_i + R_i$$

(C.1-15)

Equation (C.1-15) describes the concentration distribution of species i, where N_i is the flux, and R_i is the source term that includes the consumption/production of species i through homogeneous chemical reactions. The flux of any given species can be described through Equation (C.1-16) [68].

$$N_i = -z_i u_i F C_i \nabla \phi - D_i \nabla C_i + v C_i$$

(C.1-16)

where the terms on the right hand side describe the effect of electromigration, molecular diffusion, and convective flow, respectively.

Table C.1-2. Reference diffusion coefficients at 25 °C.

Species	Diffusion coefficient $\times 10^9$ (m²/s)	Reference
H_2S	1.93	287
HS^-	1.731	70
S^{2-}	1.5	Estimated
H^+	9.312	68
OH^-	5.273	70
Na^+	1.334	68
Cl^-	2.032	68,70

Considering the symmetry of the electrode, the tangential and radial species flux components of Equation (C.1-15) and Equation (C.1-16) can be neglected. Furthermore, the mobility of ions can be estimated using the Nernst-Einstein relationship

($u_i = D_i/RT$), with the diffusion coefficients listed in Table C.1-2. Hence, the equations above can be simplified to Equation (C.1-17) and Equation (C.1-18):

$$N_i = -D_i \frac{\partial C_i}{\partial x} - \frac{z_i D_i F C_i}{RT} \frac{\partial \phi}{\partial x} + v_x C_i \tag{C.1-17}$$

$$\frac{\partial C_i}{\partial t} = D_i \frac{\partial}{\partial x} \frac{\partial C_i}{\partial x} + \frac{\partial}{\partial x} \left(\frac{z_i D_i F C_i}{RT} \frac{\partial \phi}{\partial x} \right) - v_x \frac{\partial C_i}{\partial x} + R_i \tag{C.1-18}$$

In the convective term, v_x describes the local velocity inside the diffusion layer. For example, for the case of a rotating disk electrode (RDE), the analytical solutions for the velocity profile (v_x) and the diffusion layer thickness (δ) are shown as Equation (C.1-19), where $a = 0.510$, and Equation (C.1-20), respectively [69].

$$v_x = -a\omega \left(\frac{\omega}{v}\right)^{1/2} x^2 \tag{C.1-19}$$

$$\delta = \left(\frac{3 D_{lim}}{av}\right)^{1/3} \left(\frac{\omega}{v}\right)^{-1/2} \tag{C.1-20}$$

As mentioned above, the rates of consumption/production of the chemical species, via homogeneous chemical reactions, are incorporated in these calculation through the R_i term in Equation (C.1-18). The rate of chemical reaction j, presented in the form of Reaction (C.1-21) is expressed as Equation (C.1-22).

$$\sum_{r=1}^{n_r} C_r \rightleftharpoons \sum_{p=1}^{n_p} C_p \tag{C.1-21}$$

$$R_j = k_{f,j} \prod_{r=1}^{n_r} C_r - k_{b,j} \prod_{p=1}^{n_p} C_p \tag{C.1-22}$$

where $k_{f,j}$ and $k_{b,j}$ are the reaction rate constants of the forward and backward reactions. Here, the solution inside the diffusion boundary layer is treated as a single aqueous phase.

The relevant chemical reactions are, therefore, the dissociation of H_2S, HS^-, and H_2O. The kinetic rate constants for these reactions can be found in Table C.1-1. For each chemical species, R_i is the sum of the rates corresponding to all j chemical reactions involving this species, as shown in Equation (C.1-23).

$$R_i = \sum_j R_j \, s_{i,j}$$

(C.1-23)

In Equation (C.1-23), the rate of reaction where species i is produced is expressed as a positive value, and when it is consumed as a negative value, and $s_{i,j}$ is the stoichiometric coefficient of species i in reaction j.

In addition to the concentration of species, the potential of the solution inside the diffusion boundary layer has to be specified in order to calculate the effect of electromigration, as seen in Equation (C.1-18). This parameter can be obtained by introducing an additional relationship known as the "electroneutrality" constraint, which is already introduced as Equation (C.1-14).

C.1.3.3: Initial and boundary conditions

As a second order partial differential equation, Equation (C.1-18) can only be solved if the appropriate boundary and initial conditions are specified. At the initial time ($t = 0$), it can be assumed that a well-mixed solution comes into contact with the metal surface. Hence, the concentrations of the chemical species throughout the diffusion layer are constant known values, defined by the chemical equilibria of the solution as obtained from the water chemistry calculations. Furthermore, at the bulk solution boundary, where $x = \delta$, the concentration of chemical species remains unchanged at all times (t $\geq$ 0).

The boundary condition at the metal/solution interface can be specified in terms of the flux of the chemical species as defined by electrochemical reactions. For an electroactive chemical species, the flux at the metal/solution interface is equal to the rate of its consumption/production through the heterogeneous electrochemical reactions. Therefore, for species i involved in an electrochemical reaction, it can be stated that:

$$N_i|_{x=0} = -\frac{s_i i}{nF}$$
(C.1-24)

The negative sign in Equation (C.1-24) is due to a sign convention where cathodic currents are taken as negative. Furthermore, for the reactions written in "cathodic" form (e.g. Reactions (C.1-5)), the reactants on the left hand side are represented with a negative stoichiometric coefficient (s_{ij}) and the products on the right hand side are represented as positive values.

The present study is focused on the reactions that define the cathodic portion of the corrosion current, in typical experimental and industrial conditions. Therefore, the anodic iron dissolution and water reduction reactions are not included in the present discussion. Additionally, the present study attempts to investigate if the polarization curves can be explained without considering the direct reduction of sulfide species (Reactions (C.1-6) and (C.1-7)). Therefore, the only electrochemical reaction in the present model is the one describing H^+ reduction. Due to the negligible concentration of H_2 in the solution, no significant contribution of the hydrogen oxidation reaction over the potential range of interest is expected. Hence, the cathodic current density resulting from hydrogen ion reduction was calculated in the form shown in Equation (C.1-25). The kinetic parameters, including transfer coefficient $\alpha_{H^+} = 0.5$, the reaction rate constant

$k_{0_{H^+}} = 1.2E - 8$, and the reaction order $m_{H^+} = 0.5$, used in this model, were estimated based on the experimental data previously reported in the literature, as discussed in the following section.

$$i_{c,H^+} = -n_{H^+}Fk_{0_{H^+}}C_{H^+}^{s\ m_{H^+}}e^{\left(\frac{-\alpha_{H^+}n_{H^+}F\left(E_{app}-E_{0_{H^+}}\right)}{RT}\right)} \qquad (\text{C.1-25})$$

For non-electroactive species, the flux at the metal surface is zero, as it is a non-porous non-reactive barrier for these species:

$$N_i|_{x=0} = 0 \qquad (\text{C.1-26})$$

The flux Equations (C.1-25) and (C.1-26) can be used to describe the boundary conditions for all chemical species at the metal surface. Considering that the N_i appears in these relationships, the solution potential should also be specified at the solution/metal boundary. This can be done similarly to that in the governing equations, using the electroneutrality constraint as described by Equation (C.1-14).

C.1.3.4: Numerical Solution

Mathematical relationships required to develop a comprehensive mathematical model, as discussed above, are summarized in Table C.1-3. These equations form a set of non-linear, coupled, partial differential equations. Considering the simple one-dimensional spatial computational space, the finite difference method can be used to solve these equations numerically. This method is commonplace in mathematical modeling of electrochemical systems with similar geometry, and has been discussed in detail elsewhere [43,68,201].

Table C.1-3. Summary of equations used in the mathematical model.

Electrode surface boundary

$$N_i|_{x=0} = -\frac{s_{ij} i_j}{n_j F}$$ For electroactive species

$$N_i|_{x=0} = 0$$ For non-active species

$$\sum_i z_i C_i = 0$$

Diffusion boundary layer

$$\frac{\partial C_i}{\partial t} = D_i \frac{\partial}{\partial x}\frac{\partial C_i}{\partial x} + \frac{\partial}{\partial x}\left(\frac{z_i D_i F C_i}{RT}\frac{\partial \phi}{\partial x}\right) - v_x \frac{\partial C_i}{\partial x} + R_i$$ For all species

$$\sum_i z_i C_i = 0$$

Bulk boundary conditions

$$C_i = C_i^b$$

$$\Phi = 0$$ Arbitrary reference potential

The partial differential equations are discretized using non-uniform mesh second order Taylor's series approximations as discussed in Chapter B.3: . The time integration is done explicitly, using the Euler approximation. The resulting algebraic equations can be written in a matrix format, as a sparsely populated coefficient matrix multiplied by the unknown concentrations and solution potential. The final solution can then be obtained through different solution algorithms, such as with Newman's "Band-J" (open-source code) where it is solved by the LU decomposition method [68]. The presence of nonlinear terms, such as those in the electro-migration or chemical reaction relationships, makes some of the terms in the coefficient matrix to be a function of other concentrations and/or potential, i.e., they are not explicitly known. In the approach used in the present model,

the final solution was obtained iteratively by using an initial guess for the unknown terms

of the coefficient matrix, usually the last calculated value of the unknown term, until the

desired accuracy ($R^2=10^{-12}$) was achieved.

C.1.4: Results and discussion

C.1.4.1: A theoretical discussion

Let us first entertain the idea that the buffering effect of H_2S can become

significant if the environmental conditions are favorable. This is expected from any weak

acid, including H_2S, as a result of their partial dissociation in an aqueous environment. As

shown in the water chemistry calculations, the extent of dissociation is pH dependent.

Considering the recent findings in similar systems, weak acids with relatively low pKa

(about 4), such as acetic acid, and carbonic acid, are excellent buffers [11,12,200,201]. This

means that their equilibrium and kinetic properties allow them to readily dissociate as the

surface pH, due to mass transfer limitation, is increased. In terms of reaction kinetics, the

association of H_2S is categorized as "diffusion controlled", similar to association of

water, carbonic acid, and acetic acid [274]. The term "diffusion controlled" refers to

reactions with extreme rates that occur as soon as the reactants "collide" [65,274,288]. With

pKa of about 7, H_2S appears to be thermodynamically and kinetically capable to exhibit,

at least partially, the same buffering abilities.

The theoretical significance of the buffering ability of H_2S is first discussed in

terms of the simulated cathodic polarization curves, using the mathematical model

developed above. As described, in this model H^+ reduction is the only cathodic reaction

considered. Figure C.1-2 demonstrates the predicted steady state polarization curves at

the pH range from 3 to 5 and pH_2S of 0 to 1 bar. The results clearly demonstrate that the

buffering effect of H_2S is indeed significant at almost all conditions, which results in a

significant increase in the observed cathodic currents with increasing pH_2S. Furthermore,

the characteristic cathodic "double wave", which was previously associated with its direct

reduction [13,16,17,259,283], was predicted in these voltammograms as well. As is observed in

Figure C.1-2, the first limiting current can be associated with the mass transfer limitation

of H^+ reduction, which is not affected by pH_2S and remains constant at a constant pH.

The second limiting current is due to the presence of H_2S in the solution. As the pH is

increased, the potential at which this wave is observed shifts towards more positive

potentials. Also, the pH_2S at which the second wave appears decreases with increasing

pH values. On the other hand, the characteristic double wave shape rapidly diminished at

higher pH values. Considering that the predicted results are solely based on H^+ reduction,

these characteristic behaviors are all associated with the relative dominance of two

processes that supply the H^+ at the electrode surface:

a) The mass transfer of H^+ from the bulk solution.

b) The dissociation of H_2S at the vicinity of the metal surface.

In order to further analyze the nature of the observed double wave, the calculated

surface chemistry during the polarization was studied. Figure C.1-3 illustrates the current

response of the simulation at pH 3 and pH_2S of 0.2 bar on the secondary axis, versus the

calculated surface pH on the horizontal axis. The behavior of the surface concentration of

H_2S and HS^- are shown in the same graph, on the primary vertical axis. As it appears in

Figure C.1-3, up to the current density of about 10 $A.m^{-2}$, the surface pH remains

practically unchanged; which corresponds to the charge transfer controlled cathodic range observed in Figure C.1-2.A. In this range, the surface concentration of all species is the same as that in the bulk solution. As the first limiting current density at about 40 $A.m^{-2}$ is reached, the surface pH starts to increase, as expected from a mass transfer limiting scenario. In this range, although the current density does not increase, the surface pH increases as the potential (the driving force of the reaction) decreased to more negative values. Ultimately, at a negative enough potential, the surface pH reaches a sufficiently high value to favor the dissociation of H_2S. This reaction becomes significant at surface pH values of about 5 and reaches its maximum at about pH 9. The crossing pH of H_2S and HS^- concentration trends occurs almost at the pKa value of H_2S. Considering the much higher pKa of HS^- (about 17), no significant contribution from this reaction is expected in the surface pH range at these conditions.
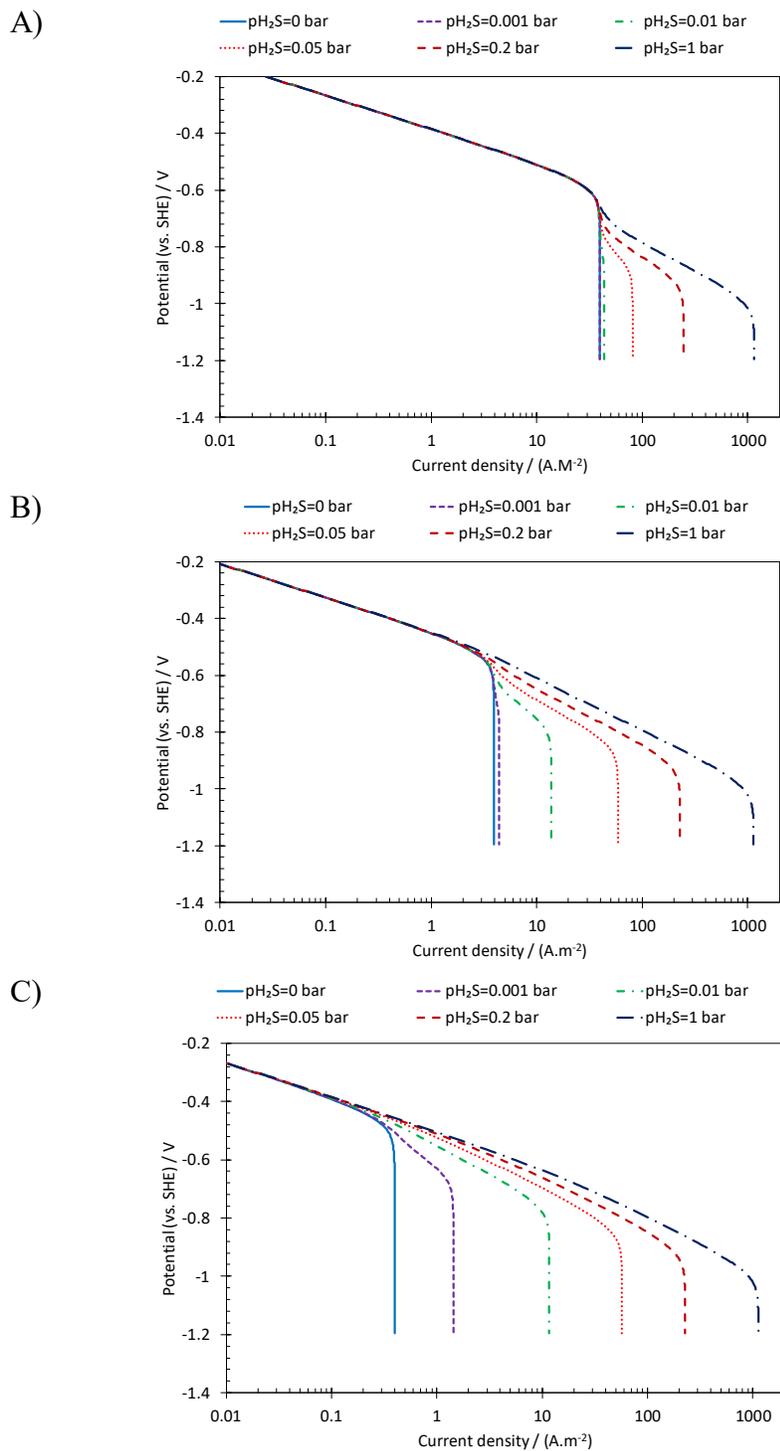
Figure C.1-2. Simulated steady state cathodic polarization behavior of acidic solutions containing H_2S, at 25°C, 0.1 M NaCl, 2000 rpm RDE. A) pH 3. B) pH 4. C) pH 5.

As rule of thumb, when the mass transfer limited current of H^+ reduction starts to appear, the surface pH is about 1-2 units higher than the bulk pH. Considering the case of a bulk pH of 5, that suggests the surface pH rapidly reaches the range that favors H_2S dissociation. That is the reason why a double wave is not clearly observed in this condition, as shown in Figure C.1-2.C. On the other hand, at a bulk pH of 3, the surface pH favorable for H_2S dissociation is only reached at potentials substantially into the H^+ reduction limiting current range; thus, the double wave is observed in an extended pH_2S range of Figure C.1-2.A.
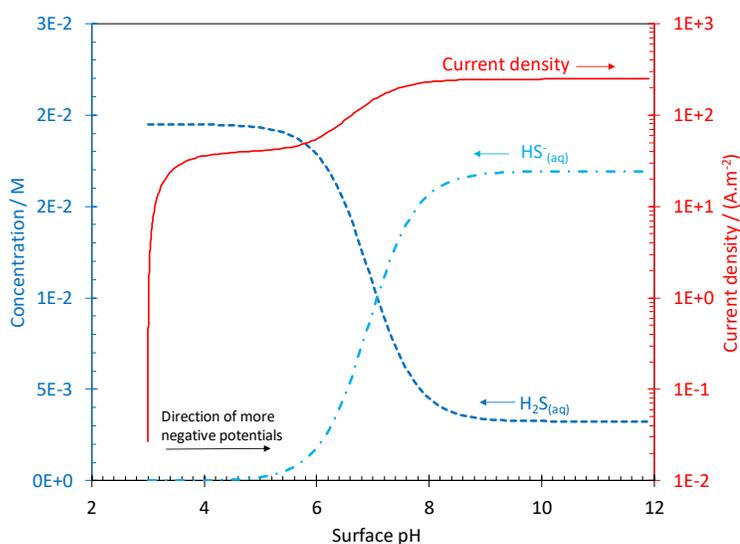
Figure C.1-3. The relationship between the calculated surface pH and the surface concentration of H_2S and HS^-, on the primary vertical axis, and the calculated current density, on the secondary vertical axis. Conditions: 25°C, 2000 rpm RDE, pH 3, pH_2S=0.2 bar, and the potential range from -0.2 to -1.2 V vs. SHE.

C.1.4.2: Experimental verification

In order to further examine the validity of the above mechanistic observations, the results obtained from this model were compared with the experimental data reported in

the literature. The experimental data of the present discussion was taken from two recent studies by Zheng, et al.,[13] and Esmaeely[283], et al., that reported a series of polarization curves obtained at various environmental conditions. The experiments in these studies were done using rotating cylinder electrodes. In order to properly estimate the mass transfer effect, the equivalent rotating speed of a rotating disk electrode was obtained by equating the mass transfer coefficient from the two well-known Eisenberg [144] and Levich equations. The equivalent rotation speed (rpm) was obtained as:

$$\Omega_{RDE} = (0.0785 \times \Omega_{RCE}^{0.7} \, d_{RCE}^{0.4} \, v^{-0.177} \, D^{0.023})^2 \qquad\qquad (\text{C.1-27})$$

Considering these studies together [13,283], the conditions from pH 3 to 5 and pH_2S from 0 to 1 bar were covered experimentaly. The authors themselves proposed a mechanistic model, where both H^+ and H_2S were considered to be reduced at the metal surface. The comparison of the present model of cathodic currents, solely based on H^+ reduction and the buffering effect of H_2S, are shown in Figure C.1-4 and Figure C.1-5. A reasonable agreement with the experimental data was found, where the model was able to predict the main characteristic features of the cathodic polarization curves. Even though the present model does not include the direct reduction of H_2S, the simulated cathodic polarization curves were found to be at the same level of agreement with the experimental data as those reported in the original studies [13,283].
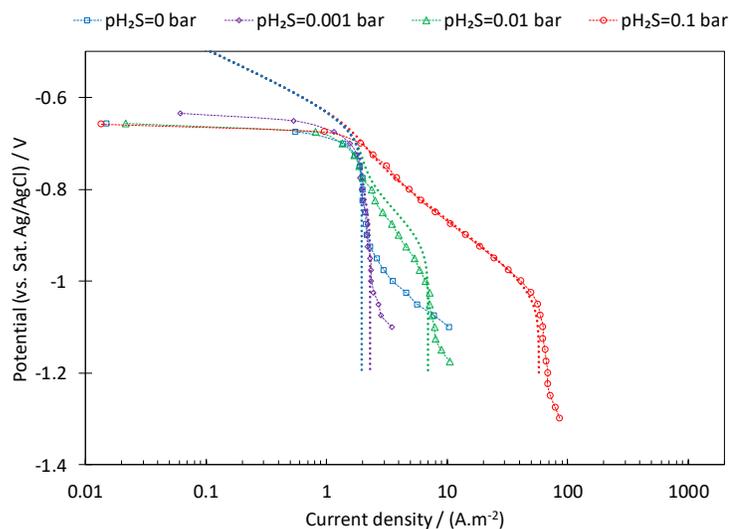
Figure C.1-4. Cathodic polarization curves at pH 4, 30ºC, 1000 rpm RCE (405 rpm RDE equivalent), at various H₂S partial pressures. The dotted lines show the results from the present model. The experimental data was taken from Zheng, et al.[13].

Figure C.1-4 shows the comparison of the results for the present model with the experimental cathodic polarization data reported by Zheng, et al., at pH 4 and H_2S partial pressures up to 0.1 bar [13]. The limiting current densities were in good agreement with the experimental data. The presence of the double wave, and its position, was also reasonably predicted by the model. It is noteworthy that the current densities in between the two limiting currents show a clear dependence on the pH_2S. Nonetheless, they are properly estimated by the model solely based on H^+ reduction. This can be understood considering the fact that the surface concentration of H^+ at this range is defined by the H_2S dissociation reaction. Naturally, the increased concentration of this species results in an increased rate of dissociation and, hence, higher concentration of H^+ at the surface. This process is of more mechanistic significance in the results obtained at higher pH values, as shown in Figure C.1-5.
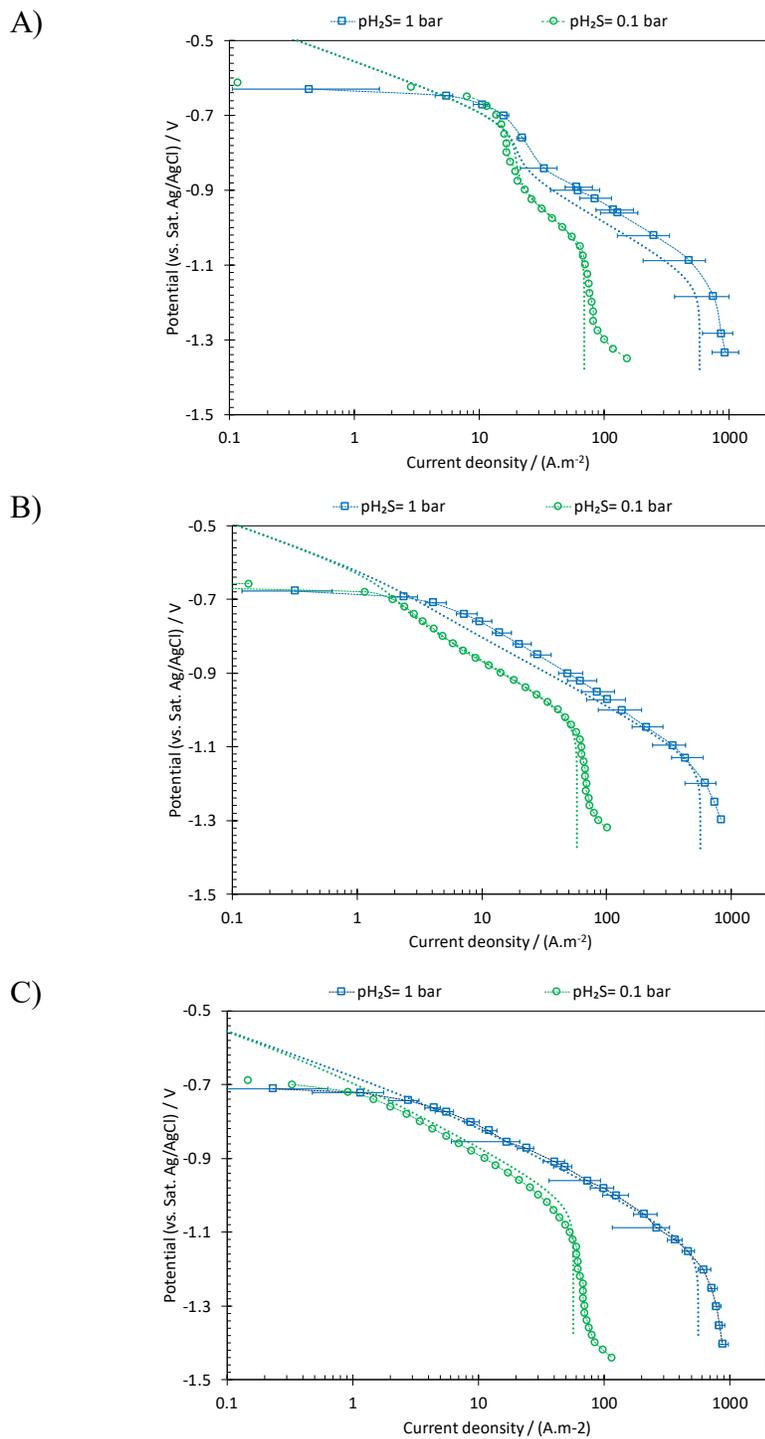
Figure C.1-5. Cathodic polarization curves at 30°C, 1000 rpm RCE (405 rpm RDE equivalent), at pH_2S=0.1 bar (green circles) and pH_2S= 1 bar (blue squares) partial pressures and the dotted lines show the results from the present model. A) pH 3. B) pH 4. C) pH 5. The experimental data at pH_2S=0.1 bar was taken from Zheng, et al.[13], and the experimental data at pH_2S=1 bar was taken from Esmaeely, et al.[283].

Figure C.1-5 demonstrates the comparison of the model with the experimental data at pH_2S up to 1 bar as reported by Esmaeely, et al.[283]. At such elevated H_2S partial pressures, the reproducibility of the experiments decreased, as seen from the large error bars. Even at such high H_2S partial pressures, the model was found to agree reasonably well with the experimental polarization curves; the main characteristic behavior at all pH values were correctly predicted.

The results at pH 5, as reported in Figure C.1-5.C, are of particular significance in the generic scope of corrosion in the presence of a weak acid. At this condition, only one limiting current was observed after a linearly decreasing range of current densities. By its appearance, this range of current densities could be mistaken for a pure charge transfer controlled range. In previous research on the mechanism of cathodic reactions in the presence of acetic acid and carbonic acid [12,62,200,201] it was argued that at a fixed pH, if the charge transfer controlled currents were increased in response to an increase in concentration of the weak acid, the weak acid is electrochemically active. From that perspective, the results reported here could have been taken as evidence for the direct reduction of H_2S; however, the simulated results clearly demonstrate that is not the case. As mentioned above, the observed current densities in this range are in between the two limiting currents (See Figure C.1-2). Therefore, this range of current densities were not governed purely by the charge transfer kinetics, but rather they were influenced by the kinetics of the H_2S dissociation, which defines the surface H^+ concentration. This range corresponds to the range of decaying surface H_2S concentrations seen in Figure C.1-3. The apparent H_2S dependence of this range of current densities is therefore the result of

the increased rate of H_2S dissociation. The difference between the case of H_2S and that of

acetic acid or carbonic acid is in its relatively lower dissociation kinetics ($\sim 10^4$ vs. $\sim 10^7$)

that becomes the limiting step.

C.1.5: Summary

The theoretical analysis of the buffering effect of H_2S showed that at the typical

conditions considered in the previous literature, the direct reduction of H_2S is not

significant, what is similar to the cases of acetic acid and carbonic acid presented above.

The increased limiting currents and the observed "double wave" behavior are fully

explained through the homogeneous dissociation of H_2S inside the diffusion boundary

layer. It is shown that the buffering effect of H_2S is only observed when the surface pH

approaches the pKa of this species. This behavior results in the observation of the

secondary limiting current at lower pH values, and explains why the second wave is not

observed as clearly in the solutions of higher bulk pH. The comparison of the results from

the present model with experimental cathodic polarization curves showed that this

mechanistic behavior remains valid for a wide range of conditions from pH 3 to 5 and

H_2S partial pressures up to 1 bar.

PART D:GENERALIZATION AND CONCLUSION

The discussions in Parts A, B, and C of this study addressed the mechanism of mild steel corrosion in the presence of carboxylic acids, carbon dioxide, and hydrogen sulfide, respectively. That covers all the main corrosive environments encountered in the oil and gas production and transportation industry. In all scenarios the experimental and theoretical investigation of the electrochemical behavior of these systems showed that the dissociation of the weak acids present in these solutions is the main cause for the observed high corrosivity. That is in contrast with conventional mechanistic understandings, where the observed high corrosivity was associated with the direct reduction of these weak acids. In that sense, the results of the present study suggest that neither carboxylic acids, carbon dioxide, nor hydrogen sulfide are inherently corrosive, they merely exacerbate an existing acidic corrosion process.

The significance of the buffering effect of weak acids, and it universal implication in corrosion mechanisms, is perhaps the most significant finding of the present study. In this study, it is shown that the buffering effect, as an inherent property of any weak acid, can account for all characteristic behaviors observed in cathodic currents in the cases here considered. The findings, based on the individual environments discussed above, can be recast into a more generic mechanistic view of *corrosion in weak acid solutions*. In order to elucidate this general property, the mathematical model developed in Chapter A.2: is repurposed for a hypothetical weak acid HA, with equilibrium constant of K_{HA}, and the dissociation rate constant of $k_{f,HA}$.
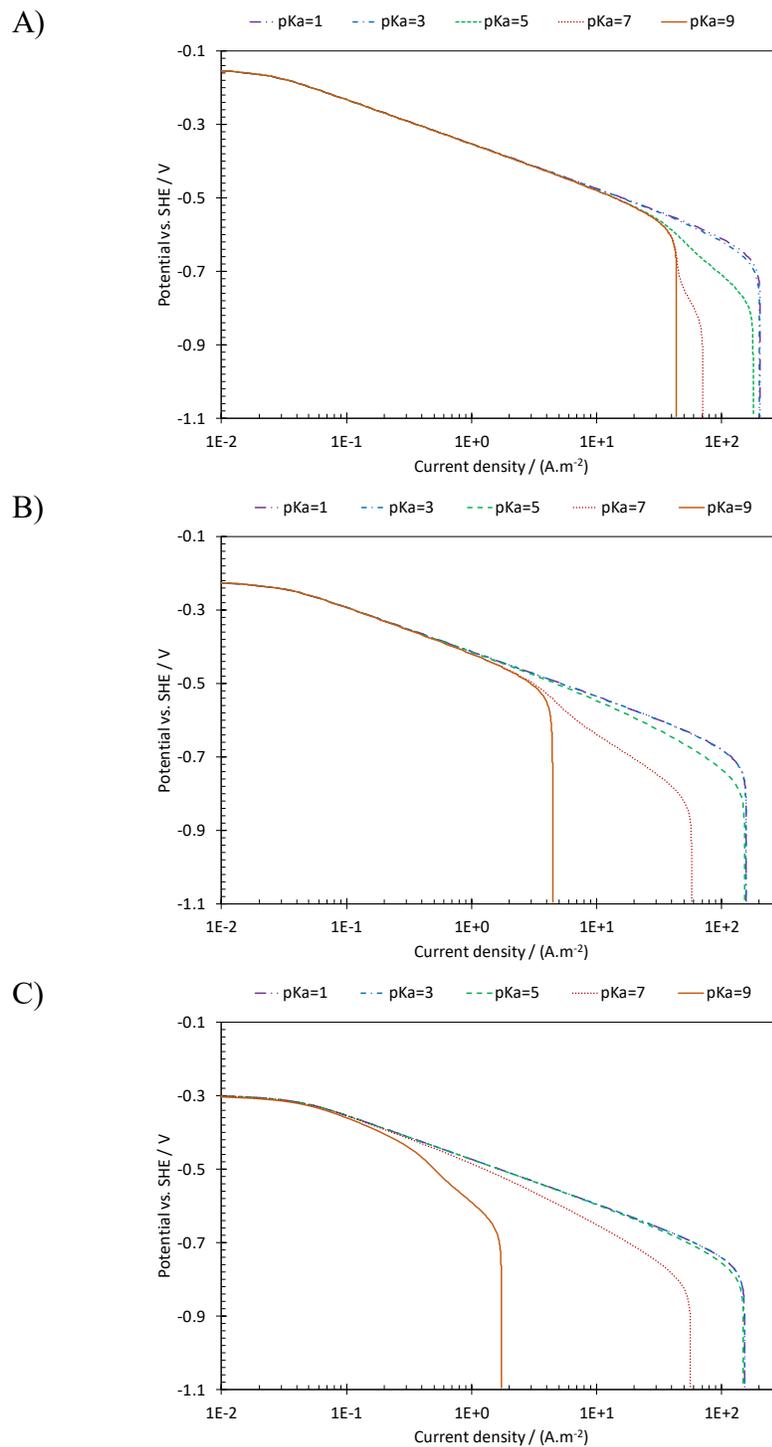
Figure D-1. Calculated cathodic polarization curves at 30ºC, 2000 rpm RDE, for a hypothetical weak acid with pKa ranging from 1 to 9 and $k_{b,HA}=10^{10}$. A) at pH 3. B) at pH 4. C) at pH 5.

As shown in Figure D-1, the expected behavior of the polarization curves, and the extent of the buffering ability of a weak acid, is defined by its pKa. These results demonstrate that any weak acid can significantly influence the electrochemical response of the system, if the conditions are favoring the dissociation reaction. Considering the typical conditions in the discussion of corrosion in the oil and gas industry, one can categorize the weak acids into three groups:

I- *Strongly buffering weak acids*: weak acids with pKa below 5, which readily dissociate when the mass transfer limiting current of H^+ is reached. The cathodic limiting current in the presence of these weak acids behave similarly to those of strong acids. Carbonic acid and most short chain carboxylic acids fall within this group.

II- *Moderately buffering weak acids*: weak acids with pKa between 5 and 11, which are able to exhibit a significant buffering ability. Depending on the environmental condition and the solution pH, the extent of this effect may vary. The cathodic polarization behavior in the presence of such weak acids deviates significantly from that of strong acids. The observation of a "double wave" can be considered a characteristic behavior of this group, such as those observed in the case of hydrogen sulfide (Figure C.1-4) and bicarbonate ion (Figure B.4-4). The second dissociation of sulfurous acid and phosphoric acid can also be placed in this group.

III- *Non-buffering weak acids*: weak acids with pKa values above 11 generally do not have favorable conditions for their dissociation to occur to any significant

extent, considering the typical conditions considered here; especially considering that the water reduction reaction covers any possible effect that such species may have on the surface concentration of H^+. Bisulfide ion and water can be considered as examples of such species.

The above categorization based on pKa values is a thermodynamic measure of the significance of the buffering effect. The kinetics of the dissociation reaction are also an important factor in defining the extent of dissociation. For example, in the case of acetic acid and carbonic acid, it was shown in the present study that the rate of dissociation is so fast that it allows this weak acid to fully dissociate when the thermodynamic conditions are satisfied. Nevertheless, the case of bicarbonate ion showed that this is not always the case and the kinetics of dissociation may become the limiting factor.

The protonation reactions associated with the weak acids discussed in this study are considered to be extremely fast, i.e., are diffusion limited. That puts the $k_{b,HA}$ of these reactions in a rather narrow range of 10^9-10^{11}. Hence, one may suggest that the kinetics of the dissociation reactions are also represented by the pKa values ($k_{f,HA} = k_{b,HA} \times K_{HA}$). That is, the lower pKa values correspond to dissociation reactions with large kinetic rate constants. As pKa values increase, for the case of moderately buffering weak acids, the kinetic rate constant of the dissociation reaction decreases, which limits the extent of dissociation of such weak acids. The species, which are already thermodynamically categorized as non-buffering weak acids, also have very slow dissociation reactions. An example of such a case is water, with a dissociation rate constant of the order of 10^{-3}.

While the buffering ability of weak acids is well undesrstood at this point, their electrochemical behavior needs to be investigated on a case-by-case basis. The findings of this study suggest that there is no indication for a significant electrochemical activity of carboxylic acids, carbonic acid, bicarbonate ion, and hydrogen sulfide. Among the significant species commonly present in oil and gas production and transmission facilities, the only weak acid that is known to be directly reduced with certainty is water. Water is present is these systems as the solvent with an extreme concentration, and even at this level the water reduction reaction is not considered as a significant player in the corrosion of mild steel. Therefore, the direct reduction of weak acids to produce hydrogen, at the concentrations typically encountered in the oil and gas industry, appear to be generally of low significance. One cannot state with absolute certainty that such reactions are impossible, nonetheless, such an argument is confidently presented relative to the rather high rate of H^+ reduction and even water reduction.

In addition to their influence on the cathodic currents, weak acids were found to alter the kinetics of the iron dissolution reaction in different ways, depending on the species. Acetic acid was found to decrease the rate of electrochemical reactions by adsorbing on the metal surface (Chapter A.1: and Chapter A.2:). In the case of CO_2 corrosion, the carbonate species were found to increase the rate of dissolution, especially in the transition and pre-passivation ranges (Chapter B.3: and Chapter B.4:). Hydrogen sulfide is known to influence the rate of this reaction. This species is believed to reduce the rate of iron dissolution at low concentration, with the similar mechanism as that of acetic acid [13,259]. At high concentration H_2S is believe to replace hydroxide intermediates,

thus increasing the rate of this reaction [13,259]. Such effects were, to some extent, quantified for acetic acid and CO_2 corrosion, in the present study, and for the case of H_2S in earlier studies [13,259]. Nevertheless, the effect of weak acids on the mechanism of iron dissolution remains one of the least understood aspects of the corrosion process in such systems. Conventionally, such processes were believed to have a negligibly small impact on the overall observed corrosion rates. However, the findings of the present study, especially when considering that the weak acids are not significantly reduced, puts the mechanism of the iron dissolution reaction in the spotlight. An extensive mechanistic investigation on the iron dissolution reaction, including the effect of various weak acids, is required before it can be fully represented in corrosion rate predictions.

REFERENCES

1. "Alaska Hit by 'Massive' Oil Spill," BBC news (2006), http://news.bbc.co.uk/2/hi/americas/4795866.stm.

2. Krauss, C., and J.W. Peters, "Biggest Oil Field in U.S. Is Forced to Stop Pumping," The New York Times (2006), http://www.nytimes.com/2006/08/08/business/08oil.html.

3. "Alaska to Collect $255 Million for 2006 BP Pipeline Leaks," Chicago Tribune (2012), http://articles.chicagotribune.com/2012-11-08/news/sns-rt-us-bp-alaskaspillbre8a800m-20121108_1_prudhoe-bay-pipeline-leaks-bp-plc.

4. "State Wins $255 Million in 2006 Pipeline Leak Arbitration," Alaska Journal of Commerce (2012), http://www.alaskajournal.com/business-and-finance/2012-11-08/state-wins-255-million-2006-pipeline-leak-arbitration#.WqgtZnwpCUl.

5. NACE international, "CORROSION FAILURES: Sinopec Gas Pipeline Explosion" (2014), https://www.nace.org/CORROSION-FAILURES-Sinopec-Gas-Pipeline-Explosion.aspx.

6. NACE international, "CORROSION FAILURES: El Paso Natural Gas Pipeline Explosion" (2014), https://www.nace.org/CORROSION-FAILURES-El-Paso-Natural-Gas-Pipeline-Explosion.aspx.

7. Mandke, J.S., *Oil Gas J.* 88 (1990): pp. 40–44.

8. Coco, J.C., ed., *The 100 Largest Losses 1972-2011*, Marsh's Risk Consulting practice, 20th ed. (2003).

9. Koch, G.H., M.P.H. Brongers, N.G. Thompson, Y.P. Virmani, and J.H. Payer, "Corrosion Costs and Preventive Strategies in the United States," Federal Highway Administration, Publication No. FHWA-RD-01-156 (2002).

10. Koch, G., J. Varney, N. Thompson, O. Moghissi, M. Gould, and J. Payer, "International Measures of Prevention , Application , and Economics of Corrosion Technologies Study," NACE International (2016), http://impact.nace.org/documents/Nace-International-Report.pdf.

11. Remita, E., B. Tribollet, E. Sutter, V. Vivier, F. Ropital, and J. Kittel, *Corros. Sci.* 50 (2008): pp. 1433–1440.

12. Tran, T., B. Brown, and S. Nešic, *Corrosion* 70 (2014): pp. 223–229.

13. Zheng, Y., B. Brown, and S. Nešic, *Corrosion* 70 (2014): pp. 351–365.

14. Gray, L.G.S., B.G. Anderson, M.J. Danysh, and P.R. Tremaine, "Mechanisms of Carbon Steel Corrosion in Brines Containing Dissolved Carbon Dioxide At pH 4," in CORROSION (1989), Paper No. 464.

15. Nordsveen, M., S. Nešić, R. Nyborg, and A. Stangeland, *Corrosion* 59 (2003): pp. 443–456.

16. Tribollet, B., J. Kittel, A. Meroufel, F. Ropital, F. Grosjean, and E.M.M. Sutter,

Electrochim. Acta 124 (2014): pp. 46–51, http://dx.doi.org/10.1016/j.electacta.2013.08.133.

17. Kittel, J., F. Ropital, F. Grosjean, E.M.M. Sutter, and B. Tribollet, *Corros. Sci.* 66 (2013): pp. 324–329, http://dx.doi.org/10.1016/j.corsci.2012.09.036.

18. Nešić, S., J. Postlethwaite, and S. Olsen, *Corrosion* 52 (1996): pp. 280–294.

19. de Waard, C., and D.E. Milliams, *Corrosion* 31 (1975): pp. 177–181.

20. Nešić, S., "Carbon Dioxide Corrosion of Mild Steel," in Uhlig's Corros. Handb. Third Ed. (2011), pp. 229–245.

21. Menaul, P., *Oil Gas J.* 43 (1944): pp. 80–81.

22. Barth, T., *Appl. Geochemistry* 6 (1991): pp. 1–15.

23. Gunaltun, Y.M., and D. Larrey, "Corrolation of Cases of Top of the Line Corrosion with Calculated Water Condensation Rates," in CORROSION (2000), Paper No. 71.

24. Utvik, T.R., *Chemosphere* 39 (1999): pp. 2593–2606.

25. Crolet, J.-L., N. Thevenot, and A. Dugstad, "Role Of Free Acetic Acid On The CO_2 Corrosion Of Steels," in CORROSION (1999), Paper No. 24.

26. Amri, J., E. Gulbrandsen, and R.P. Nogueira, *Corrosion* 66 (2010): pp. 35001-1-35001–7.

27. Crolet, J.-L., and M.R. Bonis, "Why so Low Free Acetic Acid Theresholds in Sweet Corrosion at Low pCO_2?," in CORROSION (2005), Paper. No. 272.

28. Nešić, S., and W. Sun, "Corrosion in Acid Gas Solutions," in Shreir's Corros. (2010), pp. 1270–1298.

29. Singer, M., D. Hinkson, Z. Zhang, H. Wang, and S. Nesic, *Corrosion* 69 (2013): pp. 719–735.

30. Zhu, S.D., A.Q. Fu, J. Miao, Z.F. Yin, G.S. Zhou, and J.F. Wei, *Corros. Sci.* 53 (2011): pp. 3156–3165.

31. Garsany, Y., D. Pletcher, and B. Hedges, *J. Electroanal. Chem.* 538–539 (2002): pp. 285–297.

32. George, K.S., and S. Nešic, *Corrosion* (2007): pp. 178–186.

33. George, K., S. Nešić, and C. de Waard, "Electrochemical Investigation and Modeling of Carbon Dioxide Corrosion of Carbon Steel in the Presence of Acetic Acid," in CORROSION (2004), Paper No. 379.

34. Gulbrandsen, E., "Acetic Acid and Carbon Dioxide Corrosion of Carbon Steel Covered with Iron Carbonate," in CORROSION (2007), Paper No. 322.

35. Gulbrandsen, E., and K. Bilkova, "Solution Chemistry Effects on Corrosion of Carbon Steels in Presence of CO_2 and Acetic Acid," in CORROSION (2006), Paper No. 364.

36. Amri, J., E. Gulbrandsen, and R.P. Nogueira, "Role of Acetic Acid in CO_2 Top of the Line Corrosion of Carbon Steel," in CORROSION (2011), Paper No. 329.

37. Garsany, Y., D. Pletcher, and B. Hedges, "The Role of Acetate in CO_2 Corrosion of Carbon Steel: Has the Chemistry Been Forgotten?," in CORROSION (2002), Paper No. 273.

38. Okafor, P.C., B. Brown, and S. Nešić, *J. Appl. Electrochem.* 39 (2009): pp. 873–877.

39. Sun, Y., K. George, and S. Nešić, "The Effect of Cl^- and Acetic Acid on Localized CO_2 Corrosion in Wet Gas Flow," in CORROSION (2003), Paper No. 327.

40. Fajardo, V., C. Canto, B. Brown, and S. Nešić, "Effects of Organic Acids in CO_2 Corrosion," in CORROSION (2007), Paper No. 319.

41. Matos, M., C. Canhoto, M.F. Bento, and M.D. Geraldo, *J. Electroanal. Chem.* 647 (2010): pp. 144–149.

42. Jia, Z., X. Li, C. Du, Z. Liu, and J. Gao, *Mater. Chem. Phys.* 132 (2012): pp. 258–263, http://dx.doi.org/10.1016/j.matchemphys.2011.08.034.

43. Kahyarian, A., M. Singer, and S. Nesic, *J. Nat. Gas Sci. Eng.* 29 (2016): pp. 530–549, http://dx.doi.org/10.1016/j.jngse.2015.12.052.

44. Turgoose, S., R.A. Cottis, and K. Lawson, "Modeling of Electrode Processes and Surface Chemistry in Carbon Dioxide Containing Solutions," in Comput. Model. Corros. ASTM STP 1154 (1992), pp. 67–81.

45. Pots, B.F.M., "Mechanistic Models for the Prediction of CO_2 Corrosion Rates under Multi-Phase Flow Conditions," in CORROSION (1995), Paper No. 137.

46. Nešić, S., M. Nordsveen, R. Nyborg, and A. Stangeland, "A Mechanistic Model for CO_2 Corrosion with Protective Iron Carbonate Films," in CORROSION (2001), Paper No. 040.

47. Nešić, S., *Corros. Sci.* 49 (2007): pp. 4308–4338.

48. de Waard, C., U. Lotz, and A. Dugstad, "Influence of Liquid Flow Velocity on CO_2 Corrosion: A Semi-Empirical Model," in CORROSION (1995), Paper No. 128.

49. Nesic, S., G.T. Solvi, and J. Enerhaug, *Corrosion* 51 (1995): pp. 773–787.

50. Tran, T., B. Brown, and S. Nešić, "Corrosion of Mild Steel in an Aqueous CO_2 Environment – Basic Electrochemical Mechanisms Revisited," in CORROSION (2015), Paper no. 671.

51. Navabzadeh, S., B. Brown, and S. Nesic, *Corrosion* 72 (2016): pp. 1220–1222.

52. Beverskog, B., and I. Puigdomenech, *Corros. Sci.* 38 (1996): pp. 2121–2135.

53. Bard, A.J., and L.R. Faulkner, *Electrochemical Methods : Fundamentals and Applications* (John Wiley & Sons, Inc., 2001).

54. Bockris, J.O., and D. Drazic, *Electrochim. Acta* 7 (1962): pp. 293–313.

55. Kahyarian, A., M. Achour, and S. Nesic, "CO_2 Corrosion of Mild Steel," in Trends Oil Gas Corros. Res. Technol., ed. A. M. El-Sherik (Elsevier, 2017), pp. 149–190.

56. Kermani, M.B., and A. Morshed, *Corrosion* 59 (2003): pp. 659–683.

57. Gunaltun, Y.M., "Combining Research and Field Data for Corrosion Rate Prediction," in CORROSION (1996), Paper No. 27.

58. Garber, James D, Perkins, Richard S., Jangama, Vamishidhar, R. Alapati, R.R., "Calculation of Downhole pH and Delta pH in the Presence of CO_2 and Organic Acids," in CORROSION (1996), Paper No. 176.

59. Utvik, T.I.R., *Chemosphere* 39 (1999): pp. 2593–2606.

60. Kahyarian, A., M. Achour, and S. Nesic, "Mathematical Modeling of Uniform CO_2 Corrosion," in Trends Oil Gas Corros. Res. Technol., ed. A.M. El-Sherik (Elsevier, 2017), pp. 805–849.

61. Kahyarian, A., B. Brown, and S. Nesic, *J. Electrochem. Soc.* 164 (2017): pp. H365–H374.

62. Kahyarian, A., B. Brown, and S. Nesic, *Corrosion* 72 (2016): pp. 1539–1546.

63. Harned, H.S., and R.W. Ehlers, *J. Am. Chem. Soc.* 55 (1933): pp. 652–656.

64. Marshall, W.L., and E.U. Franck, *J. Phys. Chem. Ref. Data* 10 (1983): pp. 295–304.

65. Eigen, M., and E. Eyring, *J. Am. Chem. Soc.* 84 (1962): pp. 3254–3256.

66. Eigen, M., *Angew. Chem. Int. Ed. Engl.* 3 (1964): pp. 1–72.

67. Stillinger, F.H., *Theor. Chem. Adv.* 3 (1978): pp. 177–234.

68. Newman, J., and K.E. Thomas-Alyea, *Electrochemical Systems*, 3rd ed. (Wiley-interscience, 2004).

69. Cochran, W.G., *Math. Proc. Cambridge Philos. Soc.* 1 (1934): pp. 365–375.

70. Haynes, W.M., ed., *CRC Handbook of Chemistry and Physics*, 84th ed. (CRC Press LLC, 2004).

71. Bockris, J.O., D. Drazic, and A. R. Despic, *Electrochim. Acta* 4 (1961): pp. 325–361.

72. El Miligy, A.A., D. Geana, and W.J. Lorenz, *Electrochim. Acta* 20 (1975): pp. 273–281.

73. Drazic, D., *Mod. Asp. Electrochem.* 19 (1989): pp. 62–192.

74. Nešić, S., N. Thevenot, J.L. Crolet, and D. Drazic, "Electrochemical Properties of Iron Dissolution in the Presence of CO_2 - Basics Revisited," in CORROSION (1996), Paper No. 03.

75. Pentland, N., J.O. Bockris, and E. Sheldon, *J. Electrochem. Soc.* 104 (1957): p. 182.

76. Bockris, J.O., J. McBreen, and L. Nanis, *J. Electrochem. Soc.* 112 (1965): pp.

1025–1031.

77.   Dražić, D.M., and C.S. Hao, *Electrochim. Acta* 27 (1982): pp. 1409–1415.

78.   Keddam, M., "Anodic Dissolution," in Corros. Mech. Theory Pract. Third Ed. (CRC Press, 2011), pp. 149–215, http://dx.doi.org/10.1201/b11020-4.

79.   Korson, L., W. Drost-Hansen, and F.J. Millero, *J. Phys. Chem.* 73 (1969): pp. 34–39.

80.   Olsen, S., A.M. Halvorsen, Per G. Lunde, and R. Nyborg, "CO_2 Corrosion Prediction Model - Basic Principles," in CORROSION (2005), Paper No. 551.

81.   de Waard, C., U. Lotz, and D.E. Milliams, *Corrosion* 47 (1991): pp. 976–985.

82.   Dugstad, A., L. Lunde, and K. Videm, "Parametric Study of CO_2 Corrosion of Carbon Steel," in CORROSION (1994), Paper No. 14.

83.   Revie, R.W., ed., *Uhlig's Corrosion Handbook*, First (Hoboken, NJ, USA: John Wiley & Sons, Inc., 2011).

84.   Richardson, T., ed., *Shreir's Corrosion*, First (Elsevier Science, 2009).

85.   Nyborg, R., "Overview of CO_2 Corrosion Models for Models for Wells and Pipelines," in CORROSION (2002), Paper No. 233.

86.   Nešić, S., J. Postlethwaite, and M. Vrhovac, *Corros. Rev.* 15 (1997): pp. 211–240.

87.   Olsen, S., "CO_2 Corrosion Prediction by Use of the Norsok M-506 Model - Guidelines and Limitations," in CORROSION (2003), Paper No. 623.

88.   Kapusta, S.D., B.F.M. Pots, and I.J. Rippon, "The Application of Corrosion Prediction Models to the Design and Operation of Pipelines," in CORROSION (2004), Paper No. 30.

89.   Nyborg, R., "Field Data Collection, Evaluation and Use for Corrosivity Prediction and Validation of Models," in CORROSION (2006), paper no. 118.

90.   Stumm, W., and J.J. Morgan, *Aquatic Chemistry: Chemical Equilibria and Rates in Natural Waters* (1995).

91.   Zeebe, R.E., and D. Wolf-Gladrow, *CO_2 in Seawater: Equilibrium, Kinetics, Isotopes*, Elsevier Oceanography Series (Elsevier, 2001).

92.   Butler, J.N., *Carbon Dioxide Equilibria and Their Applications* (CRC Press, 1991).

93.   Dickson, A.G., and C. Goyet, eds., *DOE Handbook of Methods for the Analysis of the Various Parameters of the Carbon Dioxide System in Sea Water*, 2nd ed. (1994).

94.   Weiss, R.F., *Mar. Chem.* 2 (1974): pp. 203–215.

95.   Millero, F.J., *Geochim. Cosmochim. Acta* 59 (1995): pp. 661–677.

96.   Delahay, P., *J. Am. Chem. Soc.* 74 (1952): pp. 3497–3500, http://pubs.acs.org/doi/pdf/10.1021/ja01134a013%5Cnhttp://pubs.acs.org/doi/abs/

10.1021/ja01134a013.

97. Palmer, D.A., and R. Van Eldik, *Chem. Rev.* 83 (1983): pp. 651–731.

98. Roy, R.N., L.N. Roy, K.M. Vogel, C. Porter-Moore, T. Pearson, C.E. Good, F.J. Millero, and D.M. Campbell, *Mar. Chem.* 44 (1993): pp. 249–267.

99. Green, N., ed., *Comprehensive Chemical Kinetics, Volume 6* (Amsterdam, The Netherlands: Elsevier Inc, 1972).

100. Han, J., J. Zhang, and J.W. Carey, *Int. J. Greenh. Gas Control* 5 (2011): pp. 1680–1683.

101. Ogundele, G.I., and W.E. White, *Corrosion* 42 (1986): pp. 71–78.

102. Ogundele, G.I., and W.E. White, *Corrosion* 43 (1987): pp. 665–673.

103. Gray, L.G.S., B.G. Anderson, M.J. Danysh, and P.R. Tremaine, "Effect of pH and Temperature on the Mechanism of Carbon Steel Corrosion by Aqueous Carbon Dioxide," in CORROSION (1990), Paper No. 40.

104. Hurlen, T., S. Gunvaldsen, and F. Blaker, *Electrochim. Acta* 29 (1984): pp. 1163–1164.

105. de Waard, C., and D.E. Milliams, "Prediction of Carbonic Acid Corrosion in Natural Gas Pipelines," in Intern. Extern. Prot. Pipes (1975), pp. F1-1-F1-8.

106. Więckowski, A., E. Ghali, M. Szklarczyk, and J. Sobkowski, *Electrochim. Acta* 28 (1983): pp. 1619–1626.

107. Schmitt, G., and B. Rothmann, *Werkstoffe Und Korrosion* 28 (1977): p. 816.

108. Więckowski, A., E. Ghali, M. Szklarczyk, and J. Sobkowski, "The Behaviour of Iron Electrode in CO_2- Saturated Neutral electrolyte—II. Radiotracer Study and Corrosion Considerations," Electrochimica Acta (1983).

109. Conway, B.E., and B. V. Tilak, *Electrochim. Acta* 47 (2002): pp. 3571–3594.

110. Bockris, J.O., and A.K.N. Reddy, *Modern Electrochemistry : An Introduction to an Interdisiplinary Area, Volume 2* (New york: Plenum Press, 1973).

111. Juodkazis, K., J. Juodkazyte, B. Šebeka, and S. Juodkazis, *Appl. Surf. Sci.* 290 (2014): pp. 13–17.

112. Juodkazis, K., J. Juodkazyt, A. Grigucevičien, and S. Juodkazis, *Appl. Surf. Sci.* 258 (2011): pp. 743–747.

113. Brug, G.J., M. Sluyters-Rehbach, J.H. Sluyters, and A. Hemelin, *J. Electroanal. Chem.* 181 (1984): pp. 245–266.

114. Sheng, W., H.A. Gasteiger, and Y. Shao-Horn, *J. Electrochem. Soc.* 157 (2010): pp. B1529–B1536.

115. Bockris, J.O., and D.F.A. Koch, *J. Phys. Chem.* 65 (1961): pp. 1941–1948.

116. Stern, M., *J. Electrochem. Soc.* 102 (1955): pp. 609–616.

117. Bockris, J.O., and E.C. Potter, *J. Electrochem. Soc.* 99 (1952): p. 169.

118. Conway, B.E.B., and M. Salomon, *Electrochim. Acta* 9 (1964): pp. 1599–1615.

119. Gennero de Chialvo, M.R., and A.C. Chialvo, *J. Electrochem. Soc.* 147 (2000): pp. 1619–1622.

120. Tavares, M.C., S.A.S. Machado, and L.H. Mazo, *Electrochim. Acta* 46 (2001): pp. 4359–4369.

121. Tilak, B. V., and C.P. Chen, *J. Appl. Electrochem.* 23 (1993): pp. 631–640.

122. Gennero de Chialvo, M.R., and A.C. Chialvo, *Electrochem. Commun.* 1 (1999): pp. 379–382.

123. Gennero de Chialvo, M.R., and A.C. Chialvo, *Phys. Chem. Chem. Phys.* 3 (2001): pp. 3180–3184.

124. Gennero de Chialvo, M.R., and A.C. Chialvo, *Electrochim. Acta* 44 (1998): pp. 841–851.

125. Thomas, N.T., and K. Nobe, *J. Electrochem. Soc.* 117 (1970): p. 622.

126. Schuldiner, S., *J. Electrochem. Soc.* 108 (1961): p. 384.

127. Bockris, J.O., I.A. Ammar, and A.K.M.S. Huq, *J. Phys. Chem.* 61 (1957): pp. 879–886.

128. Schuldiner, S., *J. Electrochem. Soc.* 101 (1954): pp. 426–432.

129. Schuldiner, S., *J. Electrochem. Soc.* 101 (1954): pp. 488–494.

130. Qian, S.Y., B.E. Conway, and G. Jerkiewicz, *J. Chem. Soc. Faraday Trans.* 94 (1998): pp. 2945–2954.

131. Qian, S.Y., B.E. Conway, and G. Jerkiewicz, *Phys. Chem. Chem. Phys.* 1 (1999): pp. 2805–2813.

132. Delahay, P., ed., *Advances in Electrochemistry and Electrochemical Engineering: Volume 7 Electrochemistry* (Interscience, 1970).

133. Safizadeh, F., E. Ghali, and G. Houlachi, *Int. J. Hydrogen Energy* 40 (2015): pp. 256–274.

134. Hurlen, T., *Acta Chem. Scand.* 14 (1960): pp. 1533–1554.

135. McCafferty, E., and N. Hackerman, *J. Electrochem. Soc.* 119 (1972): pp. 999–1009.

136. Chin, R.J., and K. Nobe, *J. Electrochem. Soc.* 119 (1972): pp. 1457–1461.

137. Felloni, L., *Corros. Sci.* 8 (1968): pp. 133–148.

138. Mishra, B., S. Al-Hassan, D.L. Olson, and M.M. Salama, *Corrosion* 53 (1997): pp. 852–859.

139. Videm, K., "Fundamental Studies Aimed At Improving Models for Prediction of CO_2 Corrosion of Carbon Steels," in Prog. Underst. Prev. Corros. (1993), p. 507.

140. Davies, D.H., and T. Burstein, *Corrosion* 36 (1980): pp. 416–422.

141. Almeida, T.D.C., M.C.E. Bandeira, R.M. Moreira, and O.R. Mattos, "The Role of CO_2 on Carbon Steel Corrosion," in CORROSION (2015), Paper No. 807.

142. Anderko, A., "Modeling of Aqueous Corrosion," in Shreir's Corros. (Elsevier, 2010), pp. 1585–1629.

143. Nyborg, R., P. Andersson, and M. Nordsveen, "Implementation of CO_2 Corrosion Models in a Three-Phase Fluid Flow Model," in CORROSION (2000), Paper No. 048.

144. Eisenberg, M., C.W. Tobias, and C.R. Wilke, *J. Electrochem. Soc.* 101 (1954): pp. 306–320.

145. Berger, F.P., and K.-F.F.-L. Hau, *Int. J. Heat Mass Transf.* 20 (1977): pp. 1185–1194.

146. Coney, M.W.E., and G.B.C.E.G. Board, *Erosion-Corrosion: The Calculation of Mass-Transfer Coefficients* (CEGB, 1981).

147. Poulson, B., *Chem. Eng. Sci.* 46 (1991): pp. 1069–1082.

148. Wang, J., S. a. Shirazi, J.R. Shadley, E.F. Rybicki, and E. Dayalan, "A Correlation for Mass Transfer Coefficients in Elbows," in CORROSION (1998), paper no. 42.

149. Wang, J., and S. a Shirazi, *Int. J. Heat Mass Transf.* 44 (2001): pp. 1817–1822.

150. Cussler, E.L., *Diffusion: Mass Transfer in Fluid Systems*, Engineering, Third Edit (Cambridge University Press, 2007).

151. Aravinth, S., *Int. J. Heat Mass Transf.* 43 (2000): pp. 1399–1408.

152. Davies, J.T., "Chapter 3: Eddy Transfer Near Solid Surfaces," in Turbul. Phenom. (Elserviere Inc., 1972), pp. 121–174.

153. de Waard, C., and U. Lotz, "Prediction of CO_2 Corrosion of Carbon Steel," in CORROSION (1993), Paper No. 069.

154. Jangama, V.R., and S. Srinivasan, "A Computer Model for Prediction of Corrosion of Carbon Steels," in CORROSION (1997), Paper No. 318.

155. Pots, B.F.M., R.C. John, I.J. Rippon, M.J.J.S. Thomas, S.D. Kapusta, M.M. Grigs, and T. Whitham, "Improvements on de Waard-Milliams Corrosion Prediction and Applications to Corrosion Management," in CORROSION (2002), Paper No. 235.

156. de Waard, C., L.M. Smith, and B.D. Craig, "Influence of Crude Oils on Well Tubing Corrosion Rates," in Corros. 2003 (2003), Paper No. 629.

157. Dayalan, E., G. Vani, J.R. Shadley, S.A. Shirazi, and E.F. Rybicki, "Modeling CO_2 Corrosion of Carbon Steels in Pipe Flow," in CORROSION (1995), Paper No. 118.

158. Dayalan, E., F.D. de Moraes, J.R. Shadley, S.A. Shirazi, and E.F. Rybicki, "CO_2 Corrosion Prediction in Pipe Flow under $FeCO_3$ Scale-Forming Conditions," in CORROSION (1998), Paper No. 51.

159. Nešić, S., J. Postlethwaite, and N. Thevenot, *J. Corros. Sci. Eng.* 1 (1995): pp. 1–

14.

160. Han, J., J.W. Carey, and J. Zhang, *J. Appl. Electrochem.* 41 (2011): pp. 741–749.

161. Rajappa, S., R. Zhang, and M. Gopal, "Modeling the Diffusion Effects through the Iron Carbonate Layer in the Carbon Dioxide Corrosion of Carbon Steel," in CORROSION (1998), Paper No. 026.

162. Sundaram, M., V. Raman, M.S. High, D.A. Tree, and J. Wagner, "Deterministic Modeling of Corrosion in Downhole Environments," in CORROSION (1996), Paper No. 30.

163. Han, J., J.W. Carey, and J. Zhang, *Int. J. Greenh. Gas Control* 5 (2011): pp. 777–787, http://dx.doi.org/10.1016/j.ijggc.2011.02.005.

164. Newman, J.S., *Electrochemical Systems*, 1st ed. (Prentice Hall, Inc., 1973).

165. Choi, Y., D. Duan, S. Jiang, and S. Nešić, *Corrosion* 69 (2013): pp. 551–559.

166. Song, F.M., D.W. Kirk, J.W. Graydon, and D.E. Cormack, *Corrosion* 60 (2004): pp. 736–748.

167. Song, F.M., *Electrochim. Acta* 55 (2010): pp. 689–700.

168. Amri, J., E. Gulbrandsen, and P.R. Nogueira, "Effect of Acetic Acid on Propagation and Stifling of Localized Attacks in CO_2 Corrosion of Carbon Steel," in CORROSION (2009), Paper No. 284.

169. Nešić, S., H. Li, J. Huang, and D. Sormaz, "An Open Source Mechanistic Model for CO_2/ H_2S Corrosion of Carbon Steel," in CORROSION (2009), paper No. 09572.

170. van Hunnik, E.W.J., B.F.M. Pots, and E.L.J.A. Hendriksen, "The Formation of Protective $FeCO_3$ Corrosion Product Layers in CO_2 Corrosion," in CORROSION (1996), Paper No. 006.

171. Sun, W., S. Nešić, and R.C. Woollam, *Corros. Sci.* 51 (2009): pp. 1273–1276.

172. Ruzic, V., M. Veidt, and S. Nešić, *Corrosion* 63 (2007): pp. 758–769.

173. Dugstad, A., "Mechanism of Protective Film Formation during CO_2 Corrosion of Carbon Steel," in CORROSION (1998), Paper No. 31.

174. Johnson, M.L., and M.B. Tomson, "Ferrous Carbonate Precipitation Kinetics and Its Impact on CO_2 Corrosion," in CORROSION (1991), Paper No. 268.

175. Pfennig, A., and A. Kranzmann, *Corros. Sci.* 65 (2012): pp. 441–452.

176. Pfennig, A., and R. Bäßler, *Corros. Sci.* 51 (2009): pp. 931–940, http://dx.doi.org/10.1016/j.corsci.2009.01.025.

177. Pfennig, A., and A. Kranzmann, *Int. J. Greenh. Gas Control* 5 (2011): pp. 757–769, http://linkinghub.elsevier.com/retrieve/pii/S1750583611000363.

178. Farelas, F., Y.-S. Choi, S. Nešić, A.A.O. Magalhães, and C. de Azevedo Andrade, *Corrosion* 70 (2014): pp. 137–145.

179. Choi, Y.-S., F. Farelas, S. Nešić, A.A.O. Magalhães, and C. de Azevedo Andrade, *Corrosion* 70 (2014): pp. 38–47.

180. Nešić, S., and K.L.J. Lee, *Corrosion* 59 (2003): pp. 616–628.

181. Anderko, A., "Simulation of $FeCO_3$/FeS Scale Formation Using Thermodynamic and Electrochemical Models," in CORROSION (2000), No. 102.

182. Ruzic, V., M. Veidt, and S. Nešsić, *Corrosion* 62 (2006): pp. 598–611.

183. Ruzic, V., M. Veidt, and S. Nešsić, *Corrosion* 62 (2006): pp. 419–432.

184. Pots, B.F.M., and E.L.J.A. Hendriksen, "CO_2 Corrosion under Scaling Conditions - the Special Case of Top-of-Line Corrosion in Wet Gas Pipelines," in CORROSION (2000), Paper No. 031.

185. Sun, W., and S. Nesic, "Basics Revisited: Kinetics of Iron Carbonate Scale Precipitation in CO_2 Corrosion," in CORROSION (2006), Paper No. 365.

186. Lasaga, A.C., *Kinetic Theory in the Earth Sciences* (Princeton University Press, 1998).

187. Oddo, J., and M. Tomson, *J. Pet. Technol.* 34 (1982): pp. 1583–1590.

188. Sun, W., and S. Nešić, *Corrosion* 64 (2008): pp. 334–346.

189. Nešić, S., M. Nordsveen, R. Nyborg, and A. Stangeland, *Corrosion* 59 (2003): pp. 489–497.

190. Nešić, S., J. Lee, and V. Ruzic, "A Mechanistic Model of Iron Carbonate Film Growth and the Effect on CO_2 Corrosion of Mild Steel," in CORROSION (2002), Paper No. 237.

191. Ruhl, A.S., and A. Kranzmann, *Int. J. Greenh. Gas Control* 9 (2012): pp. 85–90.

192. Ruhl, A.S., and A. Kranzmann, *Int. J. Greenh. Gas Control* 13 (2013): pp. 9–16.

193. Bich, N.N., and K.E. Szklarz, "Crossfield Corrosion Experience," in CORROSION (1988), Paper No. 196.

194. Joosten, M., D. Owens, A. Hobbins, H. Sun, M. Achour, and D. Lanktree, "Top-of-Line Corrosion – A Field Failure," in EuroCorr (2010), paper No. 9524.

195. Paillassa, R., M. Dieumegard, and M.M. Estavoyer, "Corrosion Control in the Gathering System at LACQ Sour Gas Field," in 2nd Intl. Congr. Met. Corros. (1963), pp. 410–417.

196. Nyborg, R., and A. Dugstad, "Top of Line Corrosion and Water Condensation Rates in Wet Gas Pipelines," in CORROSION (2007), Paper No. 555.

197. Zhang, Z., D. Hinkson, M. Singer, H. Wang, and S. Nešić, *Corrosion* 63 (2007): pp. 1051–1062.

198. Linter, B.R., and G.T. Burstein, *Corros. Sci.* 41 (1999): pp. 117–139.

199. Bus, E., and J.A. van Bokhoven, *Phys. Chem. Chem. Phys.* 9 (2007): pp. 2894–2902.

200. Tran, T., B. Brown, S. Nesic, B. Tribollet, and S. Nešic, *Corros. 2013* 70 (2017): pp. 223–229.

201. Kahyarian, A., A. Schumaker, B. Brown, and S. Nesic, *Electrochim. Acta* 258 (2017): pp. 639–652.

202. Farelas, F., M. Galicia, B. Brown, S. Nesic, and H. Castaneda, *Corros. Sci.* 52 (2010): pp. 509–517.

203. Yang, Y., "Removal Mechanisms of Protective Iron Carbonate Layer in Flowing Solutions," Ohio University, PhD dissertation, 2012.

204. Li, W., "Mechanical Effects of Flow on CO_2 Corrosion Inhibition of Carbon Steel Pipelines," Ohio University, PhD dissertation, 2016.

205. Yang, Y., B. Brown, S. Nesic, M.E. Gennaro, and B. Molinas, "Mechanical Strength And Removal Of A Protective Iron Carbonate Layer Formed On Mild Steel In CO_2 Corrosion," in CORROSION (2010), paper no. 10383.

206. Li, W., B.F.M. Pots, B. Brown, K.E. Kee, and S. Nesic, *Corros. Sci.* 110 (2016): pp. 35–45.

207. Farelas, F., B. Brown, and S. Nesic, "Iron Carbide and Its Influence on the Formation of Protective Iron Carbonate in CO_2 Corrosion of Mild Steel," in CORROSION (2013), Paper No. 2291.

208. Soli, A.L., and R.H. Byrne, *Mar. Chem.* 78 (2002): pp. 65–73.

209. Li, D., and Z. Duan, *Chem. Geol.* 244 (2007): pp. 730–751.

210. Kahyarian, A., B. Brown, and S. Nesic, *Corros. Sci.* 129 (2017): pp. 146–151.

211. Castro, E.B., and J.R. Vilche, *Corros. Sci.* 32 (1991): pp. 37–50.

212. Simard, S., M. Drogowska, H. Menard, and L. Brossard, *J. Appl. Electrochem.* 27 (1997): pp. 317–324.

213. Tanupabrungsun, T., D. Young, B. Brown, and S. Nešić, *CORROSION* (2012): p. 1418.

214. Duan, Z., R. Sun, C. Zhu, and I.-M. Chou, *Mar. Chem.* 98 (2006): pp. 131–139.

215. Zhenhao, D., N. Moller, and J.H. Wear, *Geochim. Cosmochim. Acta* 56 (1992): pp. 2605–2617.

216. Lal C. Garg, T.H.M., *Biochim. Biophys. Acta* 261 (1971): pp. 70–76.

217. Kern, D.M., *J. Chem. Educ.* 37 (1960): pp. 14–23.

218. Wang, X., W. Conway, R. Burns, N. McCann, and M. Maeder, *J. Phys. Chem. A* 114 (2010): pp. 1734–1740.

219. Alberty, R., *J. Phys. Chem.* 99 (1995): pp. 11028–11034.

220. Amri, J., E. Gulbrandsen, and R.P. Nogueira, *Corros. Sci.* 52 (2010): pp. 1728–1737, http://dx.doi.org/10.1016/j.corsci.2010.01.010.

221. Wissbrun, K.F., D.M. French, and A. Patterson Jr., *J. Phys. Chem.* 58 (1954): pp.

693–695.

222. Pines, D., J. Ditkovich, T. Mukra, Y. Miller, P.M. Kiefer, S. Daschakraborty, J.T. Hynes, and E. Pines, *J. Phys. Chem. B* 120 (2016): pp. 2440–2451.

223. Adamczyk, A., M. Prémont-Schwarz, D. Pines, E. Pines, and E. Nibbering, *Science (80-.).* 326 (2009): pp. 1690–1694.

224. Duan, Z., and D. Li, *Geochim. Cosmochim. Acta* 72 (2008): pp. 5128–5145.

225. Wagner, W., and H.-J. Kretzschmar, *International Steam Tables: Properties of Water and Steam Based on the Industrial Formulation IAPWS-IF97*, second edi (Springer, 2008).

226. Cooper, J.R., Q. Mary, M.E. Road, and S.I. Associates, *Int. Assoc. Prop. Water Steam* (2012).

227. Song, F.M., D.W. Kirk, J.W. Graydon, and D.E. Cormack, *J. Electrochem. Soc.* 149 (2002): pp. B479–B486.

228. Keddam, M., O.R. Mattos, and H. Takenout, *J. Electrochem. Soc.* 128 (1981): pp. 257–266.

229. Nešic, S., and K. Lee, *Corrosion* 5 (2003): pp. 616–628.

230. Plonski, I.H., *Int. J. Hydrogen Energy* 21 (1996): pp. 837–851.

231. Atkinson, A., and A. Marshall, *Corros. Sci.* 18 (1978): pp. 427–439.

232. Hibert, F., Y. Miyoshi, G. Eichkorn, and W.J. Lorenz, *J. Electrochem. Soc.* 118 (1971): pp. 1919–1926.

233. Barcia, O.E., and O.R. Mattos, *Electrochim. Acta* 35 (1990): pp. 1601–1608.

234. Lorenz, W.J., G. Staikov, W. Schindler, and W. Wiesbeck, *J. Electrochem. Soc.* 149 (2002): pp. K47–K59.

235. Heusler, K.E., *Encyclopedia of Electrochemistry of the Elements. Vol. 9* (New York: Marcel Dekker, 1982).

236. Keddam, M., O.R. Mattos, and H. Takenout, *J. Electrochem. Soc.* 128 (1981): pp. 266–274.

237. Douglas R. MacFarlane, S.I.S., *J. Electrochem. Soc.* 133 (1986): pp. 2240–2244.

238. Lorbeer, P., and W.J. Lorenz, *Corrosion* 20 (1980): pp. 405–412.

239. Swamee, P.K., and A.K. Jain, *J. Hydraul. Div.* 102 (1976): pp. 657–664.

240. Colebrook, C.F., and C.M. White, *Proc. R. Soc. A Math. Phys. Eng. Sci.* 161 (1937): pp. 367–381.

241. Akeer, E.S., "Effect of Carbon Steel Composition and Microstructure on CO_2 Corrosion," Ohio University, 2014.

242. Akeer, E., B. Brown, and S. Nesic, *Corros. 2013* (2013): p. paper no. 2383.

243. Schulz, K.G., U. Riebesell, B. Rost, S. Thoms, and R.E. Zeebe, *Mar. Chem.* 100

(2006): pp. 53–65.

244. Coleman, D., R. White, and D. Hobbs, *J. Electrochem. Soc.* 142 (1995): pp. 1152–1161.

245. Fan, D., *J. Electrochem. Soc.* 138 (1991): pp. 1688–1691.

246. Yin, K.-M., T. Yeu, and R.W. White, *J. Electrochem. Soc.* 138 (1991): p. 1051.

247. Newman, J., *Ind. Eng. Chem. Fundam.* 7 (1968): pp. 514–517.

248. Zeebe, R.E., D.A. Wolf-Gladrow, and H. Jansen, *Mar. Chem.* 65 (1999): pp. 135–153.

249. Duan, Z., and D. Li, *Geochim. Cosmochim. Acta* 72 (2008): pp. 5128–5145.

250. Duan, Z., and R. Sun, *Chem. Geol.* 193 (2003): pp. 257–271.

251. Xiang, Y., C. Li, Z. Long, C. Guan, W. Wang, and W. Hesitao, *Electrochim. Acta* 258 (2017): pp. 909–918, https://doi.org/10.1016/j.electacta.2017.11.141.

252. Krichevsky, I.R., and J.S. Kasarnovsky, *J. Am. Chem. Soc.* 57 (1935): pp. 2168–2171.

253. Carroll, J.J., and A.E. Mather, *J. Solution Chem.* 21 (1992): pp. 607–621.

254. Majer, V., J. Sedlbauer, and G. Bergin, *Fluid Phase Equilib.* 272 (2008): pp. 65–74.

255. Garcia, J., (2001), http://escholarship.org/uc/item/6dn022hb.pdf.

256. Yaws, C.L., *The Yaws Handbook of Vapor Pressure : Antoine Coefficients*, Second Ed. (2015).

257. Roughton, F.J.W., *J. Am. Chem. Soc.* 63 (1941): pp. 2930–2934.

258. Harned, H.S., and F.T. Bonner, *J. Am. Chem. Soc.* 67 (1945): pp. 1026–1031.

259. Zheng, Y., J. Ning, B. Brown, and S. Nesic, *Corros. 2014* 71 (2014): p. 316.

260. Ho, C., and J.M. Sturtevant, *J. Biol. Chem.* 238 (1963): pp. 3499–3501.

261. Pinsent, B.R.W., L. Pearson, and F.J.W. Roughton, *Trans. Faraday Soc.* 52 (1956): p. 1512.

262. Johnson, K.S., *Limnol. Oceanogr.* 27 (1982): pp. 849–855.

263. Pinsent, B.R.W., and F.J.W. Roughton, *Trans. Faraday Soc.* 47 (1951): pp. 263–269.

264. Welch, M.J., J.F. Lifton, and J.A. Seck, *J. Phys. Chem.* 73 (1969): pp. 3351–3356.

265. Pocker, Y., and D.W. Bjorkquist, *J. Am. Chem. Soc.* 99 (1977): pp. 6537–6543.

266. Scheurer, P.G., R.M. Brownell, and J.E. Luvalle, *J. Phys. Chem.* 62 (1958): pp. 809–812.

267. Berger, R.L., and L.C. Stoddart, *Rev. Sci. Instrum.* 36 (1965): p. 78.

268. Sorensen, P.E., and A. Jensen, *Acta Chem. Scand.* 24 (1970): pp. 1483–1485.

269. Patel, R.C., R.J. Boe, and G. Atkinson, *J. Solution Chem.* 2 (1973): pp. 357–372.

270. Cooper, J.R., Q. Mary, M.E. Road, and S.I. Associates, *On the IAPWS Industrial Formulation 1997 for the Thermodynamic Properties of Water and Steam* (The International Association for the Properties of Water and Steam, 2012).

271. Pitzer, K.S., *J. Solution Chem.* 4 (1975): pp. 249–265.

272. Meyssami, B., M.O. Balaban, and A.A. Teixeira, *Biotechnol. Prog.* 8 (1992): pp. 149–154.

273. Crolet, J.-L., and M.R. Bonis, *Corrosion* 39 (1983): pp. 39–45.

274. Eigen, M., *Angew. Chem. Int. Ed. Engl.* 3 (1964): pp. 1–19.

275. Natzle, W.C., and C.B. Moore, *J. Phys. Chem.* 89 (1985): pp. 2605–2612.

276. Bolmer, P.W., *Corrosion* 3 (1965): pp. 69–75.

277. Morris, D.R., *J. Electrochem. Soc.* 127 (1980): p. 1228.

278. Shoesmith, D.W., *J. Electrochem. Soc.* 127 (1980): p. 1007.

279. Galvan-Martinez, R., J. Mendoza-Flores, R. Duran-Romero, and J. Genesca, *Mater. Corros.* 58 (2007): pp. 514–521.

280. Galvan-Martinez, R., J. Mendoza-Flores, R. Duran-Romero, and J. Genesca-Llongueras, *Mater. Corros.* 55 (2004): pp. 586–593.

281. Arzola, S., and J. Genescá, *J. Solid State Electrochem.* 9 (2005): pp. 197–200.

282. Arzola, S., J. Mendoza-Flores, R. Duran-Romero, and J. Genesca, *Corrosion* 62 (2006): pp. 433–443.

283. Esmaeely, S.N., B. Brown, and S. Nesic, *Corrosion* 73 (2017): pp. 144–154.

284. Suleimenov, O.M., and R.E. Krupp, *Geochim. Cosmochim. Acta* 58 (1994): pp. 2433–2444.

285. Suleimenov, O.M., and T.M. Seward, *Geochim. Cosmochim. Acta* 61 (1997): pp. 5187–5198.

286. Migdisov, A.A., A.E. Williams-Jones, L.Z. Lakshtanov, and Y. V. Alekhin, *Geochim. Cosmochim. Acta* 66 (2002): pp. 1713–1725.

287. Tamimi, A., E.B. Rinker, and O.C. Sandall, *J. Chem. Eng. Data* 39 (1994): pp. 330–332.

288. Eigen, M., and L. De Maeyer, *Proc. R. Soc. London, Ser. A* 247 (1958): pp. 505–533.

289. Santos, E., a. Lundin, K. Pötting, P. Quaino, and W. Schmickler, *Phys. Rev. B - Condens. Matter Mater. Phys.* 79 (2009): pp. 1–10.

290. Jafarian, M., M. Behazin, I. Danaee, and F. Gobal, *Res. J. Chem. Sci.* 3 (2013): pp. 56–63.

291. Khanova, L.A., and L.I. Krishtalik, *J. Electroanal. Chem.* 660 (2011): pp. 224–

229, http://dx.doi.org/10.1016/j.jelechem.2011.01.016.

292. Conway, B.E., and E. Gileadi, *Trans. Faraday Soc.* 58 (1962): p. 2493.

293. Chun, J.H., K.H. Ra, and N.Y. Kim, *J. Electrochem. Soc.* 150 (2003): p. E207.

294. Chun, J.H., S.K. Jeon, N.Y. Kim, and J.Y. Chun, *Int. J. Hydrogen Energy* 30 (2005): pp. 1423–1436.

295. Hamelin, A., L. Stoicoviciu, S.-C. Chang, and M.J. Weaver, *J. Electroanal. Chem. Interfacial Electrochem.* 307 (1991): pp. 183–194.

296. Lasia, A., "Hydrogen Evolution Reaction," in Handb. Fuel Cells (2010).

297. Markovic, N.M., and P.N.J. Ross, *Surf. Sci.Reports* 45 (2002): pp. 117–229.

298. Balat, M., *Int. J. Hydrogen Energy* 33 (2008): pp. 4013–4029.

299. Brug, G.J., M. Sluyters-Rehbach, J.H. Sluyters, and A. Hemelin, *J. Electroanal. Chem.* 181 (1984): pp. 245–266.

300. Perez, J., E.. R. Gonzalez, and H.M. Villullas, *J. Phys. Chem. B* 102 (1998): pp. 10931–10935.

301. Conway, B.E., and L. Bai, *Electrochim. Acta* 31 (1986): pp. 1013–1024.

302. Kuhn, A.T., and M. Byrne, *Electrochim. Acta* 16 (1971): pp. 391–399.

303. Hillson, P.J., *Trans. Faraday Soc.* 48 (1952): p. 462.

304. Ives, D.J.G., *Can. J. Chem.* 37 (1959): pp. 213–221.

305. Parsons, R., G. Picq, and P. Vennereau, *J. Electroanal. Chem.* 181 (1984): pp. 281–287.

306. Krishtalik, L.I., *Electrochim. Acta* 48 (2002): pp. 181–190.

307. Hamelin, A., *J. Electroanal. Chem.* 386 (1995): pp. 1–10.

308. Bode, D.D., J.T.N. Andersen, and H. Eyring, *J. Phys. Chem.* 71 (1967): pp. 792–797.

309. Hamelin, A., and M.J. Weaver, *J. Electroanal. Chem.* 223 (1987): pp. 171–184.

310. Enyo, M., *J. Reasearch Inst. Catal.* 25 (1977): pp. 17–36.

311. Łukaszewski, M., K. Kuśmierczyk, J. Kotowski, H. Siwek, and A. Czerwiński, *J. Solid State Electrochem.* 7 (2003): pp. 69–76.

312. Chun, J.H., and N.Y. Kim, *Int. J. Hydrogen Energy* 31 (2006): pp. 277–283.

313. Stobiński, L., L. Zommer, and R. Duś, *Appl. Surf. Sci.* 141 (1999): pp. 319–325.

314. Casarin, M., C. Maccato, and A. Vittadini, *J. Phys. Chem. B* 106 (2002): pp. 795–802.

315. Stobinski, L., R. Nowakowski, and R. Dus, *Vacuum* 48 (1997): pp. 203–207.

316. Hu, M., D.P. Linder, M.B. Nardelli, and A. Striolo, *J. Phys. Chem. C* 117 (2013): pp. 15050–15060.

317. Barrio, L., P. Liu, J.A. Rodríguez, J.M. Campos-Martín, and J.L.G. Fierro, *J. Chem. Phys.* 125 (2006).

318. Zheng, Y., Y. Jiao, M. Jaroniec, and S.Z. Qiao, *Angew. Chemie - Int. Ed.* 54 (2015): pp. 52–65.

319. Marshall, A.T., *Curr. Opin. Electrochem.* 7 (2018): pp. 75–80.

320. Holmes, H.F., R.H. Busey, J.M. Simonson, R.E. Mesmer, D.G. Archer, and R.H. Wood, *J. Chem. Thermodyn.* 19 (1987): pp. 863–890.

321. N. Moller, *Geochim. Cosmochim. Acta* 52 (1988): pp. 821–837.

322. Pabalan, R.T., and K.S. Pitzer, *Geochim. Cosmochim. Acta* 51 (1987): pp. 829–837.

323. Polya, D.A., E.M. Woolley, J.M. Simonson, and R.E. Mesmer, *J. Chem. Thermodyn.* 33 (2001): pp. 205–243.

324. Christov, C., and N. Moller, *Geochim. Cosmochim. Acta* 68 (2004): pp. 1309–1331.

325. Peiper, J.C., and K.S. Pitzer, *J. Chem. Thermodyn.* 14 (1982): pp. 613–638.

326. Harvie, C.E., N. Moeller, and J.H. Weare, *Geochim. Cosmochim. Acta* 48 (1984): p. 723.

327. He, S., and J.W. Morse, *Geochim. Cosmochim. Acta* 57 (1993): pp. 3533–3554.

328. Wong, C.S., P.Y. Tishchenko, and W.K. Johnson, *J. Chem. Eng. Data* 50 (2005): pp. 822–831.

329. Kahyarian, A., B. Brown, and S. Nesic, *Corrosion* 74 (2018): p. 2792.

APPENDICES

- I: A micro-kinetic investigation of the hydrogen evolution reaction: the case of gold in mildly acidic solutions

- II: A micro-kinetic investigation of hydrogen evolution from multiple proton donors: the case on gold in mildly acidic solutions containing acetic acid

- III: Pitzer parameters of CO_2/H_2O system

I.   A micro-kinetic investigation of the hydrogen evolution reaction: the case of gold in mildly acidic solutions [7]

I.1:Background

The hydrogen evolution reaction (HER) has been the subject of numerous studies, either as a platform for investigating the theory of electrochemical processes [118,133,289–295] , or in terms of hydrogen production, energy storage, and energy conversion [296–298], due to its significance in the alternative energy source framework. This trend had also include extensive investigations of the mechanism of the HER on gold in acidic solutions [75,291,293,295,299–305]. However, a literature survey shows no general agreement on the underlying mechanism of this reaction to date [75,291,299,301,302,304,305]. Besides, the majority of the proposed mechanisms have been developed based on experimental results obtained in highly acidic environments [75,291,293,295,299–305], but were not examined over an extended pH range.

The experimental polarization curves obtained on gold in acidic solutions are repeatedly reported to have two distinct Tafel slopes with values in the range of 50-70 mV at lower current densities and 100-130 mV at higher current densities [113,291,293,300,302,305]. A number of different explanations for the underlying mechanism based on these observed Tafel slopes have been proposed in the literature. In a study by Ives [304] in 0.1 N HCl solutions, the author reported polarization curves with an

---

[7] A version of this chapter is published as: "Mechanism of the hydrogen evolution reaction on gold in mildly acidic environments" Aria Kahyarian, Bruce Brown, Srdjan Nesic, J. Electrochem. Soc. 2017, 164 (6), H365-H374. (Reference number [61])

uncharacterized region at low current densities, preceding to the 120 mV Tafel slope

range. That uncharacterized section of the voltammograms had a significantly lower

Tafel slope with values about 50-70 mV, which was extended to the cathodic currents up

to about 1 A.m^{-2} and overpotentials up to about 150 mV. The author associated this lower

Tafel slope with the interference of the hydrogen oxidation reaction [304]. However,

considering the experimental conditions in that study, no significant interference of

anodic currents due to hydrogen gas oxidation is expected, especially at cathodic

overpotentials as high as 150 mV.

Bockris et al. [75,127] suggested that the apparent change of Tafel slope to ~ 60 mV

was caused by the change in potential drop across the diffusion double layer. This effect

was believed to be most profound at the potentials near the potential of zero charge

(PZC). Therefore, the authors suggested that for the mechanism with theoretical Tafel

slope of ~120 mV (2.3RT/βF), lower apparent Tafel slopes with a minimum of ~60 mV

can be observed in the vicinity of PZC. At the potentials notably different from the PZC,

this effect becomes insignificant, thus the apparent Tafel slope tends to reach the

theoretical value (~120 mV). However, as suggested elsewhere [302,306], the reported PZC

of gold [307,308] is significantly higher than the potentials at which the change in the Tafel

slope occurs experimentally.

Another mechanism based on the barrierless discharge of H$^+$ was also proposed to

explain the observed ~60 mV Tafel slope [291,305]. Khanova and Krishtalik [291] suggest that

barrierless discharge is feasible on a gold surface at significantly low overpotentials. This

means that the activation energy of the HER is equal to its Gibbs free energy change and

thus, the symmetry factor of the reaction is unity. Considering the Tafel slope of 2.3RT/βF for the Volmer step, the observed value is therefore ~60 mV. The transition to 120 mV Tafel slope was then associated with the change to ordinary discharge with $\beta=1/2$ [291,305]. Considering the rate determining Volmer reaction throughout the full range of cathodic currents, either as an ordinary charge transfer reaction or a barrierless reaction, the surface coverage of H_{ads} is expected to be low ($\theta \rightarrow 0$), as discussed in more detail in section 3.2.1 below. However, this was found to be in contrast with the findings from a study by Chun et al. [293] where a significant coverage of H_{ads} ($\theta \rightarrow 1$) was reported in the 120 mV Tafel slope region.

The surface diffusion limiting step has also been suggested as a possible mechanism for the observed lower Tafel slope [127,299,301]. This proposed mechanism states that the hydrogen ion discharge (adsorption) sites are different from desorption sites and the surface diffusion of the adsorbed hydrogen atoms between these sites is the limiting step in the overall HER rate. Brug et al. [299] suggested that desorption sites (surface defects such as impurities) are kinetically favored reaction sites compared to the gold itself and govern the overall reaction rate. The rate of reaction was therefore, limited by the surface diffusion of adsorbed hydrogen atoms to these reaction sites. Nevertheless, the similar behavior of Tafel slopes observed for high purity electrodes (99.99 wt. % in the present study and other studies such as the one by Perez et al. [300]) suggest that the effect of impurities may have been overemphasized.

Conway and Bai [301] also suggested a similar rate determining mechanism involving surface diffusion. However, these authors argued that the adsorption/discharge

sites were not suitable for desorption due to the interference by the strong adsorption of anions present in the electrolyte (HSO_4^- and SO_4^{2-} in that study). Hence, the following mechanism was proposed where the second step represents the surface diffusion of H_{ads}. However, their proposed mechanism also fails to address the increased Tafel slope at high current densities (~ 120 mV).

$$H^+ + e^- \rightleftharpoons H_{ads,A}$$

$$H_{ads,A} \longrightarrow H_{ads,B}$$

$$H_{ads,B} + H^+ + e^- \longrightarrow H_2$$
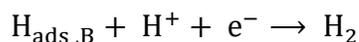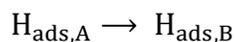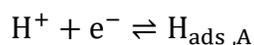
Brug et al. [299] discussed the mechanism of the HER in the context of conventional Volmer-Heyrovsky-Tafel elementary steps. The authors proposed a mechanism with the Tafel reaction being the rate determining step in the 60 mV Tafel slope region and a shift to Heyrovsky reaction being the rate determining step in the 120 mV Tafel slope region.

As discussed above, the majority of previously proposed mechanisms fail to fully address the polarization behavior of the HER as observed in the experimental results. The mechanism based on the conventional elementary steps proposed by Brug et al. [299] can be considered further as a possibility. Another mechanism including a surface diffusion step (Conway and Bai [301]) also appears to be able to explain the observed features of the polarization curves, given that some modification are introduced to address the increase of the Tafel slope. The goal of the present paper is to reevaluate these two mechanisms over an extended pH and potential range, discuss the conditions at which these mechanisms are valid, and finally, settle on a mechanism that agrees best with

polarization behavior of the HER on a gold surface for the conditions in the present study as well as those previously reported in the literature.

It is worth mentioning that the mildly acidic and near-neutral solutions are of special interest in the aqueous corrosion of steel, which is commonly encountered in industrial applications[15,18,43,56,62]. To date, most of the mechanistic corrosion rate predictive models [14,15,18,167] base the calculation of the cathodic current (rate of the HER) on studies [75,76,115] where the experimental conditions were significantly different from those encountered in the models' targeted applications. Considering the profound effect of pH [114,128], electrode material and surface structure [115,125–127,299], overpotential [129], and solution composition [128] on the kinetics of the HER, a comprehensive understanding of the reaction mechanism and its kinetics is essential for accurate modeling of such systems.

I.2:Methodology

I.2.1:Experimental procedures

The experiments were carried out in a 1 L glass cell with a conventional three electrode arrangement. A silver/silver chloride reference electrode was connected to the glass cell through a Luggin capillary filled with 1 M potassium chloride solution. A graphite rod, 5 mm in diameter and 15 cm in length, was used as the counter electrode, which was placed in a separate glass tube with a fine fritted glass connection at the bottom. A 99.99 wt.% polycrystalline gold rotating disk electrode (Pine instruments) with a 5 mm diameter was used as the working electrode. The electrode was polished with 0.05 μm silicon suspension, rinsed and sonicated for 5 minutes using deionized water and

subsequently with isopropanol, prior to each test. The working electrode was further

electrochemically cleaned in the studied solution with 10 consecutive potential cycles,

from -0.6 V to 0.8 V (vs. Ag/AgCl) at 100 mV.s^{-1} until a steady voltammogram was

achieved (typically after 7 cycles). Finally, the electrode was left at open circuit potential

for 5 minutes before starting each potential sweep. The rotation speed of the working

electrode was fixed at 2000 rpm throughout the electrochemical measurements. The

steady state voltammograms reported in the present study were obtained at 0.1 mV.s^{-1}

scan rate using a 2 s^{-1} sampling period, by sweeping the potential from the OCP towards

more negative values. The polarization curves were further corrected for Ohmic drop

using the solution resistance obtained from electrochemical impedance measurements

performed after each potential sweep.

The supporting electrolyte was 0.1 M solution of analytical grade sodium

perchlorate in deionized water. The solution temperature was maintained at 30.0±0.5 º C.

The pH was adjusted by addition of a diluted perchloric acid solution, as required. Then,

the electrolyte was deaerated for at least 90 minutes using nitrogen gas, and the outlet gas

was monitored with an oxygen sensor (Orbisphere 410). Maximum dissolved oxygen

content before initiating the experiment was 3 ppb (typically below 1 ppb). During the

electrochemical measurements, the purging was stopped and the solution was blanketed

with nitrogen gas.

I.2.2:Numerical methods

Parametric study calculations were performed using MATLAB 2012 software.

The partial derivatives were numerically calculated at a fixed pH and potential, by using

a two-point finite difference approximation, *f' = (f(x+h)-f(x))/h)*, with *h=0.001* for both

pH and potential. The values of *f(x)* and *f(x+h)* were obtained based on the known θ

values. By repeating this procedure and varying the characteristic adsorption parameters,

a map of theoretical kinetic parameters was be obtained.

Mathematical model of the system was developed by numerical solution of a set

of differential equations, as discussed in Section 4. The following set of dimensionless

variables were defined to replace distance (x), concentration (C_i), and potential (E and ϕ).

$$\zeta = \frac{x}{\delta} \qquad\qquad \xi_i = \frac{C_i}{C_i^b} \qquad\qquad \Phi = \frac{F\phi}{RT} \qquad\qquad \psi = \frac{FE}{RT}$$

The resulting set of differential equations was solved by the finite difference

method. The first and second order central difference approximations were used to

discretize the first order and the second order derivatives appearing in the governing

equation, respectively. The metal/solution interface boundary condition was discretized

using first order three point forward approximation. The coefficient matrix of the

discretized equations was then formed and solved using Newman's "Band-J" method,

which is described in detail elsewhere [164,247]. The calculations were performed with 200

spatial nodes and a maximum cumulative error of $R^2 = 10^{-12}$ for all iterations. The source

code of the model was developed using Microsoft Visual Studio 2012 and an Intel Visual

Fortran Compiler 13.0. Furthermore, a graphic user interface was developed, using

MATLAB 2012 GUI, in order to simplify input/output operations.

I.2.3:Experimental results

The steady state voltammograms of the HER obtained on a gold electrode, at the

experimental conditions described above, are shown in Figure I-1. The polarization

curves obtained at pH 4 and pH 5 showed a similar behavior. That is, a linear increase of the current density at less negative potentials, which is associated with hydrogen evolution from H^+ ions, followed by a plateau that is a result of mass transfer limitation of H^+ ions, and another linear increase at more negative potentials due to the hydrogen evolution from water. At lower pH values (2 and 3) the mass transfer limiting current and the water reduction line were not observed as they exceeded the maximum measurable current densities (~40 A.m^{-2}). The maximum measureable current density limit was imposed by the blockage effect resulting from hydrogen gas accumulation at the electrode surface. The current densities at which a significant blockage effect was observed is affected by the sweeping rate of the produced hydrogen gas *i.e.* the flow velocity parallel to the electrode surface. At 2000 rpm rotation rate used throughout this study, no significant accumulation of hydrogen gas was observed at the current densities below 40 A.m^{-2}.

The present study is focused on the polarization behavior associated with the H^+ ion reduction reaction at the current densities below the mass transfer limiting current, which was observed for all pH values as shown in Figure I-1. In this range, at low current densities (below 4 A.m^{-2}), Tafel slopes in the range of 68 ± 5 mV were observed throughout the studied pH range. Although, at pH 5 the slope of the polarization curve appears to have slightly increased due to mass transfer limitation interference. At higher current densities (above 4 A.m^{-2}) the Tafel slope increased to 120 ± 2 mV, which was most clearly observed at pH 2.
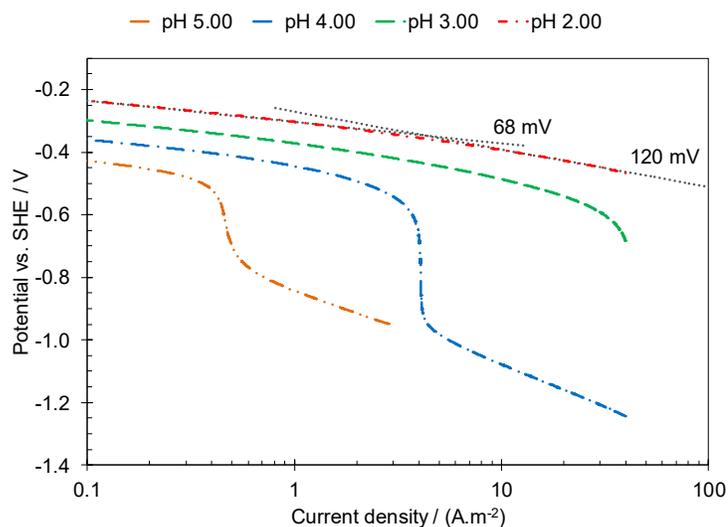
Figure I-1. Steady state voltammograms of the HER on gold RDE at 2000 rpm, 30°C and 0.1 M NaClO₄.

The experimental Tafel slopes obtained in the present study were found to agree well with the results reported in the literature. As summarized in Table I-1, the observation of two distinctive Tafel slopes for the HER on gold has been frequently reported in the literature. The lower Tafel slope was generally reported within the range of 50 mV to 70 mV. At higher current densities, the reported Tafel slopes were in the range of 100 mV to 130 mV. In the studies reporting a single Tafel slope, the values obtained were generally within the 50 mV to 70 mV Tafel slope range.

Table I-1. Literature survey for experimental Tafel slope of HER on gold in acidic solutions.

Electrolyte	Lower b (mV)	Higher b (mV)	Reference
0.1 M HClO$_4$	60	120	[300]
0.1 N HCl	71	97	
0.01, 0.001 N HCl	72 and 84	-	[75]
0.5 M H$_2$SO$_4$	60	-	[301]
0.1 M and 0.01 M HClO$_4$	50 to 70	-	[309]
1 M H$_2$SO$_4$	30	110	[302]
1M HClO$_4$	62 to 97	118	[299]
1 M and 0.1 M H$_2$SO$_4$	53 to 69	105 to 141	[291]
0.5 M H$_2$SO$_4$	30	-	[293]
1 N HCl	60	-	[303]
0.03 M HClO$_4$	60	120	[305]

In addition to the Tafel slope, the reaction order of the HER with respect to the concentration of hydrogen ions is also a characteristic kinetic parameter that can provide additional information about the underlying mechanism. Figure I-2 presents the pH dependence of the current density at two fixed potentials for the experimental data obtained in the present study. In this graph (log(i) vs. pH), the slope of the trend-line represents the apparent reaction order of HER ($-p_{(H+)}$) which was found to be approximately 0.8 at the pH range from 2 to 5, while some variation at different potentials and pH values was observed. The observed value of the apparent reaction order and its variation with pH and potential may imply a multi-step reaction mechanism and possibly multiple reaction pathways, which is not unexpected for acidic hydrogen evolution reaction. The values for reaction order were not frequently reported in the literature, however, in studies by Kuhn and Byrne[302] and by Brug et al.[299], the reaction order of 1 with significant deviations with potential were reported.
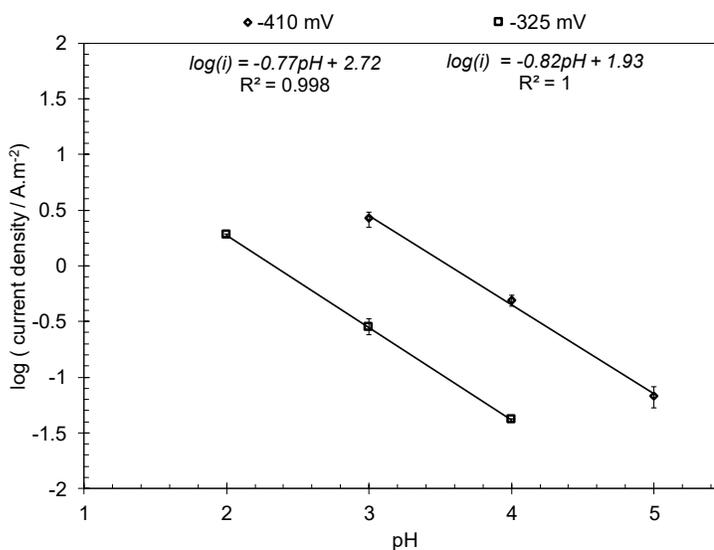
Figure I-2. pH dependence of current density at -0.410 V (vs. SHE) and -0.325 V (vs. SHE) at 2000 rpm, 30°C and 0.1 M NaClO$_4$. Error bars show the standard deviation from minimum of three repetitions. The equation of each tren-dline is shown under the corresponding legend.

I.3.4:Parametric Study of the HER Mechanisms

The hydrogen evolution reaction is conventionally described by the sequence of three elementary steps as shown *via* Reaction (II-1) to Reaction (II-3) [109]. These reactions are known as the Volmer (electrochemical hydrogen ion adsorption) reaction, Heyrovsky (electrochemical desorption) reaction, and Tafel (chemical desorption) reaction, respectively. In addition to the conventional elementary steps, Reaction (I-4) below represents the surface diffusion elementary step, similar to what was discussed by Conway and Bai [301], where A and B are distinct adsorption and desorption sites.

$$H^+ + e^- \rightleftharpoons H_{ads} \qquad\qquad (\text{I-1})$$

$$H^+ + H_{ads} + e^- \rightarrow H_2 \qquad\qquad (\text{I-2})$$

$$2H_{ads} \rightarrow H_2 \qquad\qquad (\text{I-3})$$

$$H_{ads,A} \longrightarrow H_{ads,B} \qquad\qquad (\text{I-4})$$

Here, the hydrogen oxidation reaction is assumed to be insignificant during cathodic polarization. This assumption is in accordance with the experimental procedures, which were designed to minimize the effect of hydrogen oxidation reaction on the cathodic polarization curves.

The mechanism of the HER are discussed in terms of the kinetic parameters such as Tafel slope and reaction order [110,117,127–129], these parameters are experimentally obtained by measuring the change in the current as a function of potential (Tafel slope) and pH (reaction order). The mechanism of the HER at various conditions is then determined by identifying a reaction sequence with kinetic parameters closest to the experimental values. The kinetic parameters corresponding to any given elementary step (Reaction (I-1) to Reaction (I-4)) can be calculated based on their corresponding rate equations. The rate of the elementary reactions shown above, can be described by Equation (I-5) to Equation (I-8), respectively [122,124,301,310].

$$v_V = k_{f,V}(1-\theta)[\text{H}^+]e^{-\lambda_V u\theta}e^{-\beta_V\frac{FE}{RT}} - k_{b,V}\,\theta e^{(1-\lambda_V)u\theta}e^{(1-\beta_V)\frac{FE}{RT}} \qquad\qquad (\text{I-5})$$

$$v_H = k_{f,H}[\text{H}^+]\theta e^{(1-\lambda_H)u\theta}e^{-\beta_H\frac{FE}{RT}} \qquad\qquad (\text{I-6})$$

$$v_T = k_{f,T}\theta^2 e^{2(1-\lambda_T)u\theta} \qquad\qquad (\text{I-7})$$

$$v_D = k_{f,D}\theta e^{(1-\lambda_D)u\theta} \qquad\qquad (\text{I-8})$$

In these equations, k is the reaction rate constant, θ is the surface coverage by adsorbed hydrogen atoms (H_{ads}), the first exponential terms describe the interaction of H_{ads} at the surface where u represents the correlation coefficient of the interaction energy, and where present – the second exponential term accounts for the effect of potential. Note

that, for the electrochemical Reactions (I-5) and (I-6), it can be reasonably assumed that the symmetry factors β and $(1-\lambda)$ are equal. This assumption is based on the fact that both symmetry factors are associated with the change in the Gibbs free energy of the same activated complex.

Based on the aforementioned elementary steps, three scenarios can exist.

a) H^+ adsorption rate determining step.

b) H_{ads} desorption rate determining steps.

c) Surface diffusion rate determining step.

The theoretical expression of the Tafel slope (b) and reaction order ($p_{(H+)}$) for case (a) are relatively straightforward as discussed in the following section. However, when the desorption step (b) or the surface diffusion step (c) are rate determining, these expressions become nonlinear functions of surface coverage (as shown in Table I-2) and cannot be solved analytically without introducing additional assumptions [117,118]. An alternative approach used in the present study is the numerical solution of the expressions shown in Table I-2, where the nonlinear surface coverage functions and derivatives were numerically obtained, as discussed in the Methodology section. Using this approach, the behavior of the Tafel slope and reaction order was investigated as a function of the physiochemical parameters representing the state of surface coverage by H_{ads} (u and K). In order to uncover the possible mechanisms of the HER in the conditions of the present study, the results were compared with the experimental data.

Table I-2. Theoretical expressions of reaction order and Tafel slope for various elementary steps.

	$\dfrac{1}{b} = -\left(\dfrac{\partial \log i}{\partial E}\right)_{pH}$	$p_{(H^+)} = \left(\dfrac{\partial \log i}{-\partial pH}\right)_{E}$
Heyrovsky reaction	$\dfrac{\partial \log(\theta e^{(1-\lambda)u\theta})}{\partial E} - \dfrac{\beta F}{2.303RT}$	$1 - \dfrac{\partial \log(\theta e^{(1-\lambda)u\theta})}{\partial pH}$
Tafel reaction	$2\dfrac{\partial \log(\theta e^{(1-\lambda)u\theta})}{\partial E}$	$-2\dfrac{\partial \log(\theta e^{(1-\lambda)u\theta})}{\partial pH}$
Surface diffusion	$\dfrac{\partial \log(\theta e^{(1-\lambda)u\theta})}{\partial E}$	$-\dfrac{\partial \log(\theta e^{(1-\lambda)u\theta})}{\partial pH}$

H^+ adsorption rate determining step

In the case where the H^+ adsorption step (a) is slower than the other steps, the rate of the HER is governed by the rate of the forward partial of Reaction (I-1):

$$v_V = k_{f,V}(1 - \theta)[H^+]e^{-\lambda_V r\theta}e^{-\beta_V \frac{FE}{RT}} \qquad (\text{I-9})$$

In this case, the concentration of H_{ads} can be considered to be negligibly small ($\theta \rightarrow 0$), as a result of its consumption in the faster succeeding steps [109,110,118]. Therefore, both linear and exponential surface coverage dependent terms in Equation (I-9) can be disregarded and the HER rate can be described as:

$$v_V = k_{f,V}[H^+]e^{-\beta_V \frac{FE}{RT}} \qquad (\text{I-10})$$

The reaction rate relationship shown as Equation (I-10) corresponds to a Tafel slope of ~120 mV at *T=303°K ($2 \times 2.303RT/F$)* and has a reaction order of 1.

H_{ads} desorption rate determining steps

In the case where the H_{ads} desorption steps are rate determining, the surface coverage of H_{ads} may be significant ($\theta>0$). Here, one may assume that the Volmer reaction is at quasi-equilibrium, as the reaction preceding the rate determining step. Knowing this assumption is only valid if the kinetics of the forward and backward Volmer reaction are much faster than the succeeding step. Using this simplifying assumption, Equation (I-5) can be restated as Equation (I-11), resulting in a Frumkin type adsorption isotherm, describing the surface coverage (θ) of H_{ads}:

$$\frac{\theta}{(1-\theta)}e^{r\theta} = K\,e^{\left(-\frac{FE}{RT}\right)}[H^+] \tag{I-11}$$

where $K=k_{f,V}/k_{b,V}$. As shown in Figure I-3, this equation can be used to study the response of θ to changes in pH and potential as a function of u and K. This can be further used for numerical calculation of the theoretical kinetic parameters associated with the presumed succeeding reaction, as shown in Table I-2.
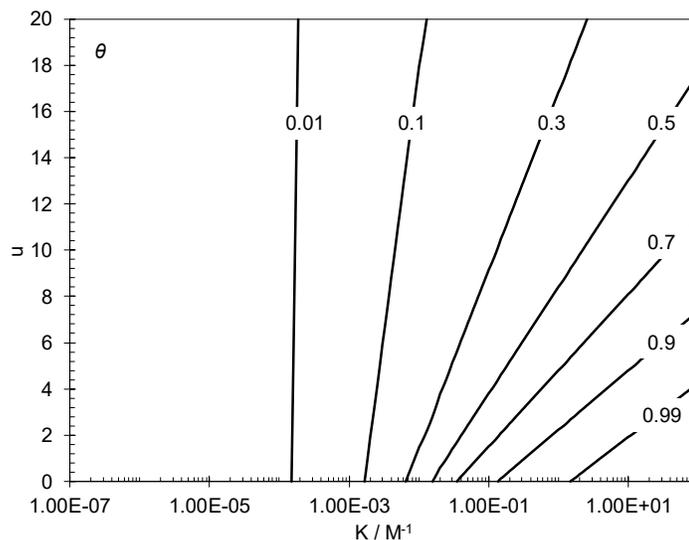
Figure I-3. Calculated value of the surface coverage of H_{ads} described *via* Equation (I-11). At pH 2, -0.230 V (vs. SHE) and 30° C.

Heyrovsky rate determining step

Considering that the Heyrovsky step is rate determining, the Tafel slope and reaction order are shown in Figure I-4.A and Figure I-4.B, respectively. These graphs demonstrate a map of these two parameters at a fixed pH and potential while the values of the interaction coefficient (u) and the equilibrium constant of the Volmer step (K) were varied. That provides a comprehensive view of how Tafel slope and reaction order may change at various conditions. The commonly reported values of Tafel slope and reaction order in literature [110,117,118] are found as limiting conditions in these graphs. As shown in Figure I-4.A for the Heyrovsky rate determining step, the Tafel slope has the minimum of ~40 mV ($2/3 \times 2.303RT/F$) observed at low values of K ($K < 10^{-5}$ M^{-1}), and the maximum of ~118 mV ($2 \times 2.303RT/F$) at high K values ($K > 10^1$ M^{-1}). At similar conditions, the reaction orders of 2 and 1 were obtained at low and high K values, respectively, as shown in Figure I-4.B. These two limits for Tafel slope and reaction order were found to

correlate with the limiting conditions of the surface coverage shown in Figure I-3, where

low K values correspond to $\theta \to 0$ and high K values correspond to $\theta \to 1$.
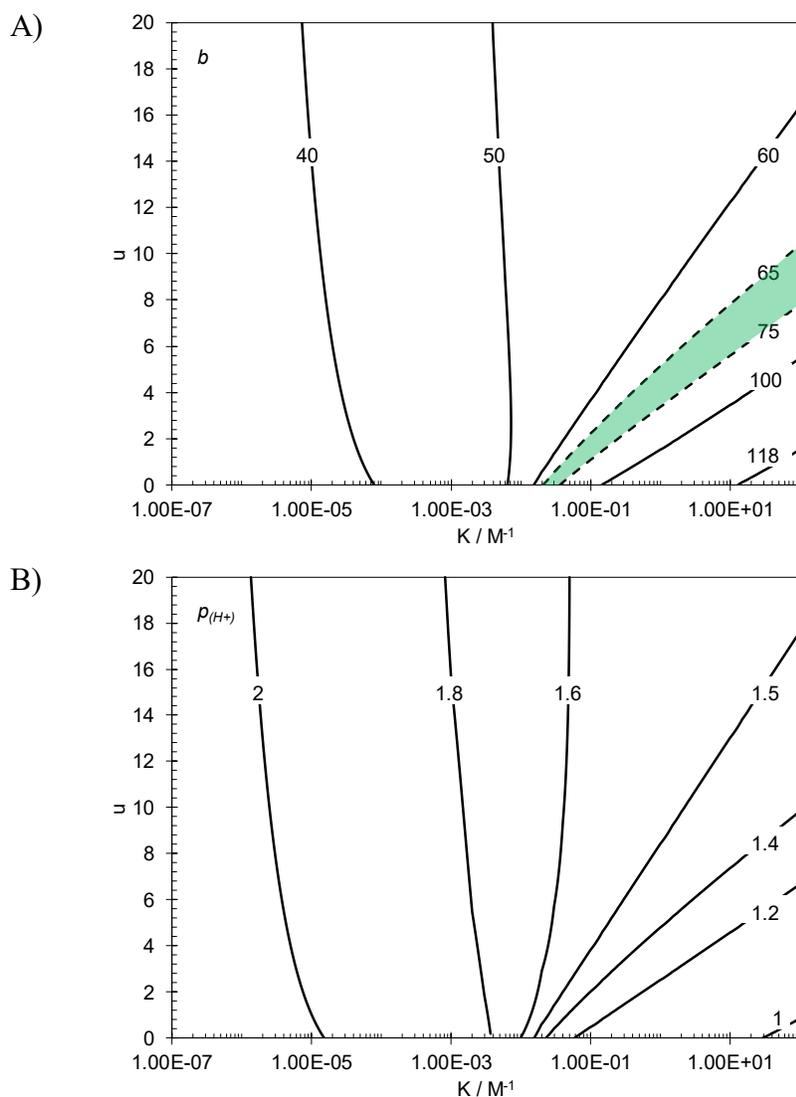
Figure I-4. Calculated values of the kinetic parameters where the Heyrovsky reaction is the rate determining step. At pH 2, -0.230 V (vs. SHE), 30° C, and λ=0.5. A) Tafel slope, and B) reaction order.

For the two limiting conditions discussed above ($\theta \to 0$ and $\theta \to 1$), as well as for

the case when u is negligibly small (along the x-axis in Figure I-4.A and Figure I-4.B),

Equation (I-11) can be further simplified. In these conditions, the change in the θ dependent exponential term in Equation (I-11) with variation of θ is negligible when compared to the θ dependent linear term. Therefore, one can assume that the exponential function is constant, which allows Equation (I-11) to be reduced to a Langmuir type isotherm. Based on this simplifying assumption, theoretical values of Tafel slope (40 mV and 120 mV) and reaction order (2 and 1, respectively) were obtained in the past studies [118,299].

On the other hand, when the value of θ is in-between the limiting conditions described above and u is high, the change in the θ dependent linear terms with variation of θ can be assumed to be negligible when compared to the θ dependent exponential terms. Equation (I-11) can then be simplified to a Temkin type isotherm and the linear θ dependent terms of the expressions in Table I-2 may be disregarded [118]. This specifically corresponds to the condition where $\theta=0.5$ in Figure I-3 (when $\theta/(1-\theta)=1$) with Tafel slope of ~60 mV (*2.303RT/F*) and reaction order of 1.5, as shown in Figure I-4.A and Figure I-4.B.

Tafel rate determining step

The results of a similar analysis as described in the previous section are reported in Figure I-5 for the case where the Tafel step is rate determining. The Tafel slope is shown in Figure I-5.A where the minimum value of ~30 mV (*1/2×2.303RT/F*) was observed at low K values (corresponding to $\theta\rightarrow0$) that increased to infinity at high K values (corresponding to $\theta\rightarrow1$), where Equation (I-11) can be simplified to a Langmuir type isotherm. As shown in Figure 5.B, these Tafel slopes coincide with the reaction

order of ~2 and ~0, respectively. At $\theta=0.5$ where Equation (I-11) can be simplified to a Temkin type isotherm, the Tafel slope of ~60 mV (*2.303RT/F*) and reaction order of 1 is observed.
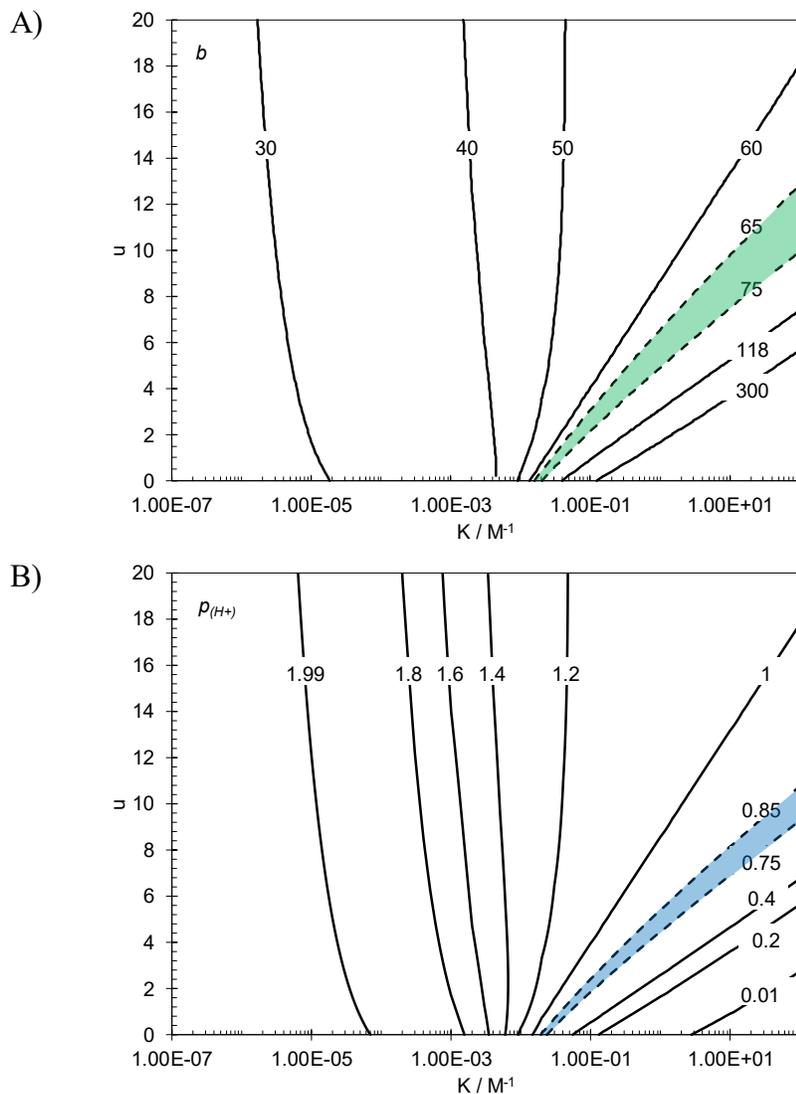
Figure I-5. Calculated values of the kinetic parameters where the Tafel reaction is the rate determining step. At pH 2, -0.230 V (vs. SHE), 30° C and λ=0.5. A) Tafel slope, and B) Reaction order.

Surface Diffusion Rate Determining Step

The theoretical values of Tafel slope and reaction order for the case when the surface diffusion is the rate determining step was calculated in a same fashion as described above for other elementary steps, and the results are shown in Figure I-6.

A)

B)
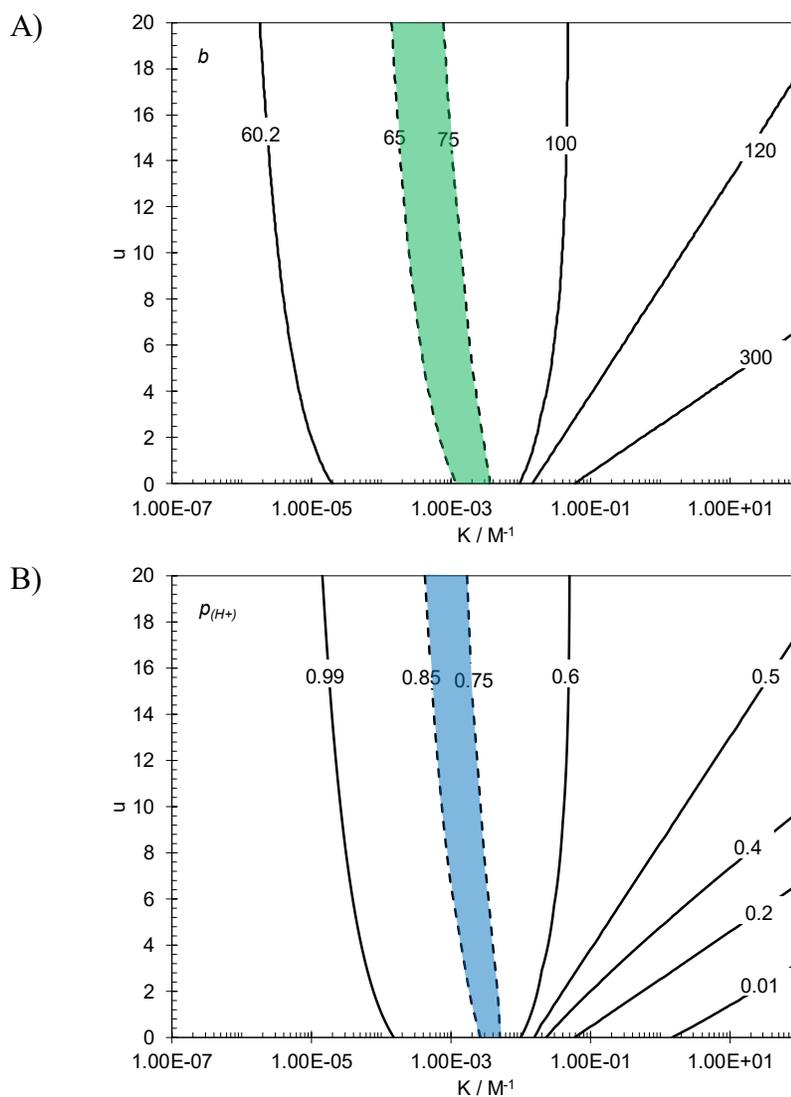


Figure I-6. Calculated values of the kinetic parameters where the surface diffusion is the rate determining step. At pH 2, -0.230 V (vs. SHE), 30° C and λ=0.5. A) Tafel slope, and B) Reaction order.

Figure I-6.A shows that the Tafel slope has a minimum value of ~60 mV

($2.303RT/F$) at low K values ($K<10^{-5}$) which corresponds to the reaction order of 1 and

$\theta\rightarrow0,$ as shown in Figure I-6.B and Figure I-3, respectively. At high K values ($K>10$), Tafel slope increases to infinity while the reaction order approaches zero and $\theta\rightarrow1$. At $\theta=0.5$, where Equation (I-11) can be simplified to a Temkin type adsorption isotherm, the Tafel slope of ~120 mV (2.303RT/F) and reaction order of 0.5 is obtained.

I.3.5:Discussion

In order to narrow down the possible mechanisms of the HER in the conditions of the present study, the theoretical values of the reaction order and Tafel slope obtained above were further examined, considering the experimentally obtained Tafel slope of 68 ± 5 mV and the reaction order of ~0.8.

Reaction mechanisms including the slow adsorption of H^+ step (Volmer reaction) with 120 mV theoretical Tafel slope can be readily eliminated, when considering the experimental Tafel slopes of 68 ± 5 mV obtained at low current densities. On the other hand, the Tafel, Heyrovsky, and surface diffusion elementary steps were found to have theoretical Tafel slopes similar to what was observed experimentally, for a certain range of K and u values. This possibility is illustrated in Figure I-4.A, Figure I-5.A, and Figure I-6.A, as a highlighted area between the dotted lines. However, a Heyrovsky rate determining step may also be eliminated, when considering that in the same range of u and K, where the Tafel slope is in agreement with experimental data, the reaction orders (shown in Figure I-4.B) differ significantly.

The reaction orders obtained when the Tafel step or the surface diffusion step were considered to be rate determining (Figure I-5.B and Figure I-6.B) suggest that a reasonable agreement with the experimental values can be achieved for both mechanisms.

Consequently, at the conditions considered for this parametric study, the rate determining step at lower current densities may be explained through either of following scenarios:

- A Tafel rate determining step when $0.5<\theta<0.8$.

- A surface diffusion rate determining step when $\theta \to 0$.

The possible mechanism underlying the ~120 mV Tafel slope, observed at higher current densities, can be analyzed in a similar fashion. Considering the discussion above, the only scenario with a reasonable agreement to the experimental data is the Heyrovsky reaction being rate determining and $\theta \to 1$. That results in a theoretical Tafel slope of ~120 mV and reaction order of 1, as shown in Figure I-4.A and Figure I-4.B, respectively.

In the above parametric study, the possible mechanism at the higher current densities (the region with ~120 mV Tafel slope) was narrowed down to a unique scenario – Heyrovsky rate determining step. However, at the lower current densities (the region with ~60 mV Tafel slope), the same type of analysis was not able to differentiate between the two possible mechanisms. The main difference between these two mechanisms was in the extent of the surface coverage (θ) by H_{ads}. The mechanism having the Tafel reaction as the rate determining step requires a high surface coverage and strong repulsive interaction of H_{ads}, whereas, the surface diffusion limiting step suggests a negligible coverage by H_{ads}. This can used as a distinguishing argument between these two mechanisms.

The measurements reported by Brug et al. [299] and Conway and Bai [301] showed that over the low cathodic overpotentials (in the ~60 mV Tafel slope range) there is no significant adsorption pseudo-capacitance, claiming a negligible coverage by H_{ads}.

However, before taking these studies in favor of the surface diffusion mechanism, one should also consider the low adsorption capacity of gold surfaces. Let us recall that θ is a relative parameter which is defined as concentration (number) of H_{ads} divided by the maximum concentration of H_{ads} (i.e. number of active sites for H_{ads}). However, the number of active sites depends on the nature of the metal surface. For example in a study by Bus and van Bokhoven [199] on the gaseous adsorption of hydrogen, the hydrogen adsorption per molecule of platinum was shown to be 2 to 5 times higher than that of gold at similar conditions [199]. In the adsorption pseudo-capacitance context, this parameter is reflected as a constant (q_{max}) representing the charge required to reach maximum coverage by H_{ads}, as discussed by Conway and Tilak [109] :

$$C_F = \frac{dq}{dE} = q_{max} \frac{d\theta}{dE}$$

Therefore, considering the smaller number of available active sites on gold (lower q_{max}), as compared to more active metals such as platinum [199] and palladium [311], it is reasonable to expect significantly lower adsorption pseudo-capacitance, for the same magnitude of the surface coverage (θ). This makes it difficult to use the adsorption pseudo-capacitance as a unambiguous measure of surface coverage (θ) across different metals.

Another parameter that affects the observed adsorption pseudo-capacitance is u, the interaction coefficient of H_{ads}. That is, higher interaction amongst adsorbed hydrogen atoms results in lower maximum coverage by H_{ads}. This effect was discussed in detail in a study by Conway and Gileadi [292]. They demonstrated that increasing u from 0 to 20 decreased the adsorption pseudo-capacitance by more than one order of magnitude at

θ=0.5. This effect may be considered significant as the Volmer-Tafel mechanism also suggested the value of u to be in the higher range discussed by Conway and Gileadi [292]. Therefore, one can argue that the adsorption pseudo-capacitance on a gold surface can be lower than what would be observed on active surfaces like platinum by a few orders of magnitude, at the same value of θ.

On the other hand, in a series of studies using phase-shift method to investigate the electro-adsorption of hydrogen atoms on various metals [293,294,312], Chun et al. reported a Langmuir isotherm to describe the adsorption of hydrogen on polycrystalline gold surface [293]. Their measurements showed a low surface coverage at the low cathodic overpotentials, which was rapidly increased to full coverage at higher cathodic overpotentials. Based on these results, authors report the value of K=2.3×10^{-6} M^{-1} for the Langmuir equilibrium constant[293]. The results reported in that study are well compatible with the HER mechanism that includes a surface diffusion rate determining step at $\theta \rightarrow 0$ over low current densities and a Heyrovsky rate determining step at $\theta \rightarrow 1$ over high current densities.

Furthermore, in studies on the chemisorption of hydrogen on gold surfaces, it was frequently reported that the low coordinated gold atoms at corner and edge positions in the crystal lattice have significantly higher activity in adsorption and dissociation of molecular hydrogen [313–316]. In a density functional theory study of H$_2$ dissociation on gold clusters, Barrio et al. [317] showed that some of the low coordination gold atoms can actively dissociate the H-H bound without any significant activation energy barrier. Since the catalytic behavior would enhance both directions of a reaction, the revers reaction,

which is essentially the Tafel recombination step, is expected to proceed with a minimal

activation energy barrier as well. These findings are in agreement with the surface

diffusion mechanism, in a sense that they suggest distinct –but scarce– reaction sites at

the gold surface with particularly higher activity for the Tafel recombination step. Similar

significant structural dependent reaction rates for the HER was also reported for other

materials such as MoS_2, as reviewed in more detail elsewhere [318].

Overall, considering the extent of hydrogen adsorption on a gold surface as a

differentiating criterion, the mechanism including a surface diffusion as a rate

determining step is a better representative of the electrochemical behavior of the HER

than the mechanism based on Tafel rate determining step. Therefore, considering the

results and discussion in the present section, a modified mechanism for the HER can be

proposed as Reaction (I-12) to Reaction (I-15).

$$H^+ + e^- \rightleftharpoons H_{ads,A} \qquad\qquad\qquad\qquad (\text{I-12})$$

$$H_{ads,A} \longrightarrow H_{ads,B} \qquad\qquad\qquad\qquad (\text{I-13})$$

$$2\, H_{ads,B} \longrightarrow H_2 \qquad\qquad\qquad\qquad (\text{I-14})$$

$$H_{ads,A\ or\ B} + H^+ + e^- \longrightarrow H_2 \qquad\qquad (\text{I-15})$$

In the reactions above, subscripts *A* represents majority of the reaction sites that

are placed at the plane gold surface, and *B* represent a small fraction of the surface with

significantly higher activity for the Tafel reaction (as compared to sites *A*). Reaction (

I-13) represents the surface diffusion step preceding the Tafel reaction, which may be

limiting the overall rate of the Tafel reaction a result of the low mobility of H_{ads}, or

perhaps because of the scarcity of B sites. On the other hand, as suggested in Reaction (I-15), the Heyrovsky reaction may occur at both sites A and B.

I.4:Mathematical model

While the arguments based on a parametric study, such as the discussion in the previous section, provide some insight into the underling mechanisms, they cannot properly reflect the complex relationship between pH, potential, K, u, surface coverage, as well as the mass transfer effect. This issue may be addressed by implementing a more comprehensive mathematical treatment. In the following, a mathematical model of the HER on a rotating disk electrode (RDE) was developed, and used to examine whether the mechanism proposed above was able to properly describe the behavior of the HER across the pH and potential range of the present study.

In order to calculate the rate of electrochemical reactions, the surface hydrogen ion concentration $[H^+]$ appearing in the reaction rate relationships (Equation (I-5) and Equation (I-6)) needs to be specified. However, the surface concentration of an electro-active species can significantly differ from its bulk concentration due to mass transfer limitation. This can be particularly pronounced during the measurements when the electrode is polarized more negatively and the cathodic reaction rate becomes mass transfer controlled. The surface concentration of hydrogen ions can be calculated by solving the mass conservation equation throughout the diffusion boundary layer. The mass conservation equation for species i includes the transport of the species due to molecular diffusion, electromigration and laminar convection, as described by the Nernst-Planck equation [68]:

$$\frac{\partial C_i}{\partial t} = -\nabla . N_i + R_i \tag{I-16}$$

Where R_i describes the homogeneous chemical reactions including species i and:

$$N_i = -z_i U_i F C_i \nabla \phi - D_i \nabla C_i + v C_i \tag{I-17}$$

Assuming a steady state condition $(\partial C_i/\partial t=0)$, a one-dimensional semi-infinite geometry in the direction x normal to the RDE electrode surface and an infinitely diluted solution, Equation (I-18) can be restated as:

$$0 = -D_i \frac{\partial}{\partial x} \frac{\partial C_i}{\partial x} - \frac{\partial}{\partial x} \left(\frac{z_i D_i F C_i}{RT} \frac{\partial \phi}{\partial x} \right) + v_x \frac{\partial C_i}{\partial x} + R_i \tag{I-18}$$

The convective flow component in direction x for a RDE electrode was described as [69]:

$$v_x = -a\Omega \left(\frac{\Omega}{v} \right)^{1/2} x^2 \tag{I-19}$$

where $a=0.510$ and the diffusion layer thickness (δ) was [69]:

$$\delta = \left(\frac{3D_{H+}}{av} \right)^{1/3} \left(\frac{\Omega}{v} \right)^{-1/2} \tag{I-20}$$

The only homogeneous chemical reaction in the present study is the water dissociation as shown in Reaction (I-21), which was mathematically described by Equation (I-22) where $i = H^+$ or OH^- . The values for reaction rate constant of water dissociation and recombination, $k_{f,w}$ and $k_{b,w}$, can be found in an earlier study [43].

$$H_2O_{(l)} \leftrightharpoons OH^-_{(aq)} + H^+_{(aq)} \tag{I-21}$$

$$R_i = k_{f,w} - k_{b,w} [H^+][OH^-] \tag{I-22}$$

Equation (I-18) was applied for each species i in the system (i.e. H^+, OH^-, Na^+, ClO_4^-). The electric potential (φ) in the solution appearing in the electromigration term can be calculated so that the electroneutrality constraint is satisfied:

$$\sum_i z_i C_i = 0 \tag{I-23}$$

The second order differential transport equations (such as Equation (I-18)) requires two sets of boundary conditions. The boundary condition at the bulk solution is a known and constant concentration of the chemical species. Also, the potential at the bulk is considered to be a constant arbitrary number (zero) serving merely as a reference value.

At the electrode/solution interface, the boundary conditions are dictated by the fluxes of species due to the electrochemical reactions, which are defined by the reaction mechanism. The flux at the electrode surface for an electroactive species i is defined as:

$$N_i = -\sum_j s_{ij} v_j \tag{I-24}$$

This equation assumes that species i can be involved in j electrochemical reactions at the surface. In the system considered here, the only electroactive species is the hydrogen ion, where the reaction rates for this species are described by Equation (I-5) and Equation (I-6).

The surface flux of non-electroactive species is zero:

$$N_i = 0 \tag{I-25}$$

Finally, the surface coverage of the adsorbed hydrogen atoms (θ) appearing in the electrochemical reaction rates needs to be accounted for. The surface coverage can be

calculated by mass conservation using the rate expressions, assuming a steady state

condition:

$$\frac{d\theta_A}{dt} = v_V - v_{H,A} - v_D = 0$$

(I-26

)

$$\frac{d\theta_B}{dt} = v_D - v_{H,B} - 2v_T = 0$$

(I-27

)

All the governing equations and boundary conditions implemented in the model

are summarized in Table I-3. These equations form a set of seven nonlinear, coupled,

differential equations which were solved to obtain the values of the seven unknowns: four

aqueous concentrations for H^+, OH^-, Na^+ and ClO_4^- ions, potential inside the diffusion

layer, and the surface coverage by the adsorbed hydrogen atoms at sites A and B.

Table I-3. Summary of equations used in the mathematical model.

Electrode surface boundary

$$N_i = -\sum_j s_{ij} v_j \qquad\qquad electro\ active\ species$$

$$N_i = 0 \qquad\qquad non-electro\ active\ species$$

$$\sum_i z_i C_i = 0$$

$$\frac{d\theta_A}{dt} = v_V - v_{H,A} - v_D = 0$$

$$\frac{d\theta_B}{dt} = v_D - v_{H,B} - 2v_T = 0$$

Diffusion layer

$$-D_i \frac{\partial}{\partial x}\frac{\partial C_i}{\partial x} - \frac{\partial}{\partial x}\left(\frac{z_i D_i F C_i}{RT}\frac{\partial \Phi}{\partial x}\right) + v_x \frac{\partial C_i}{\partial x} = 0 \qquad\qquad all\ species$$

$$\sum_i z_i C_i = 0$$

Bulk boundary conditions

$$C_i = C_i^b \qquad\qquad all\ species$$

$$\Phi = 0$$

I.5:Model verification

The simulations of the current potential behavior for the present system were done with the following assumptions:

- The desorption of $H_{ads,A}$ due to Tafel reaction was negligible.

- Both $H_{ads,A}$ and $H_{ads,B}$ were involved in Heyrovsky reaction.

- The effect of $H_{ads,B}$ interaction ($u\theta_B$) was assumed to be negligible considering $\theta_B \to 0$.

The symmetry factors (β and λ) were taken to be 0.5 and the reaction rate constants of the elementary steps, K, and u were used as adjustable parameters. The following set of parameters resulted in the best fit of the model by simultaneously

considering the experimental polarization curves at all pH values: $K = 3.3 \times 10^{-7} \ M^{-1}$,

$u = 2.3, \ k_{f,V} = 4 \times 10^{-6} \ (^m/_s), k_{f,H} = 1.2 \times 10^{-10} \ \left(\frac{m^3}{mol.s}\right), k_{f,T} = 2.5 \times$

$10^{-2} \ \left(\frac{m^2}{mol.s}\right), \ k_{f,D} = 3.5 \times 10^{-6} \ \left(\frac{m^2}{mol.s}\right).$

Figure I-7 shows the comparison of the simulated results with the experimental

data. The simulated voltammograms showed a very good agreement with experimental

results over the lower Tafel slope range, while the transition to the higher Tafel slope of

~120 mV was also predicted reasonably well. The apparent reaction order of 0.81

observed at -0.41 V (vs. SHE) in Figure I-7 also agreed well with the experimental data

as reported in Figure I-2.
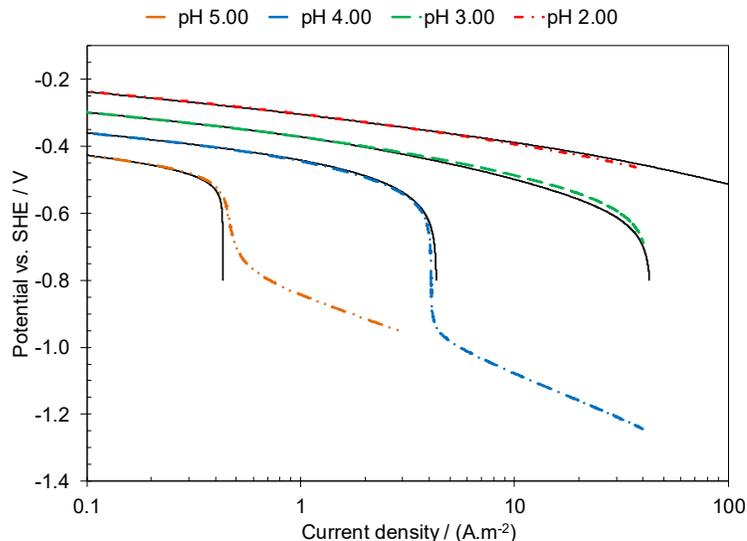
Figure I-7. Comparison of the linear sweep voltammograms obtained experimentally and the results
from the model based on surface diffusion rate determining step at 2000 rpm, 30ºC and 0.1 M NaClO₄.

The calculated change of H_{ads} coverage during polarization for both sites A and B

are demonstrated in Figure I-8 for pH 2. These results were also found to agree well with

what was suggested by the parametric study. As shown in Figure I-8, the coverage at B

(desorption) sites was negligibly small throughout the whole current density range. On

the other hand, the coverage at A (adsorption) sites was low in the ~60 mV Tafel slope

range, while at higher current densities the surface was almost fully covered with $H_{ads,A}$.

The plateau at the high surface coverage range coincides with the change of the

mechanism from surface diffusion controlled to Volmer-Heyrovsky control at high

cathodic current densities resulting in the observed ~120 mV Tafel slope (Figure I-3 and

Figure I-4).
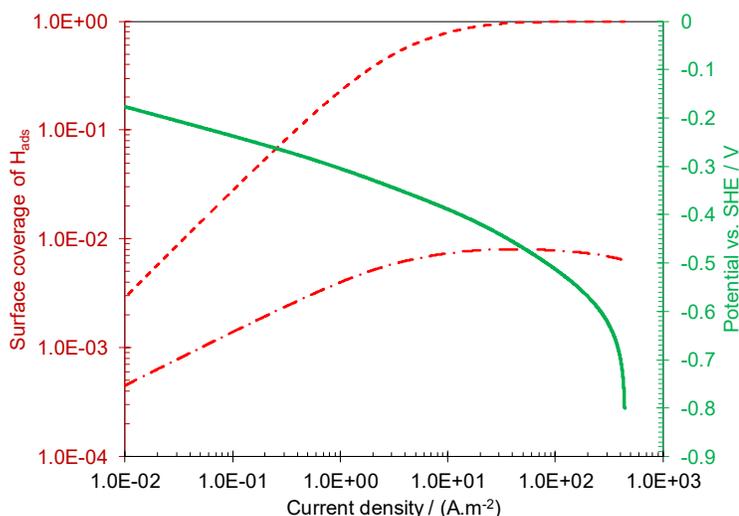
Figure I-8. The calculated surface coverage of $H_{ads,A}$ (dashed red line on the primary vertical axis), $H_{ads,B}$ (dotted-dashed red line on the primary vertical axis), and polarization curve (solid green line on the secondary vertical axis) considering surface diffusion rate determining step at pH 2, 2000 rpm, 30°C and 0.1 M NaClO$_4$.

The contribution of each reaction route to the net current density is demonstrated

in Figure I-9. This graph suggests that the Volmer-Heyrovsky route does not have any

significant contribution at low current densities and it becomes significant only at high

current densities and low pH values. The predicted results at pH 0 suggest that in a more

acidic environment a mixed controlled mechanism may be observed. Considering the

Tafel slope (~40 mV) and reaction order of 2 for the Heyrovsky reaction at such surface

conditions (Figure I-4), one can expect to observe a slight decrease in Tafel slope and

increase in reaction order when compared to higher pH values.
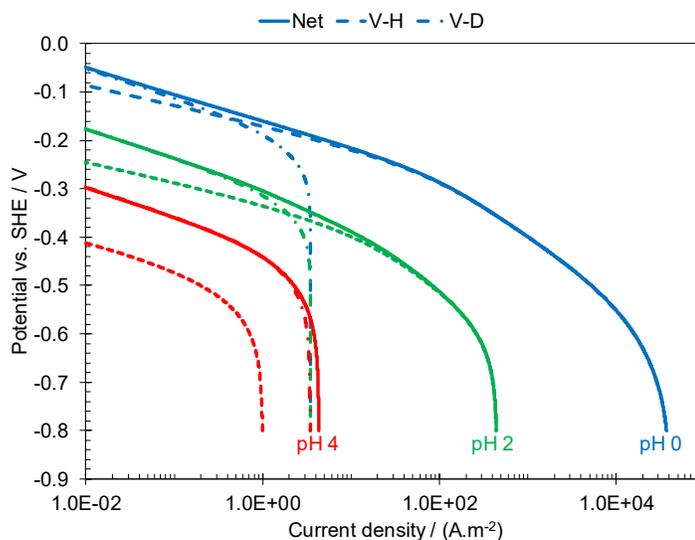
Figure I-9. Current densities corresponding to each reaction pathway based on surface diffusion rate determining step. Solid lines are the net currents, dashed lines represent the contribution of the Volmer-Heyrovsky route and dotted dash line represents the contribution of the surface diffusion route (followed by Tafel desorption step) at pH 4 (red), pH 2 (green), and pH 0 (blue).

I.6:Summary

The mechanism and the kinetics of the HER was studied in acidic perchlorate

solutions with an extended pH range up to pH 5. The existing mechanisms were

reevaluated and shown to be inadequate in explaining the steady state polarization

behavior of the hydrogen evolution reaction over extended cathodic potential range and a

broad range of acidic pH values.

The experimental data obtained in the present study for hydrogen evolution on gold in mild perchloric acid solutions showed two distinctive Tafel slopes of 68±5 mV and 120±2 mV at lower and higher current densities, respectively. At the experimental conditions of the present work, the higher Tafel slope was only observed at pH values below 3. At the same time, the apparent reaction order of the HER in the pH range from 2 to 5, was found to be approximately 0.8.

The plausible mechanisms based on the conventional Volmer, Tafel, and Heyrovsky elementary steps, as well as the mechanisms including a surface diffusion step, were analyzed *via* a parametric study of the kinetic parameters. The results suggests that the polarization behavior of HER on gold over an extended pH range was explained best when a surface diffusion step preceding the Tafel recombination reaction was considered, along with the previously known elementary steps. This diffusion step was further discussed and found to be in agreement with the atomistic level studies on adsorption and dissociation of hydrogen gas on gold surfaces.

The proposed mechanism suggests that at low current densities, the rate of the HER was limited by the surface diffusion of $H_{ads,}$ regardless of the solution pH. At higher current densities and in more acidic solutions, where a 120 mV Tafel slopes were observed, the rate limiting step was the slow electrochemical desorption reaction (Heyrovsky step). This proposed mechanism was incorporated into a comprehensive mathematical model. The simulated polarization curves showed a reasonable agreement with both the lower and the higher Tafel slopes as well as the apparent reaction order, further supporting the proposed mechanism.

Nomenclature

β_j	Electrochemical symmetry factor of reaction j
b	Tafel slope (mV)
C_i	Concentration of species i (mol.m^{-3})
C_F	Faradic capacitance (F.m^{-2})
D_i	Diffusion coefficient of species i (m^2.s^{-1})
δ	Diffusion layer thickness of RDE
E	Applied potential (V)
ξ_i	Dimensionless concentration of species i
F	Faraday's constant (C.mol^{-1})
ϕ	Potential in the electrolyte (V)
Φ	Dimensionless potential in the electrolyte
i	Current density (A.m^{-2})
K	Equilibrium constant of the Volmer reaction (M^{-1})
$k_{f,j}$	Forward reaction rate constant of reaction j
$k_{b,j}$	backward reaction rate constant of reaction j
λ_j	Symmetry factor of reaction j due to interaction of adsorbed species
N_i	Flux of species i (mol.m^{-2}.s)
v	Kinematic viscosity (m^2.s^{-1})
Ω	Rotation speed (rad.s^{-1})
$p_{(H^+)}$	Reaction order with respect to H$^+$ concentration
q	Charge required for surface coverage of θ (C.m^{-2})
q_{max}	Charge required for $\theta = 1$ (C.m^{-2})
R	Universal gas constant (J.mol^{-1}.K^{-1})
R_i	Rate of homogeneous reaction i (mol.s^{-1}.m^{-3})
s$_{ij}$	Stoichiometric coefficient of species i in reaction j
Ψ	Dimensionless applied potential
T	Absolute temperature (K)
t	Time (s)
θ	Surface coverage of H$_{ads}$
u	Correlation coefficient of H$_{ads}$ interaction energy, defined as $u = \frac{(\partial \Delta G^o_{ads} / \partial \theta)}{RT}$ where $\partial \Delta G^o_{ads}$ is the standard Gibbs free energy of adsorption.
U_i	Mobility of species i (m.s^{-1})
v_j	Reaction rate of reaction j (mol.m^{-2}.s^{-1})
v	Velocity (m.s^{-1})
x	Spatial dimension (m)
z_i	Charge of species i
ζ	Dimensionless spatial dimension

II.   A micro-kinetic investigation of hydrogen evolution from multiple proton donors: the case on gold in mildly acidic solutions containing acetic acid

II.1: Background

The investigation of the mechanism and the kinetics of the hydrogen evolution reaction (HER) at the conditions particular to metallic corrosion in acidic media is perhaps amongst the more challenging and least discussed scenarios involving this reaction. In the context of metallic corrosion in acidic aqueous environments, the hydrogen evolution reaction can be considered as a family of cathodic reactions with molecular hydrogen as their final product. These reactions serve as the electron sink required for the spontaneous anodic metal dissolution reaction, and are commonly assumed to include the reduction of hydrogen ion, as well as reduction of other weak acids such as carboxylic acids, carbonic acid, and hydrogen sulfide [43,47,55].

The conditions commonly encountered in industrial applications, as well as academic research in this field of study, do not present an ideal setting for a detailed mechanistic investigation of the HER. The reason is the complexity arising from: mixed kinetic control due to low acidity of the studied solution (charge vs. mass transfer), changing electrode substrate due to corrosion, and the presence of multiple proton donors. The present study is focused on the mechanistic implications of the HER from multiple proton donors due to the presence of a weak acid in the solution (aqueous acetic acid in the present study).

Acetic acid (HAc as shorthand for CH_3COOH) being a weak carboxylic acid, is only partially dissociated in an aqueous acidic solution. Therefore, both the undissociated

and dissociated forms are present, while their relative concentration is defined by the dissociation equilibrium. Hence, the HER could possibly occur both from reduction of the hydrogen ion (which is the product of acetic acid dissociation) and the direct reduction of the undissociated acetic acid itself.

The hydrogen evolution reaction is conventionally described for the case of hydrogen ion by the set of three elementary reaction steps known as the Volmer step, the Heyrovsky step, and the Tafel step. The mechanism of the HER from weak acids such as water (H_2O), carboxylic acids, carbonic acid (H_2CO_3), and hydrogen sulfide (H_2S) are also described by using analogous elementary steps. Using a generic formulation, these elementary steps can be expressed through Reactions (II-1) to (II-3), where HA represents the proton donor (such as H^+, H_2O, HAc, H_2CO_3, H_2S , etc.) and A^- represents the corresponding conjugate base. Note that, in order to limit the present discussion to cathodic reactions, the reverse – hydrogen oxidation reaction was assumed to be insignificant.

$$HA + e^- \rightleftharpoons H_{ads} + A^- \tag{II-1}$$

$$HA + H_{ads} + e^- \rightarrow H_2 + A^- \tag{II-2}$$

$$2H_{ads} \rightarrow H_2 \tag{II-3}$$

The overall HER mechanism can be seen as a combination of these elementary steps, while other alternative elementary steps have also been proposed [61,109,112]. The mechanism of the HER is commonly discussed in terms of the characteristic kinetic parameters such as Tafel slopes and reaction orders [110,117,127–129]. These parameters are experimentally obtained by measuring the change in the current as a function of potential

(for Tafel slope) and a function of pH or other species in solution (for reaction order).

The mechanism of the HER at various conditions is determined by identifying a reaction

sequence where theoretical kinetic parameters match the experimental values best. The

theoretic kinetic parameters are usually determined based on simplified kinetic rate

expressions, at certain limiting conditions[109,117,118]. However, the simplifying assumptions

allowing for such mathematical derivations greatly limits their range of validity.

Additionally, the resulting relationships do not provide any insight for the case of mixed

kinetics (multiple reaction pathways) or the case of the transition from one rate

determining step to another. In order to determine the reaction mechanism at these

conditions, or for even more elaborate scenarios, such as hydrogen evolution from

multiple proton donors used in the present study, the application of comprehensive

micro-kinetic mathematical models[319] is essential as they do not rely on the simplifying

assumptions. These comprehensive models are developed based on fundamental

physiochemical laws (e.g. reaction kinetics, mass conservation, and charge conservation)

and are able to simultaneously account for all plausible reaction mechanisms by including

all the elementary steps and allowing for their interaction[61]. The mechanistic scenarios

covered by these models are, of course, bound to the presumed elementary steps and the

rate expressions used in their development.

The HER on gold in mildly acidic $HClO_4$ solutions was previously shown to

follow the following set of elementary steps [61]:

$$H^+ + e^- \rightleftharpoons H_{ads,A} \qquad\qquad\qquad (\text{II-4})$$

$$H_{ads,A} \longrightarrow H_{ads,B} \qquad\qquad\qquad (\text{II-5})$$

$$H_{ads,A\ or\ B} + H^+ + e^- \rightarrow H_2 \qquad\qquad (\text{II-6})$$

$$2\ H_{ads,B} \rightarrow H_2 \qquad\qquad (\text{II-7})$$
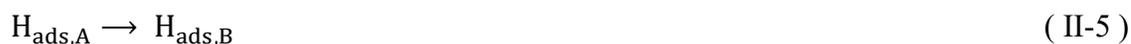
Compared to the set of generic reactions (II-1) to (II-3) the additional Reaction (II-5) represents the surface diffusion step, which may be limiting the overall rate of the Tafel step. Here, A and B represent two distinct reaction sites on the gold surface. Additionally, as suggested by Reaction (II-6), the Heyrovsky reaction may occur at either sites A or B. The rate of each elementary step (Reaction (II-4) to Reaction (II-6)) can be expressed via Equations (II-8) through (II-11) [61].

$$v_{V,H^+} = k_{f,V,H^+}(1-\theta_A)C_{H^+}e^{-\lambda_V u\theta_A}e^{-\beta_V \frac{FE}{RT}} - k_{b,V,H^+}\,\theta_A e^{(1-\lambda_V)u\theta_A}e^{(1-\beta_V)\frac{FE}{RT}} \quad (\text{II-8})$$

$$v_{H,H^+} = k_{f,H,H^+}C_{H^+}\theta_{A\ and\ B}\,e^{(1-\lambda_H)u\theta_{A\ and\ B}}e^{-\beta_H\frac{FE}{RT}} \qquad\qquad (\text{II-9})$$

$$v_T = k_{f,T}\theta_B{}^2 e^{2(1-\lambda_T)u\theta} \qquad\qquad (\text{II-10})$$

$$v_D = k_{f,D}\theta_A e^{(1-\lambda_D)u\theta} \qquad\qquad (\text{II-11})$$

In the equations above, the symbol k stands for the reaction rate constant, θ is the surface coverage by adsorbed hydrogen atoms (H_{ads}) at sites A or B. The first exponential terms describes the effect of interaction between H_{ads} on the surface where u is the correlation coefficient of the change in Gibbs free energy of adsorption , and whenever present, the second exponential term accounts for the effect of potential.

In the presence of acetic acid, two additional elementary steps are plausible and should be included in order to account for the HER by direct reduction of acetic acid: a Volmer type electro-adsorption of H_{ads} from acetic acid as shown by Reaction (II-12), and a Heyrovsky type electro-desorption as shown by Reaction (II-13). The surface

diffusion step (Reaction (II-11)) and the Tafel desorption step (Reaction (II-10)) are

not directly affected by the presence of acetic acid and remain unchanged.

$$HAc + e^- \rightleftharpoons H_{ads,A} + Ac^-$$ (II-12)

$$H_{ads,A\ or\ B} + HAc + e^- \longrightarrow H_2 + Ac^-$$ (II-13)

The rates of Reactions (II-12) and (II-13) can be expressed via Equations (

II-14) and (II-15), respectively.

$$v_{V,HAc} = k_{f,V,HAc}(1 - \theta_A)C_{HAc}e^{-\lambda_V u\theta_A}e^{-\beta_V \frac{FE}{RT}}$$ (II-14)

$$- k_{b,V,HAc}\,\theta_A C_{Ac^-}e^{(1-\lambda_V)u\theta_A}e^{(1-\beta_V)\frac{FE}{RT}}$$

$$v_{H,HAc} = k_{f,H,HAc}C_{HAc}\theta_{A\ and\ B}e^{(1-\lambda_H)u\theta_{A\ and\ B}}e^{-\beta_H\frac{FE}{RT}}$$ (II-15)

The reaction rate expressions defined above serve as the basis of the discussion in

the following sections and are able to describe various mechanistic scenarios depending

on the values of the physiochemical constants such as reaction rate constant k, correlation

coefficient u, and transfer coefficients β and λ. Besides that, the concentration of the

electroactive species at the surface, appearing in these rate expressions, needs to be

properly specified in order to account for the effect of homogeneous chemical equilibria

and the mass transfer from the bulk. This can be achieved by coupling the

abovementioned reaction rate expressions with the mass conservation equation (Nernst-

Planck equation) for the boundary layer, as described in more details in the following

section. The resulting mathematical description of the system would allow developing a

comprehensive picture of the underlying reaction mechanisms.

II.2: Materials and methods

II.2.1: Experimental procedure

The experiments were conducted in a three electrode, 1 L glass cell with a silver/silver chloride reference electrode, similar to that described in an earlier publication [61]. The supporting electrolyte was 0.1 M solution of research grade sodium chloride in deionized water in all experiments. The targeted solution composition was achieved by addition of the desired amount of glacial acetic acid and further adjusting the solution pH using small amounts of HCl or NaOH solutions. The solution was then de-aerated using nitrogen gas for minimum of 90 min while the oxygen content of the outlet gas was monitored (Orbisphere 410). The maximum allowed dissolved oxygen content before introducing the working electrode into the solution was 1 ppb_m. The solution temperature was maintained at 30 ± 0.1 $^{\circ}$C, using a hot plate.

The polycrystalline gold rotating disc electrode (Pine Instruments) was polished, rinsed, sonicated, and further electrochemically treated following the procedure described in an earlier publication [61]. The polarization curves were obtained using staircase voltammetry with the scan rate of 0.1 mV.s^{-1} and a sampling period of 1 s^{-1}. The reported results were corrected for Ohmic drop using the solution resistance obtained from electrochemical impedance spectroscopy (EIS) measurements, performed after polarization measurements. The EIS measurements were conducted at the OCP with an AC potential perturbation of ±5 mV, in the frequency range of 0.2 Hz to 5 kHz. The experimental conditions are summarized in Table II-1.

Table II-1. Summary of the experimental conditions.

Test apparatus	Rotating disk electrode (RDE) Three electrode glass cell
Electrode material	99.99 wt.% Polycrystalline gold
Rotation rate	2000 RPM
Supporting electrolyte	0.1 M NaCl
Solution Volume	1 L
Temperature	30°C
pH	2.0, 3.0, 4.0, 5.0
Total acetic acid concentration	0.00 mM 1.66 mM (100 ppm$_m$) 8.30 mM (500 ppm$_m$)

II.2.2: Mathematical modeling

II.2.2.1: Water chemistry

The solution speciation was obtained considering the chemical equilibria of the involved homogeneous reactions [43,60]. In an aqueous solutions containing acetic acid the two homogeneous reactions are the acetic acid dissociation shown via Reaction (II-16), and water dissociation shown via Reaction (II-17).
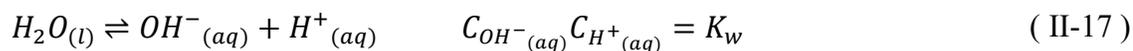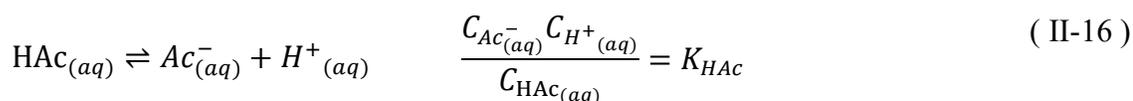
$$HAc_{(aq)} \rightleftharpoons Ac^-_{(aq)} + H^+_{(aq)} \qquad \frac{C_{Ac^-_{(aq)}} C_{H^+_{(aq)}}}{C_{HAc_{(aq)}}} = K_{HAc} \qquad \text{(II-16)}$$

$$H_2O_{(l)} \rightleftharpoons OH^-_{(aq)} + H^+_{(aq)} \qquad C_{OH^-_{(aq)}} C_{H^+_{(aq)}} = K_w \qquad \text{(II-17)}$$

The chemical equilibria corresponding to acetic acid and water dissociation can be mathematically expressed as Equation (II-16) and Equation (II-17), respectively, with the equilibrium constants listed in Table II-2. The exact speciation was obtained for a known pH value and NaCl concentration by simultaneous solution of Equations (II-16

) and (II-17), taking into account the mass balance of acetate (Equation (II-18)), and electroneutrality of the solution (Equation (II-19)).

$$C_{t,HAc} = C_{HAc} + C_{Ac^-} \qquad\qquad\text{(II-18)}$$

$$\sum_i z_i C_i = 0 \qquad\qquad\text{(II-19)}$$

Equation (II-18) relates the amount of acetic acid initially added into the solution ($C_{t,HAc}$), to the resulting equilibrium undissociated acetic acid (C_{HAc}) and acetate ion (C_{Ac^-}) concentrations, via a mass balance. In a solution without an externally induced electric field, the concentration of charged species must also satisfy the electroneutrality constraint as shown by Equation (II-19). Using the these equations, the concentration of the six chemical species ($H^+_{(aq)}$, $HAc_{(aq)}$, $Ac^-_{(aq)}$, $OH^-_{(aq)}$, $Na^+_{(aq)}$, $Cl^-_{(aq)}$) present in the solution can be obtained.

Table II-2. Equilibrium and reaction rate constants where $K=k_f/k_b$.

Reaction rate constant	Reference
$K_{HAc} = 10^{\left(-\frac{1500.65}{T} - 6.50923 \times log(T) - 0.0076792 \times T + 18.67257\right)}$ (M)	[63]
$K_w = (10^{-3}\rho_w)^2 \, 10^{-\left(a1+\frac{a2}{T}+\frac{a3}{T^2}+\frac{a4}{T^3}+\left(a5+\frac{a6}{T}+\frac{a7}{T^2}\right)log(10^{-3}\rho_w)\right)}$ (M ^{2}) a_1= -4.098, a_2= -3245.2, a_3= 2.2362, a_4= -3984E7, a_5= 13.957, a_6= -1262.3, a_7= 8.5641E5	[64]
$k_{f,HAc} = 8.7 \times 10^5$ (1/s)	[65]
$k_{b,w} = 1.4 \times 10^{11}$ (1/M.s)	[66,67]

An example of the solution speciation is shown in Figure II-1, where the calculated ratio of $C_{HAc}/C_{t,HAc}$ is shown at various pH values and two temperatures, 30°C and 60°C. It should be noted that, at a constant temperature the ratio $C_{HAc}/C_{t,HAc}$ is only a

function of solution pH, for example at 30°C, at pH 4 $C_{HAc}/C_{t,HAc}=0.8510$ and at pH 5 $C_{HAc}/C_{t,HAc}=0.3636$.
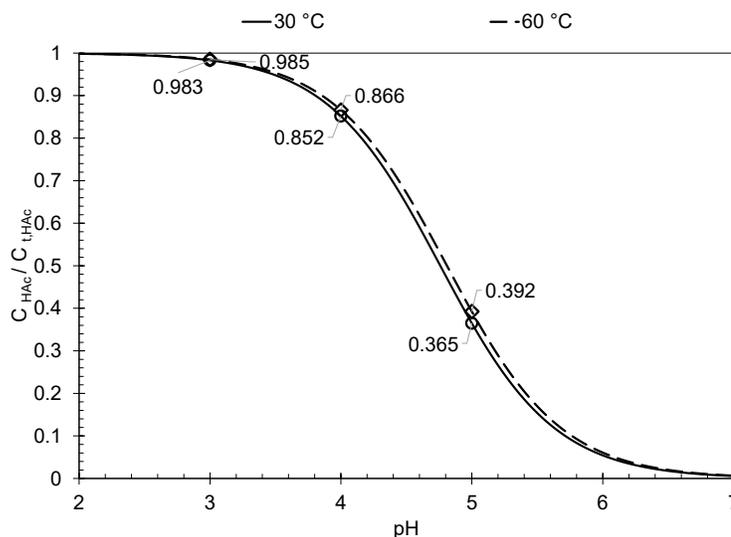
Figure II-1. Calculated ratio of undissociated acetic acid (C_{HAc}) to total acetate ($C_{t,HAc}$) concentration at various pH values.

II.2.2.2: Electrochemical Model

A comprehensive mathematical model[43,60] of the electrochemical reactions, including the effect of mass transfer and homogeneous chemical reactions was developed, similar to that described in more details elsewhere [61].

The governing rate expressions for the electrochemical reactions are presented above. In order to obtain the current/potential response of the system, one needs to know the concentration of the electroactive species at the metal surface. This can be achieved by solving the mass conservation equation (Nernst-Planck equation) for the boundary layer, as described below.

The mass conservation equations applied for the diffusion layer domain, stretching from the electrode surface to the bulk solution, are mathematically expressed through the well-known Nernst-Planck equation (Equation (II-20)), alongside with the electroneutrality constraint (Equation (II-21)):

$$\frac{\partial C_i}{\partial t} = -\nabla . N_i + R_i \qquad \text{(II-20)}$$

$$\sum_i z_i C_i = 0 \qquad \text{(II-21)}$$

The R_i term in Equation (II-20) reflects the effect of homogeneous chemical reactions such as acetic acid and water dissociation, while the flux of any given species i (N_i) is described through Equation (II-22) [68].

$$N_i = -z_i u_i F C_i \nabla \phi - D_i \nabla C_i + v C_i \qquad \text{(II-22)}$$

For a one-dimensional semi-infinite geometry in the direction x normal to the metal surface, Equation (II-20) and Equation (II-22) can be simplified to Equation (II-23) and Equation (II-24) respectively, assuming a steady state and an infinitely diluted solution.

$$N_i = -D_i \frac{\partial C_i}{\partial x} - \frac{z_i D_i F C_i}{RT} \frac{\partial \phi}{\partial x} + v_x C_i \qquad \text{(II-23)}$$

$$\frac{\partial C_i}{\partial t} = 0 = D_i \frac{\partial}{\partial x} \frac{\partial C_i}{\partial x} + \frac{\partial}{\partial x} \left(\frac{z_i D_i F C_i}{RT} \frac{\partial \phi}{\partial x} \right) - v_x \frac{\partial C_i}{\partial x} + R_i \qquad \text{(II-24)}$$

The first term in equation (II-23) describes the molecular diffusion, with diffusion coefficients listed in Table II-3, and the second term accounts for the electromigration of charged species. The effect of convective flow in the direction normal to the surface is accounted for by the convective flow term $v_x C$, where v_x is the normal

velocity component at some distance away from the metal surface. For the laminar flow regime of the rotating disk electrode, the velocity profile and the diffusion layer thickness are obtained via Equation (II-25) where $a = 0.510$, and Equation (II-26), respectively [69].

$$v_x = -a\Omega \left(\frac{\Omega}{v}\right)^{1/2} x^2 \qquad\qquad\text{(II-25)}$$

$$\delta = \left(\frac{3D_{lim}}{av}\right)^{1/3} \left(\frac{\Omega}{v}\right)^{-1/2} \qquad\qquad\text{(II-26)}$$

The rate of production/consumption of a species i due to homogenous chemical reactions (R_i in Equation (II-24)) can be expressed in a matrix format, as Equation (II-27). The kinetic rate constant of the chemical reactions in Equation (II-27) can be found in Table II-4.

$$\begin{bmatrix} R_{H^+_{(aq)}} \\ R_{HAc_{(aq)}} \\ R_{Ac^-_{(aq)}} \\ R_{OH^-_{aq}} \end{bmatrix} = \begin{bmatrix} 1 & 1 \\ -1 & 0 \\ 1 & 0 \\ 0 & 1 \end{bmatrix} \times \begin{bmatrix} k_{f,HAc}\, C_{HAc} - k_{b,HAc}\, C_{Ac^-} C_{H^+} \\ k_{f,w} - k_{b,w}\, C_{OH^-} C_{H^+} \end{bmatrix} \qquad\text{(II-27)}$$

Table II-3. Reference diffusion coefficients at 25 °C.

Species	Diffusion coefficient $\times 10^9$ (m²/s)	Reference
HAc	1.29	[70]
Ac^-	1.089	[70]
H^+	9.312	[68]
OH^-	5.273	[70]
Na^+	1.334	[68]
Cl^-	2.032	[68,70]

Boundary conditions

At the bulk solution ($x=\delta$) the concentrations of chemical species are constant, known values, dictated by the chemical equilibria of the solution. The boundary condition at the metal/solution interface ($x=0$) are fluxes defined by the rate of electrochemical reactions. For an electroactive chemical species, the flux at the metal/solution boundary is equal to the superposition of corresponding electrochemical reaction rates. Therefore, for species i involved in j electrochemical reactions, the flux at the metal surface can be described through Equation (II-28).

$$N_i|_{x=0} = -\sum_j s_{ij} v_j$$

(II-28)

For non-electroactive species, the flux at the metal surface as a non-porous barrier is zero:

$$N_i|_{x=0} = 0$$

(II-29)

Equation (II-28) and Equation (II-29) can be applied to describe the flux of all chemical species at the metal surface. The electric potential in the solution at the boundary may also be calculated with the aid of the electro-neutrality constraint (Equation (II-21)).

The surface coverage of the adsorbed hydrogen atoms (θ) appearing in the electrochemical reaction rates (Equations (II-8) to (II-11), (II-14), and (II-15)) needs to be properly specified as well. This can be expressed in terms of mass conservation of adsorbed hydrogen atoms, assuming a steady state condition:

$$\frac{d\theta_A}{dt} = v_{V,H^+} + v_{V,HAc} - v_{H,A,H^+} - v_{H,A,HAc} - v_D = 0$$

(II-30)

$$\frac{d\theta_B}{dt} = v_D - v_{H,B,H^+} - v_{H,B,HAc} - 2v_T = 0 \qquad \text{(II-31)}$$

With the governing equations, and the boundary conditions discussed above, the system is fully specified and may be solved to obtain the values of the nine unknowns: six aqueous concentrations for H^+, OH^-, HAc, Ac^-, Na^+ and Cl^- ions, electric potential inside the diffusion layer, and the surface coverage by the adsorbed hydrogen atoms at sites A and B. Table II-4 summarizes all the relevant mathematical relationships required to develop a comprehensive mathematical model as discussed above.

Table II-4. Summary of equations used in the mathematical model.

Electrode surface boundary conditions	
$N_i\|_{x=0} = -\sum_j s_{ij} v_j$	for electroactive species
$N_i\|_{x=0} = 0$	for non-electroactive species
$\sum_i z_i C_i = 0$	
$v_{V,H^+} + v_{V,HAc} - v_{H,A,H^+} - v_{H,A,HAc} - v_D = 0$	
$v_D - v_{H,B,H^+} - v_{H,B,HAc} - 2v_T = 0$	
Diffusion layer	
$\frac{\partial C_i}{\partial t} = D_i \frac{\partial}{\partial x}\frac{\partial C_i}{\partial x} + \frac{\partial}{\partial x}\left(\frac{z_i D_i F C_i}{RT}\frac{\partial \phi}{\partial x}\right) - v_x \frac{\partial C_i}{\partial x} + R_i = 0$	for all species
$\sum_i z_i C_i = 0$	
Bulk boundary conditions	
$C_i = C_i^b$	for all species
$\Phi = 0$	arbitrary reference potential

II.2.2.3: Numerical solution

The mathematical equations as summarized in Table II-4, form a set of non-linear, coupled, partial differential equations to be solved numerically. Considering the simple one-dimensional geometry, the finite difference method can be used to solve these equations. This method is commonplace in mathematical modeling of electrochemical systems with similar geometry and have been discussed in detail elsewhere [68,247].

The partial differential equations were discretized using second order Taylor's series approximations, resulting in a set of algebraic equations. These equations can further be recast in the form as a sparsely populated coefficient matrix with most of the non-zero terms along the three main diagonals. The final numerical solution can then be obtained through number of solution algorithms, such as Newman's "Band-J" open source code where the coefficient matrix is developed and solved by LU decomposition method [68]. The presence of nonlinear terms, such as in the electromigration or chemical reactions terms, means that some of the elements in the coefficient matrix include unknown parameters. In the approach used in the present model, the solution of the set of equations is obtained iteratively by using an initial guess for the unknown elements of the coefficient matrix (usually the last calculated values) and reiterating until the desired accuracy is achieved ($R^2=10^{-12}$).

II.3: Results and discussion

II.3.1: HER from hydrogen ion

The steady state voltammograms obtained in 0.1 M sodium chloride acidic solutions at various pH values are shown in Figure II-2. The cathodic polarization curves

showed a similar general behavior, with currents initially increasing linearly up to the limiting current density, associated with the charge transfer controlled hydrogen evolution from hydrogen ion. This is followed by the mass transfer limiting current at more negative potentials, and finally another linear increase of the cathodic currents, as a result of hydrogen evolution from water. The reported current densities in Figure II-2 are limited to ~50 A.m^{-2}; a practical limit that was imposed to avoid any interference caused by the blockage effect resulting from accumulation of the evolved hydrogen gas bubbles. This practical limit is influenced by experimental conditions, including the electrode rotation speed and polarization scan rate.
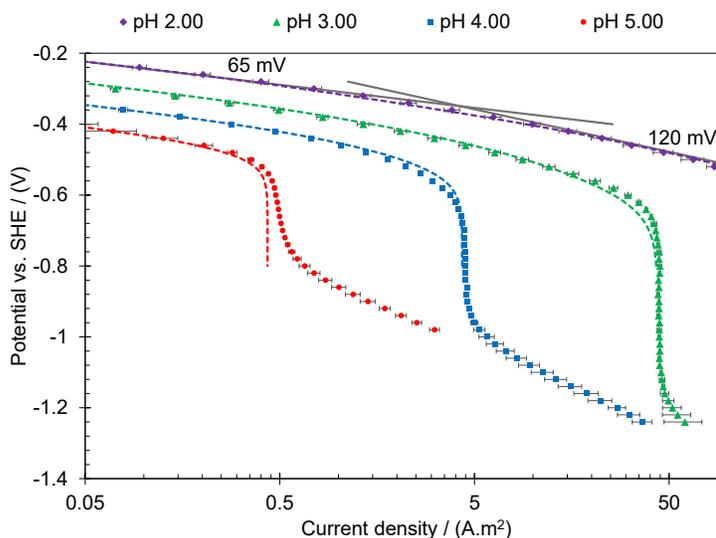
Figure II-2. Cathodic steady state voltammograms obtained in 0.1 M NaCl solution, at 30°C, 2000 rpm, and pH values from 2 to 5 on polycrystalline gold surface.

The polarization behavior associated with the hydrogen evolution reaction from hydrogen ion was found to closely resemble that previously reported in perchlorate solutions [61], where a Tafel slope of ~65 mV was observed at lower current densities and

~120 mV at higher current densities. Similarly, in the pH range from 2 to 5, the apparent

reaction order vs. H^+ at the lower current density range was found to be slightly below 1

(~0.95) as it seen in Figure II-2. The similar electrochemical behavior obtained in sodium

chloride and sodium perchlorate solutions[61], suggest that the mechanism of the HER was

not affected by addition of 0.1 M chloride ions. Therefore, the same reaction mechanism

was used to develop the mathematical model discussed in previous sections.

The kinetic parameters for elementary HER reactions from hydrogen ions in 0.1

M NaCl solution were obtained by fitting the mathematical model predictions to the

experimental data, shown in Figure II-2. The following simplifying assumptions were

used in the model:

- the interaction coefficient (u) is the same at both adsorption/desorption sites A
  and B;

- the effect of $H_{ads,B}$ interaction ($u\theta_B$) was assumed to be negligible considering
  $\theta_B \rightarrow 0$;

- all symmetry factors (β and λ) were assumed to be 0.5.

Different features of the steady state voltammograms were used to obtain the

relevant physiochemical constants. The current density at which the shift in Tafel slope

from 65 mV to 120 mV occurs is solely defined by the rate of the surface diffusion step,

which was used to estimate $k_{f,D}=2.0\times10^{-5}(m^2.mol^{-1}.s^{-1})$. With the known rate constant of

the surface diffusion step, the current density at 65 mV Tafel slope range was used to

obtain the equilibrium parameters for the Volmer step. It is of significance to note that,

when the rate of forward and backward partials of the Volmer reaction is significantly

faster than the following desorption steps, the Volmer reaction reaches a quasi-equilibrium state. At such conditions the steady sate voltammograms do not carry any explicit information with regards to the kinetics of the Volmer reaction – preceding the rate determining desorption step. Nevertheless, the kinetics of the proceeding surface diffusion (rate determining) step is proportional to the magnitude of surface coverage of adsorbed hydrogen atoms (θ), which is defined by the equilibrium of the Volmer reaction as expressed by Equation (II-32). This criteria can be used to estimate the constants defining that equilibrium: $K_v=k_{f,v}/k_{b,v}= 5.0\times10^{-7}(mol.\ m^{-3})$ and $u=3.3$.

$$\frac{\theta}{1-\theta}e^{u\theta} = K_v C_{H^+} e^{\frac{-FE}{RT}} \qquad (\text{ II-32 })$$

In addition, the minimum value of $k_{f,V}= 8.0\times10^{-6}\ (m.s^{-1})$ can be estimated based on the constraint that Volmer reaction is not rate limiting in the experimental conditions considered here. These values of K_v and $k_{f,V}$ were used to obtain $k_{b,v}=k_{f,v}/K_v$.

The ~120 mV Tafel slope range was used to determine the reaction rate constant of the Heyrovsky step ($k_{H,f}=7.0\times10^{-10}(m^3.mol^{-1}.s^{-1})$), considering the known values of θ from the previous steps. Additionally, the minimum value of the reaction rate constant for the subsequent Tafel step, $k_{f,T}=1.0\times10^{-3}\ (m^2.mol^{-1}.s^{-1})$, was estimated by using the same considerations as described for the Volmer reaction. Since the estimated constants are implicitly coupled, the abovementioned procedure was reiterated in order to refine their values.

The results of the model predictions, using the kinetic rate constants obtained above, were reasonably comparable to the experimental data as shown by the dashed lines in Figure II-2. The model was able to properly reflect both the lower and higher

Tafel slopes, while the pH dependence of the experimental polarization curves were successfully captured as well. That suggest that the kinetics and the mechanism of the HER from hydrogen ions in chloride containing solutions can be reasonably explained by the sequence of the elementary steps incorporated into the model (Reactions (II-4) through (II-6)).

II.3.2: HER from acetic acid

The change in the behavior of the steady state voltammograms due to the addition of acetic acid at pH 4 and pH 5 are shown in Figure II-3. The addition of acetic acid significantly increased the limiting current density. Theoretically, the contribution of acetic acid to the limiting current could be through two pathways: via direct reduction of acetic acid as a parallel electrochemical reaction, or by buffering the hydrogen ion concentration at the electrode surface via homogeneous dissociation of acetic acid. The relatively high equilibrium constant for acetic acid dissociation (e.g. 10^{-5} vs. 10^{-14} for water) and the fast reaction kinetics, allows acetic acid to readily dissociate when the local concentration of hydrogen ion in the vicinity of the electrode surface is decreased at mass transfer limiting current conditions. Therefore it is expected that the surface concentration of both hydrogen ions and undissociated acetic acid to be negligibly small at limiting current conditions. The limiting current could therefore be described by the superposition of the acetic acid and hydrogen ion mass transfer limiting currents. For the case of RDE electrode the mass transfer from the bulk is described by the well-known Levich equation:

$$i_{lim} = 0.62 \times 10^3 \, nFD^{2/3}\omega^{1/2}v^{-1/6}C_b \qquad\qquad (\text{II-33})$$

where C_b (M) is the bulk concentration of the reactant and D (m^2/s) is its diffusion coefficient, v (m^2/s) is the kinematic viscosity of the solution, ω (rad/s) is angular velocity, F (C/mol) is Faraday's constant, and n is the number of electron transferred.
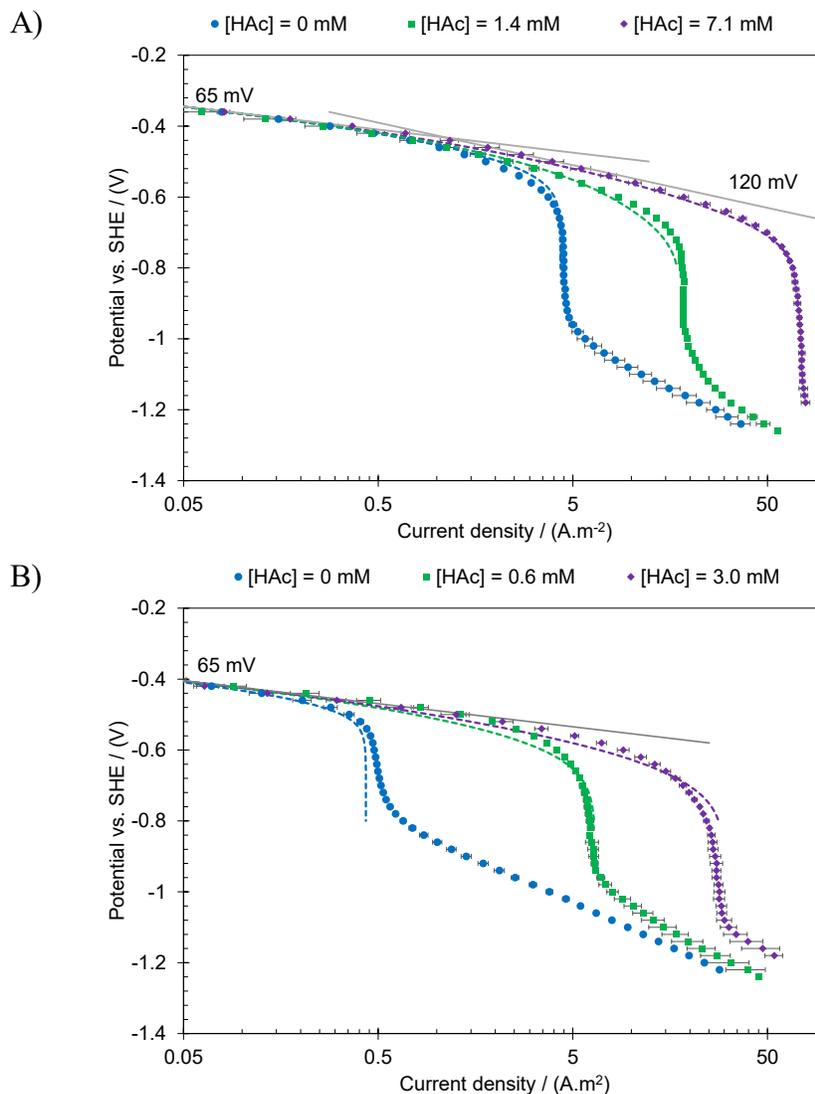

Figure II-3. Cathodic steady state voltammograms obtained in 0.1 M NaCl solution, at 30°C, 2000 rpm, and $C_{t,HAc}$=0 (blue circles), $C_{t,HAc}$=1.66 mM (green squares), $C_{t,HAc}$=8.3 (purple diamonds) on polycrystalline gold, at A) pH=4 and B) pH=5.

Figure II-4 demonstrates the magnitude of limiting current as a function of the total concentrations (hydrogen ion plus undissociated acetic acid), including the correction for different diffusion coefficients of the two species following the Levich equation. In support of the above arguments, the linear behavior of the trend-line and the fact that it is crossing the origin with a good accuracy, suggests that acetic acid is a strong buffer in the sense that the thermodynamics and kinetics allows this species to readily dissociate and buffer the hydrogen ion concentration at mass transfer limiting conditions. That results in the increased limiting currents, irrespective of whether undissociated acetic acid is directly involved in the HER or it is merely a "carrier" for hydrogen ion.

The two straight lines added to Figure II-3. A, highlight the Tafel slopes of 65 mV and 120 mV. At lower current densities, the polarization curves in the presence of acetic acid are overlapping with the one obtained when no acetic acid was present, where a 65 mV Tafel slope agrees well with the experimental results. That suggests the addition of acetic acid did not result in any significant change of the electrochemical behavior of the system in the lower Tafel slope range. At higher current densities and increasing acetic acid concentrations, a 120 mV Tafel slope gradually emerges, similar to those observed at lower pH values in HCl solutions. The higher current densities observed in ~120 mV Tafel slope range could be related to the presence of acetic acid in the solution, as described in paragraphs below. At pH 5, as shown in Figure II-3.B, no clear secondary Tafel slope is observed. Nevertheless, at low current densities, a 65 mV Tafel slope was found to fit the observed experimental behavior well. The polarization behavior of the

cathodic current at lower Tafel slope range was not altered in the presence of acetic acid at pH 5, similar to what was observed at pH 4.
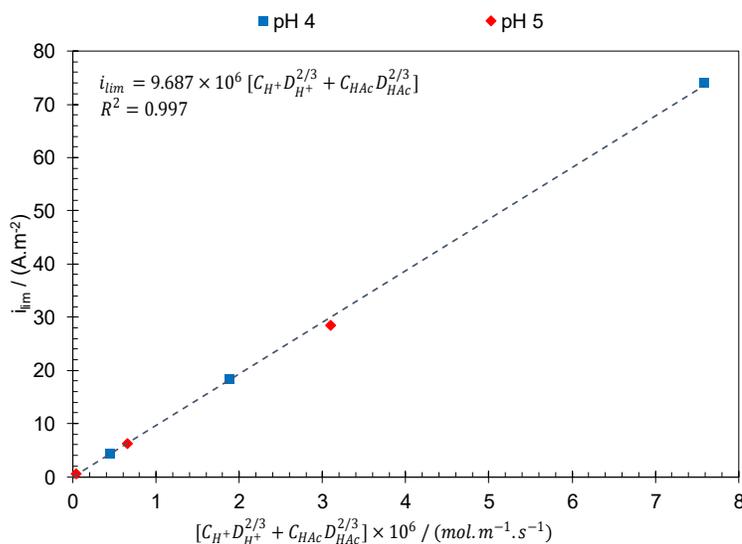

Figure II-4. cathodic limiting current density in 0.1 M NaCl solution, 30°C, 2000rpm at various pH values and undissociated acetic acid concentrations.

In order to quantify the observed electrochemical behavior shown in Figure II-3, the model developed for HER from hydrogen ion, was initially modified to accommodate the homogeneous acetic acid dissociation reaction, while no additional electron-transfer reactions were included. An example of the results obtained using the modified model is presented in Figure II-5, showing that the limiting current density can be explained even if acetic acid is not considered an electro-active species. In this initial attempt, while the current densities at 65 mV range were in good agreement with the experimental data, the model failed to properly predict the polarization behavior at higher current densities. This suggests that the HER from hydrogen ion reduction alone was not sufficient to explain the steady state polarization curves obtained in the presence of acetic acid. The main

shortcoming was a result of the Heyrovsky rate determining step. The polarization behavior at higher current density range was therefore associated with electrochemical activity of acetic acid.
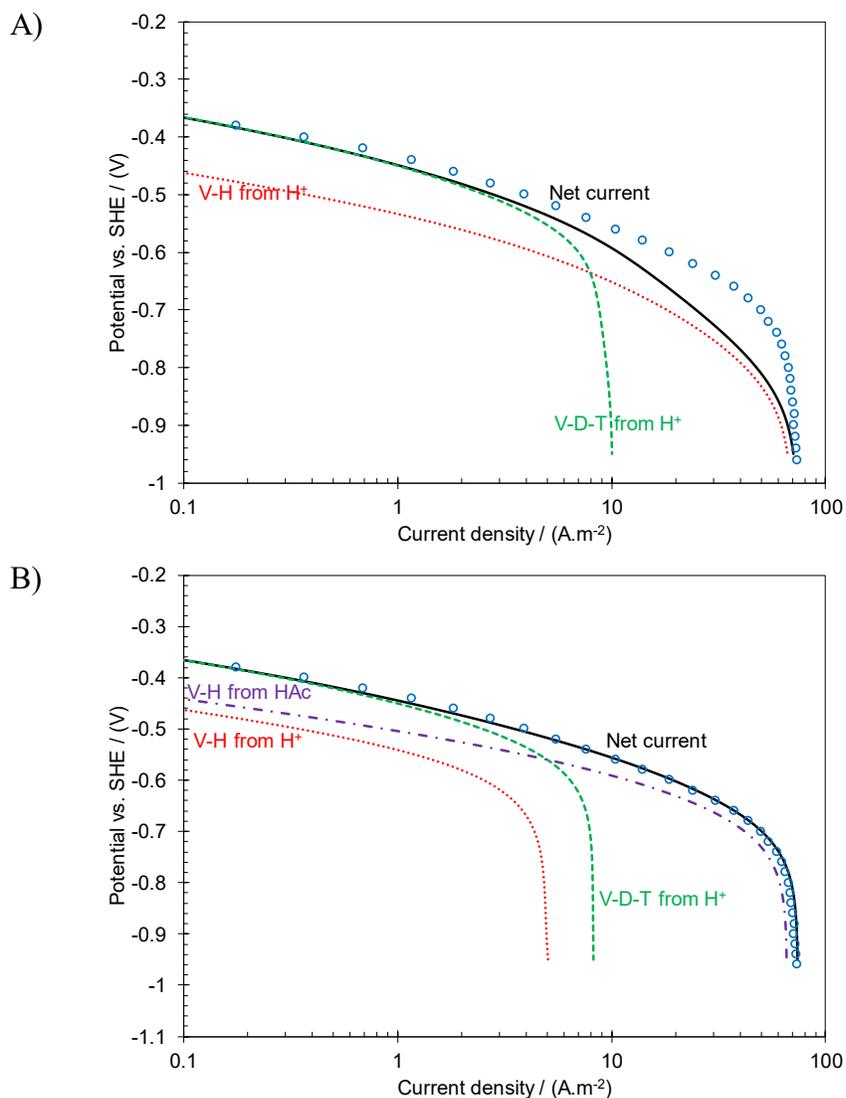

Figure II-5. The illustration of the contribution of each reaction route (V-H: Volmer-Heyrovsky, V-D-T: Volmer-Diffusion-Tafel) to the net current density at pH 4, 30°C, 2000 rpm, and $C_{t,HAc}$=8.3, undissociated acetic acid was considered A) not electroactive, B) electrochemically active. Experimental data presented as open circles.

In the mechanistic discussion of HER from elementary steps, when the HER occurs concurrently from both hydrogen ions and a weak acid (acetic acid in this discussion), the two sets of reactions should be discussed simultaneously, owing to the fact that they are sharing the same intermediate species (H_{ads}). In the conditions of the present study, considering the mechanism in HCl solutions on gold surface, the HER reaction is limited by desorption steps over the whole range of cathodic currents.

As shown in the following, that the quasi-equilibrium of the Volmer step for the weak acid reaction (e.g. Reaction (II-12)) is identical to that of the hydrogen ion reaction (Reaction (II-4)), when the surface concentration of the weak acid and its corresponding conjugate base are constrained by the dissociation equilibrium. Hence, the electrochemical equilibrium of H_{ads} (and the associated surface overage θ) at steady state, remains unaffected in the presence of a weak acid. In other words, the presence of acetic acid in the solution does not change the magnitude of the θ at a fixed pH and potential, hence, in this regards, it has no effect on the observed steady state polarization behavior. Nevertheless, the presence of a parallel Volmer reaction for the weak acid could possibly influence the kinetics, i.e. how fast the equilibrium is reached. On the other hand, the Tafel recombination and the surface diffusion steps are not directly affected by the presence of acetic acid, which leaves a Heyrovsky type electro-desorption step as the only reaction pathway for acetic acid to influence the electrochemical response of the studied system.

Using a more fundamental treatment for expressing the charge transfer rate of a redox couple [53], the rate of Volmer step (Reaction (II-4)) can be expressed via Equation (II-34).

$$v_{V,H^+} = k_{0,H^+} \left[(1-\theta)C_{H^+} e^{-\lambda_V u\theta} e^{-\beta_V \frac{F\left(E-E_{0,H^+}\right)}{RT}} \right. $$

$$\left. - \psi\, \theta e^{(1-\lambda_V)u\theta} e^{(1-\beta_V)\frac{F\left(E-E_{0,H^+}\right)}{RT}} \right]$$

(II-34)

Where k_{0,H^+} is the standard reaction rate constant, E_{0,H^+} is the standard potential, and ψ is the surface concentration of H_{ads} when $\theta=1$. At quasi-equilibrium condition, the surface coverage of H_{ads} (θ) can be expressed through Equation (II-35), considering that $v_{V,H^+} \approx 0$.

$$\frac{\theta}{1-\theta} e^{u\theta} = \frac{1}{\psi}\, C_{H^+} e^{\frac{-F\left(E-E_{0,H^+}\right)}{RT}}$$

(II-35)

A comparison of the Equation (II-35) with Equation (II-32) shows that the adsorption equilibrium constant can be expressed as :

$$K = \frac{1}{\psi}\, e^{\frac{FE_{0,H^+}}{RT}}$$

(II-36)

A similar treatment can be applied for the a Volmer type reaction from acetic acid (Reaction (II-12)).

Assuming identical symmetry factors (λ and β) to those of hydrogen ion, one can write:

$$v_{V,HAc} = k_{0,HAc} \left[(1-\theta)C_{HAc} e^{-\lambda_V u\theta} e^{-\beta_V \frac{F(E-E_{0,HAc})}{RT}} \right.$$

$$\left. - \psi\, \theta C_{Ac^-} e^{(1-\lambda_V)u\theta} e^{(1-\beta_V)\frac{F(E-E_{0,HAc})}{RT}} \right] \tag{II-37}$$

Considering the chemical equilibrium of acetic acid dissociation (Reaction (II-16)), the concentration of Ac⁻ can be expressed in terms of C_{H+} and C_{HAc} based on Equation (II-16).

By introducing Equation (II-16) into Equation (II-37), at quasi-equilibrium conditions, the surface coverage of H_{ads} (θ) resulting from Reaction (II-12), can be expressed in terms of Equation (II-38).

$$\frac{\theta}{1-\theta} e^{u\theta} = \frac{1}{\psi} \frac{C_{H^+}}{K_{diss}} e^{\frac{-F(E-E_{0,HAc})}{RT}} \tag{II-38}$$

Furthermore, by introducing the definition of Equilibrium constant ($K_{diss}=exp(-\Delta G_{diss}/RT)$) and the standard potential ($E_{0,HAc}=-\Delta G_{V,HAc}/F$) based on the Gibbs free energy, a simple mathematical manipulation shows that $exp(FE_{0,HAc}/(RT))/K_{diss}=exp(FE_{0,H+}/RT)$, hence, Equation (II-38) is simplified to that obtained for the quasi-equilibrium from hydrogen ion (Equation (II-35)).

Additionally, the quasi-equilibrium of the Volmer reaction from acetic acid can be expressed via an equivalent relationship to that of Equation (II-32) for the hydrogen ion:

$$\frac{\theta}{1-\theta} e^{u\theta} = K_{V,HAc} \frac{C_{HAc}}{C_{Ac^-}} e^{\frac{-FE}{RT}} \tag{II-39}$$

Considering Equations (II-36), (II-38) and (II-39) :

$$K_{V,HAc} = \frac{1}{\psi} e^{\frac{FE_{0,HAc}}{RT}} = K_{diss} \frac{1}{\psi} e^{\frac{FE_{0,H^+}}{RT}} = K_{diss} \times K_{V,H^+} \tag{II-40}$$

The equilibrium constant of the Volmer reaction from hydrogen ion (Reaction (II-4)) can be used to obtain the equilibrium constant for acetic acid (Reaction (II-12)), where $K_{V,HAc}=K_{V,H+}\times K_{HAc}= 8.75\times10^{-9}$. However, no information about the kinetic rate constants of this reaction could be obtained from steady state voltammograms presented in Figure II-3, hence, $k_{V,f,HAc}$ can be set to any arbitrary value (here it was set to zero). The reaction rate constant of the Heyrovsky step (Reaction (II-13)) was obtained based on the best fit of the model to the experimental data ($k_{H,f,HAc}=3\times10^{-11}$ $(m^3.mol^{-1}.s^{-1})$).The dashed lines in Figure II-3 demonstrate the results obtained from the model, using the estimated kinetic parameters.

The mechanistic discussion above suggests that the HER from acetic acid was through a Heyrovsky type recombination of adsorbed hydrogen atom with undissociated acetic acid (Reaction (II-13)) proceeding the Volmer reaction from hydrogen ions (Reaction (II-4)). Therefore, the net acetic acid reduction reaction in acidic environments on gold is best represented by Reaction (II-41):

$$H^+{}_{(aq)} + HAc_{(aq)} \rightarrow H_{2\,(g)} + Ac^-_{(aq)} \qquad\qquad (\text{ II-41 })$$

Reaction (II-41) suggests that the rate of acetic acid reduction should be sensitive to both undissociated acetic acid and hydrogen ion concentrations. This is shown in Figure II-6, where the contribution of each reaction route, calculated by the model, is presented in terms of a change in the solution pH (in Figure II-6.A) and undissociated acetic acid concentration (in Figure II-6.B). Figure II-6.A demonstrates the effect of changing pH from 4 to 5, while the concentration of undissociated acetic acid is constant (1.4 mM in both cases). Figure II-6.B shows the effect of increasing

undissociated acetic acid concentration from 1.4 mM to 14 mM while a constant solution pH of 4 is maintained. The Volmer-Heyrovsky reaction route from hydrogen ion (blue long dashed lines) and acetic acid (red dotted dashed lines) are shown in Figure II-6, which were found to behave rather similarly. At the conditions considered here, a Tafel slope of 120 mV was obtained for both routs, which is associated with *0.05<θ<0.95*, where the surface coverage can be expressed in terms of a Temkin type adsorption isotherm [61]. At such conditions the Heyrovsky rate determining step (Reaction(II-6)) has a 1.5 reaction order vs. hydrogen ion concentration, what is observed in Figure II-6.A when comparing the contribution of this reaction route at pH 4 and 5, at a constant undissociated acetic acid concentration. The rate of this reaction (Equation (II-9)) is shown to be dependent on both hydrogen ion concentration and the surface coverage of H_{ads}, therefore, the 1.5 reaction order (vs. H^+ concentration) is a result of a direct first order dependence on hydrogen ion concentration as a reactant, and a 0.5 order pH dependence through $θ$ containing terms.

A similar behavior was observed for the Volmer-Heyrovsky reaction route involving undissociated acetic acid (Reaction (II-13)). Although, the first order direct dependence on hydrogen ion concentration in the previous case is now replaced with a first order direct dependence on undissociated acetic acid concentration, as the reactant, in accordance with the reaction rate expression (Equation (II-15)). This first order dependence can be clearly observed in Figure II-6.B. On the other hand, the reaction rate dependence on surface coverage of H_{ads} remains unchanged, suggesting a 0.5 order

dependence on hydrogen ion concentration through θ dependence terms. This latter pH

dependence can also be observed in Figure II-6.A.
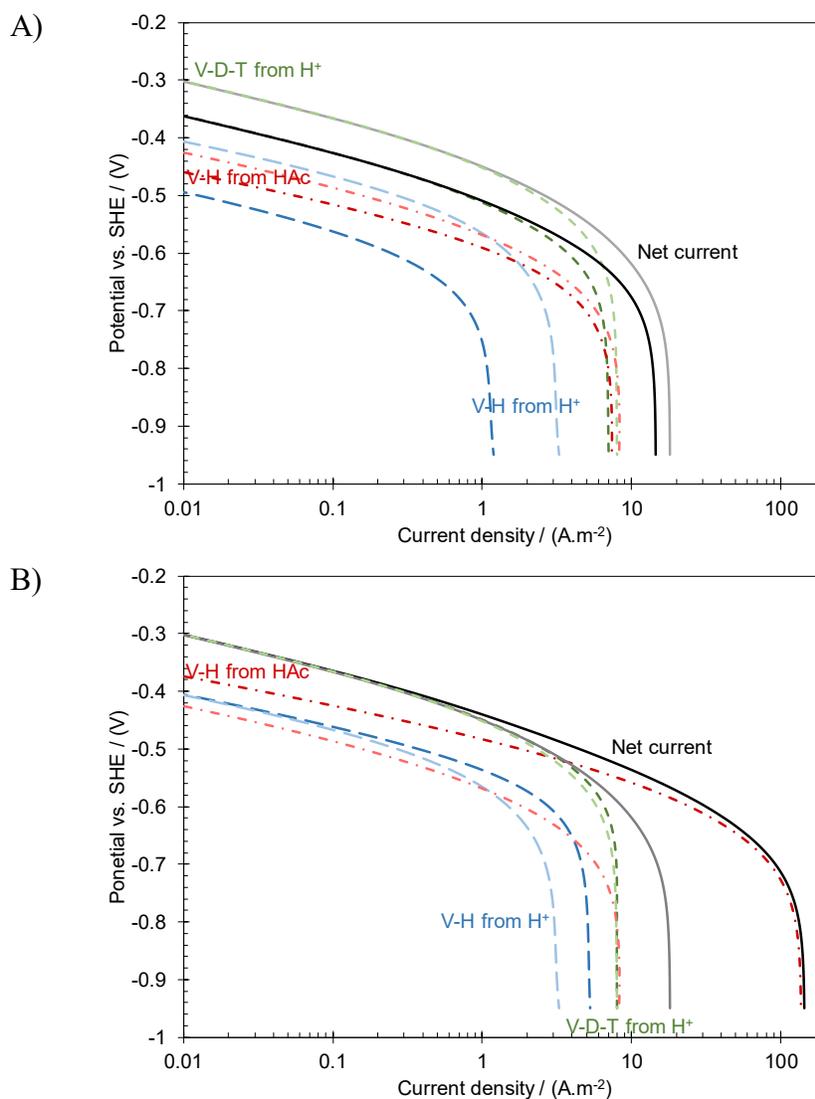
Figure II-6. The rate dependence of each reaction route (V-H from H$^+$: Volmer-Heyrovsky from H$^+$ (long dashed lines), V-D-T: Volmer-Diffusion-Tafel (Short dashed lined), Volmer-Heyrovsky from HAc (dotted dashed lines)) to the net current (solid lines) at 30ºC, 2000 rpm. A) At C_{HAc}=1.4 mM and pH 5 (dark shade) vs. pH 4 (light shad). B) At pH 4 and C_{HAc}=14 mM (dark shade) vs. C_{HAc}=1.4 mM (light shad).

II.4: Summary

The kinetics and the mechanism of the HER reaction was investigated in mildly acidic 0.1 NaCl solutions. The steady state cathodic polarization curves showed a 65 mV Tafel slope at lower current density range and a 120 mV Tafel slope in the higher current density range. The agreement of the characteristic parameters, the Tafel slopes and the reaction order, with those obtained previously in sodium perchlorate solutions suggest that the presence of chloride in the solution up to 0.1 M does not alter the mechanism of the HER.

In the presence of acetic acid, the analysis of the polarization curves revealed that the HER reaction occurs from both hydrogen ion and undissociated acetic acid, simultaneously. In the 65 mV Tafel slope range acetic acid does not significantly contribute to the cathodic currents. However, the 120 mV range was found to be dominated by the reduction of undissociated acetic acid.

The HER from acetic acid was found to occur via a Heyrovsky-type electro-desorption elementary step, where the undissociated acetic acid reacts with an adsorbed hydrogen atom. It was shown that the quasi-equilibrium of the Volmer reaction that defines the surface coverage of adsorbed hydrogen atoms, is not affected by the proton donor species. Hence, the electro-adsorption equilibrium constant obtained for hydrogen ion can be directly used to quantify the electro-adoption of hydrogen atoms from acetic acid or other weak acids.

Nomenclatures

b	Tafel slope (mV)
β_j	Electrochemical symmetry factor of reaction j

C_i	Concentration of species i (mol.m^{-3})
D_i	Diffusion coefficient of species i (m^2.s^{-1})
δ	Diffusion layer thickness of RDE
E	Applied potential (V)
F	Faraday's constant (C.mol^{-1})
Φ	Potential in the electrolyte (V)
i	Current density (A.m^{-2})
K_j	Equilibrium constant of reaction j
$k_{f,j}$	Forward reaction rate constant of reaction j
$k_{b,j}$	backward reaction rate constant of reaction j
λ_j	Symmetry factor of reaction j due to interaction of adsorbed species
N_i	Flux of species i (mol.m^{-2}.s)
ν	Kinematic viscosity (m^2.s^{-1})
Ω	Rotation speed (rad.s^{-1})
q	Charge required for surface coverage of θ (C.m^{-2})
R	Universal gas constant (J.mol^{-1}.K^{-1})
R_i	Rate of homogeneous reaction i (mol.s^{-1}.m^{-3})
u	Correlation coefficient of H$_{ads}$ Interaction energy
s_{ij}	Stoichiometric coefficient of species i in reaction j
T	Absolute temperature (K)
t	Time (s)
θ	Surface coverage of H$_{ads}$
u_i	Mobility of species i (m.s^{-1})
υ_j	Reaction rate of reaction j (mol.m^{-2}.s^{-1})
v	Velocity (m.s^{-1})
x	Spatial dimension (m)
z_i	Charge of species i

III.   Pitzer parameters of CO_2/H_2O system

The Pitzer parameters for the interaction of the species in H_2O-CO_2-NaCl system used in the present study are tabulated below. The second virial coefficients $\beta^{(0)}$ and $\beta^{(1)}$ and the single electrolyte third virial coefficient C^ϕ of H^+ and Cl^- pair are shown in Table III-1, based on the study by Holmes et al. [320]

Table III-1. Pitzer parameters for H^+, Cl^- interaction from Holmes et al. [320]

	$\beta^{(0)}_{H^+,Cl^-}$	$\beta^{(1)}_{H^+,Cl^-}$	$C^\phi_{H^+,Cl^-}$
c_1	1.7690E-1	2.973E-1	7.24E-4
c_2	-9.140E-2	1.6147E1	0.0
c_3	0.0	-1.7631E-2	0.0
c_4	-4.034E-4	0.0	-6.072E-5
c_5	6.20E-6	7.20E-5	0.0

$$parameter = c_1 + c_2 \ln\left(\frac{\rho_T}{\rho_{298.15}}\right) + c_3\left(\rho_T - \rho_{298.15}\right) + c_4\left(T - 298.15\right) + c_5(P - 1)$$

where ρ_T, density in kg.m^{-3} at temperature T, and P is pressure in bar.

The Pitzer parameters reported by Moller [321] were used to describe the interaction of the cataion-anaion pair, Na^+, Cl^- as shown in Table III-2.

Table III-2. Pitzer parameters for Na$^+$, Cl$^-$ interaction from Moller.[321]

	$\beta_{Na^+,Cl^-}^{(0)}$	$\beta_{Na^+,Cl^-}^{(1)}$	C_{Na^+,Cl^-}^{ϕ}
c_1	1.43783204E+01	-4.83060685E-01	-1.00588714E-01
c_2	5.60767406E-03	1.40677479E-03	-1.80529413E-05
c_3	-4.22185236E+02	1.19311989E+02	8.61185543E00
c_4	-2.51226677E00	0.0	1.24880954E-02
c_5	0.0	0.0	0.0
c_6	-2.61718135E-06	0.0	3.41172108E-08
c_7	4.43854508E00	0.0	6.83040995E-02
c_8	-1.70502337E00	-4.23433299E00	2.93922611E-01

$$parameter = c_1 + c_2T + \frac{c_3}{T} + c_4 \ln(T) + \frac{c_5}{T-263} + c_6 T^2 + \frac{c_7}{680-T} + c_7/(T-227)$$

The interaction of Na$^+$, OH$^-$ pair was described based on the study of Pabalan and Pitzer [322] as shown in Table III-3.

Table III-3. Pitzer parameters for Na$^+$, OH$^-$ interaction from Pabalan and Pitzer.[322]

	$\beta_{Na^+,OH^-}^{(0)}$	$\beta_{Na^+,OH^-}^{(1)}$	C_{Na^+,OH^-}^{ϕ}
c_1	2.7682478E+02	4.6286977E+02	-1.6686897E+01
c_2	-2.8141778E-03	0.0	4.0534778E-04
c_3	-7.3755443E+03	-1.0294181E+04	4.5364961E+02
c_4	3.7012540E-01	0.0	-5.1714017E-02
c_5	-4.9359970E+01	-8.5960581E+01	2.9680772E+00
c_6	1.0945106E-01	2.3905969E-01	-6.5161667E-03
c_7	7.1788733E-06	0.0	-1.0553037E-06
c_8	-4.0218506E-05	-1.0795894E-04	2.3765786E-06
c_9	-5.8847404E-09	0.0	8.9893405E-10
c_{10}	1.1931122E+01	0.0	-6.8923899E-01
c_{11}	2.4824963E+00	0.0	-8.1156286E-02
c_{12}	-4.8217410E-03	0.0	0.0

$$parameter = c_1 + c_2P + \frac{c_3 + c_4P}{T} + c_5 \ln(T) + (c_6 + c_7P)T + (c_8 + c_9P)T^2 + \frac{c_{10}}{T-227}$$
$$+ \frac{(c_{11} + c_{12}P)}{647-T}$$

The interaction of Na$^+$ with carbonate (CO$_3^{2-}$) and bicarbonate ions (HCO$_3^-$) have been studied by a number of researchers with a reasonable agreement when the whole set

of parameters are used in the model. The results reported by Polya et al. [323], as shown in

Table III-4, were used in the present study as they cover a wide pressure (up to 70 bar)

and temperature range (298 to 523 K).

Table III-4. Pitzer parameters for Na^+, HCO_3^- and CO_3^{2-} interaction from Polya et al. [323].

	$\beta^{(0)}_{Na^+,HCO_3^-}$	$\beta^{(1)}_{Na^+,HCO_3^-}$	$C^{\phi}_{Na^+,HCO_3^-}$	$\beta^{(0)}_{Na^+,CO_3^{2-}}$	$\beta^{(1)}_{Na^+,CO_3^{2-}}$	$C^{\phi}_{Na^+,CO_3^{2-}}$
c_1	6.61E-02	-4.116E+00	0.0	5.153E-01	2.044E+00	-9.140E-02
c_2	0.0	6.309E-03	0.0	-5.991E-04	-4.303E-03	0.0
c_3	0.0	9.240E+02	0.0	0.0	0.0	0.0
c_4	0.0	-5.202E+01	0.0	-2.581E+01	-2.545E+01	6.482E+00
c_5	0.0	-8.026E+01	0.0	-2.659E+00	3.618E+02	8.048E+00
c_6	3.75951E-08	0.0	0.0	0.0	0.0	0.0
c_7	0.0	1.634E-04	0.0	8.750E-05	0.0	-2.890E-05
c_8	0.0	-1.39E-07	0.0	-2.660E-08	0.0	0.0

$$parameter = c_1 + c_2 T + \frac{c_3}{T} + \frac{c_4}{T-210} + \frac{c_5}{647-T} + c_6 \frac{(T-443)^3}{3} + c_7 (P-1) + \frac{c_8(P-1)^2}{2}$$

The second virial Pitzer parameters (θ), describing the interaction of the ions with

the same charge, are listed in Table III-5 and Table III-6.

Table III-5. Pitzer parameters for Na^+, H^+ pair and Cl^-, OH^- pair interaction from Christov and Moller. [324]

	θ_{Na^+,H^+}	θ_{Cl^-,OH^-}
c_1	4.81363462E-02	1.10485703E-01
c_2	0.0	0.0
c_3	0.0	0.0
c_4	-4.05430635E00	-4.93613455E01

$$Parameter = c_1 + c_2 T + c_3 T^2 + c_4 T^3$$

Table III-6. Pitzer parameters for common ion interaction.

Parameter	Value	Reference
θ_{Cl^-,HCO_3^-}	0.0359	Piper et al. [325]
$\theta_{Cl^-,CO_3^{2-}}$	-0.053	Piper et al. [325]
$\theta_{HCO_3^-,CO_3^{2-}}$	-0.04	Harvie et al. [326]
$\theta_{CO_3^{2-},OH^-}$	0.1	Harvie et al. [326]

The ion-neutral species Pitzer interaction parameter, associated with dissolved CO_2 and Na^+ and Cl^- are listed in Table III-7, based on the study of He et al. [327]. The interaction of CO_2 with bicarbonate and carbonate ions can also be significant at high CO_2 partial pressures and also at near neutral/alkaline solutions where the concentration of these species are large. In addition to affecting the solubility of CO_2, through it's activity coefficient, the major influence of this parameter is on the activity coefficient of bicarbonate and carbonate ions.

Table III-7. Pitzer parameters for CO_2, Na^+ and Cl^- interaction from HE et al. [327]

	λ_{CO_2,Na^+}	λ_{CO_2,Cl^-}
c_1	-5496.38465	1659.944942
c_2	-3.326566	0.9964326
c_3	0.0017532	0.00052122
c_4	109399.341	33159.6177
c_5	1047.021567	315.827883

$$Parameter = c_1 + c_2 T + c_3 T^2 + \frac{c_4}{T} + c_5 \ln(T)$$

As it can be seen in Equation (B.4-28), the term $m_n \lambda_{nx}$ depends on the concentration of dissolved CO_2, which can be large at high CO_2 partial pressures (~0.5 m at 20 bar). However, the reported values for this parameter in a study by Li and Duan [209] and that reported by Wong et al. [328] are widely different, and results in significant inconsistencies in speciation calculations, therefore, not included in the present model.

This can be due to lake of sufficient experimental data in a reasonable range of

parameters (T and pCO_2), used for obtaining these parameters. No reported Pitzer

parameters for H_2CO_3 is available in the literature, perhaps due to the experimental

difficulties in its distinction from CO_2. For the lack of a better understanding, the pitzer

parameters reported for CO_2 were also used to determine the activity coefficient of

H_2CO_3.

Table III-8. Pitzer parameters for CO_2, CO_2 interaction from Li and Duan. [209]

	λ_{CO_2,CO_2}
c_1	$-8.603471564E{-}01$
c_2	$3.297141654E{-}03$
c_3	$6.309267405E{+}01$
c_4	$-4.098960500E{-}06$
c_5	$1.529493614E{+}01$
c_6	$6.506644253E{-}03$
c_7	$-9.637977140E{-}04$
c_8	$-3.238222665E{-}01$
c_9	$1.599113719E{-}02$
c_{10}	0.0
c_{11}	$-1.886733300E{-}05$

$$Parameter = c_1 + c_2 T + \frac{c_3}{T} + c_4 T^2 + \frac{c_5}{630 - T} + c_6 P + c_7 \, P \ln(T) + \frac{c_8 \, P}{T} + \frac{c_9 \, P}{630 - T} + \frac{c_{10} \, P^2}{(630 - T)2} + c_{11} \, T \ln(P)$$

Thesis and Dissertation Services